

**Influence of Architecture, Materials, and Processing on  
Low Temperature Solid Oxide Fuel Cell (LT-SOFC)  
Performance**

by

Xinge Zhang

B.A. Eng., Nanjing University of Industrial Technology, 1983

M.A. Eng., Dalian University of Technology, 1991

A DISSERTATION SUBMITTED IN PARTIAL FULFILLMENT OF  
THE REQUIREMENTS FOR THE DEGREE OF  
DOCTOR OF PHILOSOPHY

in

The Faculty of Graduate Studies

(Mechanical Engineering)

THE UNIVERSITY OF BRITISH COLUMBIA

(Vancouver)

July 2009

© Xinge Zhang, 2009

## Abstract

The goal of this dissertation is to develop low temperature solid oxide fuel cells (SOFCs) through the understanding of cell material and component fabrication technology. A typical anode supported thin electrolyte cell structure has been adopted, fabricated by wet ceramic processing and co-firing.  $\text{Sm}_{0.2}\text{Ce}_{0.8}\text{O}_{1.9}$  (SDC) electrolyte cells supported by  $\text{Ni-Y}_{0.16}\text{Zr}_{0.84}\text{O}_{1.92}$  (YSZ) cermet substrates, with  $\text{Sm}_{0.5}\text{Sr}_{0.5}\text{CoO}_3$  cathode and Ni-SDC anode, demonstrate a high performance of  $0.89 \text{ W cm}^{-2}$  at  $600^\circ\text{C}$ . A designed experiment quantitatively reveals the internal shorting problem due to the mixed ionic and electronic conductivity of the SDC electrolyte. The internal shorting current density of the thin SDC cell reaches  $0.85 \text{ A cm}^{-2}$  at  $600^\circ\text{C}$  under open circuit voltage (OCV) conditions, which limits the fuel utilization to less than 65% and electrical efficiency to below 25%. In order to eliminate the internal shorting problem, a unique bi-layered electrolyte structure has been developed by adding a thin zirconia based electrolyte layer as an electronic blocking layer. A YSZ/SDC bi-layered electrolyte cell prepared by wet ceramic processing and co-firing generated  $0.34 \text{ W cm}^{-2}$  peak power density at  $650^\circ\text{C}$ , with an open circuit voltage (OCV) of over 1.0V. Further improvement of the cell performance was achieved by using a  $\text{Sc}_{0.2}\text{Ce}_{0.01}\text{Zr}_{0.79}\text{O}_{1.9}$  (SSZ)/SDC bi-layered electrolyte. The cell reached  $0.50 \text{ W cm}^{-2}$  at  $650^\circ\text{C}$ . Electrochemical impedance analysis reveals that the ionic resistance of the bi-layered electrolyte prepared by co-firing is one order of magnitude higher than the theoretical value, indicating that interaction between the two electrolytes during the co-firing is a main limit. In order to eliminate the bi-layered electrolyte interaction, pulsed laser deposition (PLD) technology is applied for the bi-layered electrolyte cell fabrication. The cell fabricated by PLD reaches power densities of  $0.95 \text{ W cm}^{-2}$  at  $600^\circ\text{C}$ , and  $1.37 \text{ W cm}^{-2}$  at  $650^\circ\text{C}$  with open circuit voltage (OCV) values larger than 1.02 V, the highest performance ever reported in the literature. Nonetheless, the bi-layered electrolyte cells exhibit relatively high degradation rates. A study on the degradation of bi-layered electrolyte cells indicates that the cathode degradation is the main contributor. Therefore, an optimization of cathode compositions and fabrication conditions is important to improve the cell stability.

# Table of Contents

Abstract .....	ii
Table of Contents .....	iii
List of Tables.....	viii
List of Figures.....	xi
Nomenclature.....	xvi
List of Abbreviations.....	xviii
Acknowledgements.....	xix
Dedication.....	xxi
Co-authorship Statement.....	xxii

## **1. Chapter One. SOFC Fundamentals and Literature Review on Low**

<b>Temperature SOFCs.....</b>	<b>1</b>
1.1 SOFC fundamentals.....	1
1.1.1 Nernst potential and thermodynamic efficiency.....	2
1.1.2 Cell voltage and cell resistance.....	4
1.1.3 Electrical efficiency and fuel utilization.....	7
1.1.4 Stack voltage and output power.....	7
Example 1. Basic requirement of cell component resistances.....	8
1.2 Conventional SOFC materials and performances.....	8
1.2.1 Cell materials and properties.....	8
Example 2. Operating temperature of YSZ electrolyte supported cell.....	10
1.2.2 Cell structure and performance.....	13
Example 3. Anode supported planar cell with YSZ electrolyte.....	15
1.2.3 Planar stack components.....	16
Example 4. Fe-Cr alloy oxidation and contact resistance growth with time.....	17
1.3 Advantages and challenges of SOFC.....	18
1.4 Literature review on low temperature SOFCs.....	20
1.4.1 Electrolytes of high ionic conductivity.....	21
1.4.2 Challenge and approach.....	28
1.4.3 Cathode.....	29
1.4.4 Anode.....	35

1.5	Fabrication –thin film deposition techniques.....	35
1.5.1	Wet ceramic processes.....	36
1.5.2	Vacuum deposition techniques.....	37
1.6	Summary.....	40
1.7	Objective and outline of dissertation work.....	42
1.8	References.....	45
<b>2.</b>	<b>Chapter Two. Cell Fabrication and Characterization .....</b>	<b>56</b>
2.1	Cell materials.....	57
2.2	Cell structures.....	58
2.3	Cell fabrication.....	58
2.4	Composition and processing.....	59
2.4.1	NiO-YSZ composition and tape casting.....	59
2.4.2	Anode, electrolyte and cathode pastes and screen printing.....	62
2.4.3	Cell co-firing and ironing.....	64
2.5	Pulsed laser deposition (PLD).....	68
2.6	Cell characterization.....	71
2.6.1	Physical characterization.....	71
2.6.2	Electrochemical characterization.....	72
2.6.3	Post-mortem analysis.....	73
2.7	Summary.....	73
2.8	References.....	75
<b>3.</b>	<b>Chapter Three. Performance of LT-SOFCs with SDC Electrolytes.....</b>	<b>76</b>
3.1	Introduction.....	76
3.2	Results and discussion.....	78
3.2.1	Cell microstructural characterization and EDS analysis.....	81
3.2.2	Zr-micro-islands.....	84
3.3	Conclusions.....	86
3.4	References.....	87
<b>4.</b>	<b>Chapter Four. Composite Cathode Study .....</b>	<b>88</b>
4.1	Introduction.....	89
4.2	Experimental procedure.....	90

4.3	Results and discussion .....	92
4.3.1	SSC+SDC phase structure .....	92
4.3.2	Open circuit voltage (OCV).....	93
4.3.3	Effects of $T_{s,c}$ on cell performance and electrochemical resistance .....	94
4.3.4	SEM observation.....	97
4.3.5	Effects of cathode thickness.....	98
4.3.6	Effects of wet contact pastes.....	102
4.4	Conclusions.....	105
4.5	References.....	106
<b>5.</b>	<b>Chapter Five. Internal Shorting and Fuel Loss of an LTSOFC with SDC</b>	
	<b>Electrolyte.....</b>	<b>107</b>
5.1	Introduction.....	107
5.2	Experimental procedure .....	108
5.3	Results and discussion .....	112
5.3.1	Cell electrochemical performance .....	112
5.3.2	Water amount and leakage current .....	116
5.3.3	Internal shorting current density based on OCV deviation.....	118
5.3.4	Low electrical efficiency due to internal shorting of the SDC electrolyte	120
5.3.5	The SDC conductivities in this study.....	122
5.3.6	Cathode contribution.....	123
5.3.7	Cell microstructure and EDS analysis .....	124
5.4	Conclusions.....	127
5.5	References.....	129
<b>6.</b>	<b>Chapter Six. A Study on Sintering Aids for SDC Electrolyte.....</b>	<b>131</b>
6.1	Introduction.....	131
6.2	Experimental procedure .....	132
6.3	Results and discussion .....	134
6.4	Conclusions.....	142
6.5	References.....	143
<b>7.</b>	<b>Chapter Seven. A study on the Interaction between Electrolyte Materials .....</b>	<b>144</b>
7.1	Introduction.....	144

7.2	Experimental procedure .....	145
7.3	Results.....	146
7.3.1	Sintering.....	146
7.3.2	X-ray diffraction .....	147
7.4	Discussion.....	151
7.5	Conclusion .....	152
7.6	References.....	153
<b>8. Chapter Eight. Performance of LT-SOFCs with Bi-layered Electrolyte</b>		
	<b>Structure .....</b>	<b>154</b>
8.1	Introduction.....	154
8.2	Experimental procedure .....	156
8.2.1	Starting materials and cell architectures .....	156
8.2.2	Cell electrochemical and morphological characterizations .....	157
8.3	Results and discussion .....	158
8.3.1	Electrolyte thickness control.....	158
8.3.2	Cell test result .....	160
8.4	Conclusion .....	164
8.5	References.....	166
<b>9. Chapter Nine. Stability Study of Cermet Supported SOFCs with Bi-layered SDC-SSZ Electrolyte .....</b>		
	<b>SDC-SSZ Electrolyte .....</b>	<b>168</b>
9.1	Introduction.....	168
9.2	Experimental procedure .....	169
9.3	Results.....	171
9.3.1	Cell A.....	171
9.3.2	Cell B .....	174
9.3.3	Cell C .....	176
9.3.4	Cell D.....	179
9.3.5	Cell E .....	180
9.4	Discussion.....	182
9.4.1	Incubation period .....	182
9.4.2	Performance degradation .....	183

9.4.3 Bi-layered electrolyte resistance .....	185
9.5 Conclusions.....	187
9.5 References.....	188
<b>10. Chapter Ten. LT-SOFCs with Pulsed Laser Deposited Bi-Layered</b>	
<b>Electrolyte.....</b>	<b>190</b>
10.1 Introduction.....	190
10.2 Experimental procedure .....	192
10.3 Results and discussion .....	196
10.3.1 On Si(100) substrate .....	196
10.3.2 On NiO-SDC modified NiO-YSZ substrates.....	199
10.4 Conclusion .....	203
10.5 References.....	204
<b>11. Chapter Eleven. Summary of Dissertation Work and Outlook .....</b>	<b>205</b>
11.1 Cell material development .....	207
11.2 Cell structure.....	207
11.3 Ultra-thin electrolyte SOFCs operating at lower temperature .....	208
11.4 Electrolyte utilization in ultra-thin electrolyte cell .....	208
11.5 Low temperature cost-effective deposition approaches for bi-layered electrolyte cells .....	209
11.6 Metal-supported LT-SOFC development .....	209
11.7 Cathode stability issue .....	210
11.8 References.....	211
<b>12. Appendices.....</b>	<b>212</b>
Appendix A. Thermodynamic calculations .....	212
Appendix B. Electrolyte conductivity and cathode characterization.....	217
Appendix C. Publication list.....	223

## List of Tables

Table 1-1 Nernst potentials and thermodynamic efficiencies of various fuels at different temperatures .....	3
Table 1-2 Conventional SOFC component materials and properties .....	9
Table 1-3 Ni-YSZ anode electrochemical performance ( $R_a$ ).....	11
Table 1-4 Typical performance of LSM cathodes in the literature.....	12
Table 1-5 Properties of $\text{La}_{0.8}\text{Ca}_{0.2}\text{CrO}_3$ and 430 stainless steel interconnects .....	13
Table 1-6 A comparison of the tubular, monolithic, planar, and segmented cells .....	14
Table 1-7 Typical components and materials for a planar stack .....	16
Table 1-8 Typical compositions and properties of MIEC cathodes from the literature (Note: values in the parentheses are the cathode material reduction activation energies in $\text{kJ mol}^{-1}$ .).....	31
Table 1-9 Properties of BSCF cathode materials at different temperatures .....	31
Table 1-10 Typical performance of MIEC cathodes in the literature (Note: values in the parentheses are the cathode reduction activation energy in $\text{kJ mol}^{-1}$ .).....	33
Table 1-11 A brief summary of thin film manufacturing processes.....	41
Table 2-1 Chemical composition, properties, suppliers of starting materials.....	57
Table 2-2 Cell materials and properties in this work.....	57
Table 2-3 Typical print thickness of different screen meshes (one pass before drying) ...	63
Table 2-4 Samples of tape and printed cells .....	63
Table 2-5 Typical temperature profiles used in the cell fabrication .....	64
Table 2-6 Sample cells.....	67
Table 2-7 Physical characterization results of cells fired at $1400^\circ\text{C}$ for 2hr. ....	71
Table 3-1 Ionic conductivity ( $\sigma_i$ ) and electronic conductivity ( $\sigma_e$ ) of YSZ, GDC and their solid solutions at $800^\circ\text{C}$ .....	85
Table 4-1 Material and thickness of cermet supported SDC cells in this study .....	91
Table 4-2 Results of the cells operating at $600^\circ\text{C}$ with composite cathodes of different $T_{s,c}$ .....	95
Table 4-3 Cell performance with SSC#3 cathode sintered at $1050^\circ\text{C}$ .....	96
Table 4-4 Cathode loading and average thickness and the spacer thickness for the stencil printing of cathode after sintering at $1000^\circ\text{C}$ for 2hr .....	99

Table 4-5 Resistances and PPDs of cells with different cathode thicknesses operating at 600°C .....	100
Table 4-6 EIS resistances measured for the cell with 1000°C SSC#3 cathode using 170µm spacer, tested at 600°C .....	105
Table 5-1 Cell performance and EIS results at different temperatures before water test	115
Table 5-2 Cell performance and EIS results at different temperatures after water test...	115
Table 5-3 Water amount (for 20hr) and leakage current under open circuit condition at different temperatures and at 0.5 A cm <sup>-2</sup> at 600°C .....	117
Table 5-4 Leakage current densities based on either OCV value or measured water amount.....	119
Table 5-5 The conductivities of the SDC (GDC) electrolytes [14, 15, 18] .....	123
Table 6-1 Properties and supplier of starting materials .....	133
Table 6-2 Composition, particle size and surface area of powders used in this study ....	133
Table 6-3 Sintering temperature, density and grain size of SDC samples after sintering.....	138
Table 6-4 Electrolyte conductivity at 600°C.....	139
Table 7-1 Supplied materials properties .....	145
Table 7-2 Sample composition and sintering schedule.....	146
Table 7-3 Powder mixture results summary .....	151
Table 8-1 Cell materials, thicknesses, and processing conditions .....	156
Table 8-2 SSZ printed thickness with different SSZ loadings (Binder:SSZ =8:92 weight ratio).....	158
Table 8-3 Cell performance and cell resistances .....	162
Table 8-4 Ionic conductivity ( $\sigma_i$ ) and electronic conductivity ( $\sigma_e$ ) of YSZ, GDC and the mixed composites at 800°C [20].....	163
Table 9-1 Cell materials, thicknesses, and processing conditions .....	170
Table 9-2 Testing strategy of the five bi-layered electrolyte button cells .....	170
Table 9-3 Initial performance of cell A as a function of temperature .....	171
Table 9-4 A summary of the performance and degradation rates of cell B.....	176

Table 9-5 Summary of the cell resistances obtained in this work (initial and 116hr (B), 150hr (C), 90hr(D) and 100hr(E) ) quantified using series and polarization resistance (650°C, OCV).....	183
Table 10-1 Chemical composition, properties, suppliers of starting materials.....	193
Table 10-2 A summary of the cell electrochemical performance.....	2023
Table 12-1 Enthalpies and Gibbs energies of formation, entropies, and heat capacities of the reaction species (Data from Lange’s Handbook 15 <sup>th</sup> edition).....	213
Table 12-2 Thermodynamic calculation results of Reaction 1 using hydrogen as fuel...	215
Table 12-3 Thermodynamic calculation results of Reaction 2 using methane as fuel ....	215
Table 12-4 Thermodynamic calculation results of Reaction 3 using carbon monoxide as fuel.....	215
Table 12-5 Thermodynamic calculation results of Reaction 4 using carbon as fuel.....	215
Table 12-6 Relation of cell efficiency with cell voltage and cell resistance for different fuels.....	216
Table 12-7 Information of the electrolytes and symmetric cells .....	217
Table 12-8 Conductivity results of the three electrolytes SDC, SSZ, and YSZ, in this study.....	219
Table 12-9 Fitting results for electrolyte conductivity .....	219
Table 12-10 SSC and SSC#3 cathode resistances on SDC electrolyte obtained from symmetric cells .....	221

## List of Figures

Figure 1-1 Operational principle of an SOFC.....	2
Figure 1-2 Cross-section of a planar stack configuration .....	16
Figure 1-3 The area specific resistance of the Fe-Cr alloy at different times [24] .....	17
Figure 1-4 YSZ electrolyte supported cell voltage losses [12].....	20
Figure 1-5 Conductivity of SOFC electrolytes .....	21
Figure 1-6 Dependence of ionic conductivity and binding energy for $(\text{CeO}_2)_{0.8}$ - $(\text{LnO}_{1.5})_{0.2}$ at 800 °C on ionic radius of $\text{Ln}^{3+}$ [45] .....	23
Figure 1-7 Concentration dependence of conductivity for Sm-doped $\text{CeO}_2$ [28] .....	24
Figure 1-8 Schematic drawing of oxygen reduction path at cathodes .....	30
Figure 2-1 Schematic drawing of cell types in this work .....	58
Figure 2-2 Flowchart of cell fabrication by wet ceramic processing.....	58
Figure 2-3 Ni-YSZ weight, volume and porosity with different NiO content.....	60
Figure 2-4 Tape casting machine (in this study)-on the left and NiO-YSZ tape sample- on the right. ....	61
Figure 2-5 Screen printing (left- a schematic of the printing process, right- the screen printer used in this study, MC 212 Screen Printer).....	62
Figure 2-6 Thermo gravimetric analysis of burn out of organics in the NiO-YSZ green tape.....	65
Figure 2-7 Thermo-mechanical analysis of the sinterability of electrolyte powders.....	66
Figure 2-8 Linear shrinkage rate versus sintering temperature. ....	66
Figure 2-9 Microstructures of a typical Type I cell with SDC electrolyte. ....	68
Figure 2-10 Schematic of the PLD setup.....	69
Figure 2-11 A schematic setup of test equipment for cell electrochemical characterization.....	72
Figure 3-1 I-V power curves of a cell with a 15 $\mu\text{m}$ SDC single layer electrolyte co- fired with the anode at 1400°C, and with SSC cathode sintered at 900°C, tested at different operating temperatures.....	78
Figure 3-2 I-V power curves of a cell with 5 $\mu\text{m}$ YSZ+15 $\mu\text{m}$ SDC bi-layer electrolyte co-fired with Ni-YSZ anode at 1400°C, and SSC cathode sintered at 900°C, tested at different operating temperatures.....	79

Figure 3-3 Area specific resistances (ASR) of 15 $\mu$ m thick SDC and 5 $\mu$ m thick YSZ at different temperatures. ....	80
Figure 3-4 SEM observation of cell with SDC electrolyte (co-fired at 1400 $^{\circ}$ C for 2hr)..	81
Figure 3-5 EDS elemental analysis at the cell cross-section. ....	81
Figure 3-6 Microstructure and EDS analysis of the tested thin SDC cell. ....	82
Figure 3-7 Microstructure and EDS analysis of the tested thin YSZ+SDC cell.....	83
Figure 3-8 EDS elemental mapping of an irregular grain area.....	84
Figure 3-9 SEM image of a cell with spin-coated SDC electrolyte fired at 1400 $^{\circ}$ C.....	85
Figure 4-1 XRD patterns of SSC+SDC powder mixtures sintered at different temperatures.....	92
Figure 4-2 Temperature dependences of OCV for the cermet supported thin SDC electrolyte cells with cathode sintered at different $T_{s,c}$ .....	93
Figure 4-3 Electrochemical performance of cells with thin SDC electrolytes with cathodes sintered at different temperatures.....	95
Figure 4-4 EIS of cells with cathodes sintered at different temperatures.....	96
Figure 4-5 SEM images of the tested cells. ....	97
Figure 4-6 Appearance of the cells before testing in this study.....	98
Figure 4-7 Optical microscope images of SSC+SDC cathodes made with different spacer thicknesses after sintering.....	99
Figure 4-8 Typical surface height profiles of an SSC#3 cathode (prepared with 170 $\mu$ m spacer, after sintering) characterized with a profilometer.....	101
Figure 4-9 Cell peak power density vs. different cathode spacer thicknesses.....	102
Figure 4-10 Peak power density of the cell with 1000 $^{\circ}$ C-sintered SSC#3 composite cathode, tested repeatedly with or without contact pastes.....	103
Figure 4-11 Typical cathode with contact paste after cell testing. ....	104
Figure 5-1 Schematic of cell structure.....	109
Figure 5-2 Schematic of experimental setup. ....	111
Figure 5-3 OCV of the SDC electrolyte cells at different temperatures.....	112
Figure 5-4 Cell performance at different temperatures.....	113
Figure 5-5 EIS of the cell at different temperatures, a) before water test, b) after water test.....	114

Figure 5-6 Water amount collected at anode gas outlet and leakage current at different cell temperatures, with and without the cathode.....	116
Figure 5-7 Fuel utilization ( $U_f$ ) and electrical efficiency (LHV) of the cell.....	120
Figure 5-8 SEM images of the SDC electrolyte after cell test.....	125
Figure 5-9 EDS analysis results at regular grain(#1) and irregular grain(#2) on the SDC electrolyte surface after co-firing (see Figure 5-8a).....	126
Figure 6-1 TGA of SDC powders with 5at% $\text{Co}(\text{NO}_3)_3 \cdot 6\text{H}_2\text{O}$ .....	134
Figure 6-2 TGA of SDC powders with 5at% $\text{Cu}(\text{NO}_3)_2 \cdot 3\text{H}_2\text{O}$ .....	135
Figure 6-3 XRD patterns of sintered SDC with and without Cu or Co addition.....	136
Figure 6-4 SDC lattice parameter variation with Co or Cu (polished sample) content.	136
Figure 6-5 Linear shrinkage (displacement, %) versus sintering temperature at a heating rate of $5^\circ\text{C min}^{-1}$ .....	137
Figure 6-6 Linear shrinkage rate versus sintering temperature at a heating rate of $5^\circ\text{C min}^{-1}$ .....	138
Figure 6-7 Cyclic voltammetry curves at $600^\circ\text{C}$ of three SDC electrolyte cells.....	139
Figure 6-8 SEM and EDS analysis of (a) SDC, (b) 1%Co-SDC, (c) 1%Cu-SDC.....	140
Figure 7-1 Density of sintered samples.....	147
Figure 7-2 X-ray diffraction pattern for each temperature from 800 (lowest curve) to $1400^\circ\text{C}$ (highest curve) for A/ pellets of 8YSZ-SDC, B/ pellets of 8YSZ-SDC-1%Co, C/ pellets of 8YSZ-SDC-1%Cu, and D/ pellets of SSZ-SDC-1%Co.....	148
Figure 7-3 Lattice parameter of SDC (graph i), 8YSZ, SSZ (graph ii) and the forming phase (graph iii) for the different mixtures.....	150
Figure 8-1 SEM image of the bi-layered SDC/SSZ electrolyte surface.....	159
Figure 8-2 SEM image of cross-section of the bi-layered SDC/SSZ electrolyte.....	159
Figure 8-3 EDS element mapping (see Figure 8-2).....	159
Figure 8-4 I-V-Power curves of the bi-layer electrolyte cell at different operating temperatures.....	160
Figure 8-5 EIS spectra of the cell at different temperatures.....	161
Figure 9-1 Nyquist plot of the impedance evolution of cell A, tested at OCV at $650^\circ\text{C}$ . Top: Nyquist plot. Bottom: imaginary impedance vs. frequency. The legend on the right indicates the time in hours elapsed since the beginning of the test.....	172

Figure 9-2 Influence of H <sub>2</sub> dilution on the cell impedance. Top: Nyquist plot. Bottom: imaginary impedance vs. frequency. Testing conditions: 650°C, OCV, 10, 20 and 100 % H <sub>2</sub> , balance N <sub>2</sub> / air (flow rates for both anode and cathode are 100 ml min <sup>-1</sup> ).....	172
Figure 9-3 Current density delivered by cell B as a function of time, in potentiostatic mode at 0.75V. After a short activation period, the performance decays steadily throughout the testing time. ....	174
Figure 9-4 I-V and power density curves showing the time evolution of the electrochemical performance of cell B. The decay is more significant below 0.3 A cm <sup>-2</sup> than it is at high polarizations. Legend indicates time elapsed in hours....	175
Figure 9-5 Nyquist plot of the impedance evolution of cell B, taken at OCV at 650°C. An excursion to 1000°C took place between 138 and 144hr. Legend indicates time elapsed in hours. ....	175
Figure 9-6 Potential delivered by cell C as a function of time, in galvanostatic mode at 0.5 A cm <sup>-2</sup> . The data point indicated with the arrow was calculated based on the polarization curve performed at 307hr.....	177
Figure 9-7 Nyquist plot of the impedance evolution of cell C, at OCV at 650°C. An excursion to 0.75 V (OCV= 0.983 V) took place after 53hr.....	178
Figure 9-8 I-V and power density curves showing the time evolution of the electrochemical performance of cell C. Legend indicates time elapsed in hours...	178
Figure 9-9 Nyquist plot of the impedance evolution of cell D at OCV at 650°C. The cell temperature was increased to 700°C before the first test indicated as 0hr.....	179
Figure 9-10 I-V and power density curves showing the time evolution of the electrochemical performance of cell D. Legend indicates time elapsed in hours..	180
Figure 9-11 Current density delivered by cell E as a function of time, in potentiostatic mode at 0.70V.....	181
Figure 9-12 I-V and power density curves showing the time evolution of the electrochemical performance of cell E. Legend indicates time elapsed in hours. .	181
Figure 9-13 Polarization resistance evolution with time for cells B, C, D and E. Average R <sub>p</sub> increase is 2.5 mΩ cm <sup>2</sup> h <sup>-1</sup> .....	184

Figure 9-14 SEM micrograph of the bi-layered electrolyte in contact with the electrodes of cell D. While SSZ shows excellent sintering, SDC exhibits some porosity that could partially contribute to the abnormally high initial series resistance observed in all cells. The line scan mark in the SEM images shows the location of the element analysis. The element analysis results are shown in the right figure. ....	186
Figure 9-15 Post-test SEM micrograph showing a delamination between the SSZ and SDC electrolyte layers in cell D. This separation was observed in several spots across the cell, and may have been partially responsible for the large initial series resistance observed in all specimens.....	186
Figure 10-1 A schematic drawing of the cell structure and its fabrication methods. ....	193
Figure 10-2 XRD spectra of SDC/SSZ bi-layer films deposited on silicon wafers at (a) 200 °C and (b) 600 °C in 40 mTorr O <sub>2</sub> .....	197
Figure 10-3 FE-SEM micrographs of SSZ/SDC bi-layer films deposited on silicon wafers at a substrate temperature of (a) 200, and (b) 600°C in 40 mTorr of O <sub>2</sub> . ...	198
Figure 10-4 SEM Micrograph of surface view of (a) unmodified NiO-YSZ anode, (b) NiO-SDC modified NiO-YSZ and (c) cross-sectional view of NiO-SDC modified NiO-YSZ.....	200
Figure 10-5 Cross section images of cell with bi-layered electrolyte deposited by PLD.	201
Figure 10-6 I-V and power curves at different temperatures.....	202
Figure 10-7 EIS results at different temperatures. ....	202
Figure 12-1 Measured conductivities of SDC, SSZ, and YSZ electrolytes used in this study.....	218

## Nomenclature

Note: It is customary in the SOFC community to normalize currents using centimeters, because the relevant electrode areas of both test cells and commercial prototypes are of the order of a few square centimeters. Therefore,  $\text{cm}^2$  is the preferred unit to express output values for current densities and area-specific resistances. Likewise, micrometers and millimeters occasionally describe geometrical quantities such as thickness, lengths and widths.

<b>Symbol</b>	<b>Description</b>	<b>Unit</b>
$E_{act}$	activation energy	$\text{kJ mol}^{-1}$
$E_N$	Nernst potential	V
$F$	Faraday's constant	$\text{Coul mol}^{-1}$
$f$	frequency	Hz
$I$	current	A or mA
$i$	current density	$\text{A m}^{-2}$ or $\text{A cm}^{-2}$
$i_0$	exchange current density	$\text{A m}^{-2}$
$n$	number of electrons transferred in a reaction	
$P$	electrical power (density)	W ( $\text{W cm}^{-2}$ )
$p$	system gas pressure	Pa or atm
$P_{O_2}$	partial oxygen pressure	atm
$R$	universal gas constant	$\text{J mol}^{-1} \text{K}^{-1}$
$R_{el}$	(area-specific) resistance of electrolyte	$\Omega \text{ cm}^2$
$R_p$	(area-specific) polarization resistance	$\Omega \text{ cm}^2$
$R_s$	(area-specific) series resistance	$\Omega \text{ cm}^2$
$R_t$	(area-specific) total resistance	$\Omega \text{ cm}^2$
$S$	electrochemically active surface area	$\text{m}^{-1}$
$T$	absolute temperature	K
$U$	utilization	
$V$	cell operating voltage	V
$Z'$	real axial coordinate in area-specific impedance spectrum	$\Omega \text{ cm}^2$
$Z''$	imaginary axial coordinate in area-specific impedance spectrum	$\Omega \text{ cm}^2$

<b>Symbol</b>	<b>Description</b>	<b>Unit</b>
$\alpha$	charge transfer coefficient,	
$\beta$	factor coefficient depending on porosity and waviness of the TPB	
$\varepsilon$	electrical efficiency	
$\sigma$	generic conductivity	S cm <sup>-1</sup>
$\delta_p$	thickness of layer p	μm or mm
$\Delta C_p$	heat capacity change	J mol <sup>-1</sup> K <sup>-1</sup>
$\Delta G$	free energy change	J mol <sup>-1</sup>
$\Delta H$	enthalpy change	J mol <sup>-1</sup>
$\Delta S$	entropy change	J mol <sup>-1</sup> K <sup>-1</sup>

### Subscripts

<i>a</i>	anode	<i>h</i>	hole
<i>c</i>	cathode	<i>i</i>	ionic
<i>cell</i>	cell	<i>L</i>	leakage
<i>cond</i>	conductive	<i>oc</i>	open circuit
<i>cont</i>	contact	<i>ox</i>	oxidation
<i>e</i>	electronic	<i>red</i>	reduction
<i>el</i>	electrolyte	<i>t</i>	total (includes: a, c, and el)
<i>f</i>	fuel		

## List of Abbreviations

AFC	alkaline fuel cell
ASC	anode supported cell
ASR	area specific resistance ( $\Omega \text{ cm}^2$ )
BSCF	$\text{Ba}_{1-x}\text{Sr}_x\text{Co}_{1-y}\text{Fe}_y\text{O}_{3-\delta}$ ( $x=0.1-0.5$ , $y=0.2-0.8$ )
CTE	coefficient of thermal expansion (1/K)
EIS	electrochemical impedance spectrum or spectroscopy
ESC	electrolyte supported cell
EVD	electrochemical vapor deposition
GDC	gadolinia doped ceria, $\text{Gd}_{0.1}\text{Ce}_{0.9}\text{O}_{1.95}$ , or $\text{Gd}_{0.2}\text{Ce}_{0.8}\text{O}_{1.9}$ in this study
LNF	$\text{La Ni}_{1-x}\text{Fe}_x\text{O}_{3-\delta}$ ( $x=0.2-0.8$ )
LSGM	$\text{La}_{1-x}\text{Sr}_x\text{Ga}_{1-y}\text{Mg}_y\text{O}_{3-z}$ , electrolyte material with perovskite structure
LSC	$\text{La}_{1-x}\text{Sr}_x\text{CoO}_{3-\delta}$ ( $x=0.1-0.7$ )
LSCF	$\text{La}_{1-x}\text{Sr}_x\text{Co}_{1-y}\text{Fe}_y\text{O}_{3-\delta}$ ( $x=0.1-0.5$ , $y=0.2-0.8$ )
MIEC	mixed ion and electron conductor
OCV	open circuit voltage (V)
PAFC	phosphoric acid fuel cell
PEFC	polymer electrolyte fuel cell
PLD	pulsed laser deposition
PPD	peak power density ( $\text{W cm}^{-2}$ )
SDC	samarium doped ceria electrolyte material with fluorite structure, typically $\text{Sm}_{0.2}\text{Ce}_{0.8}\text{O}_{1.9}$ in this study
SOFC	solid oxide fuel cell
SSC	$\text{Sm}_{0.5}\text{Sr}_{0.5}\text{CoO}_3$ , standard cathode material in this study
SSZ	scandia stabilized zirconia electrolyte material with fluorite structure, typically $(\text{Sc}_2\text{O}_3)_{0.1}(\text{CeO}_2)_{0.01}(\text{ZrO}_2)_{0.79}$ or $10\text{Sc}1\text{CeZrO}_{2-\delta}$ , in this study
TPB	three-phase boundary, or triple phase boundary
TSC	tape casting, screen printing, and co-firing
YSZ	yttria stabilized zirconia electrolyte material with fluorite structure, typically $(\text{Y}_2\text{O}_3)_{0.08}(\text{ZrO}_2)_{0.92}$ in this study

## Acknowledgements

I am most grateful to my research supervisor, Dr. Olivera Kesler, for her trust and support throughout the duration of my PhD program. I've learned substantial knowledge through her graduate student courses, such as Materials for Clean Energy and Solid Oxide Fuel Cells. Dr. Kesler has provided an effective guidance throughout my study on the low temperature solid oxide fuel cells, shared happiness in every success I made in the past, and financially supported my attendance to international fuel cell conferences. Thank you so much, Olivera, for so much time, patience and intellectual generosity dedicated to my research work.

I sincerely thank Dr. Dave Ghosh and Dr. Radenka Maric for their constant inspiration to my motivation of pursuing the PhD study in the Mechanical Department of University of British Columbia. It has turned to be extremely useful for my enrichment of knowledge and experience on low temperature solid oxide fuel cell (LT-SOFC) development. I am deeply grateful to National Research Council Canada (NRC) and Institute for Fuel Cell Innovation (NRC-IFCI) management team for providing me pleasant work and study environment, and financial support from the NRC-National Fuel Cell and Hydrogen Program. I am happy to have made my contribution to LT-SOFC project through the metamorphosis period of the institute.

I am highly indebted to thank the following people who contributed to this dissertation work: Mark Robertson, a wonderful and skillful technical partner in my research, has been a great helper for the cell fabrication and characterization. Dr. Cyrille Decès-Petit, a very kind and versatile researcher, is always with smile to provide his help when I was in trouble with either test station or computer. Dr. Yongsong Xie, a brotherhood research partner, shared his professional knowledge and experience on bonding strength characterization of cell functional layers. He is a very good partner for after lunch walking and chatting. Wei Qu, who developed sealing materials and concept for the cell test, contributed to the quality of experimental results. Justin Roller, who engaged in the setup of analytical lab, put great efforts to maintain XRD and TMA instruments in operation. Dr. Rob Hui, a knowledgeable senior researcher, strongly supports my activities and my dissertation work at the institute. Dr. Dongfang Yang, an outstanding expert in the

PLD deposition, we had a very pleasant collaboration on PLD cell development. Sing Yick, conducted raw material characterizations in this study.

My thanks also go to all my other Committee members: Drs. Robert Evans, Elod Gyenge, and W. Kendal Bushe for their input throughout the years. Special thanks to Dr. Robert Evans for his generosity to be my UBC Supervisor after Dr. Olivera Kesler move to University of Toronto in September 2007.

This work would have never been possible without the unconditional love and understanding of my wife H and my daughter L. They have unloaded my duty for tons of household work.

*To my diligent wife and delightful daughter*

## Co-authorship Statement

The research work presented in this dissertation (and the publications stemming from it) corresponds to the work of the author and co-authors, and the supervision of Dr. Olivera Kesler. The author of the dissertation has worked on low temperature SOFC development, including the understanding of the materials and fabrication knowledge, the screening of cell materials, the design of cell structures, the fabrication of cells, the characterization and postmortem analysis of cells, and the dissemination of SOFC knowledge and cell skills to the team.

Dr. Yongsong Xie collaborated with the author on adhesion characterization of cell functional layers, developed a method for thin film adhesion measurement. Dr. Cyrille Decès-Petit worked with the author on the characterization of interaction of electrolyte materials. The author also closely collaborated with Dr. Dongfang Yang on pulsed laser deposition of bi-layered electrolyte. Mark Robertson helped the author on the cell fabrication and characterization. Sing Yick conducted raw material characterizations in this study. Wei Qu developed sealing materials and contributed to the quality of experimental results in the study of the internal shorting of SDC electrolyte cells. Dr. Javier Gazzarri conducted data summary on stability of bilayered electrolyte cells. During the last four years, Dr. Kesler provided continuous academic guidance and supervision, critical review of the results and manuscripts.

*"You do not really understand something until you can explain it to your grandmother."*

***By Albert Einstein***

# 1. Chapter One. SOFC Fundamentals and Literature Review on Low Temperature SOFCs<sup>1</sup>

Solid oxide fuel cells (SOFCs) efficiently convert chemical energy in fuels into electricity at high temperatures. Their demonstrated efficiency is up to two times higher than that of existing thermal power plants. All types of available fuels, after reforming to H<sub>2</sub> and CO, can be supplied to SOFCs to generate electrical power. Therefore, the SOFCs are an attractive power generation technology, fitting well with the present fossil fuel energy infrastructures and the future clean, sustainable and renewable energy solutions. Conventional SOFCs typically operate at 700-1000°C to achieve an adequate performance (power density  $P \geq 0.3 \text{ W cm}^{-2}$ , i.e., total area specific resistance  $R_t \leq 0.4\sim 0.5 \Omega \text{ cm}^{-2}$ ), that generates cost and lifetime issues. Low temperature SOFC (LT-SOFC) research and development are motivated by the needs of reducing material restriction and cost, improving system reliability and durability, and widening SOFC application to versatile power sources. Since cell performance decreases exponentially with operating temperature, it is critical to develop cell material and fabrication technology to fulfill this mission. In this chapter, a brief introduction of SOFC operating principles, conventional cell materials and performances, advantages and challenges are presented. Later on, a literature review on LT-SOFC, including new electrolyte materials, optimal compositions, compatible anodes and cathodes, various cell fabrication methods, and main challenges and approaches are addressed. At the end, the scope and the structure of the dissertation work is outlined.

## 1.1 SOFC fundamentals

The SOFCs generate electricity by combining a fuel and an oxidant electrochemically [1, 2]. The cell unit generally consists of three components: anode, electrolyte, and cathode, as illustrated in Figure 1-1. The anode and the cathode are separated by an electrolyte. Both the anode and the cathode are porous for gas transport,

---

<sup>1</sup> Note: In accordance with current convention, the term 'low' is used here for temperatures below 650°C while the term 'intermediate' refers to the temperature range 650-850 °C, and 'high' refers to temperatures in the range 850-1000 °C.

electrochemically active to the reactants, and electronically conductive for the electron flow. The electrolyte is a dense and gas-tight layer with high  $O^{2-}$  ionic conductivity.

At the cathode, the electrochemical reaction consumes oxygen (from air) and generates oxygen anions ( $O^{2-}$ ). The  $O^{2-}$  migrates through the electrolyte to the anode. At the anode, the fuel ( $H_2$  and/or  $CO$ ) is combined with  $O^{2-}$  to form the product,  $H_2O$  and/or  $CO_2$ , depending on the fuel composition. The electrode reactions are electronically balanced by a transfer of two electrons per  $O^{2-}$  ion through an external electrical circuit. Thus it generates electrical power with fuel and air supply. Meanwhile the reaction products of  $H_2O$  and/or  $CO_2$  as high quality hot exhaust are suitable for use in cogeneration or bottoming cycles to generate additional electrical power.

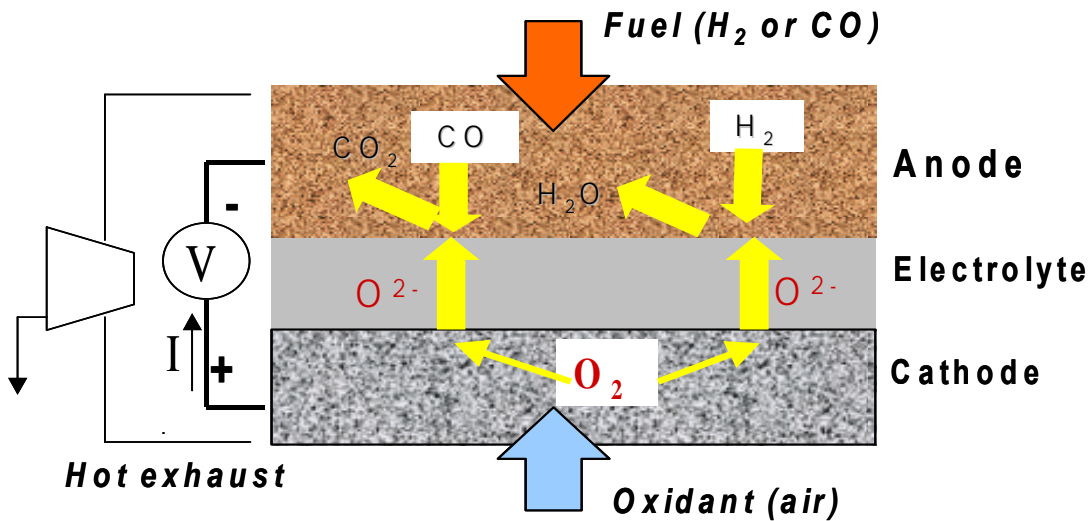


Figure 1-1 Operational principle of an SOFC

### 1.1.1 Nernst potential and thermodynamic efficiency

The operational principle of the SOFC is well illuminated by thermodynamics and electrochemistry [3, 4]. The maximum cell potential (voltage), i.e. Nernst potential,  $E_N$ , under thermodynamically reversible condition, is expressed as Equation 1-1, indicating the SOFC is an oxygen concentration cell.

Equation 1-1

$$E_N = \frac{RT}{4F} \ln \frac{p_{O_2,c}}{p_{O_2,a}}$$

Here,  $R$  is the gas constant ( $8314 \text{ J mol}^{-1} \text{ K}^{-1}$ ),  $T$  is the absolute temperature (K),  $F$  is the Faraday constant ( $96485.3 \text{ C mol}^{-1}$ ) and  $p_{O_2,a}$  and  $p_{O_2,c}$  denote the oxygen partial pressures (atm or Pa) at anode and cathode, respectively. Commonly  $p_{O_2,c} = 0.21 \text{ atm}$  for using ambient air at the cathode; therefore, the magnitude of  $E_N$  only depends on the anode oxygen partial pressure,  $p_{O_2,a}$ , and thus on the type and composition of the fuel fed to the anode.

Thermodynamic efficiency is defined as the change of free energy ( $\Delta G$ ) divided by the change of enthalpy ( $\Delta H$ ) of a fuel oxidation reaction, i.e.,  $\Delta G/\Delta H$ . It represents the highest efficiency that a fuel cell potentially reaches through an electrochemical process, and is determined by the 2<sup>nd</sup> Law of Thermodynamics.

Table 1-1 lists the thermodynamic calculation (see Appendix A) results of Nernst potential ( $E_N$ ) and thermodynamic efficiency at different operating temperatures with  $\text{H}_2$  or  $\text{CO}$  as anode fuel and air as cathode gas under ambient atmosphere. Because of the negative change in entropy ( $\Delta S < 0$ ), the values of  $E_N$  and  $\Delta G/\Delta H$  of both  $\text{H}_2$  and  $\text{CO}$  decrease with temperature. Therefore, reducing the SOFC operating temperature leads to higher thermodynamic cell voltage and efficiency.

Table 1-1 Nernst potentials and thermodynamic efficiencies of various fuels at different temperatures

Anode gas	T [K]	673	773	873	973	1073	1173	1273
97% $\text{H}_2$ +3% $\text{H}_2\text{O}$	$E_N$ [V]	1.1765	1.1651	1.1537	1.1423	1.1309	1.1195	1.1081
	$\Delta G/\Delta H$	0.863	0.842	0.820	0.799	0.778	0.757	0.737
97% $\text{CO}$ +3% $\text{CO}_2$	$E_N$ [V]	1.2432	1.2100	1.1768	1.1436	1.1104	1.0772	1.0441
	$\Delta G/\Delta H$	0.787	0.755	0.723	0.692	0.660	0.629	0.597

## 1.1.2 Cell voltage and cell resistance

The cell voltage of the SOFC at open circuit condition is commonly known as open-circuit voltage,  $V_{OC}$  or OCV. The exact OCV depends on temperature, oxygen partial pressure, reactant and product concentration, and electrolyte and seal material and quality. When the electrolyte is purely ionically conductive with good gas-tightness (dense), the OCV value is close to the  $E_N$  value ( $V_{OC} \approx E_N$ ), approximately 1.0-1.1V. When the electrolyte is constructed with a mixed oxygen-ion and electronic conductor, electronic current can flow through the electrolyte even at the open circuit condition, leading to an internal leakage (or shorting) current,  $I_L$ . Based on the equivalent electric circuit of the SOFC, the leakage current density,  $i_L$ , and the OCV follow Equation 1-2 and Equation 1-3, respectively [5].

$$i_L = \frac{\sigma_i \sigma_e E_N}{(\sigma_i + \sigma_e) \delta_{el}} = \frac{t_i \sigma_e E_N}{\delta_{el}} \quad \text{Equation 1-2}$$

$$OCV = \frac{\sigma_i}{\sigma_i + \sigma_e} E_N = t_i E_N \quad \text{Equation 1-3}$$

Here  $\sigma_i$  and  $\sigma_e$  are the ionic and electronic conductivities of the electrolyte, respectively,  $t_i$  is the ionic transference number, and  $\delta_{el}$  is the thickness of the electrolyte.

The OCV can also be reduced by reactant cross-over due to the existence of physical defects in the electrolyte such as pin-holes, micro-cracks, or cell sealing leakage. This type of OCV reduction can be easily explained by the Nernst equation by the changes of the oxygen partial pressure between anode and cathode. Both the internal current leakage and the reactant cross-over lead to losses in the reactants and cell performance.

The cell voltage under operating condition is smaller than the OCV due to irreversible losses or cell polarization. Generally, the cell polarization comes from electrode overpotential, concentration polarization, and cell ohmic loss from the electrolyte resistance and the electrode contact resistance. Since the electrode processes have fast kinetics at high temperatures, the cell voltage losses generally follow an ohmic resistance behaviour, i.e. the voltage drop is linear with the current density, at temperatures above 700°C. Equation 1-4 is applicable to the SOFC under most practical operating conditions.

(Note: All the resistance data presented in this dissertation work are area specific resistances in units of  $\Omega \text{ cm}^2$ )

$$V_{\text{cell}} = E_N - (i + i_L)R_t = V_{\text{OC}} - iR_t \quad \text{Equation 1-4}$$

and

$$R_t = R_a + R_c + R_{\text{el}} + R_{\text{cont}} \quad \text{Equation 1-5}$$

Here,  $V_{\text{cell}}$  is cell voltage,  $E_N$  is cell Nernst potential,  $i$  is cell current density,  $i_L$  is leakage current density,  $R_t$  is total cell resistance,  $V_{\text{OC}}$  is open circuit voltage (also OCV in common usage),  $R_a$  represents anode resistance,  $R_c$  is cathode resistance,  $R_{\text{el}}$  is electrolyte resistance, and  $R_{\text{cont}}$  is contact resistance.

The anode and cathode resistance,  $R_a$ ,  $R_c$  can be obtained according to Butler-Erdey-Volmer (BEV) equations or the value of the Tafel slope. The exchange current density,  $i_0$ , is a function of the electrode catalytic properties, reactant and product concentration, reaction mechanisms and temperature.

$$\eta = \frac{RT}{\alpha nF} \ln\left(\frac{i}{i_0}\right) \quad \text{Equation 1-6}$$

Here,  $\eta$  is electrode over-potential,  $R$  is universal gas constant ( $8.314 \text{ kJ mol}^{-1} \text{ K}^{-1}$ ),  $T$  is absolute temperature(K),  $\alpha$  is charge transfer coefficient,  $n$  is the number of electrons,  $F$  is Faraday's constant ( $96483.5 \text{ C/mol}$ ),  $i$  is current density, and  $i_0$  is exchange current density.

Under weak polarization (close to OCV), the following equations are electrochemically valid for  $R_a$  and  $R_c$  calculations.

$$R_a = \frac{\eta_a}{i} = \frac{RT}{nF} \left(\frac{1}{i_{0,a}}\right) \quad \text{Equation 1-7}$$

$$\text{and, } R_c = \frac{\eta_c}{i} = \frac{RT}{nF} \left(\frac{1}{i_{0,c}}\right) \quad \text{Equation 1-8}$$

Since the exchange current densities  $i_{0,a}$  and  $i_{0,c}$  follow Arrhenius equations, i.e., they are exponentially dependent on temperature, both  $R_a$  and  $R_c$  will increase exponentially with the decrease in operating temperature. That is, we have Equation 1-9 and Equation 1-10.

$$R_a = R_{a,0} T \exp\left(\frac{E_{act,a}}{RT}\right) \quad \text{Equation 1-9}$$

$$\text{and } R_c = R_{c,0} T \exp\left(\frac{E_{act,c}}{RT}\right) \quad \text{Equation 1-10}$$

Here,  $R_{a,0}$  and  $R_{c,0}$  are the pre-exponential factors for the anode and cathode, respectively.  $E_{act,a}$  and  $E_{act,c}$  are the activation energies for anode and cathode process, respectively.

The electrolyte resistance,  $R_{el}$  can be calculated according to the Ohmic Law:

$$R_{el} = \delta_{el} / \sigma_{el} \quad \text{Equation 1-11}$$

Here  $\delta_{el}$  is the thickness of the electrolyte and  $\sigma_{el}$  is the conductivity of the electrolyte.

The ionic conductivity  $\sigma_{el}$  of the electrolyte is represented by Equation 1-12, indicating its thermally-activated ionic conducting mechanism.

$$\sigma_{el} = \frac{\sigma_{el}^0}{T} \exp\left(-\frac{E_{act,el}}{RT}\right) \quad \text{Equation 1-12}$$

The values of  $\sigma^0$  and the activation energy ( $E_{act,el}$ ) vary with material composition, microstructure, thermal history, aging time, and surrounding atmosphere, and are also sensitive to trace element contamination.

The contact resistance,  $R_{cont}$  (or defined as  $R_e$  for total electronic conducting resistance including that of the anode layer, cathode layer, interconnect (IC) layer, and contact media layer) normally depends on the material and structure of the electrodes, contact media, and interconnect, as well as the compressing force (contact pressure). It varies with cell and stack design. In the case of metallic interconnects, the metal oxidation contributes to the increase of  $R_{cont}$ . The effect of oxidation can be normally described by Equation 1-13 [6]

$$R_{cont} = 2 \frac{\sqrt[m]{K_0 t}}{\sigma_0} T \exp\left(\frac{-(1/m)E_{ox} + E_{cond}}{RT}\right) \quad \text{Equation 1-13}$$

( $m=2$ , for parabolic growth of oxide)

$K_0$  and  $m$  are the constants of the oxide growth kinetics,  $\sigma_0$  is the conductivity of the oxide,  $E_{ox}$  is the activation energy for the oxide growth, and  $E_{cond}$  is the activation energy for oxide conductivity. In most cases,  $R_{cont}$  is considered small [6, 7] (at least one order of magnitude lower than the  $R_a$ ,  $R_c$ , or  $R_{el}$ ), and therefore, is often neglected, except for the case of cathode supported tubular cells with a long current path or steel-interconnect oxide

growth at elevated temperature with service time (see page 17, Example 4:  $R_{cont}$  increase due to oxide growth).

### 1.1.3 Electrical efficiency and fuel utilization

The overall electrical efficiency of the FCs,  $\varepsilon$ , is determined by the product of thermodynamic efficiency, the ratio of  $V_{cell}$  to  $E_N$ , and the fuel utilization,  $U_f$ .

$$\varepsilon = \frac{\Delta G}{\Delta H} \times \frac{V_{cell}}{E_N} \times U_f \quad \text{Equation 1-14}$$

The fuel utilization  $U_f$  is defined as the ratio of moles of reactants (fuel) consumed in the fuel cell to the moles of reactants supplied into the fuel cell. Since high utilization of fuel results in increased reactant concentration polarization, SOFCs are often operated at  $U_f$  of 0.6-0.9.

### 1.1.4 Stack voltage and output power

Individual cells are assembled into a stack to achieve certain electrical power outputs for particular applications. The stack voltage ( $V_s$ ) and power ( $P_s$ ) from a typical stack in a series-connection are simply the sum of the number ( $n$ ) of the individual cell voltages ( $V_i$ ) and power outputs ( $P_i$ ).

$$V_s = \sum_i^n V_i \quad \text{Equation 1-15}$$

$$P_s = I \times V_s = I \sum_i^n V_i = \sum_i^n P_i \quad \text{Equation 1-16}$$

It is necessary to know basic requirements of cell component resistances for an SOFC having an adequate performance at a designed operating temperature.

## **Example 1. Basic requirement of cell component resistances**

Assuming a cell fuelled with 97% $H_2$ +3% $H_2O$  and air at 873K with an OCV ( $V_{oc}$ ) of approximately 1.0V and at targeted electrical efficiency of 50% at a current density of 0.5A  $cm^{-2}$ , according to Equation 1-14, Equation 1-4, and Table 1-1 data, we know that the SOFC has to be operated at  $V_{cell}=0.80V$  and  $U_f=0.80$ , and the total cell resistance,  $R_t$ , should be less than  $0.4\Omega cm^2$  (refer to Appendix A). Since both the cathode and the electrolyte practically show higher resistances than that of the anode, especially at reduced operating temperature, a rational allocation for cell component resistances:  $R_{el}$ ,  $R_a$ , and  $R_c$  is 0.15, 0.10, and  $0.15 \Omega cm^2$ , respectively.

## **1.2 Conventional SOFC materials and performances**

The first solid oxide fuel cell was operated at 1000 °C by Baur and Preis in 1937 [3] using the oxygen-ion conductive stabilized  $ZrO_2$  electrolyte discovered in 1899 by Nernst [4]. Since then SOFC research and development have mostly encompassed optimization of the electrolyte composition, development of compatible anodes, cathodes, and interconnect materials, minimization of the cell resistance, reduction of operating temperature, and development of cost-effective thin-film fabrication methods. Nowadays, many companies, such as Siemens Westinghouse, Mitsubishi Heavy Industries, Tokyo Gas Co. Ltd., Sulzer Hexis, and Versa Power Systems, are pursuing stack and system level development. This section gives a brief summary of the conventional SOFC materials and structures, fabrication methods, and state-of-the-art performances.

### **1.2.1 Cell materials and properties**

Conventional cell units use YSZ ( $Y_xZr_{1-x}O_{2-x/2}$ ,  $x=0.16$  or 8mol%  $Y_2O_3$ ) as the electrolyte, Ni-YSZ as the anode, and LSM ( $La_{1-y}Sr_yMnO_{3-\delta}$ ,  $y=0.1-0.3$ )-YSZ composites as the cathode, and doped  $LaCrO_3$  (with Sr, Ca or Mg) as interconnect. This material system has provided the best fulfillment of strict requirements for high temperature SOFCs. Table 1-2 lists the conventional SOFC component materials and properties.

Table 1-2 Conventional SOFC component materials and properties

Component	Material	Composition	Conductivity [S cm <sup>-1</sup> ] at 1273K	Thermal expansion coefficient [10 <sup>-6</sup> K <sup>-1</sup> ]
Anode	Ni-YSZ	30-35vol.%Ni 30-50%porosity	~1000	12-13
Electrolyte	YSZ	Dense (gas-tight) <5% porosity	~0.1	10-11
Cathode	LSM-YSZ	50-100vol.% LSM 30-50%porosity	60 ~100	11-12
Interconnect	Doped- LaCrO <sub>3</sub>	Dense (gas-tight) <5% porosity	35	10-11

### 1.2.1.1 Electrolyte

The ionic conductivity of the YSZ electrolyte comes from oxygen ion (O<sup>2-</sup>) movement through the oxygen vacancies (V<sub>O</sub><sup>••</sup>) created by the substitution of Y<sup>3+</sup> to Zr<sup>4+</sup>, and is influenced by dopant concentration, temperature, atmosphere, grain size, and aging time. Equation 1-17 gives the ionic conductivity of the YSZ as function of temperature over the range from 800°C to 1050°C, and partial pressure of oxygen over the range from 0.21 atm to 10<sup>-17</sup> atm [4].

$$\sigma_{i,YSZ} = 1.63 \times 10^2 \exp\left(\frac{-76.2 \times 10^3}{RT}\right) \quad [\text{S cm}^{-1}] \quad \text{Equation 1-17}$$

Under these conditions the electronic conductivities (electron,  $\sigma_{e,YSZ}$  and hole,  $\sigma_{h,YSZ}$ ) are negligible (as calculated by the equations below) [4]. Thus, the YSZ electrolyte is regarded as a purely ionic conductor under operating conditions.

$$\sigma_{e,YSZ} = 1.31 \times 10^7 \exp\left(\frac{-374.8 \times 10^3}{RT}\right) p_{O_2}^{-1/4} \quad [\text{S cm}^{-1}] \quad \text{Equation 1-18}$$

$$\sigma_{h,YSZ} = 2.35 \times 10^2 \exp\left(\frac{-161.3 \times 10^3}{RT}\right) p_{O_2}^{1/4} \quad [\text{S cm}^{-1}] \quad \text{Equation 1-19}$$

From Equation 1-17, the ionic conductivities of the YSZ electrolyte are approximately  $0.12 \text{ S cm}^{-1}$  at  $1000^\circ\text{C}$ ,  $0.066 \text{ S cm}^{-1}$  at  $900^\circ\text{C}$ , and  $0.032$  at  $800^\circ\text{C}$ . The low ionic conductivity of the electrolyte material is the main reason why the conventional SOFC typically operates at high temperature. The following example gives a further explanation.

### **Example 2. Operating temperature of YSZ electrolyte supported cell**

A typical YSZ electrolyte supported cell has an electrolyte thickness of  $150\mu\text{m}$  to provide sufficient mechanical strength to the cell. In order to achieve cell performance as stated in Example 1 (see section 1.2)  $R_{el} = 0.15 \Omega\text{cm}^2$  or lower is required. The YSZ ionic conductivity needs to be  $0.12 \text{ S cm}^{-1}$  or higher based on Equation 1-17, which corresponds to an operating temperature of  $970^\circ\text{C}$  according to Equation 1-11. Therefore, YSZ electrolyte supported SOFCs are commonly regarded as high temperature SOFCs operating at temperatures of  $950\text{-}1000^\circ\text{C}$ .

#### **1.2.1.2 Anode**

Nickel has been used as anode catalyst in the SOFC since the early 1960s [8]. It meets most requirements of the anode material for the SOFC: good catalytic activity for fuel oxidation, high electrical conductivity ( $10^6 \text{ S cm}^{-1}$ ). NiO is normally used as Ni anode starting material, which is chemically stable up to  $1500^\circ\text{C}$ , chemical compatibility with common electrolytes and interconnects, and relatively cheap. The thermal expansion coefficient ( $16 \times 10^{-6} / \text{K}$ ) of nickel is practically matched to the YSZ electrolyte material ( $10.5 \times 10^{-6} / \text{K}$ ) by mixing with YSZ powder to form a Ni-YSZ cermet anode. Generally, the Ni content in the cermet anode is well controlled to a range of 30-35v% in order to balance the requirement for the electronic conductivity and the thermal expansion match with the YSZ electrolyte [9], which is very important in the development of anode supported planar SOFCs for good interfacial bonding strength and cell flatness. Besides thermal expansion matching, adding YSZ enhances the anode triple phase boundary (TPB) length, which increases the anode performance, and increases the microstructural stability by making the anode more resistant to coarsening of the Ni during the operation due to sintering. Table

1-3 lists the Ni-YSZ anode electrochemical resistances ( $R_a$ ) at different operating temperatures, reported in the literature.

Table 1-3 Ni-YSZ anode electrochemical performance ( $R_a$ )

Anode composition	Anode area specific resistance, $R_{a, Ni-YSZ}$ [ $\Omega \text{ cm}^2$ ]					$E_a$ kJ mol <sup>-1</sup>	Ref.
	500°C	600°C	700°C	800°C	900°C		
Ni + YSZ (1)		0.04		0.02			10
Ni + YSZ (2)				1.0		125	11
Ni +YSZ (3)			1.1	0.7	0.4		12

(1) Anode sintering temperature,  $T_{s,a}$ : 1400°C for 2-4 hours, anode supported (10 $\mu$ m) YSZ electrolyte cell fabricated by co-firing with LSM-YSZ cathode. (2)  $T_{s,a}$ : 1430°C for 2hr, symmetric anode supported cell. (3) 150  $\mu$ m YSZ electrolyte-supported cell with 50 $\mu$ m thick Ni-YSZ anode, operated at 100mA cm<sup>-2</sup>.

Although the SOFC has good fuel adaptability, pre-reforming or large steam-carbon ratio of a hydrocarbon fuel is necessary before the fuel contacts the nickel anode because of carbon deposition. Besides, many fuels containing sulphur species can cause poisoning of the nickel in the anode at ppm levels of sulphur, resulting in cell performance loss and cell structural damage. Therefore, adding de-sulfurization and fuel reformation sub systems to process fuel is necessary for the SOFC system, which increases system complexity, malfunction possibility, and total investment cost. In addition, Ni anodes deteriorate under redox cycling. Therefore, alternative anode materials with good carbon-, sulphur-, and redox-tolerance are of importance in future SOFC development.

### 1.2.1.3 Cathode

$\text{La}_{1-x}\text{Sr}_x\text{MnO}_{3-\delta}$  (LSM,  $x=0.1-0.3$ ) shows sufficiently high electronic conductivity (~200-300 S cm<sup>-1</sup> at 900-1000°C) and electrochemical activity for the oxygen reduction reaction, chemical stability and compatibility with the YSZ electrolyte, and a thermal expansion rate (12 x10<sup>-6</sup> /K) that is close to that of YSZ. The addition of YSZ (15-50 vol.%) to the cathode forms a composite electrode with enhanced reaction area of the electrode and enhanced interfacial bonding with the electrolyte.

LSM ( $x=0.2$ ) cathodes exhibit limited oxygen ion conductivity, 10<sup>-7</sup> S cm<sup>-1</sup> at 800 °C [2, p305]. Even at 1000°C in air, the oxide ion diffusion co-efficient in LSM is approximately 10<sup>-12</sup> cm<sup>2</sup> /s and the surface exchange coefficient of oxygen on LSM is

approximately  $10^{-7}$  cm/s [3, p128 and p242]. The overall cathode reaction occurs at the triple phase boundary (TPB) of LSM (e) / YSZ ( $O^{2-}$ ) /  $O_2$  (gas phase, air), which limits the cathode performance and the cell performance. Barbucci *et al* [13] reported that at low temperatures, an activation energy for the cathode reaction  $E_{a,LSM} = 1.21$  eV ( $1\text{eV}=96.5\text{kJ/mol}$ ) is obtained, while at high temperatures it is 1.50 eV. The discrepancy between low and high temperature activation energies has been observed by Divisek *et al.* [14] for pure LSM cathodes with  $E_a$  in the order of 2 eV between 800 °C and 1000 °C and of approximately 1 eV for temperatures below 800 °C. Table 1-4 lists area specific resistance  $R_{c, LSM}$  data of LSM cathodes reported in recent publications. It is clear that the LSM cathode is most suitable for high temperature SOFCs operating over 800°C. Recent research on cathodes for both intermediate and low temperature SOFCs (see Section 1.4.3) is active on novel cathode materials with mixed ionic and electronic conductivity (MIEC).

Table 1-4 Typical performance of LSM cathodes in the literature

Cathode composition	Cathode area specific resistance, $R_{c, LSM}$ [ $\Omega \text{ cm}^2$ ]					Ref.
	500°C	600°C	700°C	800°C	900°C	
LSM +YSZ		1~2	~0.5	0.2		10
LSM(1)+50v%YSZ	52.5	15.3	2.6	0.32	0.10	13
$\text{La}_{0.8}\text{Sr}_{0.2}\text{MnO}_3$				0.3		15
LSM(2)+50v%YSZ				0.5		16
LSM(3) +YSZ				0.58		17

LSM(1):  $(\text{La}_{0.75}\text{Sr}_{0.25})_{0.95}\text{MnO}_3$ ;    LSM(2):  $(\text{La}_{0.8}\text{Sr}_{0.2})_{0.98}\text{MnO}_3$ ;    LSM(3):  $\text{La}_{0.85}\text{Sr}_{0.15}\text{MnO}_3$

#### 1.2.1.4 Interconnect (IC)

Lanthanum chromite doped with an alkaline-earth element (Sr, Ca or Mg) has been the only qualified interconnect material for the high temperature SOFC although it is expensive and mechanically weak. The conduction mechanism of doped  $\text{LaCrO}_3$  in air is based on an exchange reaction of electrons between  $\text{Cr}^{3+}$  and  $\text{Cr}^{4+}$  ions, and is thermally-activated with an activation energy of approximately  $10\text{-}20 \text{ kJ mol}^{-1}$  for different compositions. The oxygen ion transference number is less than 0.01 even in reducing atmospheres. Thus, oxygen leakage through the interconnect is negligible. The thermal

expansion exactly matches with the YSZ electrolyte. However, the loss of oxygen in a reducing atmosphere leads to lattice expansion, approximately 0.1-0.3% at 1000°C, which has the potential of causing cracking problems [3]. In addition, the sinterability of this type of material is relatively low, which generates fabrication challenges. Interaction (or interdiffusion) between the doped LaCrO<sub>3</sub> interconnect and the doped LaMnO<sub>3</sub> cathode, and Cr-poisoning from the interconnect to the cathode cause durability problems at high temperature.

In recent decades, with the development of intermediate temperature SOFCs (700-800°C), metallic interconnects have been attractive [2, 3]. The advantages of using metallic interconnects instead of ceramic interconnects are obvious: much lower material and fabrication costs, better electrical and thermal conductivity, and more flexible interconnect configuration. Currently Ni-based, Cr-based and Fe-based alloys are under investigation. Since Fe-Cr ferrite alloys have better thermal expansion coefficient match with the conventional cell components, and are cheap and commercially available, they have been widely adopted by many intermediate temperature planar SOFC developers. Table 1-5 lists properties of La<sub>0.8</sub>Ca<sub>0.2</sub>CrO<sub>3</sub> and 430 stainless steel interconnects.

Table 1-5 Properties of La<sub>0.8</sub>Ca<sub>0.2</sub>CrO<sub>3</sub> and 430 stainless steel interconnects

Materials	Electronic conductivity [S cm <sup>-1</sup> ]	Thermal conductivity [W (mK) <sup>-1</sup> ]	Thermal expansion coefficient [K <sup>-1</sup> ]	Mechanical strength[MPa]		Material cost [\$ kg <sup>-1</sup> ]
				bending	tensile	
La <sub>0.8</sub> Ca <sub>0.2</sub> CrO <sub>3</sub>	35, at 900°C	1.5-2	10-11 x 10 <sup>-6</sup>	20-60		200-500
Fe-Cr alloy	10 <sup>5</sup> -10 <sup>6</sup> , 25°C	200	11-12 x 10 <sup>-6</sup>		500	<3

## 1.2.2 Cell structure and performance

Because of its use of all-solid-state construction, the SOFC can be configured into many geometries. Tubular, monolithic, planar, and segmented-cell designs are well-developed cell structures. With a mechanical support, the cell components can be extremely thin to reduce internal resistance losses and material costs. Table 1-6 gives a

comparison of the tubular, monolithic, planar and segmented cells developed at the industrial level [7].

Generally speaking, the cathode-supported cell structure is relatively expensive due to its high material and fabrication cost. Low mechanical strength of the porous structure limits the cell configuration to tubular and/or flattened and ribbed tubular. Relatively low conductivity of the cathode support and long current collection paths require that tubular cells even with thin YSZ electrolytes of 30-50 $\mu\text{m}$  operate at temperatures over 900°C.

Since the 1990s, modern technologies such as tape casting, screen printing, wet spraying and thermal spraying and co-firing promise lower costs for the fabrication of anode-supported planar cells. In this type of cell structure, the electrolyte resistance is further reduced, and the power density of a cell with a 10 $\mu\text{m}$  thick YSZ electrolyte can reach 0.5 W cm<sup>-2</sup> with hydrogen or reformat at 700-800°C [9, 20]. SOFCs operating at this temperature range, commonly called intermediate temperature SOFCs, allow the use of cheap steel for the stack components and the balance of plant (BOP). Table 1-6 gives a comparison of different cell configurations.

Table 1-6 A comparison of the tubular, monolithic, planar, and segmented cells

<b>Cell structure</b>	<b>Advantage</b>	<b>Disadvantage</b>
<b>Tubular</b> <sup>[3]</sup> Siemens Westinghouse 30-50 $\mu\text{m}$ YSZ (by electrochemical vapour deposition, EVD) LSM cathode-support (by extrusion) Ni-felt interconnect 0.2-0.3W cm <sup>-2</sup> 900-1000°C, 85% fuel utilization, $U_f$	Mature fabrication Easy gas-sealing Less thermal stress than all of others Longer lifetime than all of others	Long current collection path Low power density High material cost High thermally-activated cell component degradation
<b>Monolithic</b> <sup>[4]</sup> Mitsubishi Heavy Industries 50-150 $\mu\text{m}$ YSZ (by co-firing) Doped LaCrO <sub>3</sub> interconnect-support	Relatively high power density Relatively easy assembly Relatively easy flow	Difficult fabrication Difficult gas-tight sealing Strict requirement on thermal expansion match High thermally-activated

<b>Cell structure</b>	<b>Advantage</b>	<b>Disadvantage</b>
0.2-0.3W cm <sup>-2</sup> 900-1000°C, 80%U <sub>f</sub>	arrangement	cell component degradation
<b>Planar</b> <sup>[18, 22]</sup> Versa Power Systems ~10 μm YSZ or less (by screen printing and cofiring) Anode (cermet)-support (by tape casting) 0.3-0.5W cm <sup>-2</sup> 700-750°C at 60-70% U <sub>f</sub> Fe-Cr steel interconnect Compressive ceramic seal	Low fabrication cost Potentially low material cost by using steels High power density Ease in flow arrangement Suitable for small power source	Difficult gas-tight sealing Relatively high assembly cost Strict requirement on thermal expansion match Relatively high degradation due to IC oxidation and Cr-cathode poisoning Size limitation of cermet support
<b>Segmented-cell</b> <sup>[19]</sup> Rolls-Royce 10-20 μm YSZ or less (by screen printing and co-firing) Porous ceramic support for anode side (by tape casting) 950°C, cell resistance R <sub>t</sub> 0.4 <sup>+</sup> Ω cm <sup>2</sup>	Simplest stack Relatively low cost High durability Suitable for small power sources	Difficult fabrication and quality control Low power density

### Example 3. Anode supported planar cell with YSZ electrolyte

Similar to Example 1 calculations, for an SOFC with a practical target operating voltage of 0.75V and a power density of 0.3W cm<sup>2</sup>, the cell resistance, R<sub>t</sub>, should be less than 0.5 Ω cm<sup>2</sup>. The current anode supported planar SOFC with YSZ electrolyte of thickness 10-15μm needs to operate at 700°C or higher temperature to meet the R<sub>el</sub> = 0.15 Ω cm<sup>2</sup> cell performance target. However, the contribution of R<sub>c</sub> and R<sub>a</sub>, to the R<sub>t</sub> value will increase due to slow electrode kinetics, especially R<sub>c</sub>. New cathodes such as Sr-doped LaFeO<sub>3</sub> show better performance than LSM [21].

### 1.2.3 Planar stack components

The conventional high temperature SOFC uses a tubular design because of its relative stability against mechanical and thermal stresses, and intrinsically easy sealing. The disadvantage of this design is high ohmic resistance for current collection, leading to low power density and high stack and system cost. The anode-supported planar configuration has become popular since the 1990s. It has advantages of high power density and energy density, 700°C-800°C operation, easy fabrication, and low cost. Figure 1-2 illustrates components in a planar SOFC stack with anode-supported cells. Table 1-7 lists the typical components and materials for a planar stack.

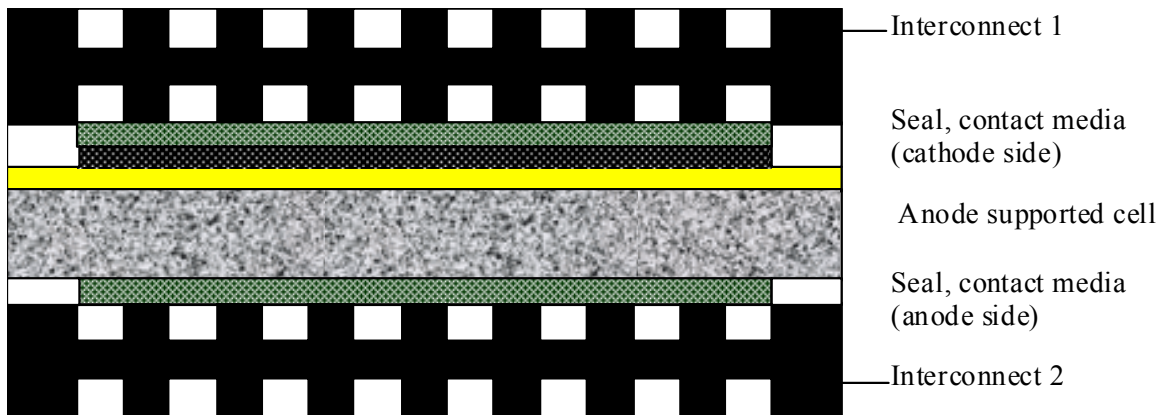


Figure 1-2 Cross-section of a planar stack configuration

Table 1-7 Typical components and materials for a planar stack

Component		Material	Thickness	Porosity
Cell (ASC)	Cathode	LSM-YSZ or LSF*	30-50μm	30-50%
	Electrolyte	8YSZ	8-10μm	< 5%
	Anode	Ni-YSZ	0.5-1.5mm	30-50%
Interconnect		Fe-Cr ferritic alloy	1-3mm	Dense
Anode contact media		Ni foam	1~2mm	>70%
Cathode contact media		LaCoO <sub>3</sub> paste	50-200 μm	30-50%
Seal		Glass-ceramic composites	Based on stack design	Dense or low porosity

\* LSF, Sr-doped LaFeO<sub>3</sub>

#### Example 4. Fe-Cr alloy oxidation and contact resistance growth with time

The durability of planar SOFC stacks is a big challenge today. The reported degradation rate is approximately 4-6% per 1000hr [22], much higher than the 0.3%/khr degradation rate target set by the Solid State Energy Conversion Alliance (SECA) of the US Department of Energy (DOE) for a lifetime of 40,000hr [23]. The oxidation of the Fe-Cr alloy interconnects is one of the degradation causes of the intermediate temperature SOFC. According to the Equation (1-13) with the experimental values in air, Hou *et al* [24] plotted the area-specific resistance (ASR) of a typical Fe-Cr alloy vs. temperature and at speculated times (1000h, 10000h, 25000h) (cf. Figure 1-3). It can be seen that the area specific resistance (ASR) of the Fe-Cr alloy increases exponentially with an increase in temperature. Based on the increase of the ASR value at different times, if a cell is operating at 700°C at 0.5A cm<sup>-2</sup> with an initial cell voltage of 0.75V, a calculation reveals that the degradation rate owing to cathode contact resistance growth is 3.5%/khr for the 1<sup>st</sup> khrs, 1.2%/khr for the 1<sup>st</sup> 10khrs and 0.8% for 25khr. It indicates that for a stack using Fe-Cr alloy interconnects operating over 700°C, it is difficult to meet the lifetime requirement (0.3%/khr for stack degradation rate). However, if the operating temperature moves down to below 600°C, the projected loss due to interconnect oxidation can be as low as 0.4%/khr for 25khrs operation, which is close to the degradation criteria set by SECA.

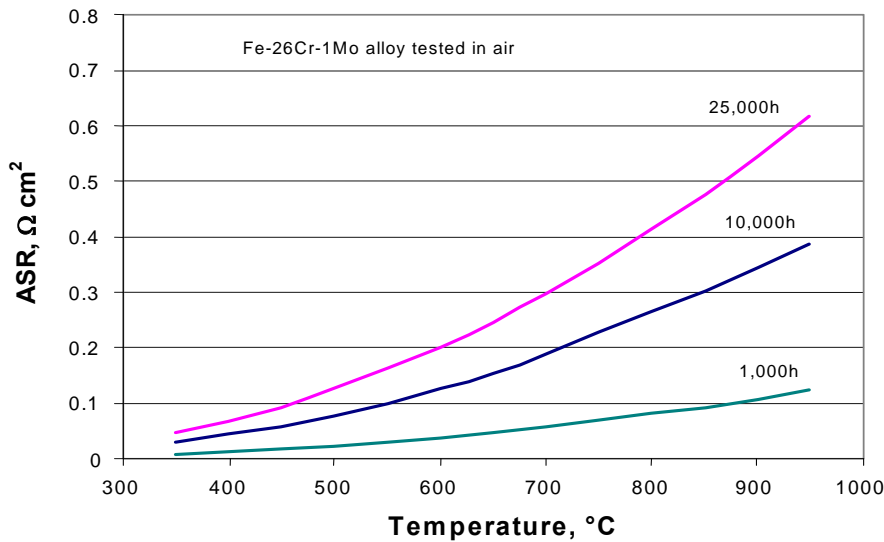


Figure 1-3 The area specific resistance of the Fe-Cr alloy at different times [24] (© The Electrochemical Society Inc., 1999, by permission)

### **1.3 Advantages and challenges of SOFC**

The SOFC has a number of advantages in comparison to other types of fuel cells [7]. Firstly, because of its solid electrolyte, the SOFC does not need complex electrolyte management to maintain an optimal three-phase boundary condition, and to prevent electrolyte vapour loss and composition change. The corrosion of stack components by the electrolyte is completely avoided. Secondly, because of the use of all-solid-state construction, the SOFC can be configured into various geometries such as tubular, monolithic, planar, or segmented cells, offering flexibility in cell and stack design, simplicity of system management, and potentially low fabrication costs. The cell components can be very thin to reduce material costs and internal resistance losses (for example in a cermet-supported cell structure). Further, the SOFC operates at the widest and highest temperature range, typically 700-1000°C, at which conventional yttria stabilized zirconia (YSZ) electrolytes become highly conductive of oxygen ions ( $O^{2-}$ ). This operating temperature range is required for processing hydrocarbon fuels, and therefore simplifies thermal management at the system level (through internal reforming). The high operating temperature also makes noble metal catalysts unnecessary and allows CO to be used as a fuel and not a poisoning gas to the anode. The typical nickel-based anode materials and the lanthanum-manganite-based cathode materials are both much cheaper than Pt- electrodes commonly used in other types of fuel cells: Alkaline Fuel Cell (AFC), Polymer Electrolyte Fuel Cell (PEFC) and Phosphoric Acid Fuel Cell (PAFC). Moreover, the  $O^{2-}$ -conducting electrolyte intrinsically permits the use of all types of hydrocarbon fuels,  $H_2$ , CO,  $H_2S$ , and even coal-based fuels in the SOFC to generate electricity without the need for the extensive fuel purification (as required by AFC, PEFC, and PAFC). Furthermore, high temperatures facilitate the electrode process kinetics and the mass transport of reactants and products, leading to high electrical efficiency of 45-50% in a practical operation with power density over  $0.3 \text{ W cm}^{-2}$  [7, 25]. In addition, high temperature exhaust from the SOFC is suitable for use in cogeneration or a bottoming cycle, which provides additional electrical efficiency of 25-35% by a gas turbine. Finally, using SOFC-Gas Turbine combined power generation, both the fossil fuel consumption rate and  $CO_2$  emission to the atmosphere can be reduced by half compared to existing thermal power generation.

For commercial application, the durability and reliability of the SOFCs need to be demonstrated along with cost reduction. These are the biggest challenges for the SOFC and for other types of fuel cells. Although the SOFC has many advantages (as mentioned above), its high operating temperature also generates issues, such as 1) low durability of stack performance due to thermally-activated material degradation, including electrolyte aging, electrode coarsening and/or sintering, cathode Cr poisoning, and non (or less) conductive phase generation at various interfaces; 2) high thermal stress in the cell and stack level due to either thermal expansion mismatching between functional components or non-uniform operating conditions across the cell, causing failure during the start-up, operation and cool-down, resulting in low reliability; 3) high operating temperature also leads to high cost in materials and fabrication due to material restrictions on the cell, seal, interconnect, and balance of plant; 4) meanwhile, high operating temperature limits the application for portable power sources and transportation due to time and energy consumption during start-up and cool-down. Therefore, a major thrust in the current SOFC development is trying to reduce the SOFC operating temperature to below 650°C to further alleviate the afore-cited adverse effects of high temperature on the durability, reliability and cost.

From the SOFC operational principle, we know that the conventional YSZ-based cell material system limits further operating temperature reduction. Figure 1-4 shows typical 150  $\mu\text{m}$  thick YSZ electrolyte-supported cell performance and the cell voltage losses of the cell components vs. temperature [12]. In this figure,  $\Delta U_{\text{cathode}}$ ,  $\Delta U_{\text{anode}}$ , and  $\Delta U_{\text{electrolyte}}$  stand for the voltage losses from the cathode, the anode, and the electrolyte, respectively. The area specific resistances of  $R_c$ ,  $R_a$ , and  $R_{el}$  are calculated based on the voltage loss under operating current density at 650°C. Obviously, this type of cell operating at 650°C will only have 0.05  $\text{W cm}^{-2}$  peak power density with the individual component resistance (listed on the right side of the figure) one order of magnitude higher than the values required (see Example 1). Therefore, there are many challenges to material scientists and processing engineers to maintain an adequate performance in SOFCs at lower operating temperature.

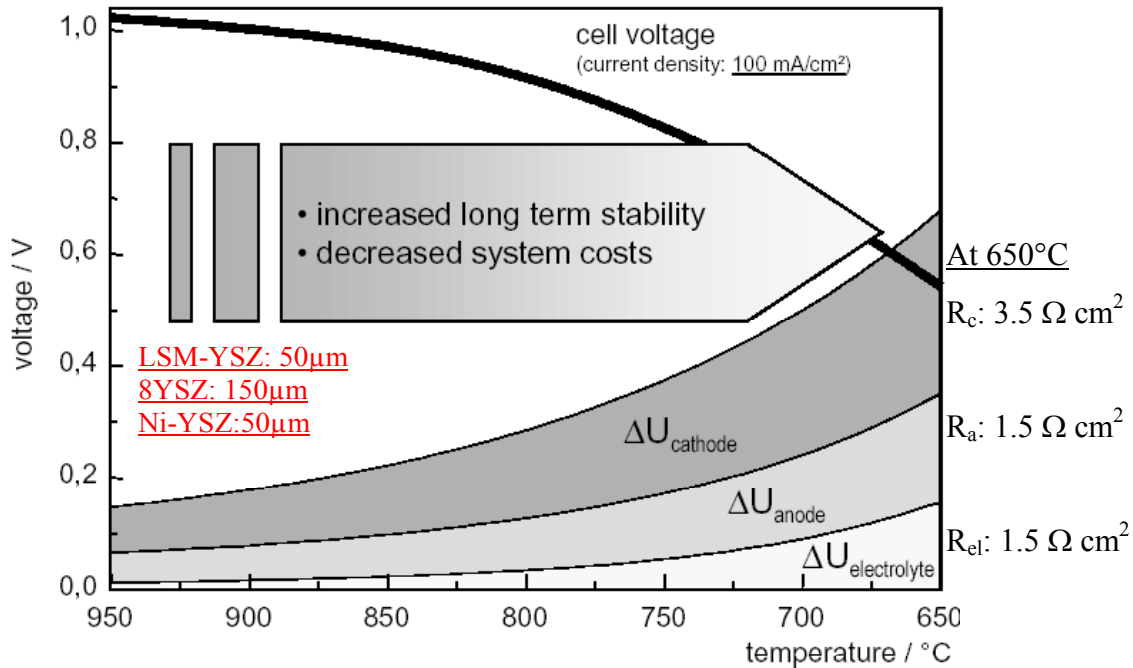


Figure 1-4 YSZ electrolyte supported cell voltage losses [12] (© Journal of the European Ceramic Society, 2001, by permission)

#### 1.4 Literature review on low temperature SOFCs

As discussed in previous sections, the operating temperature of an SOFC depends on the total cell resistance. The conventional SOFC with a 15 $\mu\text{m}$ -thick YSZ electrolyte in an anode supported cell structure needs to operate at 700°C or higher temperature if only based on the  $R_{el} < 0.15 \Omega \text{ cm}^2$  requirement.  $R_{el}$  values calculated for a 10  $\mu\text{m}$ -thick YSZ become appreciable at 600°C, approximately  $0.5 \Omega \text{ cm}^2$ , and very large at 500°C,  $\approx 2 \Omega \text{ cm}^2$  [26]. While significantly thinner YSZ electrolytes would allow lower operating temperatures, the long-term stability and reliability of ultra-thin electrolytes as well as fabrication cost are the main issues. Meanwhile, the resistance from other cell components (anode, cathode and electrical contact) is also exponentially increased with a decrease in operating temperature, so only reducing the thickness of the electrolyte is insufficient to retain the SOFC at high power density at or below 650°C. For example, the value of  $R_{c,LSM}$  at 650°C is one order of magnitude higher than the required  $0.15 \Omega \text{ cm}^2$  (see Figure 1-4). Therefore, each cell component is the subject of a great deal of research.

### 1.4.1 Electrolytes of high ionic conductivity

As a primary material in the SOFC, an electrolyte of high ionic conduction and good compatibility with high performance electrodes is essential to retain adequate performance at lower operating temperatures. Several alternative electrolyte materials of high ionic conductivity have been discovered and studied for LT-SOFC development, such as Er-doped  $\text{BiO}_{2-\delta}$  [27], Sm-doped  $\text{CeO}_2$  (SDC) [28], Gd-doped  $\text{CeO}_2$  (GDC) [29],  $(\text{LaSr})(\text{GaMg})\text{O}_{3-\delta}$  (LSGM) [30], and scandia-doped  $\text{ZrO}_2$  (SSZ) [31]. Recent reviews on the electrolytes for SOFCs can be found [32, 33]. Figure 1-5 reproduces the reported conductivities of these electrolyte materials in their optimal composition along with YSZ at a temperature range from 800 °C to 400°C in ambient air. From the interception of conductivity curves with the dotted line in Figure 1-5, with a 15 $\mu\text{m}$  thick electrolyte at  $R_{\text{el}} = 0.15 \Omega \text{ cm}^2$ , those oxygen-ion conductors can be used for operation below 650°C, while the same thickness of YSZ has to be operated above 650°C.

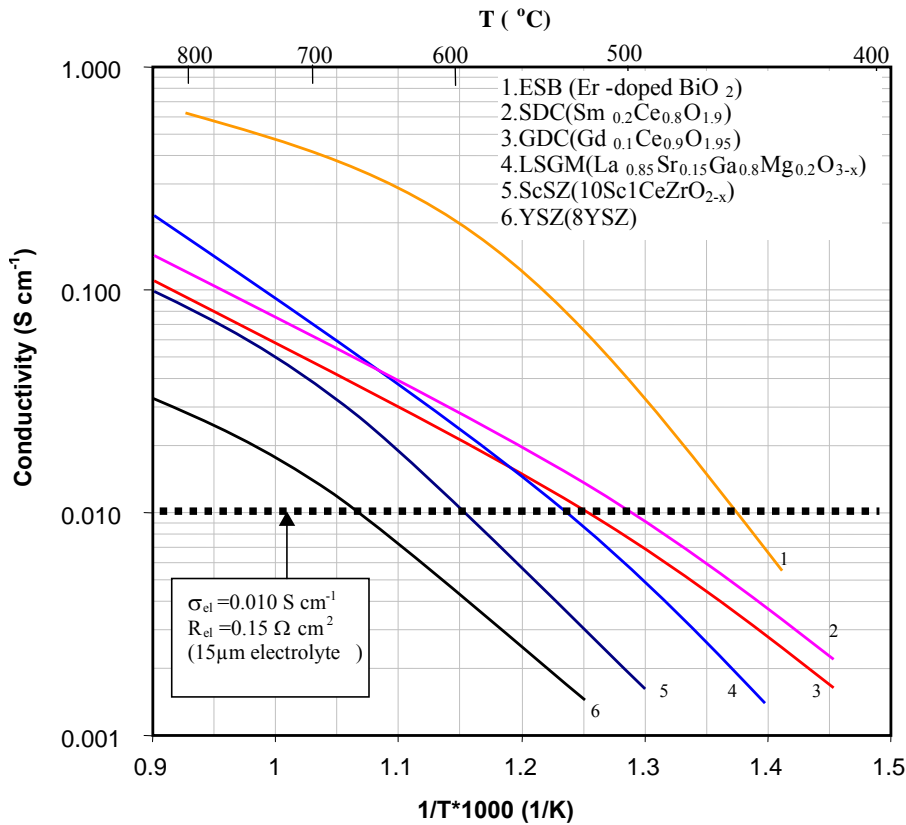


Figure 1-5 Conductivity of SOFC electrolytes

### 1.4.1.1 SSZ

Doped  $\text{ZrO}_2$  is known to have a high ionic conductivity with 8-12 mol%  $\text{Sc}_2\text{O}_3$  dopant. It is stable under both reducing and oxidizing atmospheres and is purely ionically conductive. The highest conductivity of SSZ with 8 mol %  $\text{Sc}_2\text{O}_3$  at  $800^\circ\text{C}$  was found to be  $0.159 \text{ S cm}^{-1}$  [34], while only 0.032 for 8YSZ. The higher conductivity of SSZ is attributed to the smaller mismatch in size between  $\text{Zr}^{4+}$  (0.086nm radius) and  $\text{Sc}^{3+}$  (0.089nm), as compared to that between  $\text{Zr}^{4+}$  and  $\text{Y}^{3+}$  (0.098nm), leading to a smaller energy for defect association, which increases mobility and thus conductivity [4, 31].  $\text{ZrO}_2$  with 8-12mol%  $\text{Sc}_2\text{O}_3$  exhibits a significant aging effect at high temperature. With annealing at  $1000^\circ\text{C}$ , its conductivity drops from  $0.3 \text{ S cm}^{-1}$  to  $0.12 \text{ S cm}^{-1}$  after 1000hr [35]. The conductivity of SSZ below  $500^\circ\text{C}$  is similar to that of YSZ, indicating that the activation energy for conduction in SSZ tends to increase with decreasing temperature [36]. It has been well reported that the highly conductive cubic phase of SSZ transforms to a low conductive rhombohedral phase at lower temperatures [37-39]. The phase change can be alleviated or avoided by co-doping with other oxides, such as those of cerium [31], ytterbium [38] or bismuth [40]. The mechanism of the stabilizing effect has been introduced in [41]. The typical composition of SSZ is 10 mol% $\text{Sc}_2\text{O}_3$  and 1mol%  $\text{CeO}_2$  co-doped  $\text{ZrO}_2$ , with conductivities of approximately  $0.09 \text{ S cm}^{-1}$  at  $800^\circ\text{C}$  and  $0.01 \text{ S cm}^{-1}$  at  $600^\circ\text{C}$ , showing no degradation over 600 hrs at  $1000^\circ\text{C}$  [31]. The reported activation energy is approximately  $62.7 \text{ kJ mol}^{-1}$  [42] and  $60\text{-}80 \text{ kJ mol}^{-1}$  [40] in the temperature range of  $800\text{-}1000^\circ\text{C}$ , the thermal expansion coefficient is between  $10 \times 10^{-6} \text{ K}^{-1}$  [3] and  $11.9 \times 10^{-6} \text{ K}^{-1}$  [34], and the mechanical strength is approximately 250 MPa [3], similar to that of YSZ. The problem with SSZ is the difficulty in synthesis of the electrolyte. A high sintering temperature is needed to densify SSZ. SSZ powders often lack compositional uniformity, and the conductivity of the sintered solid depends on the preparation methods [43]. Currently only Daiichi Chemicals (Daiichi Kigenso Kagaku Kogyo, Japan) company provides pre-commercial SSZ powder. Since scandium is rarer and more expensive than yttrium, SSZ powder is relatively costly.

### 1.4.1.2 Doped Ceria

Doped ceria has the same fluorite structure as doped zirconia. As shown in Figure 1-6, the highest conductivity occurs with dopants  $\text{Sm}^{3+}$  (ionic radius: 0.110 nm) and  $\text{Gd}^{3+}$  (0.108nm) of the lowest size mismatch with  $\text{Ce}^{4+}$  (0.111 nm) [28, 44, 45]. Like zirconia, the conductivity increases with increasing dopant concentration to a maximum (Figure 1-7), at 0.10-0.20 for both Sm [28] and Gd [46], and then decreases. The conductivities for  $\text{Ce}_{0.8}\text{Gd}_{0.2}\text{O}_{1.9}$  and  $\text{Ce}_{0.9}\text{Gd}_{0.1}\text{O}_{1.95}$  are close, and  $\text{Ce}_{0.9}\text{Gd}_{0.1}\text{O}_{1.95}$  has been shown to have better stability than  $\text{Ce}_{0.8}\text{Gd}_{0.2}\text{O}_{1.9}$  at low oxygen partial pressures [47]. The most widely used ceria-based electrolytes  $\text{Ce}_{0.8}\text{Sm}_{0.2}\text{O}_{1.9}$  (SDC) [28] and  $\text{Ce}_{0.9}\text{Gd}_{0.1}\text{O}_{1.95}$  (GDC) [29] have higher conductivity and lower activation energy [48], particularly at temperatures below 650°C, in comparison to those of YSZ or SSZ (Figure 1-5). The conductivity of the SDC is approximately 0.1- 0.15  $\text{S cm}^{-1}$  at 800°C in air, slightly higher than that of GDC [28, 29], with the activation energy 40-65  $\text{kJ mol}^{-1}$  [4]. The thermal expansion coefficients of both are approximately  $12 - 13 \times 10^{-6} \text{ K}^{-1}$  [33].

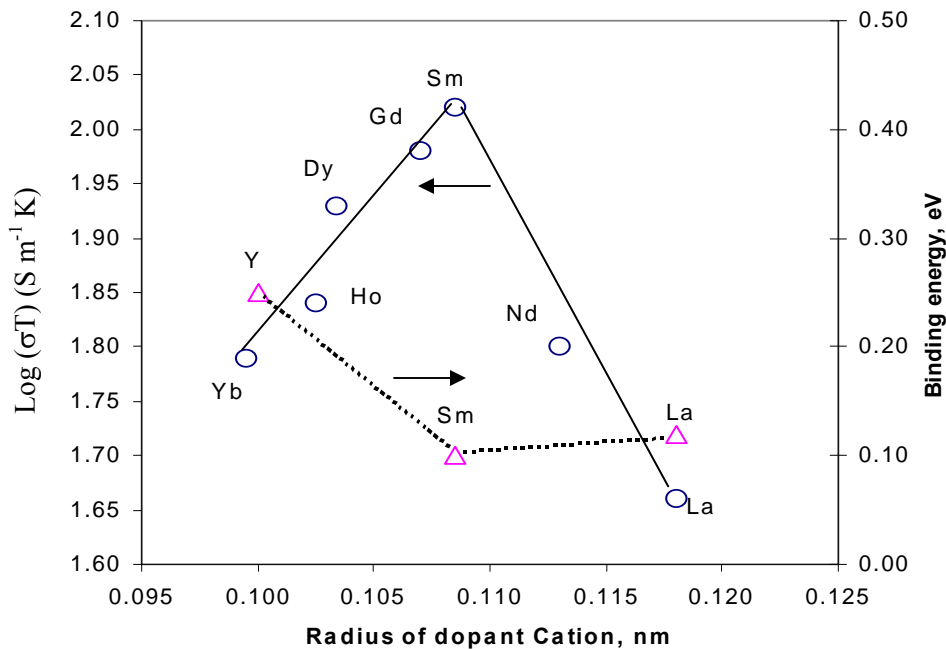


Figure 1-6 Dependence of ionic conductivity and binding energy for  $(\text{CeO}_2)_{0.8}-(\text{LnO}_{1.5})_{0.2}$  at 800 °C on ionic radius of  $\text{Ln}^{3+}$  [45] (© Solid State Ionics, 1989, by permission)

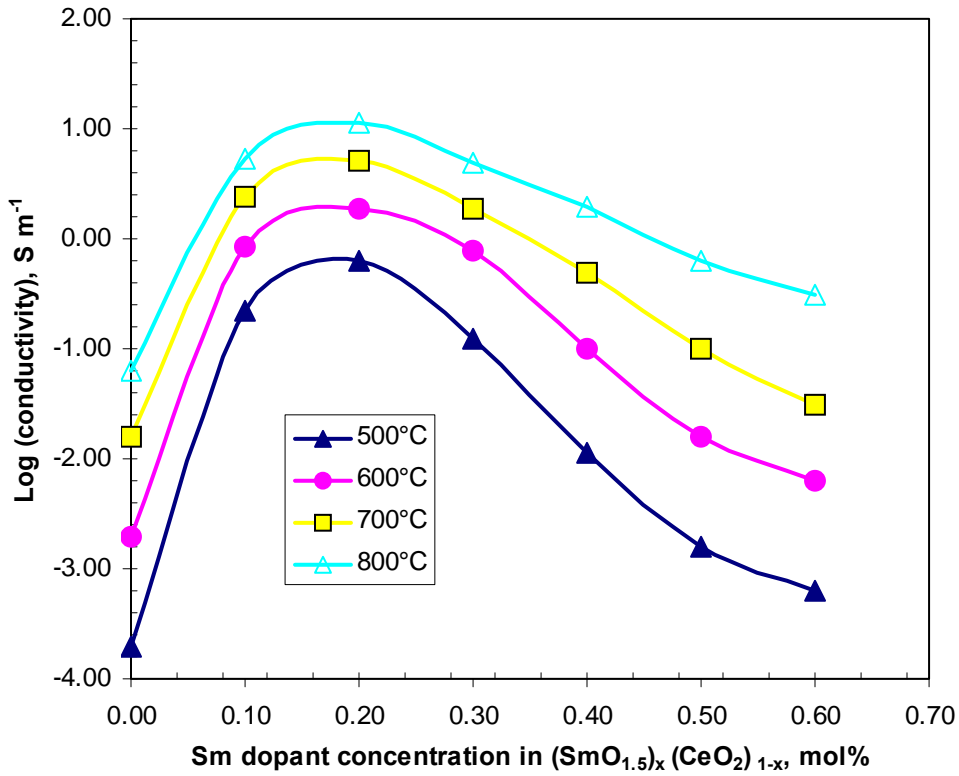


Figure 1-7 Concentration dependence of conductivity for Sm-doped CeO<sub>2</sub> [28] (© Journal of Applied Electrochemistry, 1988, by permission)

The primary disadvantage of ceria is electronic conduction at low oxygen partial pressures [49-54]. The oxygen ionic conductivity ( $\sigma_i$ ) and electronic conductivity ( $\sigma_e$ ) of the doped-ceria electrolyte can be estimated as

$$\sigma_i = \frac{\sigma_{0,i}}{T} \exp\left(-\frac{E_{a,i}}{RT}\right) \quad \text{Equation 1-20}$$

$$\sigma_e = \sigma_{0,e} \frac{(p_{O_2,el})^{-1/4}}{T} \exp\left(-\frac{E_{a,e}}{RT}\right) \quad \text{Equation 1-21}$$

For Gd<sub>0.1</sub>Ce<sub>0.9</sub>O<sub>1.95</sub>,  $\sigma_{0,i} = 2.706 \times 10^6$  [S K m<sup>-1</sup>],  $E_{a,i} = 61.748 \times 10^3$  [J mol<sup>-1</sup>];  $\sigma_{0,e} = 2.342 \times 10^{11}$  [S K atm<sup>1/4</sup> m<sup>-1</sup>],  $E_{a,e} = 238.78 \times 10^3$  [J mol<sup>-1</sup>] [54]. However, Mogensen *et al* [49] reported much lower  $E_{a,e}$  approximately, 20-40 x 10<sup>3</sup> [J mol<sup>-1</sup>], much lower than their reported  $E_{a,i}$  value of 67.5 x 10<sup>3</sup> [J mol<sup>-1</sup>], according to the mobility of electron and oxygen ion in GDC.

Due to the electronic conduction, the maximum efficiency based on the Gibbs free energy is 50% at 800°C and 60% at 600°C [51, 52]. An SOFC with an SDC electrolyte should be operated at temperatures below 600°C to avoid such efficiency loss due to electronic leakage. Theoretical analysis indicates that under operation temperature below 600°C with ceria-based electrolytes, the efficiency loss is limited to low current densities. At cell voltages of 0.6-0.7V the penalty is small and acceptable [33, 55]. A thin coating of YSZ can effectively prevent the electronic conduction of the ceria electrolyte [56]. However, the performance of bi-layered electrolyte cell is not encouraging, and interdiffusion at the YSZ/ceria interface could be an issue in practical use [55, 57].

Although the stability of ceria in low oxygen partial pressures ( $p_{O_2}$ ) is inferior to that of zirconia, the chemical compatibility of ceria with cathode materials is superior to that of zirconia. Both GDC and SDC have been shown to be stable with a wide variety of electrodes including mixed ion and electron conductor (MIEC) cathode materials, such as LSCF [53] and BSCF [58]. In fact, GDC and SDC are also commonly used as anode materials mixed with Ni or NiO for high performance anode application [59, 60]. Because of the excellent stability with cathode materials, ceria-based interlayers are applied between YSZ and MIEC cathodes to prevent detrimental interactions [61-63]. However, interaction occurs between the YSZ and the ceria layer at high temperature [64-66]. Since both the ceria and YSZ have the same cubic fluorite phase structure, interdiffusion can occur and results in the formation of a region with low conductivity. Therefore, strict processing conditions have to be followed.

### 1.4.1.3 LSGM

Perovskite-type LSGM possesses an ionic conductivity higher than that of stabilized zirconia and close to or lower than that of GDC or SDC below 550°C. The maximum ionic conductivity (0.175 S/cm at 800°C, with activation energy  $E_{a,i} \sim 82 \text{ kJ mol}^{-1}$ ) is achieved with the composition of  $\text{La}_{0.85}\text{Sr}_{0.15}\text{Ga}_{0.8}\text{Mg}_{0.2}\text{O}_{3-\delta}$ , and further acceptor-type doping leads to progressive vacancy association processes [67, 68]. A decrease in conductivity is also observed on doping with a smaller radius A-site cation, or creating A-site deficiency. Surprisingly, introduction of small amounts of cations with variable valence, such as cobalt, onto the gallium sites increases the ionic conduction in LSGM, and produces only a

small increase in the electronic conductivity [69-71]. However, the concentration of transition metal dopants should be limited to below 3–7 mol%, as further additions lead to increasing electronic and decreasing ionic conductivities. Similarly to zirconia electrolytes, the electrolytic domain of LSGM extends to substantially lower oxygen partial pressure ( $p_{O_2}$ ), and LSGM exhibits pure ionic conductivity, and has relatively lower thermal expansion ( $11 \times 10^{-6}$  1/K) than those of the ceria-based electrolytes. Disadvantages of LaGaO<sub>3</sub>-based materials include possible reduction and volatilization of gallium oxide, formation of stable secondary phases in the course of processing, the relatively high cost of gallium, and significant reactivity with perovskite electrodes under oxidizing conditions as well as with metal anodes in reducing conditions [72-74]. The interaction of LSGM with electrodes makes it almost impossible to use wet ceramic processing to fabricate either anode supported or cathode supported thin LSGM electrolyte cells, which is necessary for LT-SOFC to reduce the electrolyte resistance. The reaction of LSGM with cathodes is different from that of zirconia or ceria, because most of the common cathode materials have the perovskite structure. Thus, rather than forming a separate phase, the interaction typically occurs through interdiffusion. The most common diffusion species is cobalt [75, 76]. Interdiffusion also occurs between LSGM and LSCF [77] and lanthanum nickelate cathode [78]. Therefore, the cathode sintering temperature is normally below 1100°C to avoid interdiffusion induced low cathode performance. Since small amounts of Co, Ni, and Fe can be beneficial to electrolyte performance, and there is no highly resistive layer formed at the electrolyte/cathode interface, therefore, the electrolyte-cathode interdiffusion is not necessarily detrimental to fuel cell performance, but it will generate long-term stability concerns. Excessive interdiffusion would eventually degrade the properties of both components, so a ceria layer has been applied to prevent cobalt diffusion from LSC into LSGM [79]. However, a resistive phase can form between GDC (SDC) and LSGM and degrade fuel cell performance [80, 81]. The most common anode material is a Ni-based cermet. For LSGM electrolytes, a resistive phase can form between the LSGM and Ni-containing anode at 1300°C or even lower temperature [60, 82]. Alternative anode materials are being developed including perovskite oxides, such as (La,Sr)(Cr,Mn)O<sub>3</sub>. However, easy interdiffusion between anode and electrolyte was observed during processing, leading to a resistive phase. Such degradation can be avoided by limiting the

sintering time and temperature [83]. However, restrictions on the processing conditions can be a substantial challenge for the fabrication of thin LSGM electrolytes by cost-effective processes.

#### 1.4.1.4 Doped Bismuth Oxide

Doped bismuth oxides have extremely high oxygen ionic conductivities in comparison with the above-mentioned ceramic electrolytes. Bismuth oxide ( $\text{Bi}_2\text{O}_3$ ) itself exhibits a number of polymorphs,  $\alpha$ ,  $\beta$ ,  $\gamma$  and  $\delta$ -phases. In the fluorite structure of the  $\delta$ - $\text{Bi}_2\text{O}_3$  phase ( $\text{BiO}_{1.5}$ ), a quarter of the available oxide ion sites are vacant. This fact, together with the polarizability of the Bi  $6s^2$  lone pairs and suitable conduction pathways, results in high ion conductivity in this compound [84, 85]. In pure  $\text{Bi}_2\text{O}_3$ , the  $\delta$ -phase is only stable over a narrow temperature range from 730–825 °C [84]. Substitution of Bi by Er, Y, Yb, or Nb [85-87] results in the stabilization of this phase to room temperature through solid solution formation with oxide dopants. At 20%-25% substitution of Bi by Er, the cubic  $\delta$ -phase of formula  $\text{Bi}_3\text{ErO}_{7-x}$  shows the highest conductivity in air (see Figure 1-5), of  $0.023 \text{ Scm}^{-1}$  at 500°C, and  $0.37 \text{ Scm}^{-1}$  at 700°C, with an ionic transference number equal to unity [85]. Verkerk and Burggraaf showed that the conductivity of  $(\text{Bi}_2\text{O}_3)_{0.8}(\text{Er}_2\text{O}_3)_{0.2}$ , in the temperature range 300–1100 K, displayed a clear bend in the Arrhenius behaviour [88]. The activation energy was found to change from 115 to 52  $\text{kJ mol}^{-1}$  at temperatures between 550°C and 650°C. At low temperatures below 870 K, short-range ordering in the oxygen lattice was apparent, while at higher temperatures the short-range ordering diminishes. This decrease brings about an increase in the lattice constant and a subsequent decrease in the activation energy. Unfortunately, doped bismuth oxide decomposes easily at low oxygen partial pressures, which prevents it from being used in solid oxide fuel cells. One approach of overcoming this limitation is to combine doped bismuth oxide with a ceria-based electrolyte, with the ceria at the anode side and the bismuth oxide at the cathode side [89, 90]. If the thicknesses are selected appropriately, the bismuth oxide will remain above the oxygen partial pressure of its decomposition and the electronic conduction in the ceria will be blocked by the bismuth oxide [91]. However, the effectiveness of this approach has not been well demonstrated.

## 1.4.2 Challenge and approach

Although the new electrolyte materials have higher ionic conductivity, material stability and compatible electrodes are remaining issues. For example, doped ceria and  $\text{Bi}_2\text{O}_3$  are thermodynamically unstable in reducing environments. Thermodynamic calculations on  $\text{Bi}/\text{Bi}_2\text{O}_3$  indicate a stability down to only  $10^{-13}$  atm oxygen partial pressure ( $p_{\text{O}_2}$ ), thus limiting the SOFC cell voltage to  $\sim 600\text{mV}$  at  $700^\circ\text{C}$  (relative to air) [85]. The lower  $p_{\text{O}_2}$  limit of ceria materials is dictated by an increase in electronic conduction with reduction from  $\text{Ce}^{4+}$  to  $\text{Ce}^{3+}$ , resulting in mixed ionic and electronic conduction ( $t_i < 1$ ) with decreasing  $p_{\text{O}_2}$  and increasing temperature [92]. This limits the usefulness of  $\text{CeO}_2$  as an electrolyte due to the lower open circuit voltage (OCV) and the power loss caused by the electronic conduction through the electrolyte. As stated previously, although LSGM exhibits pure ionic conductivity and suitable thermal expansion, disadvantages of this type of material include possible reduction and volatilization of gallium oxide, formation of stable secondary phases in the course of processing, the relatively high cost of gallium, and significant reactivity with perovskite electrodes under oxidizing conditions as well as with nickel cermet anodes in reducing conditions [93, 94]. The interaction of LSGM with electrodes makes it difficult to use wet ceramic processing to fabricate either anode supported or cathode supported LSGM electrolyte cells. Therefore, an alternative electrolyte configuration is necessary to reduce the electrolyte resistance so that the electrolyte can be used in LT-SOFCs [95, 96].

As a compromised approach, bi-layered electrolytes have been investigated in order to overcome the inherently limited thermodynamics and chemical stability of highly conductive oxides and to take advantage of the high ionic conductivity of the new electrolyte materials [26, 56, 97]. These investigations can be catalogued into 2 types based on the purposes:

- 1) A thin layer (dense if possible) of a more stable oxide protects these highly conductive materials from reduction by preventing contact with the reducing gas. For example, Yahiro *et al* [56] demonstrated that a thin protective layer of YSZ on the fuel side of a Y-doped ceria electrolyte SOFC increased the OCV and enhanced power density. Recently, Wang *et al* [98] used a multi-layer tape casting procedure to

fabricate an anode-supported 5 $\mu\text{m}$  SSZ/10 $\mu\text{m}$  GDC bi-layered electrolyte cell. With an LSCF-GDC composite cathode sintered at 1100°C, they obtained a maximum power density of 0.63 W cm<sup>-2</sup> and an area-specific resistance (ASR) of 0.99  $\Omega$  cm<sup>2</sup> at 850°C in the single cell with H<sub>2</sub>/O<sub>2</sub> as the operating gases.

2) A thin layer (dense if possible) of oxide(s) more chemically compatible with the electrodes enhances the electrode performance and the cell durability. For example, doped ceria electrolyte on ZrO<sub>2</sub>-based electrolyte SOFC prevents the possible detrimental interaction between the cathode and the ZrO<sub>2</sub> electrolyte. By introducing a doped-ceria barrier layer at the cathode side, cobalt-containing cathodes of high performance can be implemented. A high performance of 0.5 W cm<sup>-2</sup> at 700°C has been demonstrated by Nguyen *et al* [99, 100]. However, there is little success when using this cell structure operating below 650°C to meet cell performance requirements for commercial application.

### 1.4.3 Cathode

The cathodes reviewed in this section are made of mixed ionic-electronic conducting (MIEC) perovskites (ABO<sub>3</sub>) of which both the A site and the B site can be substituted in order to tailor the material properties. Commonly, the A-site is a rare earth element, such as La, Sm, Gd, or Pr, partially substituted by alkaline-earth elements with similar ionic radius, such as Sr, Ba, or Ca; while the B-site is a transition metal, such as Co, Ni, Fe, Cu, Mo, or Mn, either a single element or a combination of two or more elements. For example, in La<sub>1-x</sub>Sr<sub>x</sub>CoO<sub>3- $\delta$</sub>  (LSC, x = 0.1-0.7) cathode materials [101, 102], the A-site is partially substituted by strontium. The substitution of La<sup>3+</sup> by Sr<sup>2+</sup> creates a fully ionized acceptor ( $Sr'_{La}$ ) whose charge is compensated by holes ( $Co^{\bullet}_{Co}$ ) in the valence band and oxygen vacancies ( $V_{O}^{\bullet\bullet}$ ) at the O-sites. Therefore, LSC perovskites are p-type electronic conductors with a noticeable amount of oxygen vacancies [103, 104]. Because of the presence of oxygen vacancies, oxygen can be transported through the bulk of the MIEC cathode by diffusion. Thus as illustrated in Figure 1-8, the cathode reaction zone expands to the full cathode area and is no longer limited to the three-phase boundary (TPB) area as

in the case of LSM [105]. It has been well reported that the cathode performance of certain MIECs is sufficiently high even below 650°C.

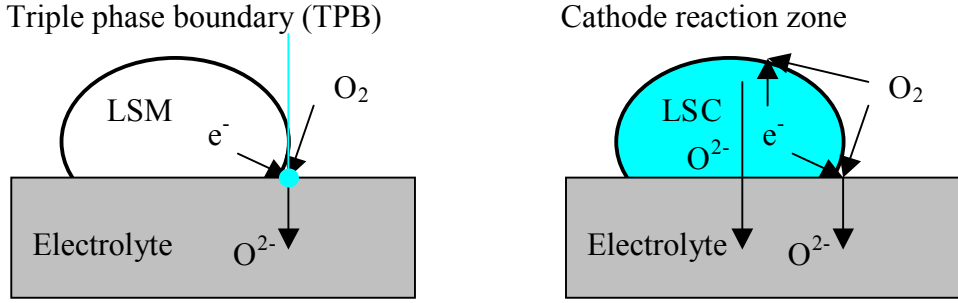


Figure 1-8 Schematic drawing of oxygen reduction path at cathodes

The concentrations of the defects in the MIECs are dependent on the chemical composition, the microstructure (particle size), the temperature, the oxygen partial pressure and the electrochemical potential. The electrical conductivity of  $\text{La}_{0.6}\text{Sr}_{0.4}\text{CoO}_{3-\delta}$  is as high as  $1500 \text{ S cm}^{-1}$ , with an ionic conductivity of  $0.22 \text{ S cm}^{-1}$  at  $800^\circ\text{C}$  in air [3, 4]. Other well known MIEC cathode materials are  $\text{Sm}_{1-x}\text{Sr}_x\text{CoO}_{3-\delta}$  (SSC,  $x = 0.2-0.7$ ) [106],  $\text{La}_{1-x}\text{Sr}_x\text{FeO}_{3-\delta}$  (LSF,  $x = 0.2-0.7$ ) [21],  $\text{LaNi}_{1-x}\text{Fe}_x\text{O}_{3-\delta}$  (LNF,  $x = 0.2-0.8$ ) [107, 108],  $\text{La}_{1-x}\text{Sr}_x\text{Co}_{1-y}\text{Fe}_y\text{O}_{3-\delta}$  (LSCF,  $x = 0.1-0.5$ ,  $y = 0.2-0.8$ ) and  $\text{Ba}_{1-x}\text{Sr}_x\text{Co}_{1-y}\text{Fe}_y\text{O}_{3-\delta}$  (BSCF,  $x = 0.1-0.5$ ,  $y = 0.2-0.8$ ) [109].

Typical composition and properties of LSC, SSC, LNF, LSCF, and BSCF are listed in Table 1-8. In this table,  $\sigma_e$  is the electronic conductivity,  $\sigma_i$  is the ionic conductivity,  $k_s$  is the surface exchange coefficient,  $D_o$  is the oxygen diffusion coefficient, and CTE is the coefficient of thermal expansion. It is clear that the Co-containing MIEC cathode materials show higher ionic conductivity ( $\sigma_i$ ) and higher coefficient of thermal expansion (CTE) than those of LNF, LSF and LSM. The higher CTE of the Co-containing MIEC materials is due to formation of oxygen vacancies, reduction of the smaller  $\text{Co}^{4+}$  ions to the larger  $\text{Co}^{3+}$  ions, spin-state transitions associated with  $\text{Co}^{3+}$  from low spin ( $t_{2g}^6 e_g^0$ ,  $r = 0.0545\text{nm}$ ) to high spin ( $t_{2g}^4 e_g^2$ ,  $r = 0.061\text{nm}$ ), and the relatively weaker Co-O bond compared to the Fe-O, Ni-O and Mn-O bonds [110]. In general, the variations in CTE could be related to the tendency to form oxygen vacancies, and thus to the ionic conductivities. Ullmann *et al* [111] presented an empirical correlation between the CTE and  $\sigma_i$  at  $800^\circ\text{C}$  in air, for MIEC

cathode materials and certain electrolyte materials such as LSGM, presented in Equation 1-22.

$$\text{Log } \sigma_i = -7.08 + 2.9 \times 10^5 \text{ CTE} \quad (\sigma_i \text{ in S cm}^{-1}, \text{ CTE in } 10^{-6} \text{ K}^{-1}) \quad \text{Equation 1-22}$$

Table 1-8 Typical compositions and properties of MIEC cathodes from the literature (Note: values in the parentheses are the cathode material reduction activation energies in kJ mol<sup>-1</sup>.)

<b>Cathode</b>	<b>Typical Composition</b>	<b><math>\sigma_e</math></b> <b>S cm<sup>-1</sup></b>	<b><math>k_S</math></b> <b>cm s<sup>-1</sup></b>	<b><math>D_O</math></b> <b>cm<sup>2</sup> s<sup>-1</sup></b>	<b><math>\sigma_i</math></b> <b>S cm<sup>-1</sup></b>	<b>CTE x 10<sup>6</sup></b> <b>1/K</b>	<b>Ref</b>
LSM	La <sub>0.8</sub> Sr <sub>0.2</sub> MnO <sub>3-<math>\delta</math></sub>	175 (8.7)	10 <sup>-8</sup>	10 <sup>-12</sup>	10 <sup>-7</sup>	11-12	3, 4
LSC	La <sub>0.6</sub> Sr <sub>0.4</sub> CoO <sub>3-<math>\delta</math></sub>	10 <sup>3</sup>	10 <sup>-5</sup>	10 <sup>-7</sup>	0.22	22-26	3, 4
LSF	La <sub>0.6</sub> Sr <sub>0.4</sub> FeO <sub>3-<math>\delta</math></sub>	158			0.004	12.8, 14.9	21, 112
SSC	Sm <sub>0.5</sub> Sr <sub>0.5</sub> CoO <sub>3-<math>\delta</math></sub>	10 <sup>3</sup>	10 <sup>-4</sup>	10 <sup>-6</sup>	>0.1	19-22	3, 113
LNF	LaNi <sub>0.6</sub> Fe <sub>0.4</sub> O <sub>3-<math>\delta</math></sub>	257 (4-6)				11.4	107, 108
LSFC	La <sub>0.8</sub> Sr <sub>0.2</sub> Fe <sub>0.8</sub> Co <sub>0.2</sub> O <sub>3-<math>\delta</math></sub>	83	10 <sup>-6</sup>	10 <sup>-8</sup>	0.0023	14.8	112
LSCF	La <sub>0.8</sub> Sr <sub>0.2</sub> Co <sub>0.8</sub> Fe <sub>0.2</sub> O <sub>3-<math>\delta</math></sub>	10 <sup>2</sup>	10 <sup>-5</sup>	10 <sup>-7</sup>	0.08	18-22	114, 115
BSCF	Ba <sub>0.8</sub> Sr <sub>0.2</sub> Co <sub>0.8</sub> Fe <sub>0.2</sub> O <sub>3-<math>\delta</math></sub>	25.4	10 <sup>-3</sup>	10 <sup>-4</sup>	0.88	19-23	112, 116, 117

Note: For LSM: CTE for 25-1000°C and other properties at 1000°C, in air

For other cathodes: CTE for 25-800°C and other properties at 800°C, in air

Table 1-9 Properties of BSCF cathode materials at different temperatures [116] (© Solid State Ionics, 2006, by permission)

<b>T</b> <b>°C</b>	<b><math>\delta</math></b>	<b><math>D_V \times 10^5</math></b> <b>cm<sup>2</sup> s<sup>-1</sup></b>	<b><math>\sigma_i</math></b> <b>S cm<sup>-1</sup></b>
700	0.258	1.72	0.53
750	0.270	2.26	0.70
800	0.282	2.87	0.88
825	0.289	3.25	1.01

BSCF shows the highest ionic conductivity among the reported cathode materials. Based on the oxygen permeability experimental results, Lu *et al* [116] calculated the oxygen nonstoichiometries  $\delta$ , oxygen vacancy diffusivity  $D_v$  and oxygen ion conductivities  $\sigma_i$  at different temperatures, as listed in Table 1-9. Clearly, the vacancy concentration and diffusivity as well as the ionic conductivity increase with temperature, i.e., are thermally activated.

J. Fleig [118] conducted modeling on the MIEC cathode, and found that only if the  $\sigma_i$  value is of the order of magnitude of the electrolyte conductivity does a broadening of the electrochemically active zone occur in order to lower the current constriction resistance in the electrolyte. Assuming that the MIEC cathodic reaction via the bulk path occurs mainly close to the three-phase boundary (TPB), the corresponding cathode resistance  $R_c$  is almost proportional to the inverse TPB length, and a resistance per TPB length can be defined as

$$R_c = \frac{L_p}{\beta \sigma_{i,MIEC}} \quad \text{Equation 1-23}$$

Here,  $L_p$  is the particle size, and  $\beta$  is a factor coefficient depending on porosity and waviness of the TPB. A value of 4 has been derived for  $\beta$  [118, 119]. Since the cathode particle size is normally approximately  $1\mu\text{m}$  in a real cell, for cathode resistance to be  $0.15\ \Omega\ \text{cm}^2$  the necessary value of  $\sigma_{i,MIEC}$  is approximately in the range of  $10^{-3}$  to  $10^{-4}\ \text{S}\ \text{cm}^{-1}$  according to Equation 1-23.

The performance of cathodes is not only influenced by the choice of the cathode material, but also by the microstructure and the processing, as well as the electrolyte materials. To provide an overview of cathode performance, Table 1-10 lists reported cathode resistance  $R_c$  data for several types of cathodes. Different performances of the same material are included on purpose, to illustrate the broad range of performance that can be achieved by nominally the same material. From Table 1-10, it is noticeable that the cathode performance generally follows the order of the  $\sigma_i$  value of the MIEC cathode materials, i.e.,  $\text{BSCF} \geq \text{SSC} > \text{LSC} > \text{LSCF} > \text{LSFC} > \text{LSF} > \text{LNF} > \text{LSM}$ . The high

performance of BSCF demonstrates the importance of high  $\sigma_i$  for the MIEC cathode materials.

Table 1-10 Typical performance of MIEC cathodes in the literature (Note: values in the parentheses are the cathode reduction activation energy in  $\text{kJ mol}^{-1}$ .)

Cathode, electrolyte and sintering temperature	Area specific resistance, $R_c$ [ $\Omega \text{ cm}^2$ ]					Ref.
	550°C	600°C	650°C	700°C	800°C	
LSM+50v%YSZ on YSZ, 1200°C-2hr	33.8	15.3	6.5	2.6	0.32	13
LSM on SASZ*, 1300°C-4hr				2.5	1.3 (60)	120
LSC			1.2		0.23	121
LSC+45wt%La-doped Ceria			0.61		0.16	121
SSC on LSGM, 1150°C-2hr	5.5	2.0	0.74	0.33	0.10 (133)	113
SSC on GDC, CCVD (1300°C)	3.6	1.6	0.70	0.32	(120)	122
SSC+30%SDC on SDC, 950°C-2hr	0.27	0.15			(77)	123
SSC+10%SDC on SDC, 950°C-2hr	0.61	0.33			(78)	
LSF			5.5		0.13	124
LSFC+30%GDC on GDC,	0.65	0.20	0.084	0.026	0.01 (124)	125
LSFC+30%GDC on YSZ,	2.5	1.0	0.29	0.13	0.03 (135)	
LSFC+30wt% GDC on GDC, 1000°C			0.2- 0.3		(134-138)	126

Cathode, electrolyte and sintering temperature	Area specific resistance, $R_c$ [ $\Omega \text{ cm}^2$ ]					Ref.
	550°C	600°C	650°C	700°C	800°C	
BSCF on GDC, 1100°C-3hr			0.80	0.52	0.17	127
BSCF on SDC, 1000°C-5hr	0.19	0.07	0.03	0.01	(121)	109
LNF on SASZ*, 1000°C-2hr					1.6(initial) 0.5(after100hr)	128
LNF on SASZ*, 1000°C-4hr				1.5	0.6 (64)	120
LNF on YSZ, 1000°C-2hr					2.5	129

\* SASZ:  $\text{ZrO}_2$  stabilized with 10% $\text{Sc}_2\text{O}_3$  and 1% $\text{Al}_2\text{O}_3$

Although MIEC cathodes show good performance at lower temperature, challenges for MIEC cathodes still exist. One is the large CTE mismatch with the electrolyte. This mismatch will generate thermal stresses between the cathode and the electrolyte during fabrication and operation, leading to cathode cracks and delamination. LSFC is a good candidate from the viewpoint of the better CTE match with the electrolyte compared to BSCF and SSC; however its low temperature cathode performance is not high. Therefore, the balancing of sufficient  $\sigma_{i,MIEC}$  and CTE match with the electrolyte is an engineering challenge. An effective approach is using composite cathodes, i.e., adding an electrolyte material composition to the MIEC, such as LSC-GDC or SDC, or SSC-SDC, to tailor the cathode CTE. A second challenge is the interaction with the doped- $\text{ZrO}_2$  electrolyte. Most of the Co-containing cathode materials have the tendency to react with the  $\text{ZrO}_2$ -based electrolyte during the cell fabrication and operation [108, 130, 131]; thus either ceria based electrolytes or protective layers of ceria [108] or LSGM [107, 109, 110] on YSZ electrolytes should be used. The third challenge is the long-term stability issue. The cathode long-term stability of the MIEC materials has not been fully investigated in the low temperature SOFCs. As for BSCF, although it shows the highest performance at lower temperature, both its electronic conductivity and stability are lower than LSFC and SSC. Its low conductivity limits the composite cathode approaches to accommodate its larger CTE mismatch with the electrolyte. Furthermore, its low chemical stability in  $\text{CO}_2$  containing atmospheres causes real concerns regarding long-term stability [132].

#### 1.4.4 Anode

Anode materials for the low temperature SOFCs are commonly the same as those for the high or intermediate temperature SOFCs, i.e. based on Ni catalyst. Depending on the electrolyte materials the cermet anode can be either Ni-YSZ (and/or Ni-SSZ) for ZrO<sub>2</sub>-based electrolytes, or Ni-SDC (and/or Ni-GDC) for ceria-based electrolytes and for LSGM-based electrolytes as well. Since the anode process is kinetically fast enough, the anode resistance  $R_a$  for the typical Ni-YSZ is less than  $0.1 \Omega \text{ cm}^2$  [10] at 600°C. Therefore, the electrochemical resistance of Ni-based anodes in low temperature SOFC development is not an issue. In fact since the SDC or GDC behave as MIECs under reducing atmospheres, those Ni-SDC or Ni-GDC cermet anodes show a better performance in comparison to the Ni-YSZ anode. The main issues of the anode are still its multi-fuel capability, impurity tolerance and redox resistance. Recently Goodenough *et al* [133] and Sun *et al* [134] have reviewed anodes for SOFC. Some interesting MIEC anode materials have been introduced such as Ce<sub>0.84</sub>Ti<sub>0.15</sub>Pt<sub>0.01</sub>O<sub>2- $\delta$</sub>  and Cu-Ru + GDC in a fluorite structure, La<sub>1-x</sub>Sr<sub>x</sub>Cr<sub>0.5</sub>Mn<sub>0.5</sub>O<sub>3- $\delta$</sub>  in a perovskite and Sr<sub>2</sub>Mg<sub>1-x</sub>Mn<sub>x</sub>MoO<sub>6- $\delta$</sub>  in double perovskite structure, and showing certain performance advantages with hydrocarbon fuels and with fuel containing high content of H<sub>2</sub>S impurities. However, those ceramic anode materials are less active in comparison to Ni-based anodes, and are still in an initial R&D stage.

#### 1.5 Fabrication –thin film deposition techniques

Traditionally, tubular cells were fabricated by extrusion of the cathode tube, then electrochemical vapour deposition (EVD) was used to deposit the YSZ electrolyte on the cathode tube. The anode Ni is deposited by slurry coating, and YSZ is impregnated by EVD to form the Ni-YSZ cermet anode layer [3]. For the monolithic cell, the layers of the anode, cathode, and electrolyte are prepared by tape casting or wet slurry coating, then corrugated through molding and stacked with green LaCrO<sub>3</sub> interconnect, and co-fired at a temperature of approximately 1400 -1600°C. For the planar SOFC, cells are made by tape casting the NiO-YSZ anode support, fabrication of the YSZ electrolyte either by screen printing or by tape calendaring to combine with the anode, co-firing at a high temperature over 1350°C, then applying the LSM-YSZ cathode and sintering it at a lower temperature,

approximately 1100-1250°C. Details on the fabrication process for the SOFCs can be found in [3, 4]. Porosity of an electrode can be tailored either by adding a pore-former to the electrode slurry or by sintering at a different temperature [135].

A great variety of new techniques have been developed in the past decades, such as physical vapour deposition; chemical or electrochemical vapour deposition; thermal spray deposition; and wet ceramic processing. Here I briefly summarize the wet ceramic processing techniques and vacuum deposition techniques based on the reference [136].

### **1.5.1 Wet ceramic processes**

Wet ceramic processes are used extensively to produce coatings and thin films for fuel cells, protective coatings, or microelectronic devices. The different techniques used to apply the coating material to the substrate can be divided into dipping, spinning, spraying, and screen-printing, normally followed by drying, thermal decomposition, and high temperature sintering [136]. The ceramic thin film can be formed either from liquid precursors or from crystallized ceramic particulates. Thin films can be deposited on surfaces in patterns by standard photolithographic lift-off processes or shadow masks.

#### **1.5.1.1 *Forming ceramic thin film from liquid precursor***

*Spin-coating and dip-coating:* The spin-coating and dip-coating processes are utilized to produce thin ceramic coatings on a variety of substrate materials. Thin film deposition with spin-coating consists of applying a precursor solution on one side of a rapidly rotating substrate, whereas during the dip-coating process the substrate is partly or fully immersed in the precursor solution and then withdrawn from the liquid. A variety of precursors may be used for these techniques [136].

*Spray pyrolysis deposition (SPD):* In SPD, a fine aerosol, or a mist of droplets, of a liquid precursor solution is generated by atomization, which is then directed towards a hot substrate surface. The droplets evaporate or decompose completely to form a particulate before, upon, or after their landing on the substrate. Perednis and Gauckler recently reviewed thin film deposition using SPD with emphasis on SOFC electrolyte materials [136, 137]. In terms of atomization method and heat source, SPD can be

further categorized into electrostatic spray deposition [138-140], flame spray deposition [141-144], pressurized gas spray deposition [145-152], and ultrasonic spray pyrolysis [153]. Perednis *et al.* [147-148] reported the successful deposition of dense YSZ films with thicknesses <500 nm and porous buffer layers of yttria doped ceria (YDC). Cells fabricated with these films reached power densities in excess of  $750 \text{ mW cm}^{-2}$  at  $770 \text{ }^\circ\text{C}$ .

### **1.5.1.2 Forming ceramic thin film from crystallized particulate**

Electrophoretic deposition (EPD): EPD is a simple and fast deposition technique to produce thin films from colloidal particles. Powder particles are charged and suspended in a colloidal system. Under the forces of an externally applied electric field, the particles move to the substrate surface and coagulate in a compact layer [136]. Liu *et al.* [154, 155] utilized EPD to deposit dense YSZ layers on porous LSM cathode substrates, and others ([156, 157]) have deposited YSZ on NiO-YSZ anode substrates.

Slurry-coating: Dip-coating or spraying with ceramic particulate or colloidal suspensions (“slurry-coating”) produce films with thickness generally larger than a few microns and limited sometimes to the particle diameter in the dipping solution, which is usually a few hundred nanometers [136, 158, 159]. Advances towards finer particulate suspensions for YSZ electrolyte layers have been reported [160].

Screen printing: Screen printing is a process by which an “ink” consisting of a suspension of the deposition material and binder is forced through a fine wire mesh, or printing frame, depositing the ink on the substrate surface. Screen printing is a moderately priced process, with good process capability for 3-5 $\mu\text{m}$  films [161, 162]. In this study, precise screen-printing technology was used for preparation of cell functional components such as anode, electrolyte, and cathode.

## **1.5.2 Vacuum deposition techniques**

Vacuum deposition techniques are generally categorized into physical vapour deposition (PVD) and chemical vapour deposition (CVD). For thin film growth in

vacuum deposition, gas-phase atoms of the chosen material are transported from the source to the substrate, upon which the film will nucleate and grow. The whole process takes place in a vacuum chamber, where the atmosphere and gas-phase reactions can be controlled carefully [136]. Review of the application of vacuum techniques to SOFC materials in general can be found in [163, 164]. The main disadvantages of vacuum deposition techniques are that both are expensive techniques from the point of view of equipment, and have similarly low deposition rates of a few nm per minute.

### 1.5.2.1 Physical vapor deposition (PVD)

PVD techniques have the common feature that atoms are brought to the gas phase through a physical process from a solid or molten target. Simple oxides and nitrides can be grown from metallic substrates by introducing oxygen or nitrogen gas during processing. The processes include: evaporation, sputtering, laser ablation and hybrid methods. The most prevalent of these techniques for SOFC materials is sputtering, but pulsed laser deposition (PLD) is becoming more and more popular. Since many SOFC components are complex materials, evaporation is difficult and scarcely used [136].

*Sputtering*: In the sputtering process, material is removed from a solid cathode target by bombardment with charged ions emitted from a noble gas (commonly Ar) discharge at high voltage (3–5 kV) in a process of momentum transfer [136]. A radio frequency (RF) source is needed for sputtering dielectric materials. Deposition is usually performed at low temperature (<400 °C) in a partial pressure of oxygen on the order of 10 mTorr [136]. Post-deposition thermal treatment in air is then necessary for crystallization and densification of the electrolytes. The sputtering process was employed prior to PLD for thin film deposition in the SOFC field. Thin film electrolytes have been prepared, particularly YSZ [165, 166] and GDC [167, 168]. However, porous Ni/YSZ anodes [169] on dense YSZ substrates as well as anodes and electrolytes on porous substrates such as alumina [170] have been successfully grown as thin films. The deposition of the cathode material lanthanum strontium cobaltite (LSC) was also reported [171]. Even the deposition of an entire SOFC was reported [172].

Pulsed laser deposition (PLD): PLD uses a pulsed laser beam, usually of wavelength in the UV range, to ablate a target composed of the desired thin film material, which is subsequently deposited onto a substrate [136]. PLD has attracted much attention over the last 20 years, as it enables fabrication of multi-component stoichiometric films from a single target. The obstacle for the application of PLD in industrial production is the difficulty in scaling-up the process. However, possible evolutions of PLD that would allow for large-scale deposition have been proposed [172, 173]. Reviews on applications of PLD to SOFCs can be found elsewhere [174, 175]. Porous and dense perovskite electrodes [176-178], electrolytes such as GDC [179-181], YSZ [182], lanthanum strontium gallium manganite (LSGM) [183, 184] and samaria doped ceria (SDC)/LSGM bi-layers [185] have been deposited by PLD. Amorphous dense films or nano-size grains can be obtained in low oxygen partial pressure (<10 mTorr) at low temperature and then crystallized by annealing in air. In the cases of GDC and YSZ, it was found that the porosity and the presence of cracks were strongly influenced by the deposition pressure [186], and higher density was obtained at lower pressure.

#### **1.5.2.2 Chemical vapor deposition (CVD)**

In the CVD process, gaseous precursors of the desired materials are transported to the substrate. They react or decompose under the energy provided by heaters or by a plasma discharge to form a film of desired material on the substrate [136]. CVD does not require the use of high vacuum, and enables the production of high quality and high purity films. It is widely employed in the semiconductor industry. For SOFC application, CVD processes have been mainly used to produce dense, gas-tight, electrolyte films, 1–10  $\mu\text{m}$  thick, on dense and porous substrates [187-191]. Another example is electrochemical vapour deposition (EVD), where film growth proceeds because of an electrochemical potential gradient existing between the two sides of the substrate [192]. EVD has been extensively used for SOFC cathode supported cell fabrication by Siemens Westinghouse [3].

## 1.6 Summary

SOFCs electrochemically convert chemical energy in available fuels into electricity at high temperature. Conventional SOFCs with YSZ electrolyte operate at 700° - 1000°C in order to obtain an adequate power density ( $\geq 0.3 \text{ W cm}^{-2}$ , i.e.,  $R_t \leq 0.4\sim 0.5 \ \Omega \text{ cm}^{-2}$ ). Although cell performance decreases exponentially with operating temperature, low temperature SOFC development is a way to meet the lifetime and the cost requirements from the market.

Among the electrolyte materials reviewed in low temperature SOFC development, ceria based materials show a good combination of higher ionic conductivity and better compatibility with the high performance electrodes than the conventional zirconia-based electrolyte, especially mixed ionic and electronic conductive (MIEC) cathode materials which are promising for low temperature SOFC development. However, these benefits of ceria-based electrolytes are partially offset by their considerable electronic conductivity under operating temperature and atmosphere conditions. Cells with bi-layered electrolyte structures seem like an effective way to tackle this issue.

Since thin film deposition is crucial for low temperature SOFCs, various processes have been suggested to enable cost effective and high volume manufacturing of SOFCs [193]. Table 1-11 gives a brief summary of specific processing techniques reviewed so far. Plasma spraying, showing advantages in metal supported SOFC fabrication, is also listed in the table. Each of these processes has been reported to produce workable cells in a laboratory setting. However, to insure cell performance, control of process variability for process parameters such as material thickness, in-film defect levels, material dopant concentrations, and porosity, becomes critical for each process. Up to now, ceramic wet processing has been the dominant fabrication method for the planar anode supported thin electrolyte cell development, well adopted by most of the planar SOFC developers and research groups due to its low cost, easy parameter control, and scalable manufacturability.

Table 1-11 A brief summary of thin film manufacturing processes

Process	Materials	Cost	Pros	Cons
Electrochemical vapour deposition (EVD)	YSZ, cermet anodes	High	Widely used in microelectronics+SOFCs. Produces uniform, adherent films, good conformality	High reaction temp, precursor corrosiveness, low deposition rates
Pulsed laser deposition (PLD)	YSZ	High	Suitable for almost any material, intermediate deposition temperature, controllable microstructure	Vacuum, Film cracking, uneven deposition reported
Magnetron Radio Frequency (RF) Sputtering	YSZ	High	Good film conformality, material deposition flexibility, good deposition rate control, low deposition temps	Thermal cracking during annealing, dimension limitation
Plasma spraying	YSZ, NiO, LCO, LSM, SSZ		Multi-layer devices by single spray process, dense films, porosity controlled, high deposition rates	More process optimization needed for dense electrolyte and porous electrode
Tape calendaring	YSZ	Moderate	Multi-layer deposition capability, can deposit on porous or dense substrates	Crack formation
Electrophoretic deposition (EPD)	YSZ, GDC, LSGM, LSFC	Moderate	Less substrate shape restriction, high powder packing density, manufacturability, dense film, fast deposition rates	Inhomogeneous thickness, cracking when thickness over 50 $\mu$ m. multiple parameters.
Tape casting	YSZ	Low	Robust multilayer tech., manufacturability	Crack formation, not for thin film <25 $\mu$ m
Screen printing	YSZ, Ni-YSZ, SDC, Ni-SDC	Low	Multi-layer deposition, film thickness down to 5 $\mu$ m, good uniformity, porosity control	Minimum deposit > 5 $\mu$ m, Co-firing cracks

Process	Materials	Cost	Pros	Cons
Slurry coating	YSZ	Low	Robust tech., good dense film, no shape restriction	Crack formation risk
Sol gel coating	YSZ, LSM, SSC	Low	Create fine structure and high density films, sintering at lower temps, good thickness control	Crack risk, low deposition rates, time consuming.

## 1.7 Objective and Outline of dissertation work

The general goal of this dissertation work is to obtain a thorough understanding of cell materials and cell processing technologies in order to develop solid oxide fuel cells (SOFCs) operating at temperatures below 650°C. The ultimate objective of this work is to develop a cell technology by rational cell material and structure design through a cost-effective fabrication process that can deliver the cell performance to meet the following practical cell performance:

Cell operating temperature ( $T_{op}$ ):  $600 \pm 50^\circ\text{C}$

Cell operating voltage ( $V_{cell}$ ): 0.70-0.75V

Cell power density (PD):  $\geq 0.30\text{W cm}^{-2}$

For meeting the targeted cell performance, the scope of the dissertation work includes:

1. *Establish cell material system.* According to the literature review in this chapter, the following cell material system has been selected:  $\text{Sm}_{0.2}\text{Ce}_{0.8}\text{O}_{1.9}$  (SDC) as the main electrolyte candidate, Ni-SDC as anode,  $\text{Sm}_{0.5}\text{Sr}_{0.5}\text{CoO}_{3-\delta}$  (SSC) or composite SSC-SDC as cathode.
2. *Define cell structure.* In order to reach high cell performance, planar-anode supported electrolyte cell structures with Ni-YSZ cermet as cell support are adopted for cell development in this work. Two types of cell structures are investigated. One type of cell is with single layered SDC electrolyte, the other type of cell is with bi-layered electrolyte.
3. *Develop cell fabrication processes.* Both wet processing and PLD processing are investigated. The electrolyte deposition processes used in this study are either

screen-printing and high temperature co-firing or low temperature pulsed laser deposition (PLD). Cell size is scaled up for short stack development. With these, thin electrolyte cells are fabricated and used for cell characterization and performance evaluation.

4. *Cell material characterization and cell material studies.* Powder morphology, particle size, surface area, phase purity, electrochemical properties, and thermal properties of raw materials used for cell components and cell fabrication are characterized. Cell material studies cover the enhancement of SDC electrolyte sinter-ability and electrolyte material interaction. Transition metal oxides are used as dopants to facilitate the SDC sintering with a purpose of engineering the bi-layered electrolyte for low temperature SOFCs by cost-effective wet processing methods.
5. *Composite cathode study.* Since the cathode is one of the important components at low operating temperatures, composite cathodes are investigated with the purpose to enhance the cathode performance by optimizing composition, microstructure, and processing condition.
6. *Internal shorting of low temperature SOFC with SDC electrolyte.* The severity of the internal shorting is studied and a mechanistic understanding is reached. Consequently, bi-layered electrolyte structure solutions are proposed.
7. *Low temperature SOFC with bi-layered electrolyte.* A thin purely ionic conducting zirconia-based electrolyte is added between the anode and the main SDC electrolyte with a purpose to eliminate the electronic conductivity of the electrolyte. Cells prepared by both wet processing and PLD processing are investigated.
8. *Stability of low temperature SOFCs with bi-layered electrolyte.* The stability of cells developed in this work is studied to understand the potential degradation mechanism.

Chapter one has been devoted to the basics of SOFCs and a literature review on low temperature SOFCs. Chapter two describes cell structure, fabrication technology and experimental methods. The results of the cermet supported thin SDC electrolyte cells are reported in chapter three. In chapter four, a study on composite cathodes and cathode

thickness is presented. Chapter five discusses internal shorting, fuel utilization, and electrical efficiency of thin SDC electrolyte cells. In chapter six, a study on sintering aids for SDC electrolytes is presented. Chapter seven presents a study on interaction between different electrolyte materials. In chapter eight, low temperature SOFCs with bi-layered electrolyte fabricated by TSC and the cell performance are presented. Chapter nine discusses the stability of low temperature SOFCs with bi-layered electrolyte fabricated by TSC. In chapter ten, low temperature SOFC with bi-layered electrolyte fabricated by PLD and the cell performance are presented. Conclusions and future work are presented in Chapter eleven. In appendices, thermodynamic calculations of various fuels are included; and the details of materials properties characterization are also presented. Finally, a list of journal papers and conference presentations during the dissertation work is also attached.

## **1.8 References**

1. M. C. Williams, Fuel Cells, 1(2007) 78.
2. S. Basu, Recent Trends in Fuel Cell Science and Technology, Anamaya Publisher, New Delhi, India, ISBN 0-387-35537-5(HB), 2007.
3. S. C. Singhal, K. Kendall, High Temperature Solid Oxide Fuel Cells: Fundamentals, Design and Applications, Elsevier Advanced Technology, UK, 2003.
4. N. Q. Minh, T. Takahashi, Science and Technology of Ceramic Fuel Cells, Elsevier, Amsterdam, Netherlands, 1995.
5. R. Bove, Solid oxide fuel cells: principles, designs and state-of the art in industries in Recent Trends in Fuel Cell Science and Technology, edited by S. Basu, Anamaya Publisher, New Delhi, India, ISBN 0-387-35537-5(HB), 2007.
6. W. Z. Zhu, S. C. Deevi, Materials Research Bulletin 38 (2003) 957.
7. X. Li, Principles of Fuel Cells, Taylor & Francis Group, NY 10016, ISBN 1-59169-022-6 (2006) 478
8. H. S. Spacil, US patent 3,558,360; filed 1964, granted 1970.
9. J.-H. Lee, H. Moon, H.-W. Lee, J. Kim, J.-D. Kim and K.-H. Yoon, Solid State Ionics 148 (2002) 15.
10. Y. Jiang, A. V. Virkar, J. Electrochem. Soc. 148(2001) A706.
11. M. C. Verbraeken, B. A. Boukamp, D. H. A. Blank, P. Holtappels, U. Vogt, in SOFC IX, S. C. Singhal and J. Mizusaki, Editors, The Electrochemical Society Proceedings Series, Pennington, NJ, PV 2005-07 (2005) 1218.
12. E. Ivers-Tiffée, Q. Weber, D. Herbstritt, J. Eur. Ceram. Soc. 21 (2001) 1805.
13. A. Barbucci, M. Viviani, P. Carpanese, D. Vladikova, Z. Stoyanov, Electrochimica Acta 51 (2006) 1641.
14. J. Divisek, L. G. J. Haart, P. Holtappels, T. Lennartz, W. Mallener, U. Stimming and K. Wippermann, Journal of Power Sources 49 (1994) 257.
15. R. Chiba, F. Yoshimura, Y. Sakurai, Y. Tabata, M. Arakawa, Solid State Ionics 175 (2004) 23.
16. K. Barthel, S. Rambert, S. Siegmann, J. Thermal Spray Technology 9 (2000) 343.

17. H. S. Song, S. H. Hyun, J. Moon, R. H. Song, *Journal of Power Sources* 145 (2005) 272.
18. V. P. McConnell, *Fuel Cells Bulletin* 9 (2007) 12.
19. F. J. Gardner, M. J. Day, N. P. Brandon, M. N. Pashley and M. Cassidy, *Journal of Power Sources* 86 (2000) 122.
20. J. W. Kim, A. V. Virkar, K. Z. Fung, K. Mehta and S. C. Singhal, *J. Electrochem. Soc.* 146 (1999) 69.
21. S. P. Simner, J. F. Bonnett, N. L. Canfield, K. D. Meinhardt, J. P. Shelton, V. L. Sprenkle, and J. W. Stevenson, *J. Power Sources* 113 (2003) 1.
22. E. Tang, F. Martell, R. Brule, K. Marcotte, B. Borglum (Versa power), in SOFC VIII, S.C. Singhal and M. Dokiya, Editors, *The Electrochemical Society Proceedings Series*, Pennington, NJ, PV 2003-07 (2003) 935.
23. Seca program SOFC target  
(<http://www.netl.doe.gov/technologies/coalpower/fuelcells/seca>, Sept. 15, 2006)
24. P. Y. Hou, K. Huang, and W. T. Bakker, *Electrochemical Society Proceedings of the Sixth International Symposium on SOFC*, 99-19(1999) 741 .
25. N. Minh, SECA solid oxide fuel cell program-general electric SECA industry team. *Proceedings of the SECA Annual workshop and core technology program peer-reviewed abstract*, Boston, MA, May 11-23, 2004, p.2.
26. E. D. Wachsman, P. Jayaweera, N. Jiang, D. M. Lowe, and B. G. Pound, *J. Electrochem. Soc.* 144 (1997) 233.
27. A. Jaiswal, E. D. Wachsman, *Solid State Ionics* 177 (2006) 677.
28. H. Yahiro, Y. Eguchi, K. Eguchi and H. Arai, *J. Appl. Electrochem.* 18 (1988) 527.
29. S. Wang, T. Kobayashi, M. Dokiya, and T. Hashimoto, *J. Electrochem. Soc.* 147 (2000) 3606.
30. K. Huang, R. S. Tichy and J. B. Goodenough, *J. Am. Ceram. Soc.* 81 (1998) 2565.
31. D. S. Lee, W. S. Kim, S. H. Choi, J. Kim, H. W. Lee, J. H. Lee, *Solid State Ionics* 176 (2005) 33.
32. J. W. Fergus, *J. Power Sources* 162 (2006) 30.
33. V. V. Kharton, F. M. B. Marques, and A. Atkinson, *Solid State Ionics* 174 (2004) 135.

34. D. Lee, I. Lee, Y. Jeon and R. Song, *Solid State Ionics* 176 (2005) 1021.
35. H. Uchida, H. Suzuki, and M. Watanabe, *J. Electrochem. Soc.* 146 (1998) 615.
36. M. Kurumada, H. Hara, E. Iguchi, *Acta Mater.* 53 (2005) 4839.
37. M. Weller, F. Khelifaoui, M. Kilo, M. A. Taylor, C. Argirusis, G. Borchardt, *Solid State Ionics* 175 (2004) 329.
38. R. Chiba, T. Ishii, F. Yoshimura, *Solid State Ionics* 91 (1996) 249.
39. S. P. S. Badwal, F. T. Ciacchi, D. Milosevic, *Solid State Ionics* 136-137 (2000) 91.
40. S. Sarat, N. Sammes, A. Smirnova, *J. Power Sources* 160 (2006) 892-896.
41. Y. Arachi, T. Asai, O. Yamamoto, Y. Takeda, N. Imanishi, K. Kawate and C. Tamakoshi, *J. Electrochem. Soc.* 148 (2001) A520.
42. S. P. S. Badwal, *J. Mater. Sci.* 22 (1987) 4125.
43. Z. Lei and Q. Zhu, *Solid State Ionics* 176 (2005) 2791.
44. V. Butler, C. R. A. Catlow, B. E. F. Fender and J. H. Harding, *Solid State Ionics* 8 (1983) 109.
45. H. Yahiro, K. Eguchi, H. Arai, *Solid State Ionics* 36 (1989) 71.
46. D. J. Seo, K. O. Ryu, S. B. Park, K. Y. Kim, R.-H. Song, *Mater. Res. Bull.* 41 (2006) 359.
47. V. V. Kharton, F. M. Figueiredo, L. Navarro, E. N. Naumovich, A. P. Viskup, A. A. Yaremchenko, R. T. Baker, B. Gharbage, G. C. Mather, and F. M. B. Marques, *Solid State Ionics* 132 (2000) 119.
48. B. Dalslet, P. Blennow, P. V. Hendriksen, N. Bonanos, D. Lybye, M. Mogensen, *J. Solid State Electrochem.* 10 (2006) 547.
49. M. Mogensen, D. Lybye, K. Kammer, N. Bonanos, *Electrochemical Society Proceedings, 2005-07, SOFC IX, 2005* p.1068.
50. R. S. Gordon, *Electrochemical Society Proceedings, 2003-07, SOFC VII, 2003,* p.141.
51. M. Godickemeier, K. Sasaki, L. J. Gauckler, *J. Electrochem. Soc.* 144 (1997) 1635.
52. M. Godickemeier, and L. J. Gauckler, *J. Electrochem. Soc.* 145 (1998) 414.
53. N. Oishi, A. Atkinson, N. P. Brandon, J. A. Kilner, and B. C. H. Steele, *J. Am. Ceram. Soc.* 88 (2005) 1394.

54. M. Sahibzada, R. A. Rudkin, B. C. H. Steele, I. S. Metcalfe, and J. A. Kilner, in: U. Stimming, et al.(Eds.), SOFC V, Proceedings Vol. 97-40, Electrochemical Society, NJ, 1997, p. 244.
55. P. Singh, N. Q. Minh, *Appl. Ceram. Technol.* 1 (2004) 5.
56. H. Yahiro, Y. Baba, K. Eguchi, and H. Arai, *J. Electrochem. Soc.* 135 (1988) 2077.
57. T. Tsai, E. Perry, and S. Barnett, *J. Electrochem. Soc.* 144 (1997) L130.
58. Z. Shao, S. M. Haile, *Nature* 431 (2004) 170.
59. R. Maric, T. Fukui, S. Ohara, T. Inagaki, and J. Fujita, *Electrochem. Solid-State Lett.* 1 (1998) 201.
60. X. Zhang, S. Ohara, R. Maric, K. Mukai, T. Fukui, H. Yoshida, M. Nishimura, T. Inagaki, and K. Miura, *J. Power Sources* 83 (1999)170.
61. D. Perednis, L. J. Gauckler, *Solid State Ionics* 166 (2004) 229.
62. T. L. Nguyen, K. Kobayashi, T. Honda, Y. Iimura, K. Kato, A. Neghisi, K. Nozaki, F. Tappero, K. Sasaki, H. Shirahama, K. Ota, M. Dokiya, T. Kato, *Solid State Ionics* 174 (2004) 163.
63. M. Price, J. Dong, X. Gu, S. A. Speakman and E. A. Payzant, *J. Am. Ceram. Soc.* 88 (2005) 1812.
64. J. M. Ralph, C. Rossignol, R. Kumar, *J. Electrochem. Soc.* 150 (2003) A1518-A1522.
65. C. Rossignol, J. M. Ralph, J.-M. Bae, J. T. Vaughey, *Solid State Ionics* 175 (2004) 59.
66. A. Tsoga, A. Gupta, A. Naoumidis, P. Nikolopoulos, *Acta Mater.* 48 (2000) 4709.
67. K. Huang, M. Feng, J. B. Goodenough, M. Schmerling, *J. Electrochem. Soc.* 143 (1996) 3630.
68. T. Ishihara, H. Matruda, Y. Takita, *J. Am. Chem. Soc.* 116 (1994) 3801.
69. T. Ishihara, T. Akbay, H. Furutani and Y. Takita, *Solid State Ionics* 113–115 (1998) 585.
70. N. Trofimenko and H. Ullmann, *Solid State Ionics* 118 (1999) 215.
71. V. V. Kharton, A. P. Viskup, A. A. Yaremchenko, R. T. Baker, B. Gharbage, G. C. Mather, F. M. Figueiredo, E. N. Naumovich and F. M. B. Marques, *Solid State Ionics* 132 (2000) 119.
72. J. W. Stevenson, T. R. Armstrong, L. R. Pederson, J. Li, C. A. Levinsohn and S. Baskaran, *Solid State Ionics* 113–115 (1998) 571.

73. E. Djurado and M. Labeau, *J. Eur. Ceram. Soc.* 18 (1998) 1397.
74. K. Yamaji, T. Horita, M. Ishikawa, N. Sakai and H. Yokokawa, *Solid State Ionics* 121 (1999) 217.
75. W. X. Chen, H. W. Nie, W. H. Huang, R. Zheng, H. Y. Tu, T. L. Wen, *J. Mater. Sci. Lett.* 22 (2003) 651.
76. T. Horita, K. Yamaji, N. Sakai, H. Yokokawa, A. Weber, E. Ivers-Tiffée, *Solid State Ionics* 133 (3-4) (2000) 143.
77. G. C. Kostogloudis, C. Ftikos, A. Ahmad-Khanlou, A. Naoumidis, D. Stover, *Solid State Ionics* 134 (2000) 127.
78. C. N. Munnings, S. J. Skinner, G. Amow, P. S. Whitfield, I. J. Davidson, *J. Fuel Cell Sci. Technol.* 2 (2005) 34.
79. Z. Bi, M. Cheng, Y. Dong, H. Wu, Y. She, B. Yi, *Solid State Ionics* 176 (2005) 655.
80. M. Hrovat, A. Ahmad-Khanlou, Z. Samardzija, J. Holc, *Mater. Res. Bull.* 34 (1999) 2027.
81. K. Huang, J. H. Wan, J. B. Goodenough, *J. Electrochem. Soc.* 148(7) (2001) A788.
82. A. V. Joshi, J. J. Steppan, D. M. Taylor, S. Elangovan, *J. Electroceram.* 13 (2004) 619.
83. Y. Du, N. M. Sammes, *Electrochemical Society Proceedings, 2005-07, SOFC IX, 2005 pp.1127.*
84. G. Mairesse In: B. Scrosati, A. Magistris, C.M. Mari and G. Mariotto, Editors, *Fast Ion Transport in Solids*, Kluwer Academic Publications, Dordrecht (1993) 271.
85. N. M. Sammes, G. A. Tompsett, H. Nägele and F. Aldinger, *J. Eur. Ceram. Soc.* 19 (1999) 1801.
86. W. Zhou, D. A. Jefferson and J. M. Thomas, *Proc. R. Soc. Lond., A* 406 (1986) 173.
87. C. D. Ling, R. L. Withers, S. Schmid and J. G. Thompson, *J. Solid State Chem.* 137 (1988) 42.
88. M. J. Verkerk and A. J. Burggraaf, *Solid State Ionics* 3-4 (1981) 463.
89. J.-Y. Park, H. Yoon and E. D. Wachsman, *J. Am. Ceram. Soc.* 88 (2005) (9) 2402.
90. Y. J. Leng, S. H. Chan and K. A. Khor, *Electrochemical Society Proceedings, 2005-07, SOFC IX (2005) 1110.*

91. E. D. Wachsman and K. L. Duncan, annual report to DOE, 2001-2002  
(<http://www.osti.gov/bridge/servlets/purl/833871-LZ5c9u/native/833871.pdf>, May 15, 2007)
92. E. D. Wachsman, G. R. Ball, N. Jiang, D. A. Stevenson, *Solid State Ionics* 52 (1992) 213.
93. Z. Bi, Y. Dong, M. Cheng, B. Yi, J. Power Sources 161 (2006) 34.
94. K. Yamaji, T. Horita, M. Ishikawa, N. Sakai and H. Yokokawa, *Solid State Ionics* 121 (1999) 217.
95. Y. Lin, S. Barnett, *Electrochem. & Solid-state Lett.* 9 (2006) A285.
96. X. Zhang, S. Ohara, R. Maric, K. Mukai, T. Fukui, H. Yoshida, M. Nishimura, T. Inagaki, and K. Miura, *Solid State Ionics* 133 (2000) 153.
97. X. Zhang, M. Robertson, C. Deces-Petit, J. Power Sources 161 (2006) 301.
98. Z. Wang, J. Qian, J. Cao, S. Wang, T. Wen, J. Alloys and Compounds 437 (2007) 264.
99. T. L. Nguyen, K. Kobayashi, T. Honda, Y. Iimura, K. Kato, A. Neghisi, K. Nozaki, F. Tappero, K. Sasaki, H. Shirahama, K. Ota, M. Dokiya, T. Kato, *Solid State Ionics* 174 (2004) 163.
100. M. Shiono, K. Kobayashi, T. L. Nguyen, K. Hosoda, T. Kato, K. Ota, M. Dokiya, *Solid State Ionics* 170 (2004) 1.
101. Y. Teraoka, T. Nobunaga, K. Okamoto, N. Miura and N. Yamazoe, *Solid State Ionics* 48 (1991) 207.
102. S. J. Skinner, *Fuel Cells Bulletin* 33 (2001) 6.
103. S. Wang, M. Katsuki, M. Dokiya, T. Hashimoto, *Solid State Ionics* 159 (2003) 71.
104. J. Sunarso, S. Baumann, J. M. Serra, W. A. Meulenbergh, S. Liu, Y. S. Lin, J. C. Diniz da Costa, *J. Membrane Science* 320 (2008) 13.
105. S. B. Adler, *Solid State Ionics* 111 (1998) 125.
106. C. Xia, W. Rauch, F. Chen, and M. Liu, *Solid State Ionics* 149 (2002) 11.
107. R. Ciba, F. Yoshimura, Y. Sakurai, *Solid State Ionics* 124 (1999) 281.
108. R. N. Basu, F. Tietz, E. Wessel, H. P. Buchkremer, D. Stover, *Materials Research Bulletin* 39 (2004) 1335.

109. B. Wei, Z. Lu, X. Huang, S. Li, G. Ai, Z. Liu, W. Su, *Materials Letters* 60 (2006) 3642.
110. K. T. Lee, A. Manthiram, *J. Electrochem. Soc.* 153 (2006) A794.
111. H. Ullmann, N. Trofimenko, F. Tietz, D. Stover, A. Ahmad-Khanlou, *Solid State Ionic* 138 (2000) 79.
112. Q. Zhu, T. Jin, Y. Wang, *Solid State Ionic* 177 (2006) 1199.
113. H. Lv, Y. Wu, B. Huang, B. Zhao, K. Hu, *Solid State Ionics* 177 (2006) 901.
114. M. Katsuki, S. Wang, M. Dokiya, T. Hashimoto, *Solid State Ionic* 156 (2003) 453.
115. Q. Xu, D. Huang, F. Zhang, W. Chen, M. Chen, H. Liu, *J. Alloys and Compounds* 454 (2008) 460.
116. H. Lu, Y. Cong, W. S. Yang, *Solid State Ionics* 177 (2006) 595.
117. B. Wei, Z. Lu, S. Li, Y. Liu, K. Liu, and W. Su, *Electrochemical & Solid-State Letters* 8 (2005) A428.
118. J. Fleig, *Annu. Rev. Mater. Res.* 33 (2003) 361.
119. J. Fleig, J. Maier, *J. Eur. Ceram. Soc.* (2003) 325.
120. P. Sornthummalee, K. Sato, T. Komatsu, H. Orui, R. Chiba, M. Arakawa, *ECS Transactions, SOFC-X*, 7(1) (2007) 1183.
121. Z. H. Bi, M. J. Cheng, Y. L. Dong, H. J. Wu, Y. C. She, B. L. Yi, *Solid State Ionics* 176 (2005) 655.
122. Y. Liu, W. Rauch, S. Zha, M. Liu, *Solid State Ionic* 166 (2004) 261.
123. C. Xia, W. Rauch, F. Chen, M. Liu, *Solid State Ionic* 149 (2002) 11.
124. J. M. Ralph, C. Rossignol, R. Kumar, *Journal of the Electrochemical Society* 150 (2003) A1518.
125. W. G. Wang, M. Mogensen, *Solid State Ionic* 176 (2005) 457.
126. A. Esquirol, J. Kilner, N. Brandon, *Solid State Ionics* 175 (2004) 63.
127. Y. Wang, S. Wang, Z. Wang, T. Wen, Z. Wen, *Journal of Alloys and Compounds* 428 (2007) 286.
128. R. Chiba, Y. Tabata, T. Komatsu, H. Orui, K. Nozawa, M. Arakawa, H. Arai, *Solid State Ionics* 178 (2008) 1701.
129. M. Bevilacqua, T. Montini, C. Tavagnacco, G. Vicario, P. Fornasiero, M. Graziani, *Solid State Ionics* 177 (2006) 2957.

130. J. M. Ralph, C. Rossignol, R. Kumar, *Journal of the Electrochemical Society* 150 (2003) A1518.
131. H. Uchida, S. Arisaka, M. Watanabe, *Solid State Ionics* 135 (2000) 347.
132. A. Yan, M. Cheng, Y. Dong, W. Yang, V. Maragou, S. Song, P. Tsiakaras, *Applied Catalysis B. environmental* 66 (2006) 64.
133. J. B. Goodenough, Y-H. Huang, *J. Power Sources* 173 (2007) 1.
134. C. Sun, U. Stimming, *J. Power Sources* 171 (2007) 247.
135. M. Boaro, J. Vohs, R. Gorte, *J. Am. Ceram. Soc.* 86 (2003) 395.
136. D. Beckel, A. Bieberle-Hutter, A. Harvey, A. Infortuna, U. P. Mueche, M. Prestat, J. L. M. Rupp, L. J. Gauckler, *J. Power Sources* 173 (2007) 325.
137. D. Perednis, *Thin Film Deposition by Spray Pyrolysis and the Application in Solid Oxide Fuel Cells*, Ph.D. dissertation no. 15190 ETH Zurich, Zurich, Switzerland, 2003.
138. C. Y. Fu, C. L. Chang, C.S. Hsu and B. H. Hwang, *Mater. Chem. Phys.* 91 (2005) 28.
139. H. Nomura, S. Parekh, J. R. Selman and S. Al-Hallaj, *J. Appl. Electrochem.* 35 (2005) 61.
140. I. Taniguchi, R. C. van Landschoot and J. Schoonman, *Solid State Ionics* 160 (2003) 271.
141. Y. Liu and M. Liu, *J. Am. Ceram. Soc.* 87 (2004) 2139.
142. R. Kavitha, S. R. Hegde and V. Jayaram, *Mater. Sci. Eng., A* 359 (2003) 18.
143. W. B. Carter, G. W. Book, T. A. Polley, D. W. Stollberg and J. M. Hampikian, *Thin Solid Films* 347 (1999) 25.
144. S. Charojrochkul, K. L. Choy and B. C. H. Steele, *J. Eur. Ceram. Soc.* 24 (2004) 2515.
145. T. Setoguchi, M. Sawano, K. Eguchi and H. Arai, *Solid State Ionics* 40–41 (1990) 502.
146. P. Bohac and L. Gauckler, *Solid State Ionics* 119 (1999) 317.
147. D. Perednis, O. Wilhelm, S. E. Pratsinis and L. J. Gauckler, *Thin Solid Films* 474 (2005) 84.
148. D. Perednis and L. J. Gauckler, *Solid State Ionics* 166 (2004) 229.
149. J. L. M. Rupp, T. Drobek, A. Rossi and L. J. Gauckler, *Chem. Mater.* 19 (2006) 1134.

150. D. Beckel, A. Dubach, A. R. Studart and L. J. Gauckler, *J. Electroceram.* 16 (2006) 221.
151. E. S. Putna, J. Stubenrauch, J. M. Vohs and R. J. Gorte, *Langmuir* 11 (1995) 4832.
152. N. X. P. Vo, S. P. Yoon, S. W. Nam, J. Han, T. H. Lim and S. A. Hong, *On the Convergence of Bio-Information-, Environmental-, Energy-, Space- and Nano-Technologies, Pts 1 and 2* (2005) 455.
153. S. Wang, W. Wang, Q. Liu, M. Zhang and Y. Qian, *Solid State Ionics* 133 (2000) 211.
154. L. Besra, C. Compson, and M. Liu, *J. Power Sources* 173 (2007) 130.
155. Z. Y. Peng and M. Liu, *J. Am. Ceram. Soc.* 84 (2001) 283.
156. L. Jia, Z. Lu, X. Q. Huang, Z. G. Liu, K. F. Chen, X. Q. Sha, G. Q. Li and W. H. Su, *J. Alloys Compd.* 424 (2006) 299.
157. M. Matsuda, T. Hosomi, K. Murata, T. Fukui and M. Miyake, *Electrochem. Solid State Lett.* 8 (2005) A8.
158. Y. Du and N. M. Sammes, *J. Power Sources* 136 (2004) 66.
159. S. D. Kim, S. H. Hyun, J. Moon, J.-H. Kim and R. H. Song, *J. Power Sources* 139 (2005) 67.
160. Q. Zhu and B. Fan, *Solid State Ionics* 176 (2005) 889.
161. J. Gerblinger, M. Hausner and H. Meixner, *J. Am. Ceram. Soc.* 78 (1995) 1451.
162. D. H. Kim, W. S. Um, K. No and H. G. Kim, *J. Am. Ceram. Soc.* 74 (1991) 2102.
163. L. R. Pederson, P. Singh and X. D. Zhou, *Vacuum* 80 (2006) 1066.
164. J. Will, A. Mitterdorfer, C. Kleinlogel, D. Perednis and L. J. Gauckler, *Solid State Ionics* 131 (2000) 79.
165. E. S. Thiele, L. S. Wang, T. O. Mason and S. A. Barnett, *J. Vac. Sci. Technol. A* 9 (1991) 3054.
166. J. L. Hertz and H. L. Tuller, *J. Electroceram.* 13 (2004) 663.
167. E. Gourba, A. Ringuede, M. Cassir, A. Billard, J. Paiviasaari, J. Niinisto, M. Putkonen and L. Niinisto, *Ionics* 9 (2003) 15.
168. E. Gourba, P. Briois, A. Ringuede, M. Cassir and A. Billard, *J. Solid State Electrochem.* 8 (2004) 633.
169. T. Tsai and S. A. Barnett, *J. Vac. Sci. Technol. A* 13 (1995) 1073.

170. A. Nagata and H. Okayama, *Vacuum* 66 (2002) 523.
171. A. Bieberle-Hütter and H. L. Tuller, *J. Electroceram.* 16 (2006) 151.
172. J. A. Greer and M. D. Tabat, *J. Vac. Sci. Technol. A* 13 (1995) 1175.
173. J. A. Greer, M. D. Tabat and C. Lu, *Nucl. Instrum. Methods Phys. Res. Sect. B-Beam Interact. Mater. Atoms* 121 (1997) 357.
174. M. N. R. Ashfold, F. Claeysens, G. M. Fuge and S. J. Henley, *Chem. Soc. Rev.* 33 (2004) 23.
175. J. Dieleman, E. Vanderiet and J. C. S. Kools, *Jpn. J. Appl. Phys.* 1 (31) (1992) 1964.
176. N. Imanishi, T. Matsumura, Y. Sumiya, K. Yoshimura, A. Hirano, Y. Takeda, D. Mori and R. Kanno, *Solid State Ionics* 174 (2004) 245.
177. X. Chen, N. J. Wu, D.L. Ritums and A. Ignatiev, *Thin Solid Films* 342 (1999) 61.
178. M. Prestat, A. Infortuna, S. Korrodi, S. Rey-Mermet, P. Muralt and L. J. Gauckler, *J. Electroceram.* 118 (2007) 111.
179. L. G. Coccia, G. C. Tyrrell, J. A. Kilner, D. Waller, R. J. Chater and I. W. Boyd, *Appl. Surf. Sci.* 96–98 (1996) 795.
180. J. L. M. Rupp, A. Infortuna and L. J. Gauckler, *Acta Mater.* 54 (2006) 1721.
181. J. L. M. Rupp, A. Infortuna, L. J. Gauckler, *J. Am. Ceram. Soc.* 90 (2007) 1792.
182. B. Hobein, F. Tietz, D. Stover and E. W. Kreutz, *J. Power Sources* 105 (2002) 239.
183. P. Manoravi, N. Sivakumar, M. Joseph and T. Mathews, *Ionics* 10 (2004) 32.
184. T. Mathews, J. R. Sellar, B. C. Muddle and P. Manoravi, *Chem. Mater.* 12 (2000) 917.
185. J. W. Yan, H. Matsumoto, T. Akbay, T. Yamada and T. Ishihara, *J. Power Sources* 157 (2006) 714.
186. A. Infortuna, A. Harvey, L. J. Gauckler, submitted to *Adv. Func. Mater.* 18 (2008) 127.
187. J. Will, A. Mitterdorfer, C. Kleinlogel, D. Perednis and L. J. Gauckler, *Solid State Ionics* 131 (2000) 79.
188. G. Garcia, J. Caro, J. Santiso, J. A. Pardo, A. Figueras and A. Abrutis, *Chem. Vapor. Depos.* 9 (2003) 279.
189. L. Niinisto, M. Ritala and M. Leskela, *Mater. Sci. Eng. B* 41 (1996) 23.

190. C. Bernay, A. Ringuède, P. Colomban, D. Lincot and M. Cassir, *J. Phys. Chem. Solids* 64 (2003) 1761.
191. M. Cassir, F. Goubin, C. Bernay, P. Vernoux and D. Lincot, *Appl. Surf. Sci.* 193 (2002) 120.
192. J. C. Viguie and J. Spitz, *J. Electrochem. Soc.* 122 (1975) 585.
193. J. Will, A. Mitterdorfer, C. Kleinlogel, D. Perednis, L. J. Gaukler, *Solid State Ionics* 131 (2000) 79.

## 2. Chapter Two. Cell Fabrication and Characterization<sup>2</sup>

The success of SOFC technology depends on producing a cost competitive product within performance specifications that match or exceed those of other alternative energy sources. Practical and cost-effective fabrication processes of SOFCs are currently based on the fabrication technologies initially designed for the microelectronics and materials manufacturing industry [1]. One of goals of this dissertation work is to understand and then apply those manufacturing technologies to the low temperature SOFC fabrication. Two fabrication technologies are used in this work. One is wet ceramic processing, such as **T**ape casting, **S**creen printing, and **C**o-firing of cell components (TSC in short [1]) in multi-layered ceramic structures, and the other is physical vapour deposition, such as **P**ulsed **L**aser **D**eposition (PLD in short). Both technologies provide a platform for cell fabrication with which a certain level of design of electrolyte configuration can be performed at the several micron level (by screen printing) and submicron level (by PLD). Low temperature SOFCs with two types of electrolyte are developed in this dissertation work. They are single layered SDC electrolyte cells, designated as Type I, and YSZ (or SSZ)/SDC bi-layered electrolyte cells, designated as Type II. Both types of electrolyte are fabricated in a typical Ni-YSZ cermet supported cell structure, a common cell configuration used by many developers and researchers in the world. The characterization of cells includes 3 stages: physical characterization, electrochemical measurement and post-mortem analysis.

This chapter describes the cell materials and cell structures, details of the above-mentioned two fabrication methods and processing conditions, and experimental and instrumental details for cell characterization.

---

<sup>2</sup> A version of this chapter has been published as:

- a) X. Zhang, M. Robertson, C. Decès-Petit, Y. Xie, R. Hui, S. Yick, E. Styles, J. Roller, O. Kesler, R. Maric, D. Ghosh, NiO-YSZ cermets supported low temperature solid oxide fuel cells, *J. Power Sources* 161 (2006) 301.
- b) X. Zhang, M. Robertson, C. Decès-Petit, Y. Xie, R. Hui, S. Yick, O. Kesler, R. Maric and D. Ghosh, Fabrication and characterization of cermet supported cell with SDC electrolyte, *ECS Trans.* 7 (2007) 899.
- c) D. Yang, X. Zhang, C. Decès-Petit, R. Hui, R. Maric, D. Ghosh, Low temperature SOFCs with Pulsed laser deposited bi-layer electrolyte, *J. Power Sources* 164 (2007) 182.

## 2.1 Cell materials

Table 2-1 lists chemical compositions of starting materials used for the cell fabrication in this dissertation. These starting materials are purchased from reliable powder suppliers, such as YSZ powder from Tosoh (Japan) and NiO from Novamet (Inco., Canada). Organic materials (binders, dispersants, and solvents) and equipment for tape casting are supplied by specialist supplier Richard E. Mistler, Inc.

Table 2-1 Chemical composition, properties, suppliers of starting materials

Component	Material compositions	Supplier
Cathode	$\text{Sm}_{0.5}\text{Sr}_{0.5}\text{CoO}_3$ (SSC)	Praxair
Electrolyte	$(\text{SmO}_{1.5})_{0.2}(\text{CeO}_2)_{0.8}$ (SDC)	
	YSZ	Tosoh
	$10\text{Sc}1\text{CeZrO}_{2-\delta}$ (SSZ)	Daiichi Kigenso
Anode	$(\text{SmO}_{1.5})_{0.2}(\text{CeO}_2)_{0.8}$ (SDC)	Praxair
	YSZ	Tosoh
	$10\text{Sc}1\text{CeZrO}_{2-\delta}$ (SSZ)	Daiichi Kigenso
	NiO	Novamet
Cermetsupport	NiO	
	YSZ	Tosoh

Table 2-2 Cell materials and properties in this work

Component	Material	Thickness	Porosity	
Cell Type (I)	Cathode	SSC or SSC+SDC composite	30-50 $\mu\text{m}$	30-50%
Cell Type (II)	Electrolyte	SDC (or SSZ)	10-30 $\mu\text{m}$	< 5%
	Anode	Ni-YSZ, Ni-SDC, Ni-SSZ	10-20 $\mu\text{m}$	30-50%
	Cathode	SSC or SSC+SDC composite	30-50 $\mu\text{m}$	30-50%
Cermetsupport	Electrolyte	SDC (at cathode side)	4-10 $\mu\text{m}$	< 5%
		YSZ or SSZ (at anode side)	1-5	<5%
	Anode	Ni-YSZ, Ni-SSZ, or Ni-SDC	10-20 $\mu\text{m}$	30-50%
	Cermetsupport	Ni-YSZ	0.8-1.0 mm	30-40%

## 2.2 Cell structures

Figure 2-1 schematically illustrates the Ni-YSZ cermet supported thin SDC electrolyte cells and YSZ (or SSZ)/SDC bi-layered electrolyte cells developed in this work. Cell materials and properties of the components are listed in Table 2-2.

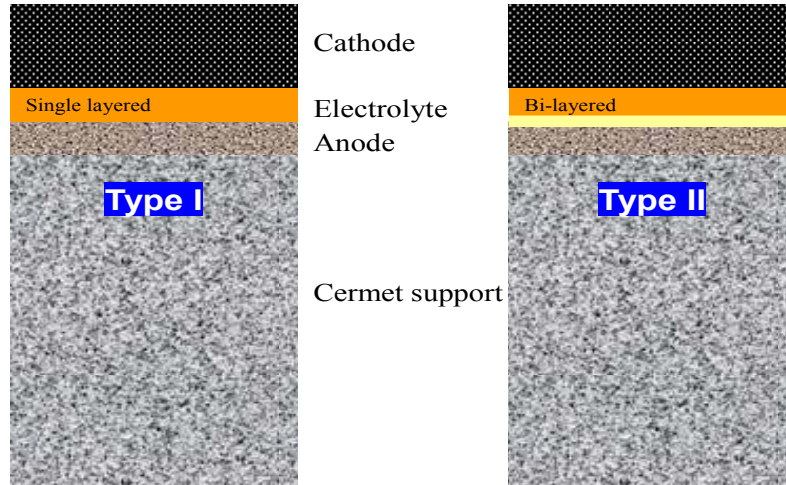


Figure 2-1 Schematic drawing of cell types in this work

## 2.3 Cell fabrication

The typical flowchart of cell fabrication by wet ceramic processing is outlined in Figure 2-2.

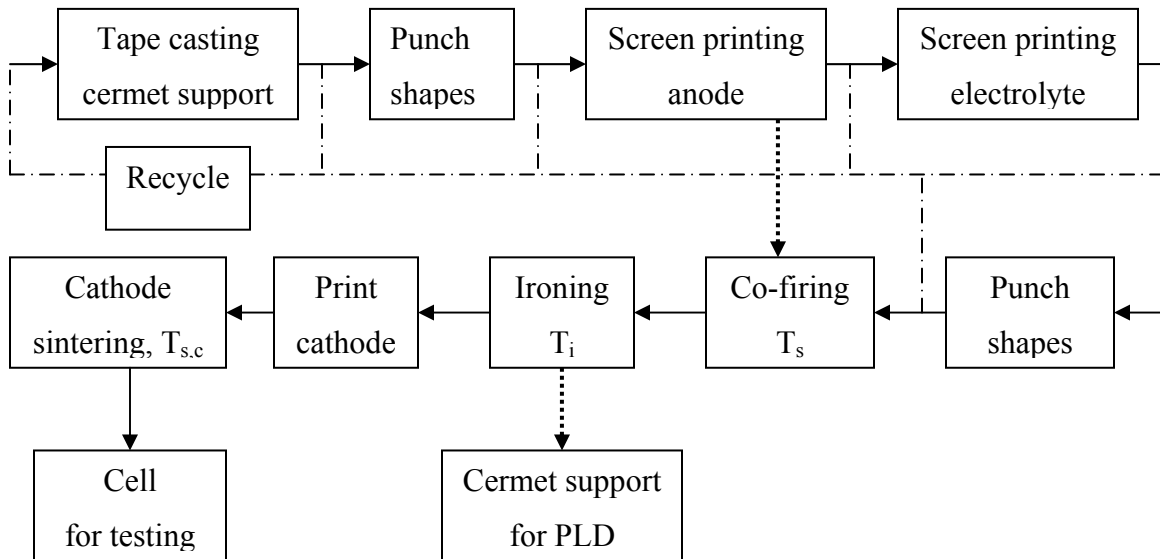


Figure 2-2 Flowchart of cell fabrication by wet ceramic processing

This process consists of (1) tape casting of the cermet support layer, (2) screen printing of the anode layer and electrolyte layer on the cermet support layer, (3) co-firing of the multi-layer of cermet support, anode and electrolyte together into half cells, followed by visual inspection of the half cell quality, (4) ironing the half cells followed by physical inspection of the half cells, and (5) printing cathode and sintering cathode, followed by the cell characterization and electrochemical measurement. The dotted line path in the flowchart is used for fabricating cermet support for PLD cell preparation.

The selected wet processing methods for fabricating SOFCs, such as tape casting and screen printing, are low cost and proven technologies. The formulations and processes are controllable and scalable, and the waste is minimized by simple recycling. Cell material knowledge and component fabrication skills are important in cell fabrication because each layer is different in chemical composition, thermal property, and sintering behaviour. Cell fabrication requires good understanding of starting material morphology and sintering behaviour and careful design of component structure and composition of the different cell component layers in order to obtain the final cell in good condition without (or with minimum) cracks, pinholes, warping, and detrimental interaction during high temperature firing. The defined cell co-firing temperature profile should accommodate the evaporation and burnout kinetics of organics and closely match the shrinkage rates of each cell component layer during sintering. Combination of suitable powders is an effective approach to tailor the sintering behaviour and to meet the different microstructural requirements of the multi-layered ceramic cells.

## ***2.4 Composition and processing***

### **2.4.1 NiO-YSZ composition and tape casting**

According to the literature (cf. Chapter 1. anode section), in order to achieve a good balance of high conductivity and good thermal expansion match with the subsequent layers of anode and electrolyte, the volume fraction of Ni in a final Ni-YSZ cermet should be within 30~35 vol.% (under an assumption of starting from a dense NiO-YSZ body) [2]. In this study, approximately 32 vol% is selected for the NiO-YSZ support, which corresponds

to a 57wt%NiO + 43wt%YSZ powder mixture based on the calculation as shown in Figure 2-3.

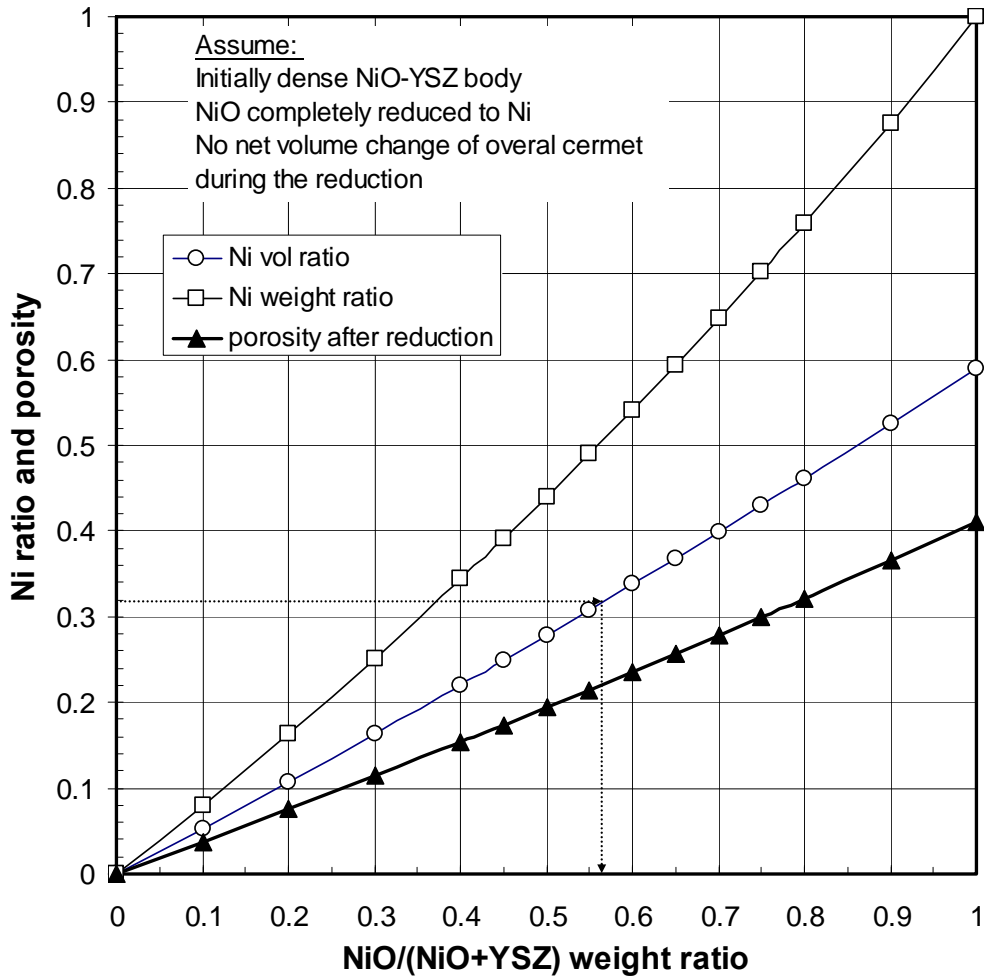


Figure 2-3 Ni-YSZ weight, volume and porosity with different NiO content

The same composition was chosen for both NiO-YSZ and NiO-SSZ anodes. For NiO-SDC anodes the composition was changed to 53wt%NiO+47wt%SDC in order to yield the same Ni volume percent (32 vol.%) as in the NiO-YSZ or NiO-SSZ anode and NiO-YSZ support according to the density difference between YSZ (5.98 g cm<sup>-3</sup>) and SDC (7.08 g cm<sup>-3</sup>).

The NiO-YSZ support was fabricated by tape casting. Tape casting is a common ceramic forming technique, which mainly involves 4 steps:

1. Binder solution preparation to dissolve the binder, the dispersant, and the plasticizer in the solvent.
2. Slurry preparation to mix the ceramic powders with binder solution, and make it homogeneous then degas it to remove existing air bubbles.
3. Casting the slurry on a moving carrier belt, by passing it under a stationary ‘doctor blade’ to adjust the tape thickness.
4. Drying the cast tape with hot air and forming rubber-like- sheet, normally called green tape, which can be easily peeled off from the carrier film.

The NiO-YSZ green tape undergoes quality inspection to check for bubbles, tape thickness evenness and green tape density. It was noticed that slurry formula, casting parameters, drying speed, and thickness control are of importance for this process and subsequent processes of cell fabrication. In general, the tape quality is affected by the slurry properties, which are related to the solvent polarity, hydroxyl content of PVB binder, and surface characteristics of the NiO powder and the YSZ powder. One of common approaches is to use a mixture solvent to obtain a suitable solvent polarity. The dissolving power of the solvent used should be sufficient to dissolve processing organic additives (especially the binder) but should not prevent the adsorption of these additives on the particles [3].

In this study, the obtained NiO-YSZ green tape after drying is approximately 1.0 mm in thickness. The measured green tape density is  $3.80 \text{ g cm}^{-3}$ , with powder loading of 86.5wt% (after solvent evaporation). Figure 2-4 shows the laboratory used casting machine, and the NiO-YSZ tape for cell substrate.

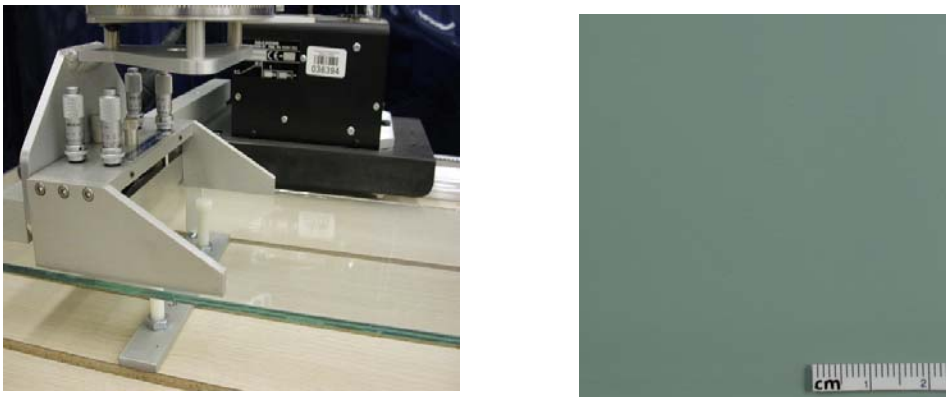


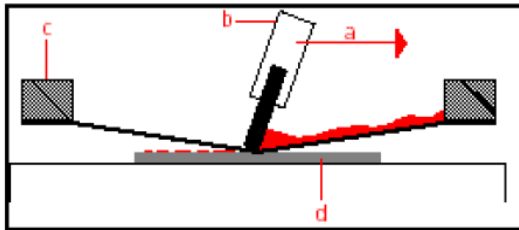
Figure 2-4 Tape casting machine (in this study)-on the left and NiO-YSZ tape sample-on the right.

## 2.4.2 Anode, electrolyte and cathode pastes and screen printing

The designed anode, electrolyte and cathode pastes have 50-60wt% ceramic powder loadings in the pastes [4], and the binder content is 8-10wt% of the ceramic powder, with the balance consisting of dispersant and solvent. Pastes were prepared by first ball milling the mixtures, and then they were gone through a 3-roll mill for quality control. A paste of viscosity within 10,000 to 30,000 cp is suitable for printing.

On adding the ceramic powder, the viscosity is changed with the powder loading. The suitable powder loading range of NiO-SDC compositions was selected as 55-57wt%, while for SDC the selected powder loading range was 53-56wt%.

The screen printing is carried out at room temperature in a clean environment (clean room). Figure 2-5 shows the screen printing process. The left drawing is a schematic of the printing process, and the right photo is the screen printer used in this study (MC 212 Screen printer, USA). Tailored NiO-YSZ green tapes are used as cell supports in this case.



a- printing direction    b- squeegee  
c- screen frame        d- NiO-YSZ tape



Figure 2-5 Screen printing (left- a schematic of the printing process, right- the screen printer used in this study, MC 212 Screen Printer).

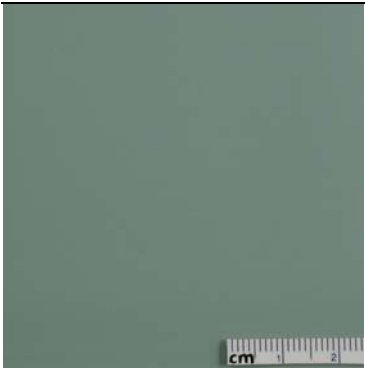

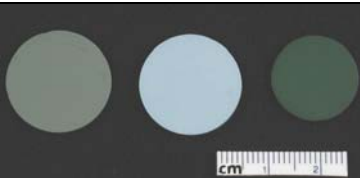
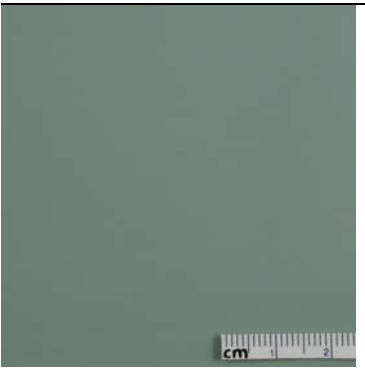
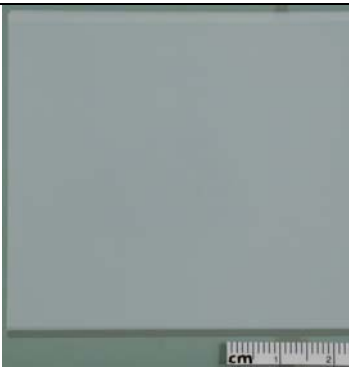
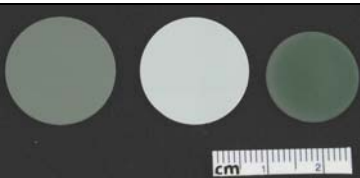
Table 2-3 lists the typical print thickness of different screen meshes based on measurement of one pass before drying. It can be seen that the screen mesh is critical to determine the desired print thickness. In fact, it has the largest effect on the printed layer properties. While the screen mesh and emulsion thickness (i.e., the masked portion of screen) provide the main control of print thickness, some variation (perhaps up to  $\pm 20\%$ ) can be made by altering the squeegee pressure and speed. Increased pressure gives a decreased print thickness. Conversely, increased speed gives an increased print thickness. The print thickness generally will decrease after drying. The thickness of the printed layer will

will further decrease after sintering. Commonly, for electrolytes printed with a 325# mesh screen (note: mesh number means the number of openings per square inch area), one print pass will produce a dense layer with a thickness of approximately 5 $\mu$ m after sintering. Samples of the tapes and of the printed cells are shown in Table 2-4. Button cells (one inch cells or half inch cells) are generated after screen printing with punches of 30mm or 19mm in diameter.

Table 2-3 Typical print thickness of different screen meshes (one pass before drying)

Screen mesh #	Wire Diameter [ $\mu$ m]	Typical print thickness [ $\mu$ m]
100	81	50
200	41	25
325	28	15

Table 2-4 Samples of tape and printed cells

NiO-YSZ Tapes	Printed 65mm x 65mm cells	Button cells after die-cut
 <p>green tape by tape casting</p>	 <p>printed with SSZ electrolyte</p>	 <p>A B C</p> <p>A)Printed with NiO-YSZ anode, B) with YSZ electrolyte, and C) after co-firing</p>
 <p>green tape by tape casting</p>	 <p>printed with SDC electrolyte</p>	 <p>A B C</p> <p>A)Printed with NiO-SDC anode, B) with SDC electrolyte, and C) after co-firing</p>

### 2.4.3 Cell co-firing and ironing

Printed cells without the cathode were co-fired at high temperatures to build mechanically strong cells with fully dense electrolyte layer. Table 2-5 lists the typical temperature profiles used in cell fabrication.

Table 2-5 Typical temperature profiles used in the cell fabrication

<b>Firing</b>	<b>Temperature, °C</b>	<b>Ramp speed, °C/hr or dwell time</b>
Cell co-firing	Room temp. ( $T_r$ ) to 150	150
	150 to 350	50
	350 to 450	25
	450 to 600	100
	600	Hold for 1hr
	600 to sintering temp. ( $T_s$ )	200
	$T_s$ (typically 1400°C)	Hold for 2hr
	$T_s$ to $T_r$	200
Cell Ironing	$T_r$ to $T_i$	250, with certain load on top of cells
	$T_i$ , ( $T_i \approx T_s - 50$ )	Hold for 2hr
	$T_i$ to $T_r$	200
Cathode sintering	$T_r$ to sintering temp. ( $T_{s,c}$ )	200
	$T_{s,c}$ (typically 1000°C)	Hold for 2hr
	$T_{s,c}$ to $T_r$	200

The temperature profiles are designed based on the results of organics burnout of the green tape and the sintering behaviour of each component layer. Thermo Gravimetric Analysis (TGA) was conducted to examine the burn out process of organics used in cell fabrication. The organic burnout of the green tape is illustrated in Figure 2-6.

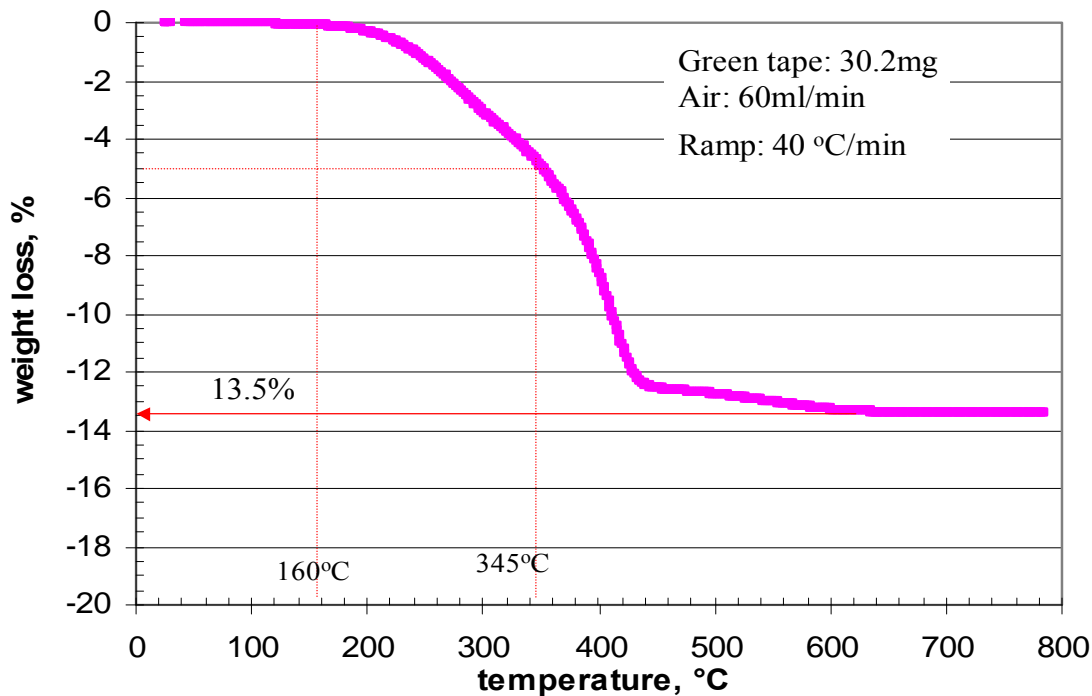


Figure 2-6 Thermo gravimetric analysis of burn out of organics in the NiO-YSZ green tape.

It can be seen that the weight loss of the green tape starts at 160°C, which reflects the beginning of evaporation of the dispersant and plasticizers, while the decomposition and burn out of binders and other organic remnants starts at approximately 345°C and is completed by approximately 600°C. It is important to use relatively slow ramp rates during the de-binding process to remove the organics in cells in order to avoid cracking or warping.

The final sintering temperature ( $T_s$ ) depends on the type of electrolyte materials and their sintering ability. Figure 2-7 and Figure 2-8 show the thermo-mechanical analysis results of the electrolyte materials used in this study. It can be seen that the maximum shrinkage rates for SDC, 8YS, 8Y, and SSZ occur at 1278°C, 1338°C, 1256°C, 1168°C, respectively. In order to obtain fully dense electrolytes, reasonable sintering temperatures  $T_s$  for SDC, 8YS, 8Y, and SSZ are 1400°C, 1400°C, 1300°C, and 1260°C, respectively. It may be necessary to modify ramp rates during the sintering stage to avoid cracking or warping due to potential shrinkage rate mismatching of different cell components.

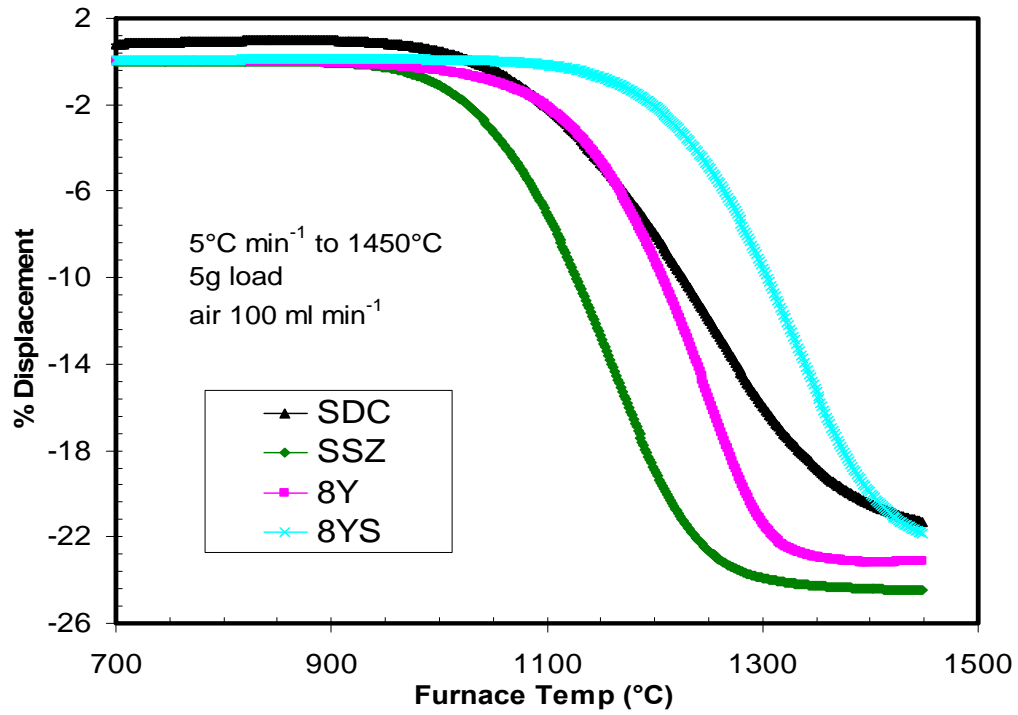


Figure 2-7 Thermo-mechanical analysis of the sinterability of electrolyte powders.

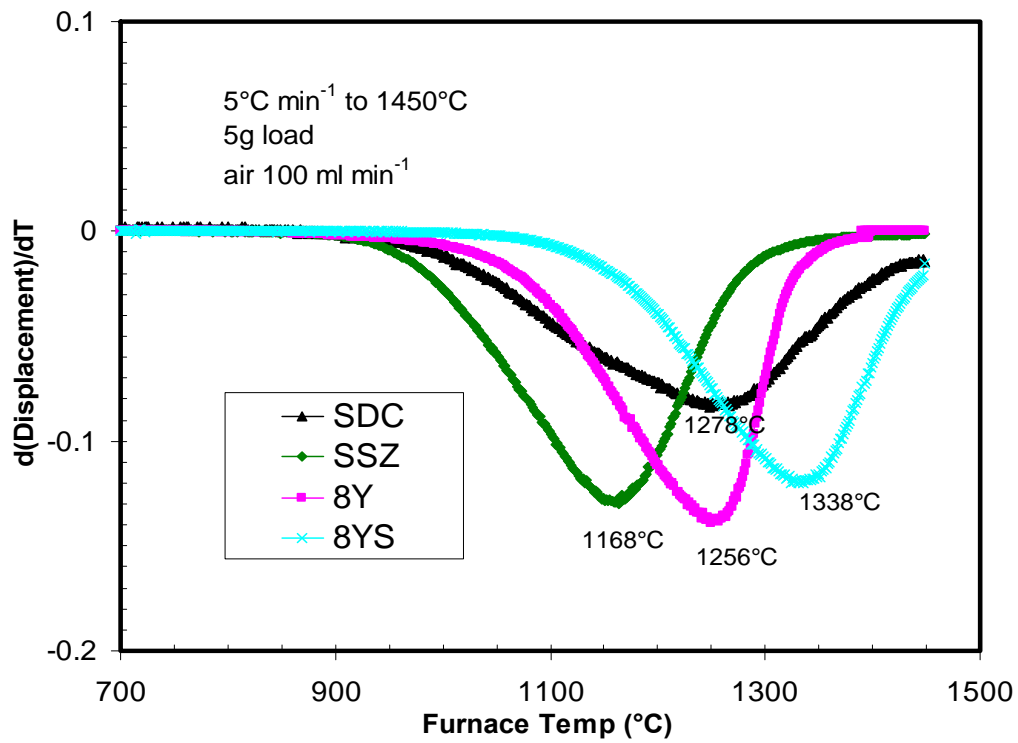


Figure 2-8 Linear shrinkage rate versus sintering temperature.

Various cell samples are illustrated in Table 2-6. Samaria-doped ceria (SDC) electrolyte cells with Ni-SDC anode and SSC-SDC composite cathode have been successfully fabricated by using the wet ceramic processing technology and the cell size has been enlarged from ½”- 1” button cell (for laboratory cell material and cell structure studies) up to 8cm x 8cm square cell with or without holes (for short stack development by industrial partners). Along with the cell fabrication technology development many engineering challenges, such as end-tape surface bubbling during tape casting, cell functional layer cracks during screen-printing, electrolyte crack and spallation and cell deformation during co-firing, and hole-zone induced cell cracks, have been solved in a timely manner. In this dissertation work, hundreds of cells of SDC electrolyte (Type I) and bi-layered electrolyte (Type II) with a uniform and dense electrolyte, of thickness down to 10µm, have been fabricated and tested.

Table 2-6 Sample cells

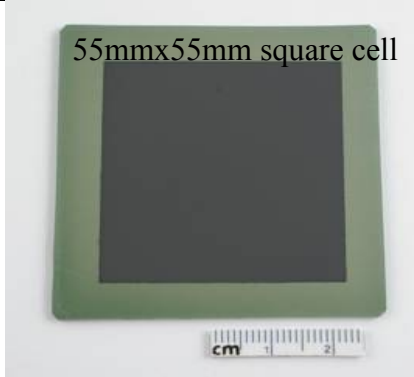


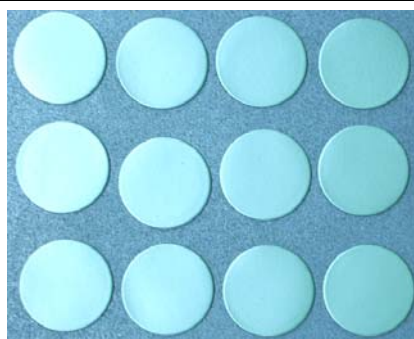
Type I cell	Type II cell
 <p>55mmx55mm square cell</p>	 <p>80mmx80mm square cells</p>
 <p>1 inch (1”) button cell</p>	 <p>half inch (1/2”) button cells</p>

Figure 2-9 shows the microstructure of a typical cell (Type I) after cell testing. The cell had a uniform porous substrate of approximately 1mm thickness prepared by tape casting, a functional anode of approximately 15-20 $\mu$ m thickness applied by screen printing with a #200 mesh screen, and a dense SDC electrolyte of 10 $\mu$ m thickness by screen printing with a #325 mesh screen. The cathode was also screen printed by using a #100 mesh screen, showing a thickness of approximately 40 $\mu$ m. The cell component compositions as marked in the figure were in wt%.

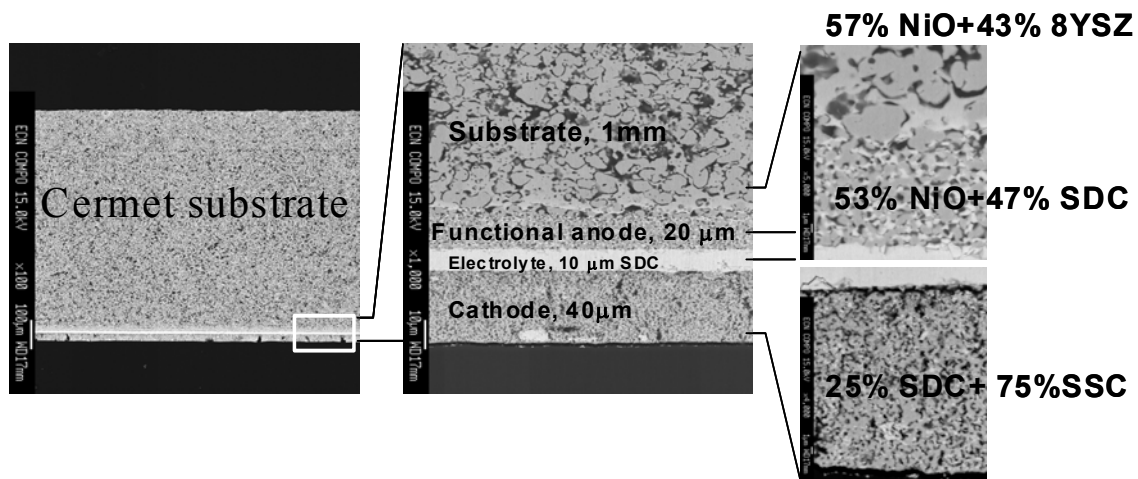


Figure 2-9 Microstructures of a typical Type I cell with SDC electrolyte.

## 2.5 Pulsed laser deposition (PLD)

This work was conducted at the Industrial Manufacturing Institute (IMI-NRC, London, Ontario) with the support of our collaborators. The experimental setup is schematically shown in Figure 2-10. It consisted of a KrF excimer laser ( $\lambda = 248$  nm, *Lambda Physik LPX-210i*), a variable beam attenuator (10-90% transmission, *Microlas*), and an advanced PLD system (*PVD. Inc.*, PLD-3000) that incorporated beam steering and shaping optics, and a high-vacuum stainless steel chamber. The pulsed laser beam (20 ns pulse duration at FWHM, pulse energy < 700 mJ) was first directed through the attenuator and a pair of expanding/collimating lenses. It was then focused onto the surface of a circular SDC target (SDC, 99.9%, from Praxair), or an SSZ target (prepared by IFCI-NRC)

by means of a 100 cm focal length lens and two guiding mirrors. To avoid trench formation, the target was rotated at 35 rpm and the laser beam was rastered during deposition. Rastering was performed using a programmable kinematic mount for the last mirror of the optical train. The laser beam spot size at the target surface was approximately  $2.5 \times 1 \text{ mm}^2$  and the optical system permitted continuous adjustment of the on-target energy density between approximately  $50 \text{ mJ/cm}^2$  and  $12 \text{ J/cm}^2$ . The beam-entrance port of the chamber had a special design that incorporated a sacrificial uncoated quartz disc to protect the antireflective-coated inlet quartz window from ablation-generated vapours. It also included an energy-meter (*Molectron*, J25), that permitted the in-situ measurement of the on-target laser beam energy. The sacrificial quartz disc could be rotated to expose a new clean area whenever the measurement of the on-target energy revealed a noticeable decrease. In the experiments, the energy was measured at the beginning and end of each deposition run; a maximum drop of approximately 15% was measured for the longest runs. A clean area of the sacrificial window was exposed at the beginning of each experiment.

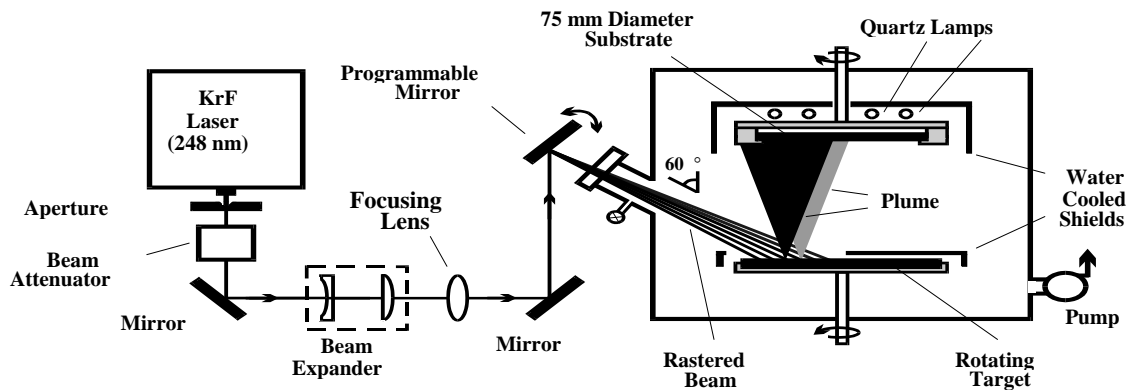


Figure 2-10 Schematic of the PLD setup.

The substrate to be coated was facing the target, with a stand-off distance of 11.5 cm. The substrate was simply supported by a ring at its circumference; it was not clamped or bonded. Silicon wafers [(100) orientation, p-type,  $\rho = 10\text{-}30 \text{ }\Omega\cdot\text{cm}$ ] of 75 mm diameter were used as substrates for initial experimental condition study. Before introducing a wafer into the deposition chamber, it was cleaned according to the following procedure: (i) acetone, ultrasonic, three minutes; (ii) isopropyl alcohol, ultrasonic, three minutes; (iii) 2.5

% HF acid etch, five minutes, and (iv) de-ionized water overflow rinse, three minutes. Once the PLD processing parameters were determined, the anode ceramic discs were used as the substrate for the PLD of electrolytes. The anode substrate was a NiO-YSZ cermet consisting of 57wt% NiO and 43wt%YSZ, prepared by tape casting. A NiO-SDC modified layer, used as the anode, was applied by screen-printing on the cell substrate. The composition of the NiO-SDC anode was 47wt% SDC and 53wt% NiO. The Ni volume percent (32 vol.%) in the modified layer is the same as that in the NiO-YSZ cermet substrate. After loading the substrate, the system was pumped down to a base pressure below  $2 \times 10^{-6}$  Torr using a turbo-molecular pump. For any experiment to be performed at high temperature, the substrate was then heated, under vacuum, using a programmable non-contact radiative heater. The input to the controller that drove the power to the quartz lamps was given by a thermocouple, placed above the wafer with no contact. A readout permitted the monitoring of the temperature. An ex-situ infrared pyrometer (*Mikron*, M90H-1X) was used to control the value of the temperature at the substrate surface (for  $T \geq 350^\circ\text{C}$ ). The oxygen gas (99.995%, *Air Liquide*) was subsequently introduced into the chamber and its flow was controlled through a mass-flow controller in the range 1-10 sccm. The processing pressure was set by adjusting the inlet flow and throttling the gas into the turbo-molecular pump. After all the parameters were adjusted and stabilized, a pre-cleaning of the target was performed for one minute with the same settings of the laser as those used for the process run. Only then, the shutter that hid the substrate surface from the ablation plume was opened and the deposition started. After a given processing time, the laser was stopped, the oxygen inlet valve was shut off, and the substrate was allowed to cool down (when necessary) under vacuum.

In order to improve the quality of deposited layers, a nano-scale fine layer of approximately  $1\mu\text{m}$  of anode NiO-SDC was first deposited by PLD on the cermet support before the electrolyte deposition. The electrolyte thickness used in this study is approximately  $5\text{-}6\mu\text{m}$  for SDC, and  $1\text{-}2\mu\text{m}$  for SSZ (in bi-layered electrolyte cell structures). The average deposition rate was approximately  $1\mu\text{m/hr}$  for all the layers deposited by PLD.

## 2.6 Cell characterization

Cells used in this work generally went through a 3-stage characterization process consisting of: 1) physical characterization, 2) electrochemical characterization, and 3) post-mortem analysis [4].

### 2.6.1 Physical characterization

The physical characterization methods used to evaluate the cells included dimension, density, optical microscopy, and helium leakage test. If no or a very low He leak rate (less than  $0.01 \text{ ml min}^{-1} \text{ cm}^{-2}$  at  $1 \text{ psi} = 6.9 \text{ kPa He}$ ) was observed through the electrolyte, then the cathode was applied on the cell for electrochemical characterization.

The results of the physical characterizations of typical cells are summarized in Table 2-7. It was found that the SDC electrolyte could be sintered to fully dense at  $1400^\circ\text{C}$ , while the YSZ electrolyte could be fully sintered at  $1350^\circ\text{C}$ . The well-sintered electrolytes appear transparent, and allow no detectable helium gas cross leakage even at  $13.8\text{kPa}$  (approximately  $2\text{psi}$ ), indicating that the electrolyte layers were fully dense. After the electrolyte quality characterizations, each cell was characterized by an Archimedes density measurement to obtain the cermet substrate density and porosity. The measured cell densities are  $5.15 \text{ g cm}^{-3}$  on average, corresponding to 19% porosity in the NiO-YSZ cermet substrate based on a composition of 57wt% NiO (nominal density of  $6.355 \text{ g cm}^{-3}$ ). The substrate porosity would increase to approximately 37% after NiO reduction to Ni based on calculation.

Table 2-7 Physical characterization results of cells fired at  $1400^\circ\text{C}$  for 2hr.

Cell Type	SDC single layer electrolyte	YSZ + SDC bi-layer electrolyte
Electrolyte appearance	transparent	transparent
Cell linear shrinkage [%]	15.6	15.8
Cell density [ $\text{g cm}^{-3}$ ]	5.15	5.16
Substrate porosity [%]	19.1	18.8
Helium leakage rate [ $\text{ml min}^{-1} \text{ cm}^{-2}$ ]	Not detectable (at $13.8\text{kPa}$ )	Not detectable (at $13.8\text{kPa}$ )

## 2.6.2 Electrochemical characterization

Figure 2-11 shows a schematic setup for button cell electrochemical tests. A split-tube furnace (Thermcraft Incorporated, USA) was used for cell temperature control. The thermocouple for furnace temperature control was located approximately 2mm away from the cell at the anode side. The cells were mounted for electrochemical testing at the end of an alumina tube and sealed with a commercial sealing paste (ceramabond #552, Aremco, USA) or home-made glass-tape seals. A thin layer of  $\text{Sm}_{0.5}\text{Sr}_{0.5}\text{CoO}_3$  (SSC) paste was applied to the Pt mesh at the cathode side to create a good contact between the cathode and the cathode current collector (Pt mesh) in the testing apparatus. A constant spring loaded force was applied to the cathode air supply alumina tube, of approximately 1.0 kgf according to the deformation of loading springs. The cell was heated up at a ramp rate of  $300^\circ\text{C h}^{-1}$  to the desired temperature, and held for 1-2 hr for cell reduction and cathode *in-situ* sintering (if the cathode was not *ex-situ* sintered). The temperature for cermet and anode reduction was typically  $600\text{-}700^\circ\text{C}$ . The hydrogen partial pressure on the anode side

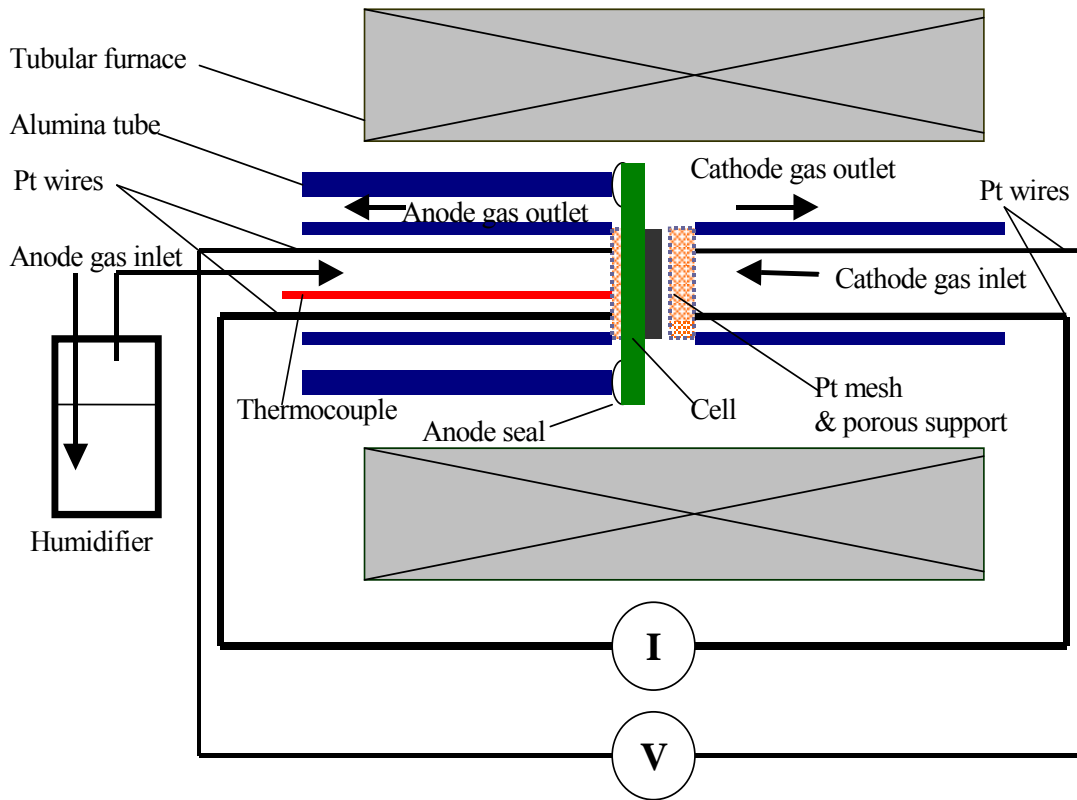


Figure 2-11 A schematic setup of test equipment for cell electrochemical characterization.

was gradually increased (10, 20, 40, 60, 100% H<sub>2</sub>, balance N<sub>2</sub>, at 15 minute intervals) to reduce the NiO to Ni. The cell reduction time was approximately 1.5 hrs. The anode fuel stream, with a flow rate of 100 ml min<sup>-1</sup>, passed first through a bubbler humidifier before entering the anode chamber, corresponding to a 3%H<sub>2</sub>O content in the anode feed, while ambient air (100 ml min<sup>-1</sup>) flowed on the cathode side. Cell electrochemical measurements were carried out after cell reduction.

Electrochemical measurements were performed at temperatures ranging from 700 to 450°C for the SDC single-layer electrolyte cells and 850 to 500°C for SDC+YSZ (or SSZ) bi-layer electrolyte cells under ambient pressure. Cell performances were measured with a Multi-channel Potentiostat/Galvanostat (Solartron 1480 8-channel multi-stat) with a computer interface and Z-plot (for impedance measurement) and Corr-ware (for cell polarization measurement) software (Solartron, USA). Impedance measurements were performed at OCV with a perturbation amplitude of 50 mV rms. The frequency range was 0.1 Hz to 100 kHz, with 10 frequencies per decade. The I-V polarization curves and power curves were obtained using linear sweep voltammetry at a sweep rate of 4 mV s<sup>-1</sup> from OCV to 0.3 V for cells with single SDC electrolyte or OCV to 0.3-0.5V for cells with bi-layered electrolytes.

### **2.6.3 Post-mortem analysis**

The morphologies of the tested cells were observed using a scanning electron microscope (SEM, Hitachi S-3500N, Japan) coupled with energy dispersive spectrometry (EDS) for elemental analysis. Generally plan-view and cross-section view microscopy was performed on hand-broken samples or polished samples embedded in epoxy resin and coated with Au-Pd alloy by sputtering.

## **2.7 Summary**

Wet processing (Tape casting, Screen printing and Co-firing, i.e. TSC) and physical vapour deposition (pulsed laser deposition, i.e., PLD) were used for low temperature SOFC fabrication. NiO-YSZ cermet supported cells with single layered SDC electrolytes (Type I) or with bi-layered YSZ (or SSZ)-SDC electrolytes (Type II) have been successfully developed. Cell characterization procedures, experimental equipment setup and test

protocols have been established and were used to study the performance of fabricated cells. Results are presented in the following chapters.

## **2.8 References**

1. E. Tang, F. Martell, R. Brule, K. Marcotte, B. Borglum (Versa power), in SOFC VIII, S.C. Singhal and M. Dokiya, Editors, The Electrochemical Society Proceedings Series, Pennington, NJ, PV 2003-07 (2003) p.935.
2. N. Q. Minh, T. Takahashi, Science and Technology of Ceramic Fuel Cells, Elsevier, Amsterdam, Netherlands, 1995.
3. J. S. Reed, Introduction to the principles of ceramic processing, published by John Wiley & Sons, Inc., ISBN 0-471-84554-X, (1988) p. 126
4. X. Zhang, M. Robertson, C. Decès-Petit, Y. Xie, S.R. Hui, S. Yick, M. Staite, E. Styles, J. Roller, R. Maric, D. Ghosh, Proc. 9<sup>th</sup> SOFC symposium - 207<sup>th</sup> ECS meeting (2005) 1102.

### 3. Chapter Three. Performance of LT-SOFCs with SDC Electrolytes<sup>3</sup>

Solid oxide fuel cells with thin electrolytes of two types,  $\text{Sm}_{0.2}\text{Ce}_{0.8}\text{O}_{1.9}$  (SDC) (15 $\mu\text{m}$ ) single-layer and 8mol% yttria stabilized zirconia (YSZ) (5 $\mu\text{m}$ ) + SDC (15 $\mu\text{m}$ ) bi-layer on NiO-YSZ cermet substrates were fabricated by screen printing and co-firing.  $\text{Sm}_{0.5}\text{Sr}_{0.5}\text{CoO}_3$  cathodes were printed and *in-situ* sintered during cell performance testing. The SDC single-layer electrolyte cell shows high electrochemical performance at low temperature, with 1180  $\text{mW cm}^{-2}$  peak power density at 650°C. The YSZ+SDC bi-layer electrolyte cell generates 340  $\text{mW cm}^{-2}$  peak power density at 650°C, and shows good performance at 700-800°C, with open circuit voltage close to theoretical value. Micro-islands with high Zr-content were found on the SDC electrolyte surface prior to the cathode preparation. The influence of co-firing temperature and thin film preparation methods on the Zr-islands' appearance was briefly investigated.

#### 3.1 Introduction

During the last decade, nickel-yttria stabilized zirconia (Ni-YSZ) anode supported solid oxide fuel cells (SOFCs) with thin-film electrolytes have been widely adopted by industrial pioneers and research groups around the world. Encouraging performance in the intermediate temperature range (700-800°C) with thin-film YSZ electrolytes has been achieved [1]. However, a high degradation rate in cell performance in a stack has been observed, which is related to thermally activated materials degradation, and in particular, high temperature corrosion of steel interconnects [2, 3]. Extensive R&D efforts are continuing to decrease cell operating temperatures to 650°C or below.

The practical operating temperature of SOFCs is mainly determined by the conductivity and thickness of the electrolyte. Doped ceria is a promising option for an

---

<sup>3</sup> A version of this chapter has been published as:

X. Zhang, M. Robertson, C. Decès-Petit, Y. Xie, R. Hui, S. Yick, E. Styles, J. Roller, O. Kesler, R. Maric, D. Ghosh, NiO-YSZ cermets supported low temperature solid oxide fuel cells, *J. Power Sources*, 161 (2006) 301.

electrolyte material for low temperature use. It has an ionic conductivity that is 2-3 times higher than that of YSZ, and better compatibility with Co-containing electrodes. Its thermal expansion coefficient ( $12.5 \times 10^{-6} \text{ K}^{-1}$ ) is also more compatible with that of the Ni-YSZ cermet substrate and commercial ferritic stainless steel interconnect, compared with YSZ. A maximum power density of  $0.25 \text{ W cm}^{-2}$  at  $550^\circ\text{C}$  with an anode-supported thin ceria based electrolyte cell has been reported [4, 5]. The main disadvantage of a ceria-based electrolyte is that it becomes a mixed conductor in anodic conditions, which causes cell voltage loss and fuel efficiency loss due to internal shorting. Chemical and mechanical stability, thermal cycle capability and redox tolerance are also concerns for long-term service.

To lower manufacturing cost, efforts have been underway to bring proven microelectronics manufacturing technology to SOFCs, such as Tape casting of cermet substrates, Screen printing of functional layers, and Co-firing of cell components (TSC technology in short). Interest is also growing in applying metal supported cell structures [6, 7].

In this study, TSC technology was used to fabricate NiO-YSZ cermet supported cells with thin electrolytes of two types,  $\text{Sm}_{0.2}\text{Ce}_{0.8}\text{O}_{1.9}$  (SDC) ( $15\mu\text{m}$ ) single-layer and 8mol% yttria stabilized zirconia (YSZ) ( $5\mu\text{m}$ ) + SDC ( $15\mu\text{m}$ ) bi-layer. It has been found that the SDC single-layer electrolyte cell shows very high performance at temperatures below  $650^\circ\text{C}$ , while the YSZ+SDC bi-layer electrolyte cell shows good performance over  $700^\circ\text{C}$ , with open circuit voltage close to the theoretical value. Elemental analysis revealed many high-Zr-content micro-islands on the surface of the thin SDC layer and at the cross-section of the SDC electrolyte. The influence of co-firing temperature and thin-film preparation methods on the appearance of the Zr-islands has been investigated.

The cells used in this study were 15mm in diameter, with cermet substrate thickness of approximately 0.6mm.  $\text{Sm}_{0.5}\text{Sr}_{0.5}\text{CoO}_3$  (SSC) cathodes of  $0.40\text{-}0.41\text{cm}^2$  were applied at the centre of each cell by stencil printing, and dried at  $100^\circ\text{C}$  for 1h. The cathode thickness was approximately  $20\text{-}30\mu\text{m}$  after *in-situ* sintering. Details of cell fabrication and experimental procedure can be found in Chapter 2.

### 3.2 Results and discussion

#### Cell electrochemical performance

Figure 3-1 shows the performance of a single-layer SDC electrolyte cell. It can be seen that the maximum power densities of the SDC electrolyte cell reached  $1187 \text{ mW cm}^{-2}$  at  $650^\circ\text{C}$ ,  $886 \text{ mW cm}^{-2}$  at  $600^\circ\text{C}$ , and  $459 \text{ mW cm}^{-2}$  at  $550^\circ\text{C}$ . Interestingly, the maximum power density at  $700^\circ\text{C}$  is  $1040 \text{ mW cm}^{-2}$  lower than that at  $650^\circ\text{C}$ . These values are higher than reported data in the literature with similar cell configurations in this temperature range [4, 5, 7, 8]. The main differences between the present cells and the cells reported in the literature are the in-situ sintering of the cathode, and a slightly thinner SDC electrolyte layer in this study.

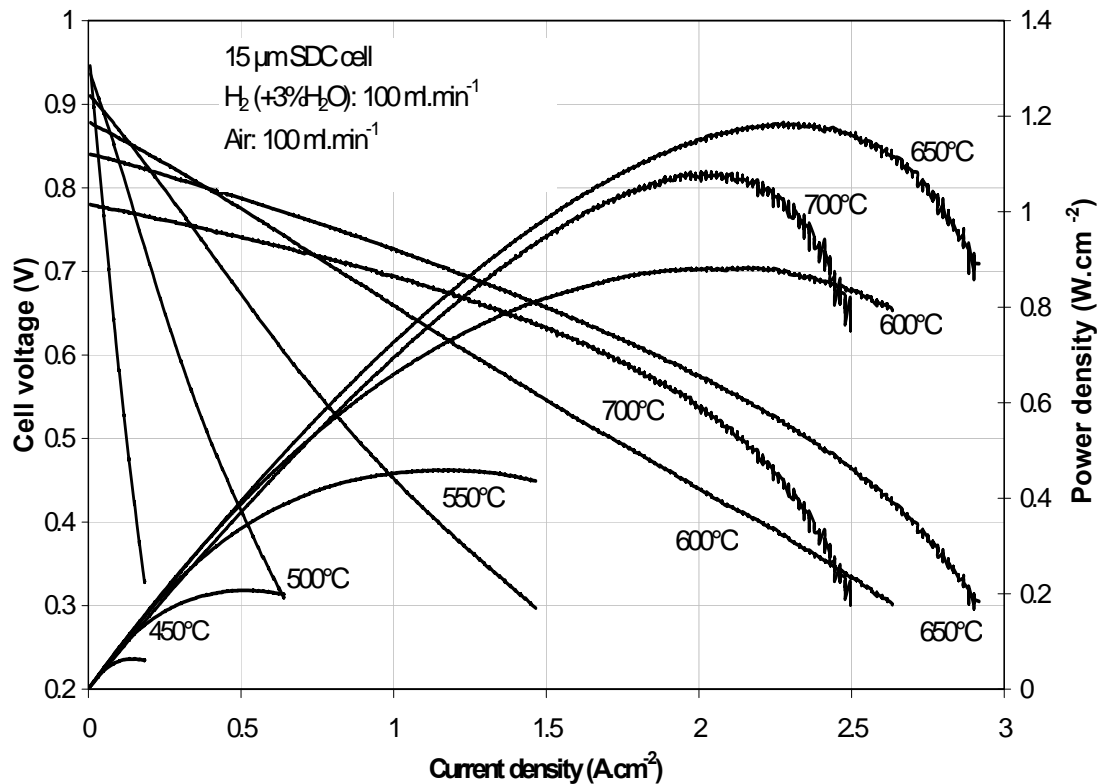


Figure 3-1 I-V power curves of a cell with a  $15 \mu\text{m}$  SDC single layer electrolyte co-fired with the anode at  $1400^\circ\text{C}$ , and with SSC cathode sintered at  $900^\circ\text{C}$ , tested at different operating temperatures.

The performance of a cell with YSZ+SDC bi-layer electrolyte is presented in Figure 3-2. Although the performance is reasonably high at an elevated temperature range, the low

temperature performance is much lower than that of the SDC cell. The maximum power density is only approximately  $340\text{mW cm}^{-2}$  at  $650^\circ\text{C}$ . It can be seen that the OCV of this bi-layer electrolyte cell is much higher than that of the SDC single layer electrolyte cell, and is very close to the theoretical OCV value in the tested temperature range. This result indicates that the dense YSZ layer prevents the anodic reducing atmosphere from directly contacting the SDC electrolyte layer, thereby preventing the electronic conductivity in the SDC electrolyte.

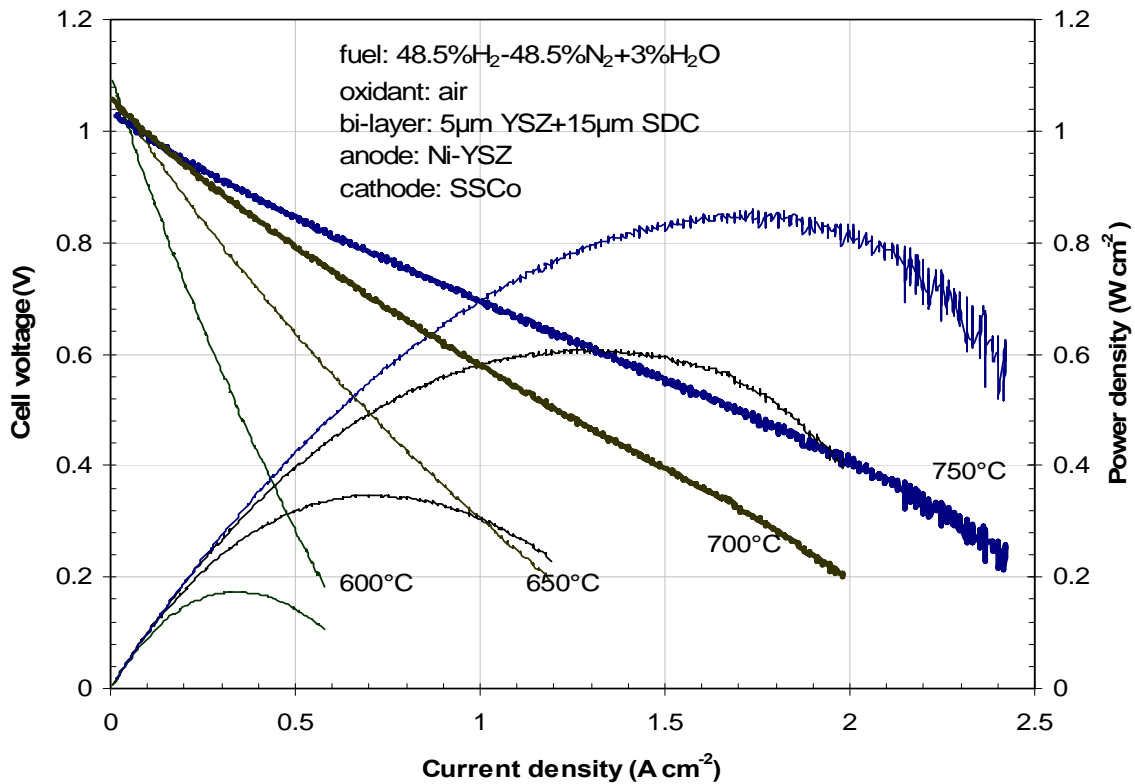


Figure 3-2 I-V power curves of a cell with  $5\mu\text{m}$  YSZ+ $15\mu\text{m}$  SDC bi-layer electrolyte co-fired with Ni-YSZ anode at  $1400^\circ\text{C}$ , and SSC cathode sintered at  $900^\circ\text{C}$ , tested at different operating temperatures.

The low cell performance of the bi-layer electrolyte cell likely results from the combination of a low ionic conductivity of the additional YSZ layer, a detrimental inter-reaction between the SDC and YSZ layer, and a lower anode performance of Ni-YSZ in comparison with Ni-SDC.

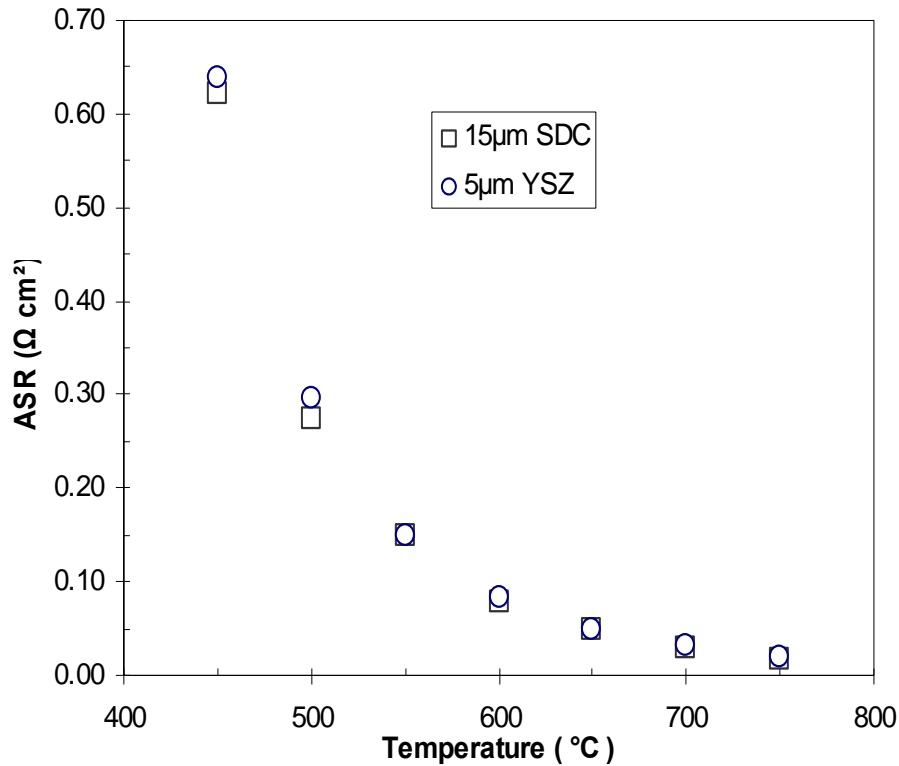
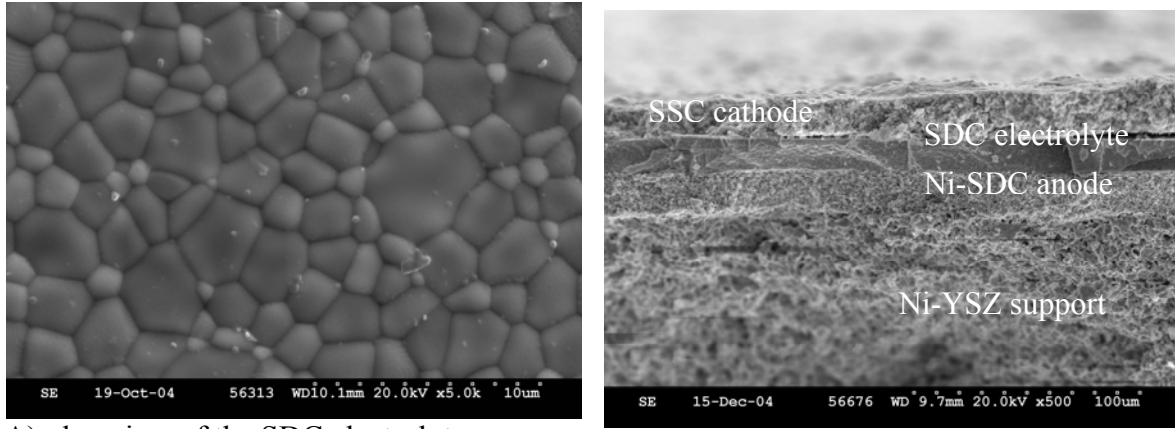


Figure 3-3 Area specific resistances (ASR) of 15μm thick SDC and 5μm thick YSZ at different temperatures.

Figure 3-3 shows the area specific resistances (ASR) of the 15μm thick SDC and 5μm thick YSZ at different temperatures. The points were generated from the reported conductivities of SDC [9] and YSZ [10]. It can be seen that the ASR value of 15μm thick SDC is almost equal to that of 5μm thick YSZ in the listed temperature range, indicating that the predicted ohmic loss of the bi-layer electrolyte cell will be twice as high as that of the single layer SDC electrolyte cell. However, the calculated electrolyte ohmic loss at 650°C is only 50mV at 1A cm<sup>-2</sup>, which is insufficient to explain the low performance of the bi-layer electrolyte cells at this temperature. Because SDC has a higher ionic conductivity and catalytic activity than YSZ, it is likely that the Ni-SDC anode in the single layer SDC electrolyte cell may perform better than the Ni-YSZ anode in the bi-layer cell. The difference of anode gas composition between the SDC electrolyte cell test (97.5% H<sub>2</sub>) and bi-layer electrolyte cell test (48.5% H<sub>2</sub>) will also have an influence. But the main contributor to the low performance of the bi-layer electrolyte cell is a detrimental interaction between YSZ and SDC.

### 3.2.1 Cell microstructural characterization and EDS analysis

Figure 3-4 and Figure 3-5 show plan and cross-section views of the tested cells, including EDS elemental analyses of the cross-section with the electrolyte/anode/support interfaces.



A) plan view of the SDC electrolyte

B) cross-section view of the cell

Figure 3-4 SEM observation of cell with SDC electrolyte (co-fired at 1400°C for 2hr)

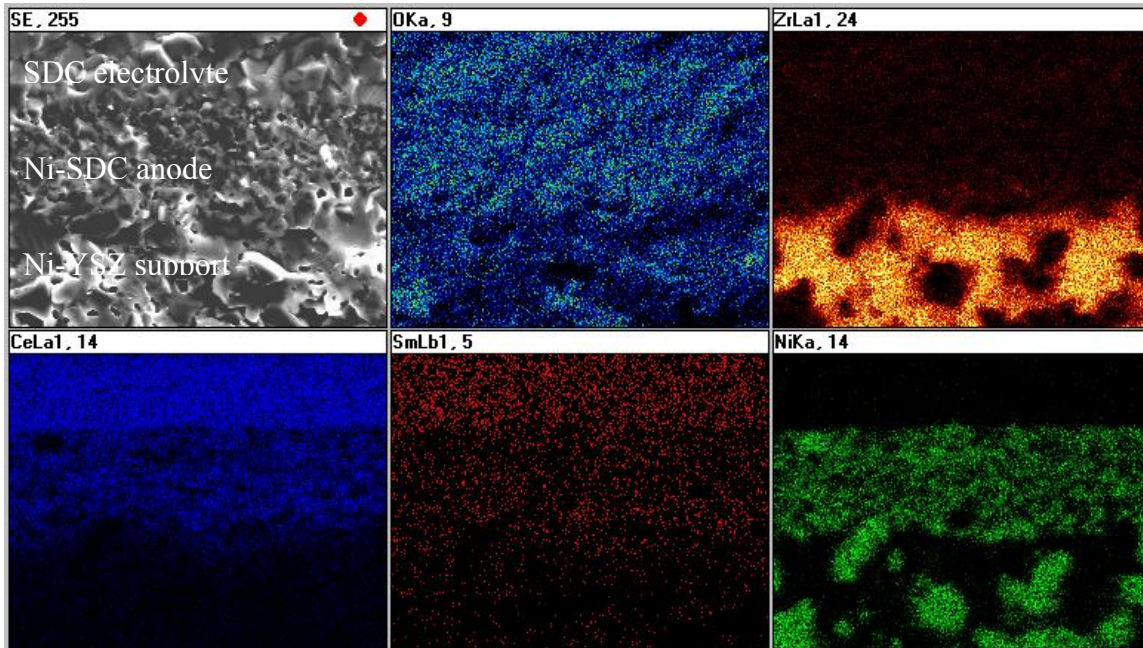


Figure 3-5 EDS elemental analysis at the cell cross-section.

It can be seen that the SDC electrolyte was fully dense with irregular grain size ranging from 1-5 $\mu$ m. The Ni-SDC anode, the Ni-YSZ support, and the SDC electrolyte were tightly sintered (bonded) together with each other. However, the cathode after testing

showed some delamination, which can be explained due to the low sintering temperature and the high thermal expansion coefficient mismatch with the SDC electrolyte. The SDC electrolyte thickness was 15 $\mu\text{m}$ , while the anode and the cathode were both approximately 20 $\mu\text{m}$  thick.

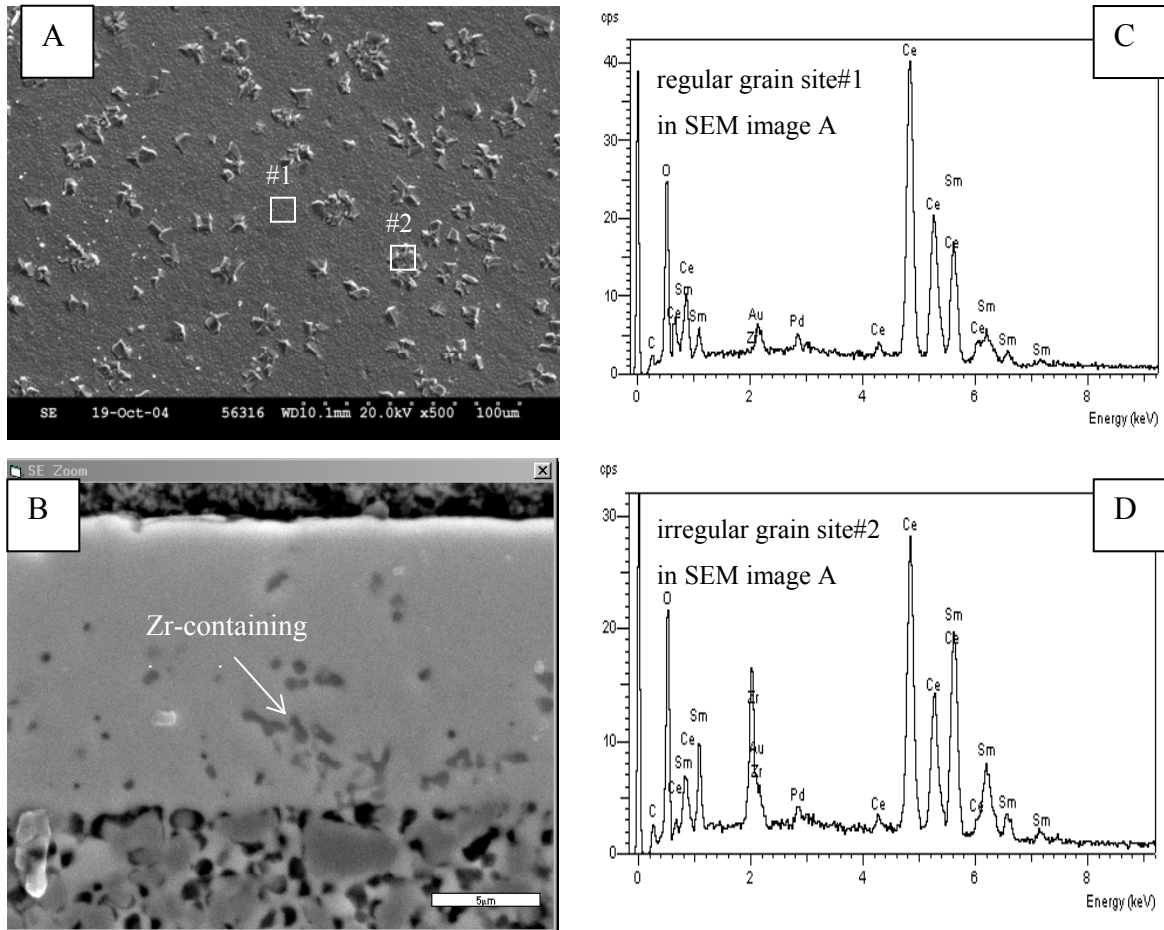


Figure 3-6 Microstructure and EDS analysis of the tested thin SDC cell.

- A. Plan view of SDC cell electrolyte surface without cathode;
- B. Cross-section of the tested SDC cell (polished);
- C. EDS analysis result of SDC electrolyte at a regular grain (see site#1 Figure 3-6.A);
- D. EDS analysis result of SDC electrolyte at an irregular grain (see site#2 in Figure 3-6.A).

Many irregular grains on the SDC electrolyte surface were observed after the 1400 $^{\circ}\text{C}$  - 2hr co-firing and prior to cathode deposition. EDS analysis results (Figure 3-6. D) show that the irregular grains have a high Zr content, and have the appearance of micro-islands, so they are referred to as Zr-micro-islands in this work. The cross-section of the

SDC electrolyte after sample polishing also reveals dark pore-like inclusions (Figure 3-6B), which in fact are Zr-content inclusions as verified by EDS analysis. There are many more of these Zr-micro-islands in the YSZ+SDC bi-layer electrolyte cell (Figure 3-7A) than in the SDC single-layer electrolyte cell (Figure 3-6A). Figure 3-7D shows the Zirconium element mapping of the cross section of the YSZ+SDC bi-layer electrolyte cell as a mechanically fractured sample without polishing (Figure 3-7B). It proves that the YSZ layer (approximately 5 $\mu\text{m}$ ) applied adjacent to the anode has not chemically mixed with the subsequently deposited SDC layer after high temperature co-firing. It is hard to see from Figure 3-7D the existence of Zr (if any) present in the cross section of the SDC layer, which could be attributed to this SEM sample being unpolished.

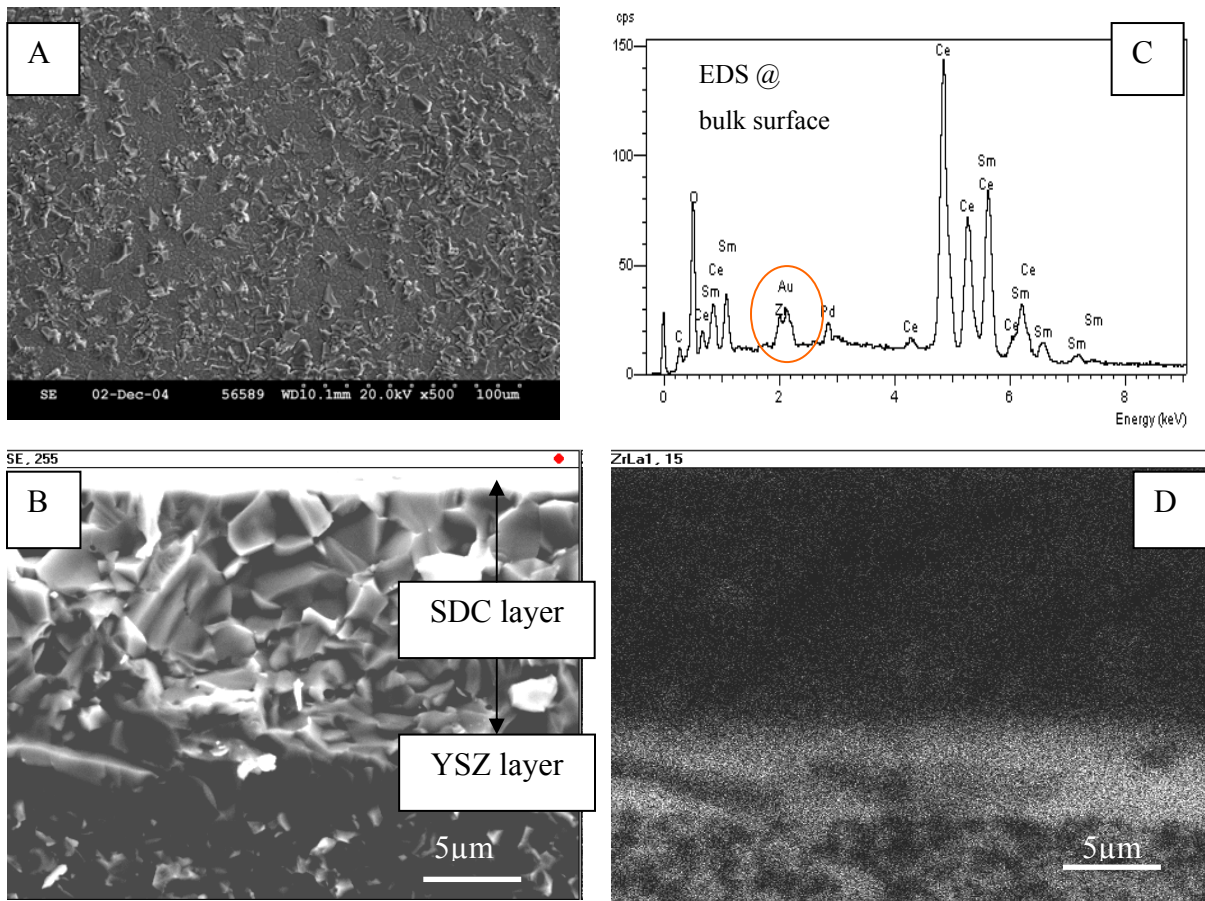


Figure 3-7 Microstructure and EDS analysis of the tested thin YSZ+SDC cell

- A. Plan view of YSZ+SDC cell electrolyte surface without cathode;
- B. Cross-section of the tested YSZ+SDC cell (not polished);
- C. EDS analysis result of the SDC bulk surface;
- D. Zirconium mapping of the cross-section of the YSZ+SDC cell.

### 3.2.2 Zr-micro-islands

EDS analysis was used to examine one of the irregular grain areas at higher resolution. Figure 3-8 shows the results. It can be seen that the irregular grain shows not only a high Zr-content, but also an enriched Sm content, while the Ce content is substantially decreased in comparison with the SDC. This result suggests that a second phase, containing Sm, Zr and Ce, separates from the SDC phase. High Sm content in the irregular grain indicates that Sm has a higher solubility in the new phase. Furthermore, since the grain size of the Zr-island is larger than that of the normal SDC grains, this second phase likely also has a higher vapour pressure or lower melting point, a faster grain growth rate, and higher sinterability than that of SDC during the cell co-firing.

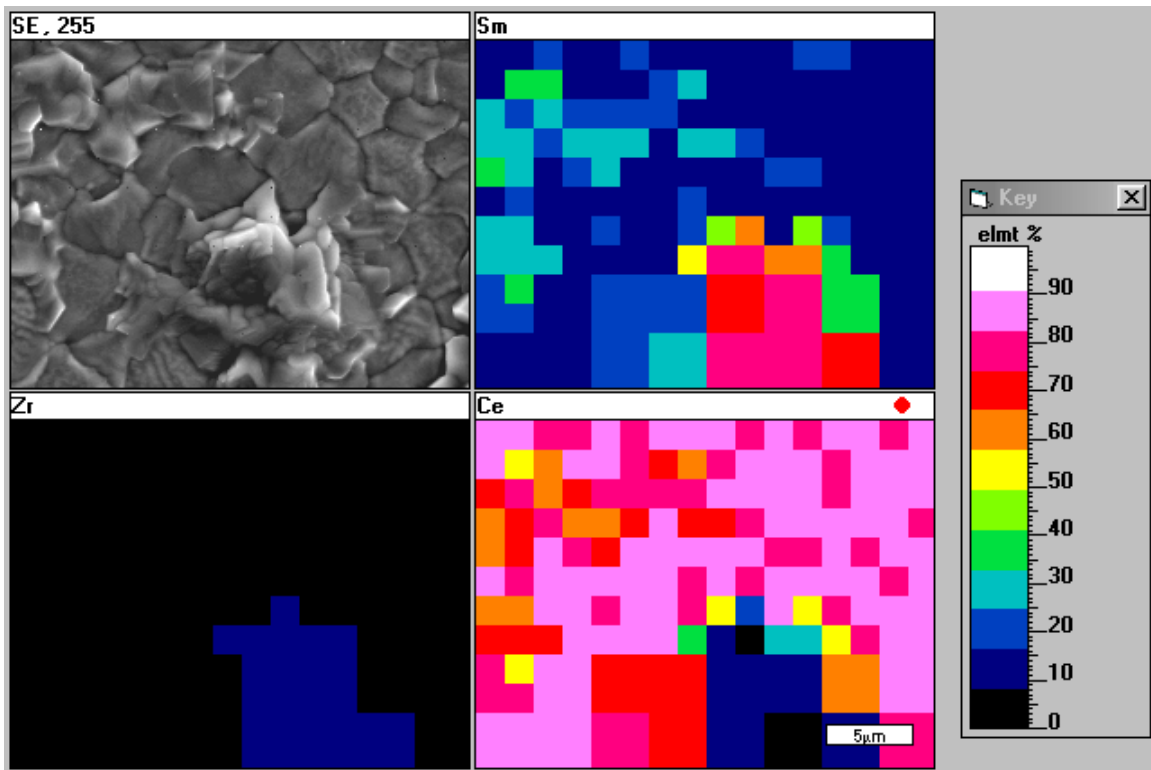


Figure 3-8 EDS elemental mapping of an irregular grain area

The Zr-micro-islands are potentially detrimental to the cell performance. Tsoga *et al* [11] reported that the Zr-Ce-Gd-Y-O phase exhibits a conductivity 1-2 orders of magnitude lower than that of either GDC or YSZ. Table 3-1 lists their conductivity data, recorded at 800°C. Since Sm-doped ceria and Gd-doped ceria have very similar

conductivities, it is likely that the Zr micro-islands observed in this work may also consist of a very low conductivity phase, based on the analyzed compositions and on their similarity with the compositions studied by Tsoga *et al.*

Table 3-1 Ionic conductivity ( $\sigma_i$ ) and electronic conductivity ( $\sigma_e^\circ$ ) of YSZ, GDC and their solid solutions at 800 °C [11] (© Solid State Ionics, 2000, by permission)

Material	Nominal composition	$\sigma_i$ (S cm <sup>-1</sup> )	$\sigma_e^\circ$ (S cm <sup>-1</sup> )
YSZ	Zr <sub>0.85</sub> Y <sub>0.15</sub> O <sub>1.93</sub>	0.054	7.29×10 <sup>-13</sup>
GDC	Ce <sub>0.80</sub> Gd <sub>0.20</sub> O <sub>1.90</sub>	0.087	8.18×10 <sup>-6</sup>
Reaction product	Ce <sub>0.37</sub> Zr <sub>0.38</sub> Gd <sub>0.18</sub> Y <sub>0.07</sub> O <sub>1.87</sub>	0.00125	3.99×10 <sup>-6</sup>
Interlayer	Ce <sub>0.43</sub> Zr <sub>0.43</sub> Gd <sub>0.10</sub> Y <sub>0.04</sub> O <sub>1.93</sub>	0.00603	3.88×10 <sup>-6</sup>

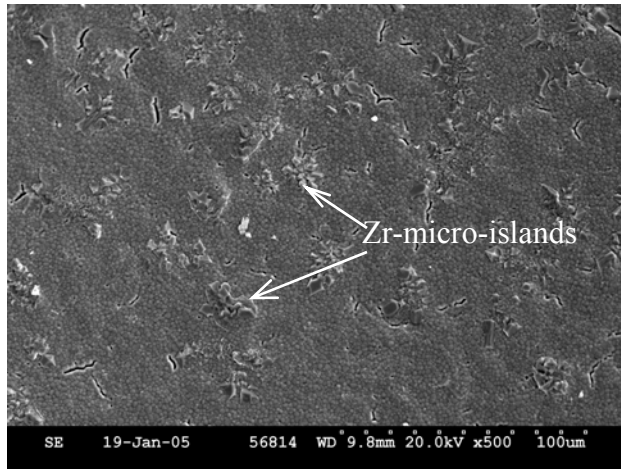


Figure 3-9 SEM image of a cell with spin-coated SDC electrolyte fired at 1400°C

The formation mechanism of the Zr-micro-islands is not clear. The SDC electrolyte paste was investigated and no any Zr contamination was found. The influence of sintering temperature was also studied, and it was found that lower sintering temperatures produced fewer obvious irregular grains. Cells co-fired at 1250°C did not show any irregular grains, which suggests either that no Zr migration (and Zr-micro-island formation) occurred, or that the grains have not grown large enough to be detected, due to the slow grain growth rates at the low sintering temperatures. No clear location showing a high Zr content on the cells sintered at 1250°C was found. Spin coating of the electrolyte layers was conducted to

determine whether the formation of Zr-islands results from potential inter-contamination during screen-printing. Similar irregular grains on the SDC surface were found after firing at 1400°C (Figure 3-9). The formation of Zr-micro-islands is therefore likely related to Zr migration from the NiO-YSZ substrate during the co-firing process.

### **3.3 Conclusions**

SDC single-layer electrolyte cells and YSZ+SDC bi-layer electrolyte cells supported by Ni-YSZ substrates were prepared by tape casting, screen printing, and co-firing technology. Using *in-situ* sintered SSC cathodes, high performance of over 1180 mW cm<sup>-2</sup> peak power density at 650°C was obtained from the SDC electrolyte cells. The bi-layer cells did show higher OCV values, but their performances were much lower than those of the SDC cells at low operating temperatures. Zr-micro-island formation on the SDC electrolyte was observed, with compositions indicating that an interaction between YSZ and SDC took place during the high-temperature co-firing of the cells.

### **3.4 References**

1. S. de Souza, S. J. Visco and L. C. de Jonghe, *Solid State Ionics* 98 (1997) 57.
2. Z. Yang, K. S. Weil, D. M. Paxton and J. W. Stevenson, *J. Electrochem. Soc.* 150 (2003) A1188.
3. W. Z. Zhu, S. C. Deevi, *Materials Research Bulletin* 38 (2003) 957.
4. C. Xia, W. Rauch, F. Chen, M. Liu, *Solid State Ionics* 149 (2002) 11.
5. S. Zha, W. Rauch and M. Liu, *Solid State Ionics* 166 (2004) 241.
6. G. Schiller, R Henne, M. Lang, and S. Schaper, 1999, *Proc. SOFC VI, Electrochem. Soc.*, p. 893.
7. N. P Brandon, A. Blake, D. Corcoran, D. Cumming, A. Duckett, K. El-Koury, D. Haigh, C. Kidd, R. Leah, G. Lewis, C. Matthews, N. Maynard, N. Oishi, T. McColm, R. Trezona, A. Selcuk, M. Schmidt, L. Verdugo, *J. Fuel Cell Science and Technology* 1 (2004) 61.
8. S. Zha, A. Moore, H. Abernathy and M. Liu, *J. of Electrochem. Soc.* 151 (2004) A 1128.
9. V. V. Kharton, F. M. B. Marques and A. Atkinson, *Solid State Ionics* 174 (2004) 135.
10. S. P. S. Badwal, *Solid State Ionics* 52 (1992) 23.
11. A. Tsoga, A. Naoumidis and D. Stover, *Solid State Ionics* 135 (2000) 403.

## 4. Chapter Four. Composite Cathode Study<sup>4</sup>

The cathode is a key component in low temperature solid oxide fuel cells. In this study, composite cathodes with the composition 75wt%  $\text{Sm}_{0.5}\text{Sr}_{0.5}\text{CoO}_3$  (SSC) + 25wt%  $\text{Sm}_{0.2}\text{Ce}_{0.8}\text{O}_{1.9}$  (SDC) were fabricated in cermet supported thin SDC electrolyte cells made by tape casting, screen-printing, and co-firing. The following two studies have been performed.

(1) Cathode sintering temperature  $T_{s,c}$  study: Single cells with composite cathodes sintered at three different temperatures  $T_{s,c}$ : 950°C, 1050°C, and 1150°C were tested from 400°C to 650°C. The best cell performance, 0.75 W cm<sup>-2</sup> peak power density operating at 600°C, was obtained from the 1050°C-sintered cathode. The measured thin SDC electrolyte resistance  $R_s$  was 0.128  $\Omega$  cm<sup>2</sup> and total electrode polarization resistance  $R_{p,a+c}$  was only 0.102  $\Omega$  cm<sup>2</sup> at 600°C.

(2) Thickness study of the composite cathodes: Different cathode thicknesses ranging from 15 to 110 $\mu\text{m}$  in average were studied both with and without cathode contact pastes. All the cathodes were sintered at 1000°C for 2hrs. The cathode morphology and the cathode performance were investigated. The best cell, showing peak power density of approximately 0.86 W cm<sup>-2</sup> operating at 600°C, was obtained with the average cathode thickness of 50 $\mu\text{m}$  with or without contact paste. The measured thin SDC electrolyte resistance  $R_s$  was 0.093  $\Omega$  cm<sup>2</sup> and total electrode polarization resistance  $R_{p,a+c}$  was 0.118  $\Omega$  cm<sup>2</sup> at 600°C. It was found that with cathode contact paste the individual cell performance could be slightly improved. The contact paste not only reduced the ohmic loss of the total cell but also the electrode reaction resistance, i.e., cathode electrochemical overpotential in this study.

---

<sup>4</sup> A version of this chapter has been published as:

X. Zhang, M. Robertson, S. Yick, C. Deêes-Petit, E. Styles, W. Qu, Y. Xie, R. Hui, J. Roller, O. Kesler, R. Maric, D. Ghosh,  $\text{Sm}_{0.5}\text{Sr}_{0.5}\text{CoO}_3 + \text{Sm}_{0.2}\text{Ce}_{0.8}\text{O}_{1.9}$  composite cathode for cermet supported thin  $\text{Sm}_{0.2}\text{Ce}_{0.8}\text{O}_{1.9}$  electrolyte SOFC operating below 600°C, J. Power Sources 160 (2006) 1211.

## 4.1 Introduction

Various processes are associated with cathode resistance in a solid oxide fuel cell (SOFC): the transport of oxygen gas through the porous cathode, the adsorption of oxygen onto the cathode surface, the reduction and dissociation of the oxygen molecule ( $O_2$ ) into the oxygen ion ( $O^{2-}$ ), and the incorporation of the oxygen ion into the electrolyte, to be transported across to the anode. As the operating temperature of an SOFC is lowered to reduce system and material cost and degradation, the cathode begins to limit the cell performance. The cathode resistance was 70-85% of the total cell resistance from 550-800°C for anode supported SOFCs with the standard (La,Sr)MnO<sub>3</sub> (LSM)-YSZ composite cathode on YSZ electrolyte [1]. There is extensive interest in mixed ionic/electronic conductor (MIEC) cathode materials for SOFCs that operate below 600°C, such as Sm<sub>0.5</sub>Sr<sub>0.5</sub>CoO<sub>3</sub> (SSC) [2, 3], (La,Sr)CoO<sub>3</sub> (LSC) [4] (La,Sr)(Co,Fe)O<sub>3</sub> (LSCF) [5], and (Ba,Sr)(Co,Fe)O<sub>3</sub> [6], as well as their combination with Sm<sub>0.2</sub>Ce<sub>0.8</sub>O<sub>1.9</sub> (SDC) or Gd<sub>0.2</sub>Ce<sub>0.8</sub>O<sub>1.9</sub> (GDC) to form composite cathodes [2, 5, 6]. Those new cathodes have provided a superior performance compared to (La,Sr)MnO<sub>3</sub> (LSM) cathodes due to electrochemically active area extension from just the triple phase boundary (TPB) to the entire MIEC surface. For example, low-current polarization resistance at 600°C of LSCF-GDC cathodes on a YSZ electrolyte was measured as 0.3 Ωcm<sup>2</sup> [7], and on a GDC electrolyte was measured as 0.19 Ω cm<sup>2</sup> [5]; and for Ba<sub>0.5</sub>Sr<sub>0.5</sub>Co<sub>0.8</sub>Fe<sub>0.2</sub>O<sub>3</sub> on an SDC electrolyte, it was measured in the range of only 0.055-0.071 Ω cm<sup>2</sup> at 600°C [6].

Sm<sub>0.5</sub>Sr<sub>0.5</sub>CoO<sub>3</sub> (SSC) has been studied as a cathode material for SOFCs with YSZ, LSGM, and SDC or GDC electrolytes [2, 3, 8-14]. Dense SSC showed overpotential approximately 50% lower than that of LSC under similar conditions. The rate-determining step of dense SSC cathodes was shown to be adsorption-desorption at the surface of the electrode, the same as for LSC, but the adsorption and desorption rate constants of SSC were approximately one order of magnitude larger than the corresponding values for LSC [2]. Furthermore, the electrochemical performance of SSC porous cathodes can be improved by adding doped ceria, which results in the suppression of growth of SSC particles, thereby maintaining the porosity and increasing the TPB area. The performance can also be improved by optimizing the conductivity and size distribution of particles of each solid phase to yield a larger TPB contact area that is accessible for oxygen reduction.

Adding SDC to the SSC cathode is also believed to be of benefit by narrowing the difference of thermal expansion coefficients between the electrolyte and cathode. SSC is also compatible both chemically and physically with ceria electrolytes [3].

In this study, the sintering temperature and thickness of 75wt% SSC ( $\text{Sm}_{0.5}\text{Sr}_{0.5}\text{Co}_3$ ) + 25wt% SDC ( $\text{Sm}_{0.2}\text{Ce}_{0.8}\text{O}_{1.9}$ ) composite cathodes were studied using SDC as an electrolyte and Ni+SDC as anode materials. Single cells were tested in the temperature range of 400 to 650°C. The cell performances with the cathodes sintered at different temperatures were also studied using electrochemical impedance measurements.

## **4.2 Experimental procedure**

### *Test Cell-- Materials and Fabrication*

Ni-YSZ cermet supported thin SDC electrolyte cells were fabricated by tape-casting, screen-printing, and high temperature co-firing, followed by cathode printing and sintering. The composite cathode consists of SSC and SDC at a weight ratio of 75% SSC : 25% SDC, and is labeled as SSC#3 in this dissertation work. Table 4-1 lists the cell structure materials and thicknesses. Three different cathode sintering temperatures, 950, 1050, and 1150°C, were used to study the influence of  $T_{s,c}$  on cathode performance and microstructure. For the cathode thickness study, tape masks of different thicknesses were used as spacers for cathode preparation. The thickness of the cathode after sintering at 950, 1000, 1050°C was measured. Table 4-1 lists the cermet supported single layer SDC electrolyte cells for the cathode thickness study. The SSC#3 cathode area of an individual cell was measured using an image analysis program (Optimas 6.1) on an optical photograph of the cathode, after sintering. The cathode area was in the range of 1.33-1.34cm<sup>2</sup> for the  $T_{s,c}$  study and 0.52-0.55 cm<sup>2</sup> for the thickness study.

Before applying the cathode, each cell was characterized by Archimedes' density measurements and helium gas cross leak tests. The average cell density was approximately 5.15g cm<sup>-3</sup>, corresponding to 37% anode porosity after NiO reduction based on the cermet substrate composition of 57wt%NiO. A helium gas cross leakage check was conducted with 6.9kPa (1 psi) He at room temperature, with a gas permeability test jig. All the cells transmitted zero gas bubbles in 5 mins, indicating that the SDC electrolyte layer was fully dense.

Table 4-1 Material and thickness of cermet supported SDC cells in this study

Cell Type I	Ni-YSZ cermet supported thin SDC cell		
	Material	Thick [ $\mu\text{m}$ ]	$T_s$ [ $^{\circ}\text{C}$ ]
Cathode (SSC#3)	75%SSC	20-40 for $T_{s,c}$ study, 1.33-1.34 $\text{cm}^2$	950-1150
	+25%SDC	20-100 for thickness study, 0.52-0.55 $\text{cm}^2$	1000
Electrolyte	SDC	18-20 for $T_{s,c}$ study	1400
		10-15 for cathode thickness study	1380
Anode	Ni-SDC	10-15	As electrolyte
Cermet Substrate	Ni-YSZ	800-1000	As electrolyte

#### *Cell characterization*

Each cell with a sintered cathode was mounted on a horizontal alumina tube with a gasket seal made from a highly dense ceramic fibre sheet. A thin SSC#3 contact paste was applied for good contact between the cathode and the Pt mesh-cathode current collector for the  $T_{s,c}$  study. For the cathode thickness study, cathodes both with and without cathode pastes were studied. A constant spring loaded force was applied by the cathode air supply alumina tube, of approximately 1.5 kgf. A split-tube furnace (Thermcraft Incorporated, USA) was used for cell temperature control. The thermocouple for furnace temperature control was located just behind the cell on the anode side.

Electrochemical measurements were performed from 650 to 400 $^{\circ}\text{C}$  under ambient pressure. Humidified (3% $\text{H}_2\text{O}$ ) hydrogen was used as the fuel and air as the oxidant, both at a flow rate of 100ml  $\text{min}^{-1}$ . I-V curves were measured using linear sweep voltammetry at a sweep rate of typically 1-4  $\text{mV s}^{-1}$ . The electrochemical impedance spectra (EIS) were typically measured in the frequency range from 0.1Hz to 65kHz. The cell resistance ( $R_c$ ) was calculated using data fitting from the I-V curve, and the electrolyte resistance ( $R_s$ ) and electrode resistance ( $R_p$ ) were calculated using EIS data fitting.

Powder characterization of the cell materials was performed by specific surface area (Surface area analyzer SA3100, Beckman Coulter, USA) and particle size (Mastersizer 2000, Malvern instruments, USA) measurements and by XRD phase analysis

(D8 Advance, Bruker AXS, USA). The morphologies of the tested cathodes were observed using a scanning electron microscope (SEM, Hitachi S-3500N) coupled with EDS analysis.

### 4.3 Results and discussion

#### 4.3.1 SSC+SDC phase structure

A powder mixture of SSC and SDC at 50% weight ratio sintered at elevated temperatures (up to 1300°C) was investigated by XRD for potential interactions between SSC and SDC. The sample sintered at 1300°C was completely melted, and no powder sample was obtained for XRD analysis. Figure 4-1 shows the XRD analysis results. It can be seen that sharpening of SSC peaks is observed during the heat treatment attributable to further crystallizing of the powder. However, no obvious reaction happens for the composites heated up to 1200°C for 4h. Similar results were reported by Xia *et al* [2]. They found that other phases were present when SSC with 10wt%SDC composite was fired at 1250°C for 4h. It seems that SSC+SDC composite is a chemically stable cathode material for SDC electrolyte-based SOFC when the sintering temperature is below 1200°C.

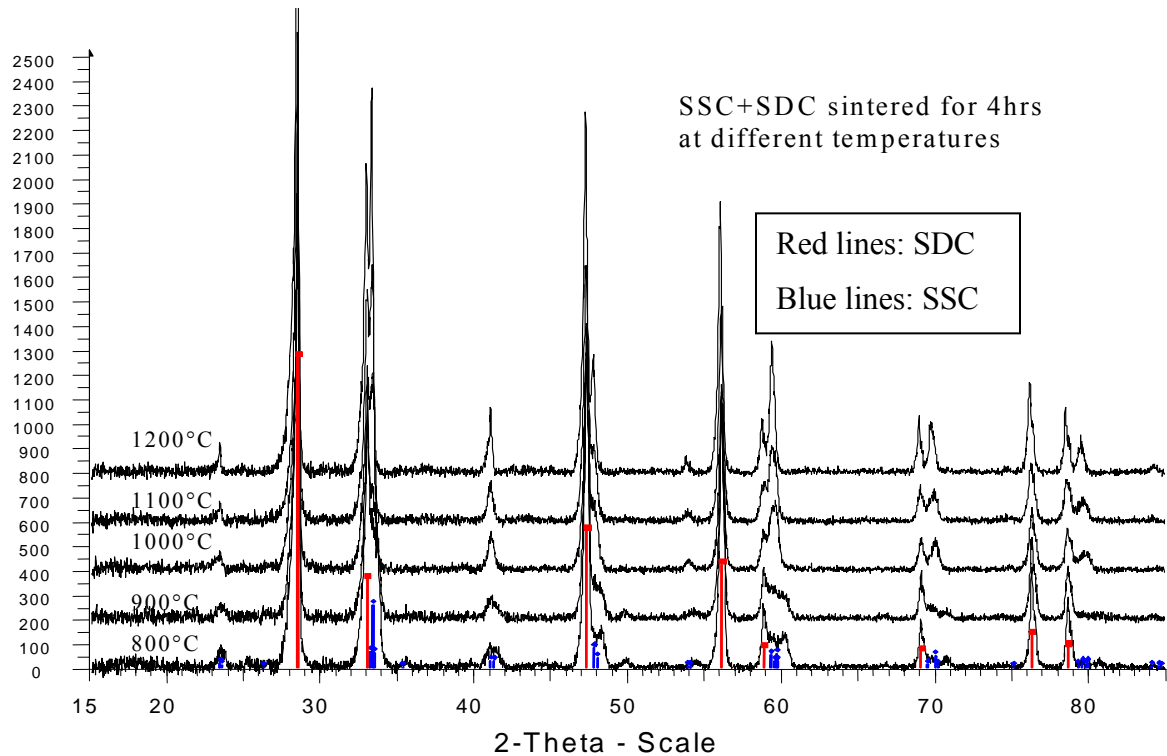


Figure 4-1 XRD patterns of SSC+SDC powder mixtures sintered at different temperatures.

### 4.3.2 Open circuit voltage (OCV)

Figure 4-2 are the temperature dependences of OCV for a hydrogen/air fuel cell based on a cermet supported 20 $\mu\text{m}$  thick SDC electrolyte cell with cathodes sintered at different temperatures,  $T_{s,c}$ . The theoretical OCV using an SDC electrolyte, as reported by Matsui *et al* [15], is also shown in this figure. It is obvious that the recorded OCV data of the tested cells are much lower than the theoretical OCV. The recorded OCV value decreased from 0.99V at 400 $^{\circ}\text{C}$  to approximately 0.85V at 650 $^{\circ}\text{C}$ . It is well known that electronic conductivity in the SDC electrolyte is increased at high temperatures under anodic fuel cell conditions. However, the recorded OCV data in this study were lower than those reported with thick SDC electrolytes. The OCVs for 0.4mm SDC electrolyte cells under the same test conditions were 1.08V at 400 $^{\circ}\text{C}$  and approximately 0.90V at 650 $^{\circ}\text{C}$  [2].

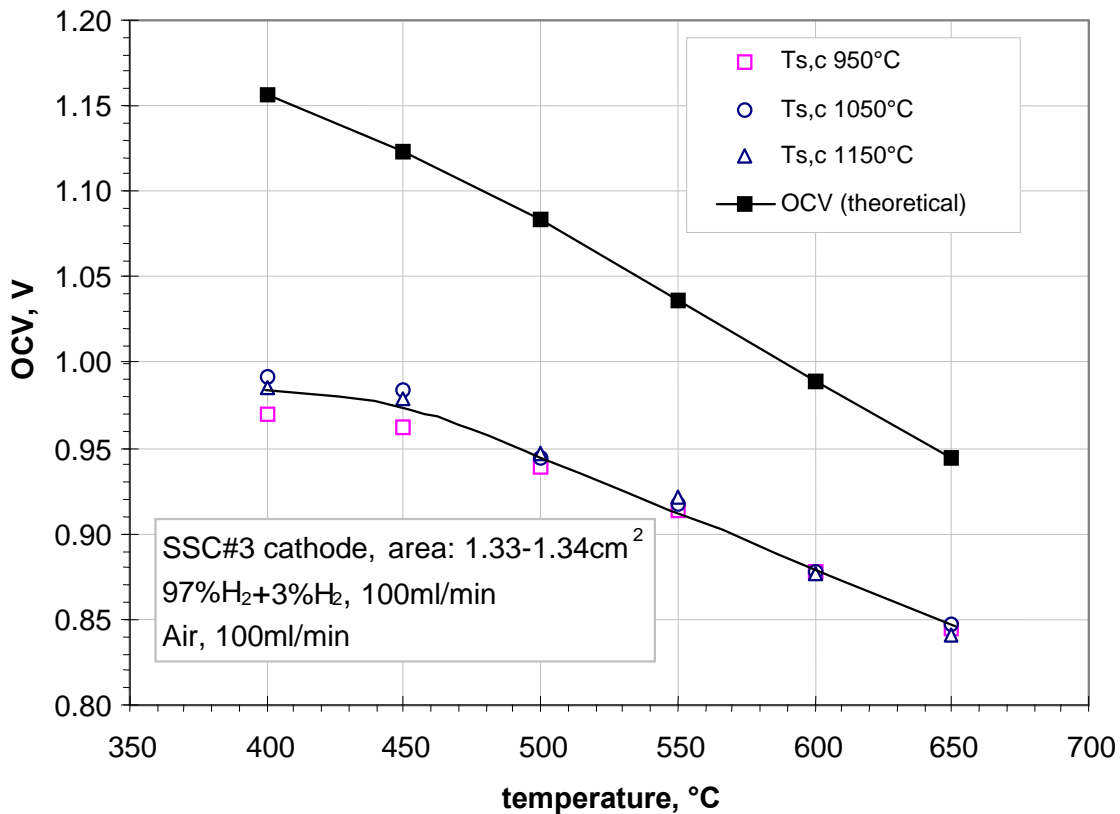


Figure 4-2 Temperature dependences of OCV for the cermet supported thin SDC electrolyte cells with cathode sintered at different  $T_{s,c}$ .

It is clear that decreasing SDC electrolyte thickness leads to a lower OCV at the temperatures studied. The OCVs were 0.98V and 0.94V at 600°C for SDC electrolyte-supported cells of thicknesses 2.2mm and 1.19mm, respectively [15], only 0.91V for a 0.4mm thick SDC electrolyte-supported cell [2], and 0.879V for the cermet-supported 20 $\mu$ m thick SDC electrolyte cell used in this study. Furthermore, it was found that there was a slight difference in OCV values for the 3 cells with different cathode sintering temperatures. The difference was enlarged at temperatures below 450°C, where the OCV could exhibit a 20-30mV difference at the same temperature due to different  $T_{s,c}$ . The highest OCV at the low temperature region was present in the cell with cathode  $T_{s,c}$ =1050°C. It has been reported that the electrode performance had an influence on the OCV value [15, 16]. A low OCV value could be related to a lower electrode performance.

#### **4.3.3 Effects of $T_{s,c}$ on cell performance and electrochemical resistance**

As shown in Figure 4-3 and Figure 4-4, the cathode sintering temperature ( $T_{s,c}$ ) had an obvious influence on the cell performance, which could be related to the microstructure, the adhesion of the electrode to the electrolyte, the grain growth, and the electrode porosity, which affects the active sites for oxygen reaction. It was found that the highest cell performance was obtained with  $T_{s,c}$ =1050°C, with 0.75W cm<sup>-2</sup> power density obtained at 600°C. The main results are summarized in Table 4-2. It was observed that the cell ohmic resistances,  $R_s$ , for these 3 different cells were very close to each other, which indicated that the SDC electrolyte thickness was approximately the same for each cell, and even the cell with cathode sintered at 1150°C showed limited interaction between the cathode and the SDC electrolyte, according to the XRD results. The performance of the cell with SSC#3 composite cathode sintered at 1050°C is summarized in Table 4-3. The measured cathode area was 1.337 cm<sup>2</sup>. The  $R_{cell}$  values were obtained from the I-V curve, and both  $R_s$  and  $R_{p,a+c}$  values were obtained from EIS measurement results by using instant data fitting with *Corr view* and *Z-view* softwares. It is notable that the sum of  $R_s$  and  $R_{p,a+c}$  is approximately equal to the  $R_{cell}$  value at temperatures over 500°C. The peak power density (PPD) reached 1W cm<sup>-2</sup> at 650°C and 0.25W cm<sup>-2</sup> at 500°C, two times higher than the values reported in [2].

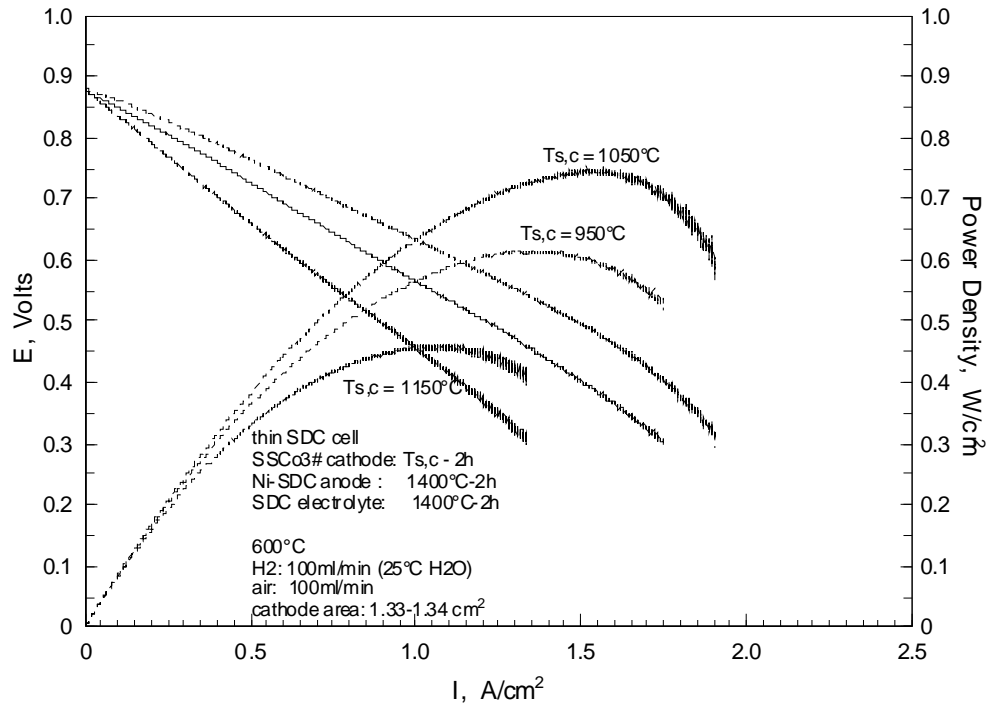


Figure 4-3 Electrochemical performance of cells with thin SDC electrolytes with cathodes sintered at different temperatures.

Table 4-2 Results of the cells operating at 600°C with composite cathodes of different  $T_{s,c}$

$T_{s,c}$ [°C]	OCV [V]	PPD [W cm <sup>-2</sup> ]	$R_{cell}$ [Ω cm <sup>2</sup> ]	$R_s$ [Ω cm <sup>2</sup> ]	$R_{p,a+c}$ [Ω cm <sup>2</sup> ]
950	0.882	0.615	0.3166	0.1312	0.1573
1050	0.879	0.749	0.2518	0.1276	0.1020
1150	0.878	0.462	0.4336	0.1322	0.3085

OCV: open circuit voltage of the cell from Fig. 4-3 or Fig.4-2

PPD: cell peak power density, from Fig. 4-3

$R_{cell}$ : cell electrochemical resistance, from Fig.4-3 (OCV-0.75V).

$R_s$ : cell ohmic loss, mostly due to SDC electrolyte, from Fig.4-4

$R_{p,a+c}$ : cell polarization resistance from both anode and cathode, from Fig.4-4

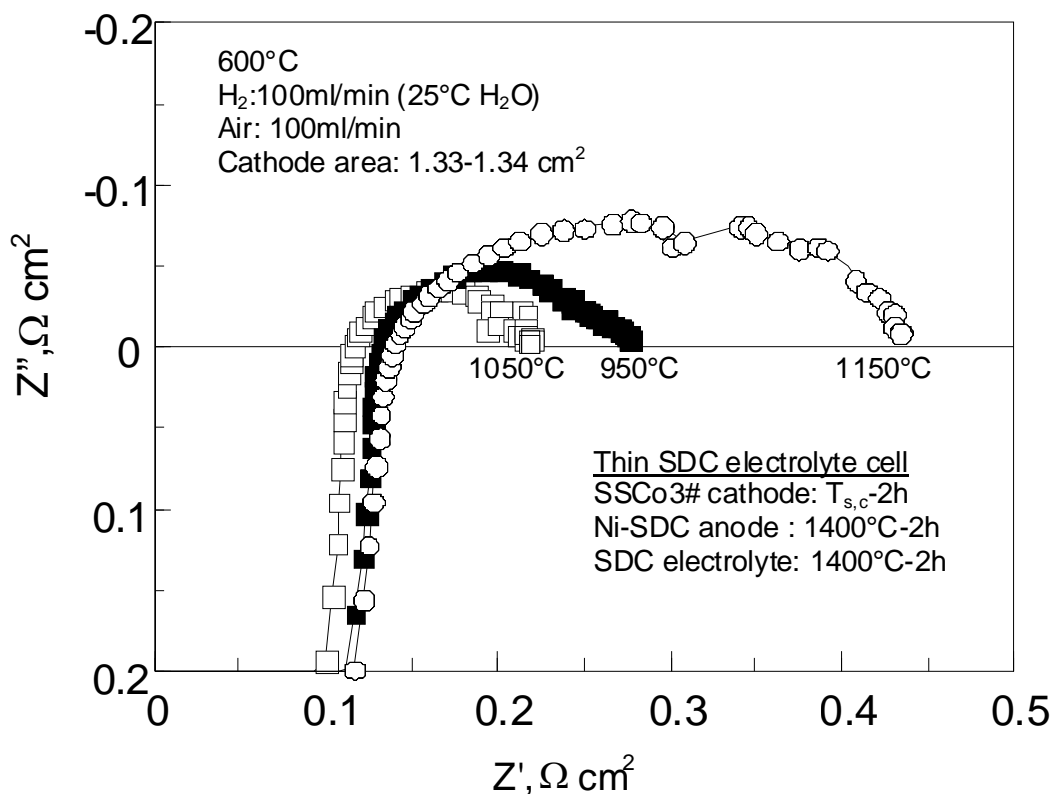


Figure 4-4 EIS of cells with cathodes sintered at different temperatures.

Table 4-3 Cell performance with SSC#3 cathode sintered at 1050°C

Cell temp. [°C]	OCV [V]	CD [A cm <sup>-2</sup> ]	CV [V]	PPD [W cm <sup>-2</sup> ]	R <sub>cell</sub> [Ω cm <sup>2</sup> ]	R <sub>s</sub> [Ω cm <sup>2</sup> ]	R <sub>p,a+c</sub> [Ω cm <sup>2</sup> ]
650	0.8491	1.8130	0.5577	1.0111	0.1436	0.0773	0.0464
600	0.8786	1.5045	0.4979	0.7491	0.2518	0.1276	0.1020
550	0.9170	1.0878	0.4210	0.4579	0.4651	0.2006	0.2164
500	0.9445	0.6629	0.3817	0.2531	0.8118	0.3951	0.4979
450	0.9843	0.2919	0.4042	0.1179	1.9453	0.9231	1.695
400	0.9912	0.1501	0.3103	0.0466	4.3683	2.188	3.846

Test condition: 97%H<sub>2</sub>+3%H<sub>2</sub>O 100ml min<sup>-1</sup>, air 100ml min<sup>-1</sup>

CD: current density at Peak power density (PPD); CV: cell voltage at PPD

#### 4.3.4 SEM observation

Figure 4-5 shows SEM images of the tested cells. It is clear that the SDC electrolyte thicknesses of the three cells are approximately equal and fairly uniform, approximately 18-20 $\mu\text{m}$ .

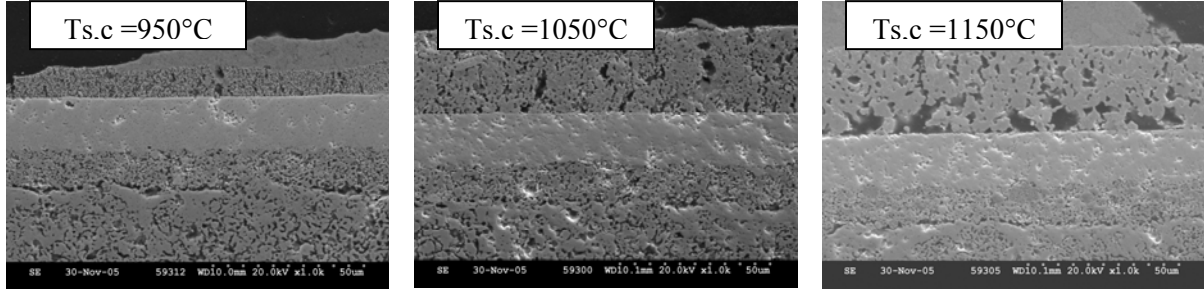


Figure 4-5 SEM images of the tested cells.

Based on the  $R_s$  data in Table 4-2, the calculated SDC conductivity was over 0.015  $\text{S cm}^{-1}$ , close to the reported SDC conductivity of 0.019  $\text{S cm}^{-1}$  at 600°C [17]. The SEM images also reveal the granular growth of the composite cathode at 1150°C, which resulted in a remarkable change in porosity and surface area of the cathode. The cathode sintered at 950°C was more porous and less sintered than the cells sintered at higher temperatures. However, the 950°C cathode was also thinner and had a less uniform thickness that may also have caused a difference in the performance.

Xia *et al.* [2] conducted a similar study. They found that the SDC cell with 950°C sintered composite cathode showed the highest performance. The difference for  $T_{s,c}$  could be attributed to the composition difference of the composite cathodes. In the reference [2], the composite cathode contained 10wt%SDC, while 25wt%SDC was used in this study. It seems that an increase in sintering temperature may be needed to accommodate an increasing SDC content in the composite cathode for cathode optimization. In fact, the total electrode resistance  $R_{p,a+c}$ , consisting of anode resistance  $R_{p,a}$  and cathode resistance  $R_{p,c}$  obtained in this study is only 0.102  $\Omega\text{cm}^2$ , which is just slightly over half of the reported 0.18  $\Omega\text{cm}^2$  for an SSC+SDC composite cathode at 600°C [2].

### 4.3.5 Effects of cathode thickness

Another study was performed to understand the influence of the cathode thickness on the cell performance. Composite cathodes SSC#3 sintered at 1000°C were investigated. Meanwhile, the influence of contact pastes on the measured cell performance was also studied. Four cathodes of different thicknesses were prepared by using different spacer thicknesses. The 12 cells used in this study are shown in Figure 4-6. The cathode area is designed for 0.50cm<sup>2</sup>, with variation within 5% in practice. Optical microscopy reveals cathode cracks after sintering (see Figure 4-7).

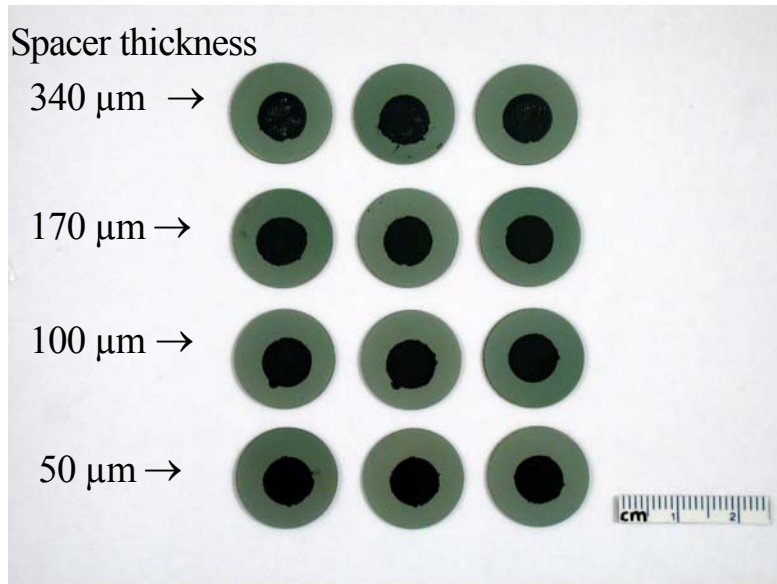


Figure 4-6 Appearance of the cells before testing in this study.

Table 4-4 lists the spacer thickness for the stencil printing of the cathodes, the cathode loading, and average thickness and after sintering at 1000°C for 2hr. It can be seen that the final cathode thickness after sintering is approximately 1/3 of the spacer thickness, indicating a shrinkage of approximately 67%. The calculated porosity ( $p$ ) of the cathode is approximately 62%, based on the loading and measured thickness of each cathode, calculated using the following Equation 5-1.

$$p = 1 - D_c/D_{th} = 1 - W_c/\delta_c/D_{th} \quad \text{Equation 5-1}$$

Here,  $p$  is the porosity,  $D_{th}$  is the cathode material density (6.64 g/cm<sup>3</sup> for SSC#3 in this study),  $D_c$  is the cathode apparent density,  $W_c$  is the cathode loading per cm<sup>2</sup>, and  $\delta_c$  is the cathode thickness.

Table 4-4 Cathode loading and average thickness and the spacer thickness for the stencil printing of cathode after sintering at 1000°C for 2hr

Spacer thickness [ $\mu\text{m}$ ]	50	100	170	340
Cathode	SSC3#: 75wt%SSC+25wt%SDC ( $D_{\text{th}}$ : 6.64g/cm <sup>3</sup> )			
Average loading, $W_c$ [mg cm <sup>-2</sup> ]	5.43	8.27	11.81	23.06
Average thickness, $\delta_c$ [ $\mu\text{m}$ ]	14.5	28.6	50.8	111.2
Calculated porosity, $p$ [%]	62	56	65	68
Porosity [%] from SEM image analysis	40-45			
Substrate density [g cm <sup>-3</sup> ]	5.10			
Porosity after NiO reduction [%]	38			

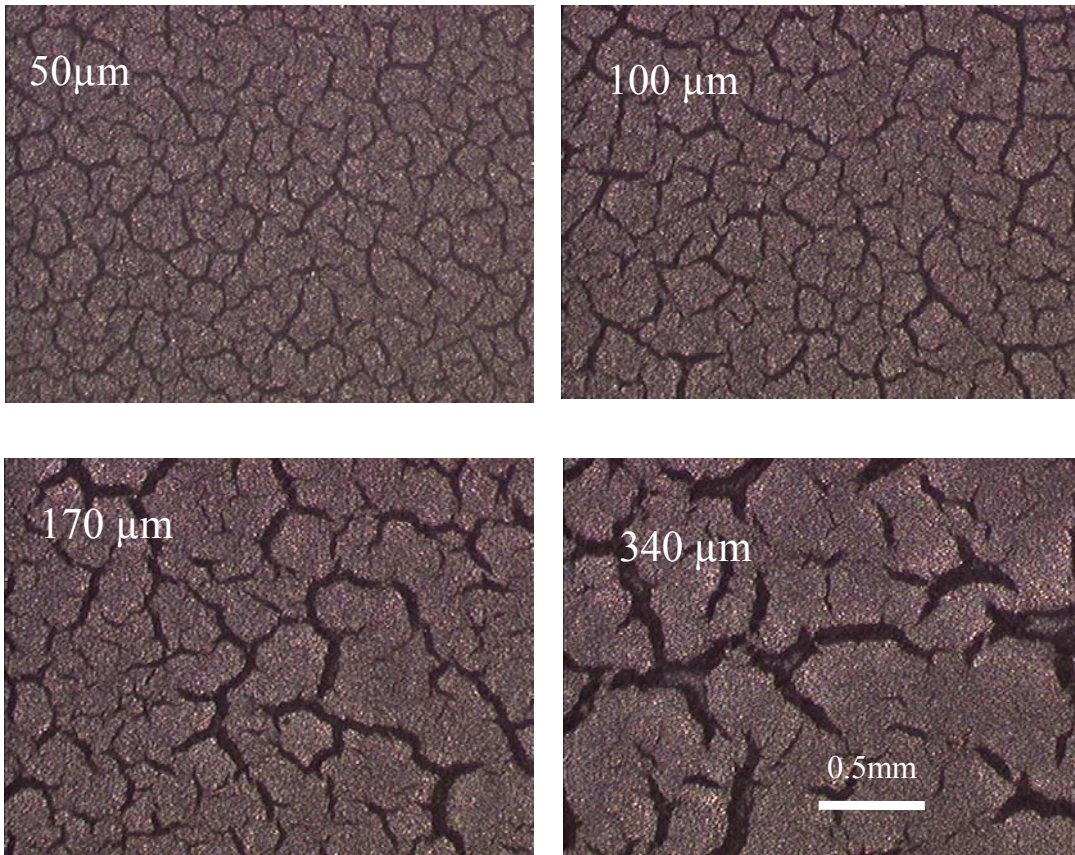


Figure 4-7 Optical microscope images of SSC+SDC cathodes made with different spacer thicknesses after sintering.

From Figure 4-7, it is clear that due to the large shrinkage of the cathode during the drying and sintering, mud-cracking patterns appear in all samples. The width of macro-cracks increases with the cathode thickness. Some cathode layer spallation was observed with the cathode prepared by using a 340 $\mu\text{m}$ -spacer, indicating that the thermal stress exceeds the interfacial bonding strength when the cathode is too thick. Because of the cathode edge thinning effect (see Figure 4-8, a profilometry profile of a sintered cathode) and the existence of the macro-cracks (see Figure 4-7), the calculated cathode porosity in Table 4-4 could be overestimated. SEM image analysis reveals 40-45% porosity for the cathode. Figure 4-9 shows the peak power densities of the cells with different cathode thickness, tested at 600°C without or with contact paste#1 (pure SSC). The highest performance was achieved with a cathode thickness of approximately 50 $\mu\text{m}$ , i.e., using a spacer of approximately 170 $\mu\text{m}$ . A slight performance improvement with contact paste was also observed. The resistances of the cell and peak power density (PPD) results are summarized in Table 4-5.

Table 4-5 Resistances and PPDs of cells with different cathode thicknesses operating at 600°C

Spacer thickness [ $\mu\text{m}$ ]	Without contact paste				With contact paste#1(SSC)			
	$R_s$ [ $\Omega \text{ cm}^2$ ]	$R_{p,a+c}$ [ $\Omega \text{ cm}^2$ ]	$R_t$ [ $\Omega \text{ cm}^2$ ]	PPD [ $\text{W cm}^{-2}$ ]	$R_s$ [ $\Omega \text{ cm}^2$ ]	$R_{p,a+c}$ [ $\Omega \text{ cm}^2$ ]	$R_t$ [ $\Omega \text{ cm}^2$ ]	PPD [ $\text{W cm}^{-2}$ ]
50	0.147	0.177	0.324	0.598	0.093	0.131	0.224	0.714
100	0.110	0.148	0.258	0.825	0.105	0.143	0.248	0.831
170	0.117	0.136	0.253	0.856	0.093	0.118	0.211	0.861
340	0.118	0.163	0.281	0.717	0.147	0.137	0.284	0.736

Note:  $R_t = R_s + R_{p, a+c}$

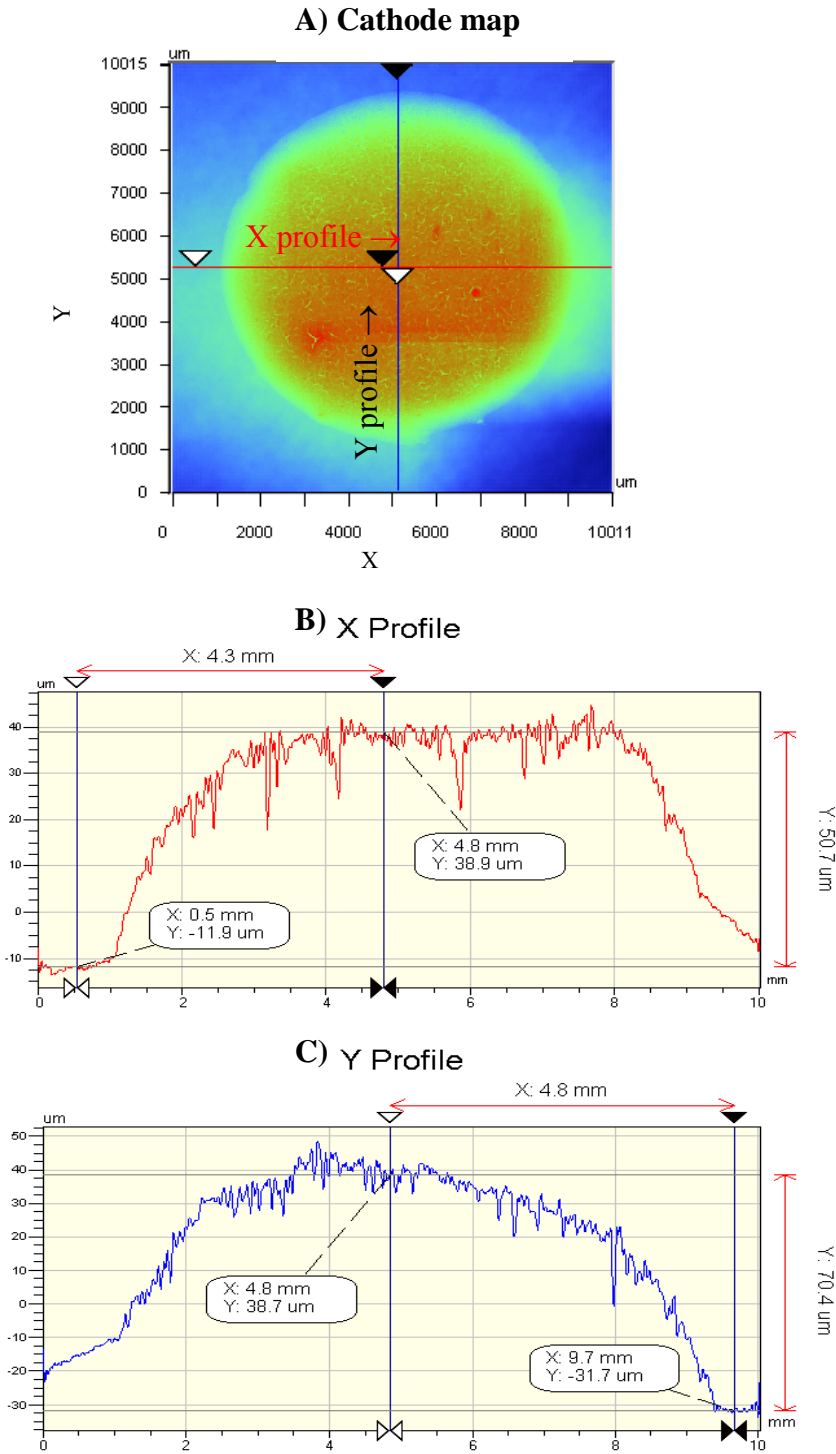


Figure 4-8 Typical surface height profiles of an SSC#3 cathode (prepared with 170  $\mu\text{m}$  spacer, after sintering) characterized with a profilometer.

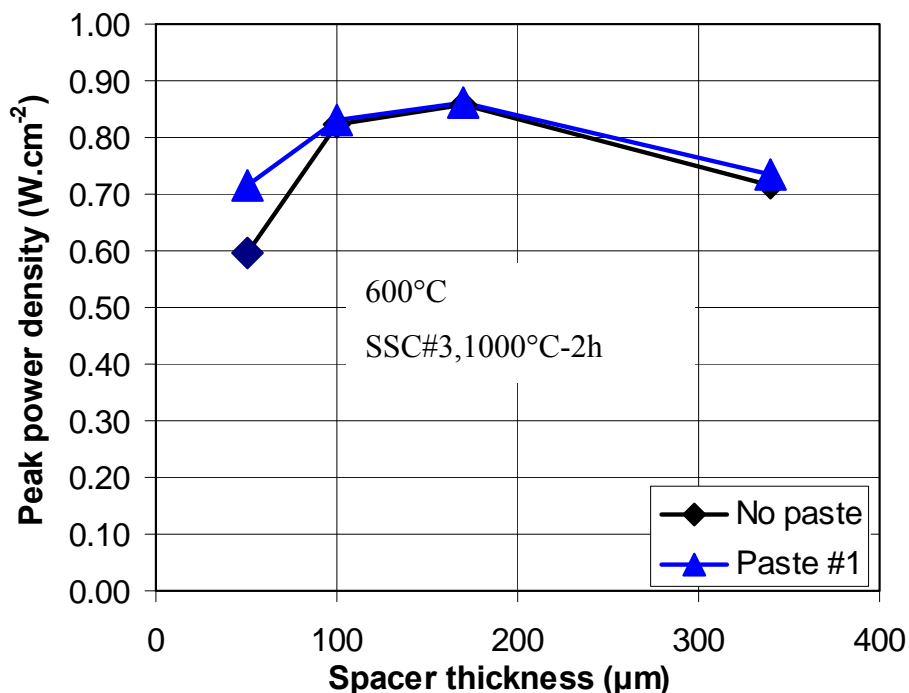


Figure 4-9 Cell peak power density vs. different cathode spacer thicknesses.

### 4.3.6 Effects of wet contact pastes

The cell with the cathode prepared by using a 170μm spacer was tested repeatedly with or without wet contact paste. The results at 600°C are shown in Figure 4-10. The related series resistance  $R_s$ , polarization resistance  $R_{p,a+c}$ , and cell total resistance  $R_t (= R_s + R_{p,a+c})$  from EIS measurement under OCV condition are summarized in Table 4-6. Paste #1 to #3 stands for the number of times the wet paste applied to this cell. For example, paste#2 meant the cell was applied a wet paste the 2<sup>nd</sup> time, after three tests: 1) no paste, 2) with the 1<sup>st</sup> wet paste (paste#1), and 3) the 1<sup>st</sup> wet paste was removed (Paste removed). The  $R_{cell}$  values in the Table 4-6 were obtained from fitting the I-V curves in the voltage range of OCV-0.75V. The recorded OCV values of the cell during the repeated tests are relatively stable between 0.858V to 0.852V. The effect of applying wet contact paste on the enhancement of cell performance is obvious. The  $R_s$  values with wet paste are smaller than

those without paste. Some possible explanations for that are: (1) The contact resistances (reflected in the  $R_s$  values) between the cathode and the Pt mesh (as cathode current collect) are reduced, which is evident from the EIS measurement results (see Table 4-6). The reason could also be that the potential existence of gaps between the wavy surface of a cathode and the Pt mesh was effectively reduced by the wet paste. (2) The effective cathode area was increased due to the wet paste filling in the macro-cracks to bridge the isolated cathode units together. This effect contributes to both the reduction in  $R_s$  and  $R_p$ . In this study, #45 platinum mesh, i.e., 45 openings per square inch, was used. It has an open area of approximately 42 %, and a gap between two adjacent wires of approximately 0.40-0.45 mm (cf. Figure 4-11). It is clear that the gaps between the Pt wires are in a similar dimensional range of a cathode unit isolated by the macro-cracks (see the cathode morphology Figure 4-7). Therefore, without the contact paste, it is possible that the platinum mesh may not contact every isolated cathode unit.

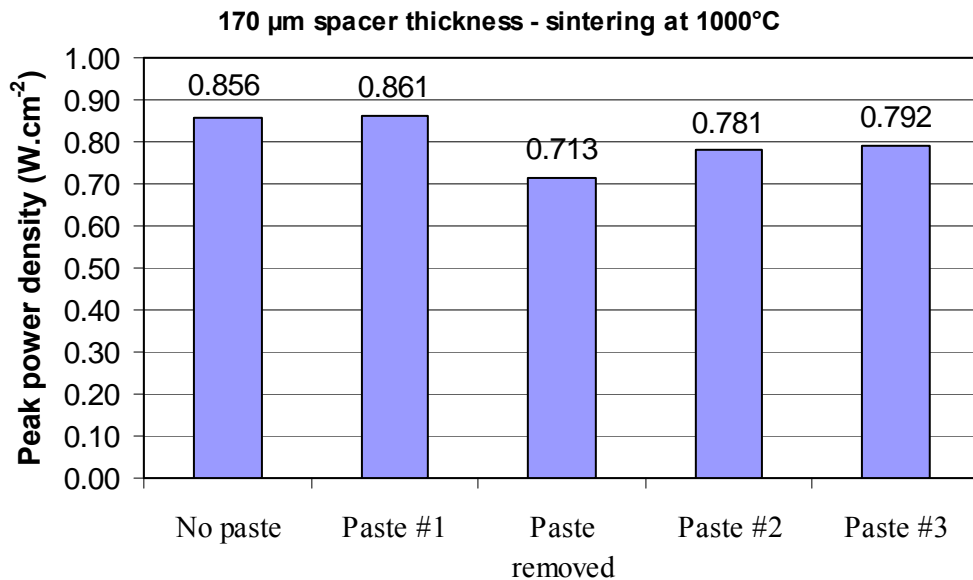
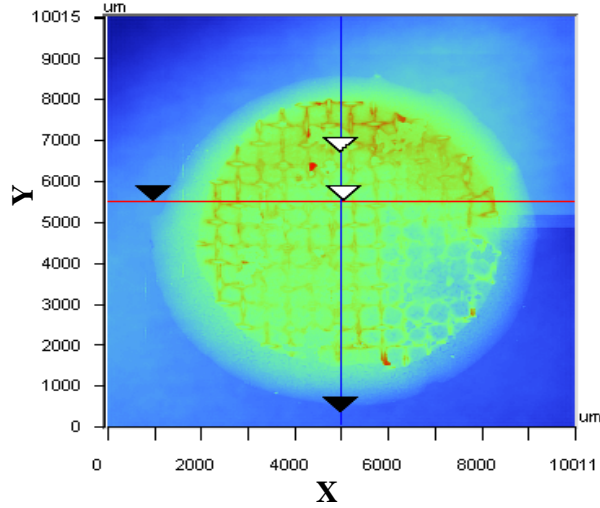
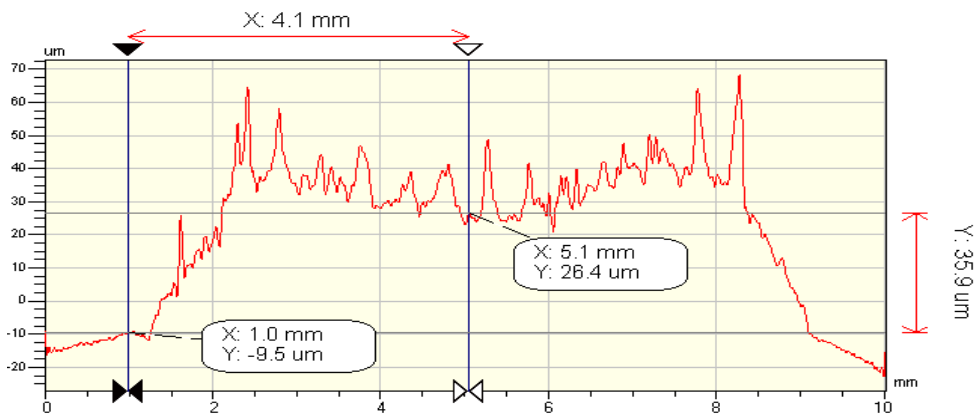


Figure 4-10 Peak power density of the cell with 1000°C-sintered SSC#3 composite cathode, tested repeatedly with or without contact pastes.

**A) Map of a cathode with wet paste after test, Pt mesh mark**



**B) X Profile**



**C) Y Profile**

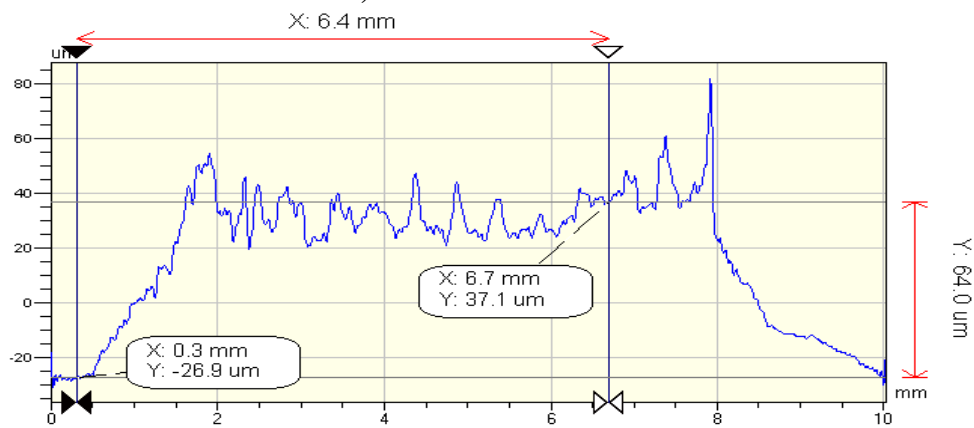


Figure 4-11 Typical cathode with contact paste after cell testing.

Table 4-6 EIS resistances measured for the cell with 1000°C SSC#3 cathode using 170µm spacer, tested at 600°C

<b>EIS resistance [Ω cm<sup>2</sup>]</b>	<b>No paste</b>	<b>Paste#1</b>	<b>Paste removed</b>	<b>Paste #2</b>	<b>Paste #3</b>
R <sub>s</sub>	0.117	0.093	0.199	0.079	0.083
R <sub>p,a+c</sub>	0.136	0.118	0.363	0.119	0.112
R <sub>t</sub>	0.253	0.211	0.562	0.198	0.195
R <sub>cell</sub>	0.204	0.215	0.261	0.244	0.239
OCV [V]	0.858	0.858	0.854	0.852	0.855

#### **4.4 Conclusions**

High performance of cermet supported thin SDC electrolyte SOFCs operating below 600°C was achieved by using a composite cathode, with 75wt%SSC + 25wt%SDC. The highest performance of the cells was observed for a cathode sintering temperature of 1050°C. The measured SDC electrolyte area-specific resistance R<sub>s</sub>, for the electrolyte of thickness 20µm was 0.128 Ωcm<sup>2</sup>. The total electrode polarization resistance R<sub>p, a+c</sub> was only 0.102 Ωcm<sup>2</sup> at 600°C.

The study on the composite cathode thicknesses ranging from 15 to 110µm and sintered at 1000°C reveals the best cell performance, 0.86 W cm<sup>-2</sup> peak power density operating at 600°C, with the average cathode thickness of 50µm. The SDC electrolyte resistance R<sub>s</sub> was 0.093 Ω cm<sup>2</sup> for the electrolyte of thickness 10-15µm, and the total electrode polarization R<sub>p,a+c</sub> was 0.118 Ω cm<sup>2</sup> at 600°C. It was found that with cathode contact paste the individual cell performance could be slightly improved. The contact paste not only reduced the ohmic loss of the total cell but also the electrode reaction resistance, i.e., cathode in this study.

## 4.5 References

1. T. Tsai and S. A. Barnett, *Solid State Ionics* 98 (1997) 91.
2. C. R. Xia, W. Rauch, F. L. Chen, M. L. Liu, *Solid State Ionics* 149 (2002) 11.
3. Z. Tang, Y. Xie, H. Hawthorne and D. Ghosh, *J. Power Sources* 157 (2006) 385.
4. S. Zha, W. Rauch and M. Liu, *Solid State Ionics* 166 (2004) 241.
5. W. Wang, M. Mogensen, *Solid State Ionics* 176 (2005) 457.
6. Z. Shao, S. M. Haile, *Nature* 431 (2004) 170.
7. E. P. Murray and S. A. Barnett, *Solid State Ionics* 148 (2002) 27.
8. C. R. Xia, M. L. Liu, *J. Am. Ceram. Soc.* 84 (8) (2001) 1903.
9. C. R. Xia, F. L. Chen, M. L. Liu, *Electrochem. Solid-State Lett.* 4 (5) (2001) A52.
10. C. R. Xia, M. L. Liu, *Solid State Ionics* 144 (2001) 249.
11. I. C. Fullarton, J. A. Kilner, B. C. H. Steele, P. H. Middleton, *Ionic and mixed conducting ceramics*, in: T.A. Ramanarayanan, W.L. Worrell, H.L. Tuller (Eds.), 2nd International Symposium, The Electrochemical Society, 94-12 (1994) 9.
12. H. Y. Tu, Y. Takeda, N. Imanishi, O. Yamamoto, *Solid State Ionics* 100 (1997) 283.
13. T. Ishihara, M. Honda, T. Shibayama, H. Minami, H. Nishiguchi, Y. Takita, *J. Electrochem. Soc.* 145 (1998) 3177.
14. L. A. Chick, L. R. Pedersen, G. D. Maupin, J. L. Bates, L. E. Thomas, G. J. Exarhos, *Mater. Lett.* 10 (1990) 6.
15. T. Matsui, T. Kosaka, M. Inaba, A. Mineshige and Z. Ogumi, *Solid State Ionics* 176 (2005) 663.
16. M. Liu, *Ionic and mixed conducting ceramics*, in: T. A. Ramanarayanan, H. L. Tuller (Eds.), 1st International Symposium, The Electrochemical Society, vol. 91-12, 1991, p.191.
17. V. V. Kharton, F. M. B. Marques and A. Atkinson, *Solid State Ionics* 174 (2004) 135.

## 5. Chapter Five. Internal Shorting and Fuel Loss of an LTSOFC with SDC Electrolyte<sup>5</sup>

A solid oxide fuel cell with  $\text{Sm}_{0.2}\text{Ce}_{0.8}\text{O}_{1.9}$  (SDC) electrolyte of  $10\mu\text{m}$  in thickness and Ni-SDC anode of  $15\mu\text{m}$  in thickness on a  $0.8\text{mm}$  thick Ni-YSZ cermet substrate was fabricated by tape casting, screen printing, and co-firing. A composite cathode of 75 wt%  $\text{Sm}_{0.5}\text{Sr}_{0.5}\text{CoO}_3$  (SSC) + 25 wt% SDC and approximately  $50\mu\text{m}$  in thickness was printed on the co-fired half-cell and sintered at  $950^\circ\text{C}$ . The cell showed a high electrochemical performance at temperatures ranging from  $500$  to  $650^\circ\text{C}$ . Peak power density of  $545\text{ mW cm}^{-2}$  at  $600^\circ\text{C}$  was obtained. However, the cell exhibited severe internal shorting due to the mixed conductivity of the SDC electrolyte. Both the amount of water collected from the anode outlet and the open circuit voltage (OCV) indicated that the internal shorting current could reach  $0.85\text{ A cm}^{-2}$  or more at  $600^\circ\text{C}$ . Zr-content inclusions were found at the surface and in the cross-section of the SDC electrolyte, which could be one of the reasons for reduced OCV and oxygen ionic conductivity. Fuel loss due to internal shorting of the thin SDC electrolyte cell becomes a significant concern when it is used in applications requiring high fuel utilization and electrical efficiency.

### 5.1 Introduction

Solid oxide fuel cells (SOFC) have been recognized as a promising energy conversion technology in terms of cleanliness, efficiency, and ability to work with various fuels. During the last decade, Nickel-Yttria Stabilized Zirconia (Ni-YSZ) anode supported solid oxide fuel cells (SOFCs) with thin-film electrolytes have been widely adopted by industrial pioneers and research groups throughout the world. Encouraging performance in the intermediate temperature range ( $700\text{--}800^\circ\text{C}$ ) with thin-film YSZ electrolytes has been

---

<sup>5</sup> A version of this chapter has been published as:

X. Zhang, M. Robertson, C. Decès-Petit, W. Qu, O. Kesler, R. Maric, D. Ghosh, Internal shorting and fuel loss of a low temperature solid oxide fuel cell with SDC electrolyte, *Journal of Power Sources*, 164 (2007) 668.

achieved [1]. However, a high degradation rate in stack performance has been observed, which is unacceptable for commercial application [2]. Thermally activated material degradation, and in particular, high temperature corrosion of Fe-Cr steel interconnects, has been identified as a serious problem [2, 3]. To date, extensive R&D efforts have been focused on decreasing cell operating temperatures below 600°C in order to expand lifetime and to reduce the cost of SOFCs [4-7].

The practical operating temperature of an SOFC is mainly determined by the conductivity and thickness of the electrolyte. Doped ceria is a promising option for an electrolyte material for low temperature use. It has an ionic conductivity that is 2-3 times higher than that of YSZ. Its thermal expansion coefficient ( $12.5 \times 10^{-6} \text{ K}^{-1}$ ) is much closer to that of the Ni-cermet substrate and commercial ferritic stainless steel interconnects, compared with YSZ ( $10.5 \times 10^{-6} \text{ K}^{-1}$ ). Moreover, it has better chemical compatibility with high performance cobalt-containing cathodes, such as  $\text{Sm}_{0.5}\text{Sr}_{0.5}\text{CoO}_3$  [4, 8],  $\text{La}_{0.6}\text{Sr}_{0.4}\text{Co}_{0.2}\text{Fe}_{0.8}\text{O}_3$  [9], and  $\text{Ba}_{0.5}\text{Sr}_{0.5}\text{Co}_{0.2}\text{Fe}_{0.8}\text{O}_3$  [10]. A maximum power density of  $1 \text{ W cm}^{-2}$  at 600°C with an anode-supported thin ceria based electrolyte cell has been reported [10]. The main disadvantage of a ceria-based electrolyte is that it becomes a mixed conductor in anodic conditions, which causes cell voltage loss and fuel efficiency loss due to internal shorting. Chemical and mechanical stability, thermal cycle capability, and redox tolerance are also concerns for long-term service.

In the present work, an anode supported, thin SDC electrolyte cell was used for internal shorting and fuel loss investigations. It was found that although the cell showed a fairly high maximum power density of  $545 \text{ mW cm}^{-2}$  at 600°C, it also showed severe internal shorting due to the mixed conductivity of the SDC electrolyte of the cell. Fuel loss due to internal shorting of the thin SDC electrolyte cell could impede its use in practical applications requiring high fuel efficiency.

## **5.2 Experimental procedure**

### *Cell Fabrication*

A NiO-YSZ cermet substrate supported  $\text{Sm}_{0.2}\text{Ce}_{0.8}\text{O}_{1.9}$  (SDC) electrolyte SOFC was used. The cell was fabricated by tape-casting the substrate, screen-printing the anode and

then the electrolyte on the substrate tape, and co-firing at 1400°C for 2 hrs, followed by cathode printing and sintering at 950°C for 2 hrs. Further details about the cell fabrication process can be found in Chapter 3 and in [21]. Figure 5-1 shows a schematic diagram of the cell structure, which consists of a NiO-YSZ cermet substrate (0.8 mm), NiO-SDC anode layer (15µm), SDC electrolyte (10µm), and SSC#3 composite cathode (50µm). A 57 wt% NiO + 43 wt% YSZ powder mixture was used for the NiO-YSZ cermet substrate. The composition of the NiO-SDC anode was 53 wt% NiO + 47 wt% SDC. The cell used in this study was 27.5 mm in diameter. The edge of the cell was sealed with alkaline borosilicate glass (Corning #0211, treated at 750°C). The SDC electrolyte after glass sealing had an effective area of 5.23 cm<sup>2</sup>. The SSC#3 composite cathode consists of 75wt% Sm<sub>0.5</sub>Sr<sub>0.5</sub>CoO<sub>3</sub> (SSC) and 25wt% SDC. The SSC#3 cathode area was 1.35 cm<sup>2</sup>. Cells with and without cathodes were investigated.

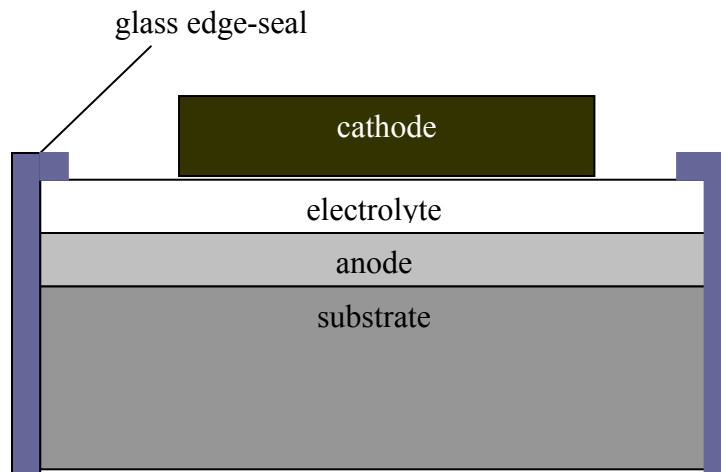


Figure 5-1 Schematic of cell structure.

### *Cell characterization*

The 1400°C-sintered electrolytes appeared transparent, crack-free, and allowed no detectable helium gas cross leakage at 13.8 kPa (approximately 2 psi), indicating that the electrolyte layers were fully dense. The measured cell density (by an Archimedes density measurement) was 5.20 g cm<sup>-3</sup>, which corresponds to 18.2% porosity in the NiO-YSZ cermet substrate based on the cermet substrate composition of 57.0 wt% NiO. The substrate porosity would be increased to approximately 36.4% porosity after NiO reduction to Ni. The porosity of the SSC#3 cathode is approximately 40 % after sintering at 950°C.

Figure 5-2 shows a schematic setup for button cell electrochemical tests. A split-tube furnace (Thermcraft Incorporated, USA) was used for cell temperature control. The thermocouple for furnace temperature control was located less than 1mm behind the cell at the anode side ( $T_a$ ). There were also two additional thermocouples, one located in the furnace chamber for overheating protection ( $T_f$ ), and the other contacting the electrolyte surface of the cell at the cathode side ( $T_c$ ). The cells were mounted for electrochemical testing at the end of an alumina tube with inner diameter of 18mm, and sealed with a borosilicate glass seal at the anode side. A thin layer of cathode paste was applied to the cell cathode to create a good contact between the cathode and the cathode current collector (Pt mesh) in the testing apparatus. A constant spring loaded force was applied to the cathode air supply alumina tube, of approximately 1.5 kg force. The cell was heated up to 750°C at a ramp rate of 180°C h<sup>-1</sup>, and held for 12h for glass seal softening and crystallization to reach an anodic hermetic sealing as well as cathodic contact paste *in-situ* sintering. The temperature was then decreased to 650°C for anode reduction and cell electrochemical measurements. Ambient air was introduced at a flow rate of 100 ml min<sup>-1</sup> to the cathode side. During the cell reduction, a combination of nitrogen and hydrogen as anode gas at the total flow rate of 100 ml min<sup>-1</sup> was first passed through a bubbler-type humidifier at room temperature, corresponding to approximately 3% H<sub>2</sub>O content, and then introduced to the anode side. The gas combination used 5 different hydrogen concentrations during the cell reduction process: 10%H<sub>2</sub> for 0.5hr, 20%H<sub>2</sub> for 0.5hr, 40%H<sub>2</sub> for 1hr, 60%H<sub>2</sub> for 0.5hr, and finally 100%H<sub>2</sub>. The outlet of the anode gas was passed through a bottle at room temperature before being vented. After the cell reduction and performance test, the water produced during the reduction and performance test was discarded. The anode outlet was then connected to a dry container for water collection. Water was collected at each cell test temperature for 20 hrs. No current was drawn from the cell during water collection, except for the test at 600°C. At 600°C, conditions both without and with current were tested.

Electrochemical measurements were performed at temperatures ranging from 650 to 500°C under ambient pressure. Cell performances were measured with a Multi-channel Potentiostat/Galvanostat (Solartron 1480 8 channel multi-stat) with a computer interface and Corrview software. The I-V curves and power curves were obtained using linear sweep

voltammetry at a sweep rate of  $4 \text{ mV s}^{-1}$  from open circuit voltage (OCV) to 0.3 V. The electrochemical impedance spectra (EIS) were typically measured in the frequency range from 65kHz to 0.1Hz with 50mV perturbation amplitude using a Solartron 1250 FRA with computer interface and *Z-view* software. The cell resistance ( $R_{\text{cell}}$ ) was calculated using data fitting from the I-V curve, and the electrolyte resistance ( $R_{\text{el}}$ ) and electrode polarization resistance ( $R_{\text{p}}$ ) were calculated using EIS data fitting. The electrochemical measurements were performed before and after water collection.

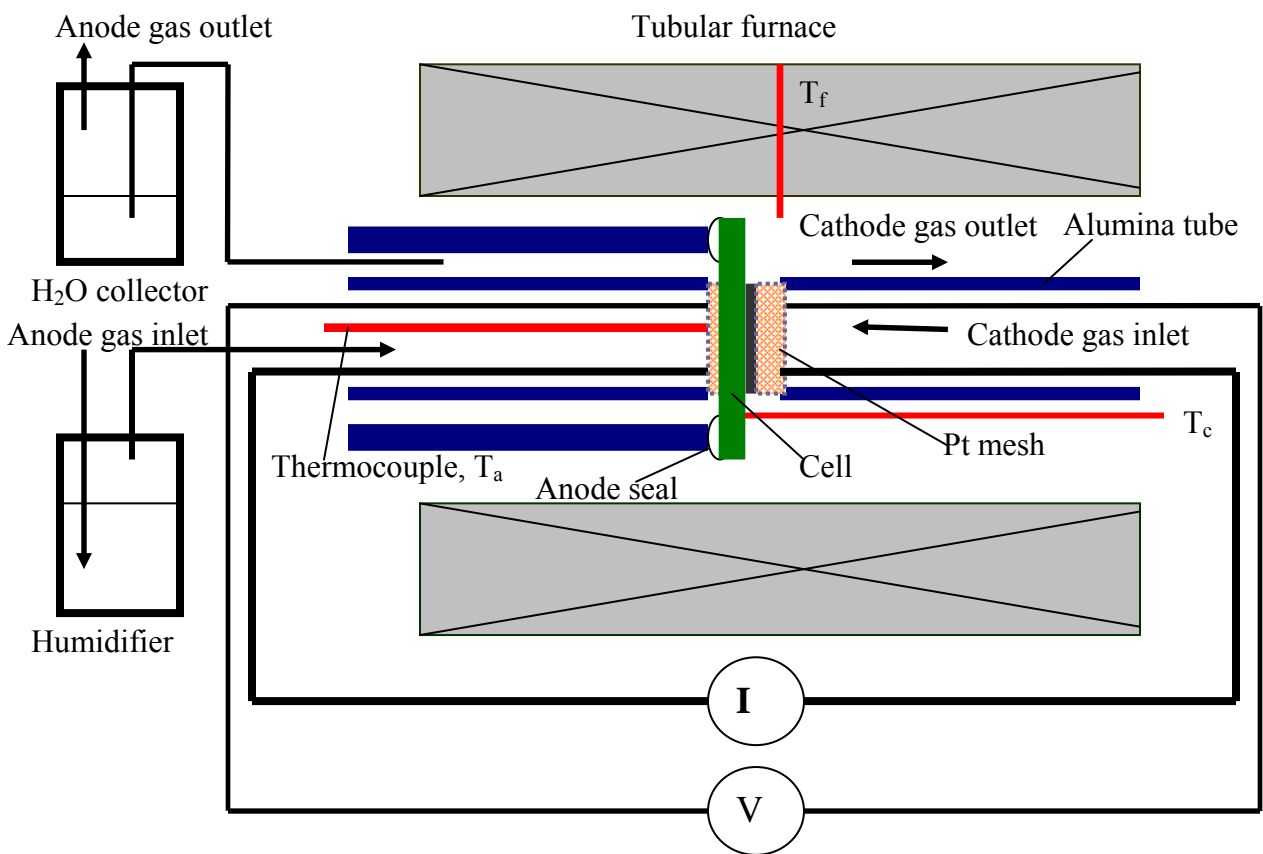


Figure 5-2 Schematic of experimental setup.

The morphologies of the tested cells were observed using a scanning electron microscope (SEM, Hitachi S-3500N, Japan), coupled with energy dispersive spectrometry (EDS) and X-ray diffraction techniques for elemental and phase analysis, respectively. The SEM sample for cross-section observation was embedded in epoxy resin and polished. Each sample was coated with Au-Pd alloy before observation.

## 5.3 Results and discussion

### 5.3.1 Cell electrochemical performance

Figure 5-3 shows the OCV of the cell in this study at different temperatures along with the Nernst potential ( $E_N$ ).  $E_N$  was calculated based on the temperature and reactant gas composition (97% $H_2$ +3% $H_2O$  for anode and 21%  $O_2$  in air for cathode, both at 1 atm), under an assumption that the entropy of the reactants is independent of temperature. The thermodynamic properties of the reactants were sourced from Lange's Handbook (15<sup>th</sup> edition). Different thicknesses and theoretical OCV of an SDC electrolyte from the literature [4, 11, 21] are also presented in this Figure. The theoretical OCV values in Figure 5-3 were obtained by multiplying the Nernst potentials by the ionic transference numbers of the SDC electrolyte at different temperatures [11].

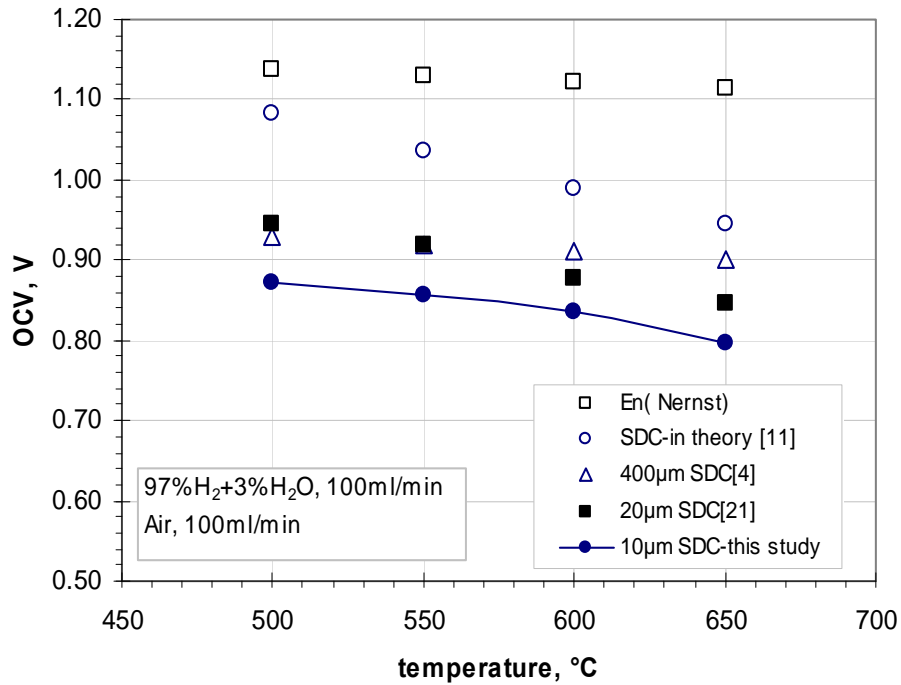


Figure 5-3 OCV of the SDC electrolyte cells at different temperatures.

As shown in Figure 5-3, the recorded OCV value in this study decreased from 0.873 V at 500°C to 0.796 V at 650°C. It is well known that electronic conductivity in the SDC electrolyte is increased at high temperatures under anodic fuel atmospheres, leading to a decrease in OCV at a higher temperature. However, the recorded OCV data in this study

were lower than those reported with thick SDC electrolytes. The reported OCVs were 0.98 V and 0.94 V at 600°C for SDC electrolyte-supported cells of SDC electrolyte thicknesses 2.2 mm and 1.19 mm respectively [11], and only 0.91 V for a 0.4 mm thick SDC cell [4], 0.87 V for a cermet-supported 20 $\mu$ m thick SDC cell [21], and 0.835 V for the 10  $\mu$ m thick SDC electrolyte cell used in this study. The explanation of the variation of OCV with thickness of the SDC electrolyte can be either that fewer defects span the entire thickness of the thick electrolyte, resulting in higher gas-tightness in the thicker electrolytes, or that the distribution of partial pressure of oxygen inside the electrolyte is thickness-dependent, causing the OCV to decrease with decreasing thickness due to an increase in the electronic conductivity. The widening deviation of the real OCV from the theoretical OCV of the SDC electrolyte at lower temperatures, as shown in Figure 5-3, may also result in part from the increasing electrode polarization resistance. As reported by Miyashita [12] and Liu [13], the electrode polarization also contributes to the total cell voltage loss even at OCV, especially when operating at lower temperature.

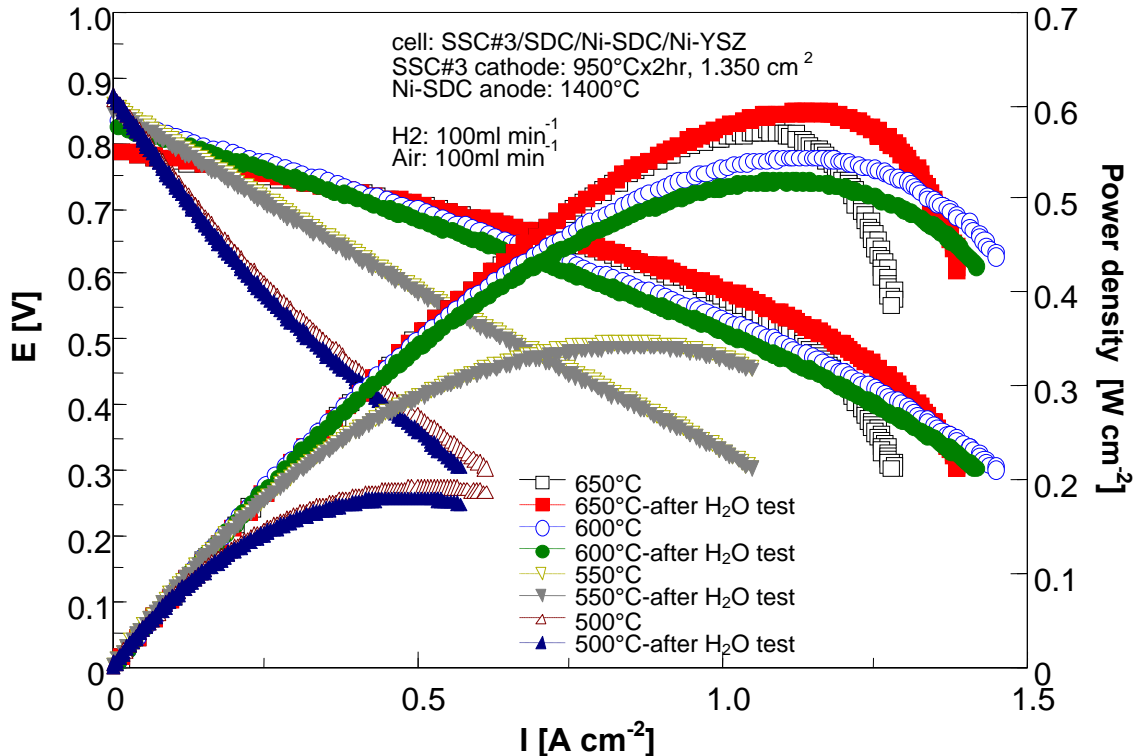


Figure 5-4 Cell performance at different temperatures.

Figure 5-4 shows the performance of the cell before and after water collection tests at different temperatures. It can be seen that the maximum power densities reached  $595 \text{ mW cm}^{-2}$  at  $650^\circ\text{C}$ ,  $545 \text{ mW cm}^{-2}$  at  $600^\circ\text{C}$ , and  $347 \text{ mW cm}^{-2}$  at  $550^\circ\text{C}$ . It was noticed that there was less than a  $2^\circ\text{C}$  difference between the cathode temperature ( $T_c$ ) and the anode temperature ( $T_a$ , the setting temperature for the cell test). However, a slight increase (at most  $5^\circ\text{C}$ ) in both  $T_a$  and  $T_c$  were observed during the I-V curve measurement, which took approximately 2-3 minutes. It was also noticed that when the hydrogen was first introduced to the anode side for cell reduction, the furnace temperature ( $T_f$ ) could drop to  $10\text{-}15^\circ\text{C}$  lower than before the hydrogen introduction. The drop of the furnace temperature ( $T_f$ ) could only be explained by heating of the cell, thus requiring less heat flow from the furnace to maintain the operating temperature ( $T_a$ ). The obvious temperature deviation indicated that the cell was generating heat even at the open circuit condition.

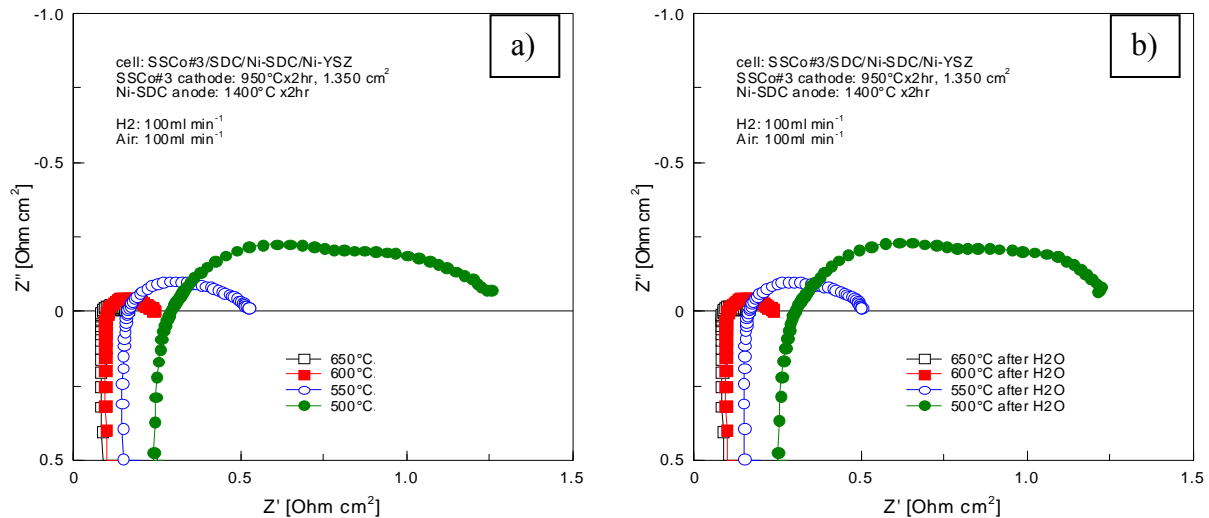


Figure 5-5 EIS of the cell at different temperatures, a) before water test, b) after water test

Figure 5-5 a) and b) show the electrochemical impedance spectra (EIS) of the cell at different temperatures before and after water collection tests. The performance of the cell is summarized in Table 5-1 and Table 5-2. The area-specific resistances of the cell ( $R_{\text{cell}}$ ) were obtained from the I-V curves (Figure 5-4) in the linear range from OCV to  $0.75 \text{ V}$ , and both electrolyte resistance ( $R_{\text{el}}$ ) and electrode polarization resistance ( $R_{\text{p,a+c}}$ , including

both anode and cathode) values were obtained from EIS results by using instant data fitting with *Corrview* and *Z-view* software. The cell area-specific resistance from EIS is  $R_t$ , which is the sum of  $R_{el}$  and  $R_{p,a+c}$ . It is notable that the sum of  $R_t$  is approximately equal to the  $R_{cell}$  value at the temperatures tested.

Table 5-1 Cell performance and EIS results at different temperatures before water test

<b>Temperature</b> [°C]	<b>OCV</b> [V]	<b>PPD</b> [W cm <sup>2</sup> ]	<b>R<sub>el</sub></b> [Ω cm <sup>2</sup> ]	<b>R<sub>p,a+c</sub></b> [Ω cm <sup>2</sup> ]	<b>R<sub>t</sub></b> [Ω cm <sup>2</sup> ]	<b>R<sub>cell</sub></b> [Ω cm <sup>2</sup> ]
650	0.796	0.575	0.073	0.066	0.139	0.152
600	0.835	0.545	0.099	0.133	0.232	0.265
550	0.857	0.347	0.152	0.361	0.513	0.570
500	0.873	0.193	0.268	0.970	1.238	1.258

OCV: open circuit voltage,

PPD: maximum power density,

$R_{el}$ : SDC electrolyte ohmic resistance from EIS,

$R_{p,a+c}$ : electrode electrochemical resistance from EIS,

$R_t$ : cell resistance from EIS ( $R_t = R_{el} + R_{p,a+c}$ ),

$R_{cell}$ : cell resistance from I-V curve (data fitting from OCV to 0.75V)

Table 5-2 Cell performance and EIS results at different temperatures after water test

<b>Temperature</b> [°C]	<b>OCV</b> [V]	<b>PPD</b> [W cm <sup>2</sup> ]	<b>R<sub>el</sub></b> [Ω cm <sup>2</sup> ]	<b>R<sub>p,a+c</sub></b> [Ω cm <sup>2</sup> ]	<b>R<sub>t</sub></b> [Ω cm <sup>2</sup> ]	<b>R<sub>cell</sub></b> [Ω cm <sup>2</sup> ]
650	0.792	0.595	0.071	0.070	0.141	0.156
600	0.831	0.521	0.098	0.130	0.228	0.277
550	0.852	0.341	0.155	0.342	0.496	0.555
500	0.875	0.181	0.282	0.959	1.241	1.336

OCV: open circuit voltage,

PPD: maximum power density,

$R_{el}$ : SDC electrolyte ohmic resistance from EIS,

$R_{p,a+c}$ : electrode electrochemical resistance from EIS,

$R_t$ : cell resistance from EIS ( $R_t = R_{el} + R_{p,a+c}$ ),

$R_{cell}$ : cell resistance from I-V curve (data fitting from OCV to 0.75V)

### 5.3.2 Water amount and leakage current

Figure 5-6 shows the water amount and leakage current calculated based on water amount. The leakage current was calculated simply based on Faraday's Law, under an assumption that the water amount collected during 20 hrs under the OCV condition resulted entirely from the internal shorting of the SDC electrolyte, and that the leakage current was constant over the 20-hour test period.

$$I_L = \frac{FW_w}{36000M_w} = 0.1489W_w \quad \text{Equation 5-1}$$

where  $I_L$  is the leakage current [A], F is Faraday's constant,  $W_w$  is the water amount [grams] accumulated during 20 hrs, and  $M_w$  is the molecular weight of water.

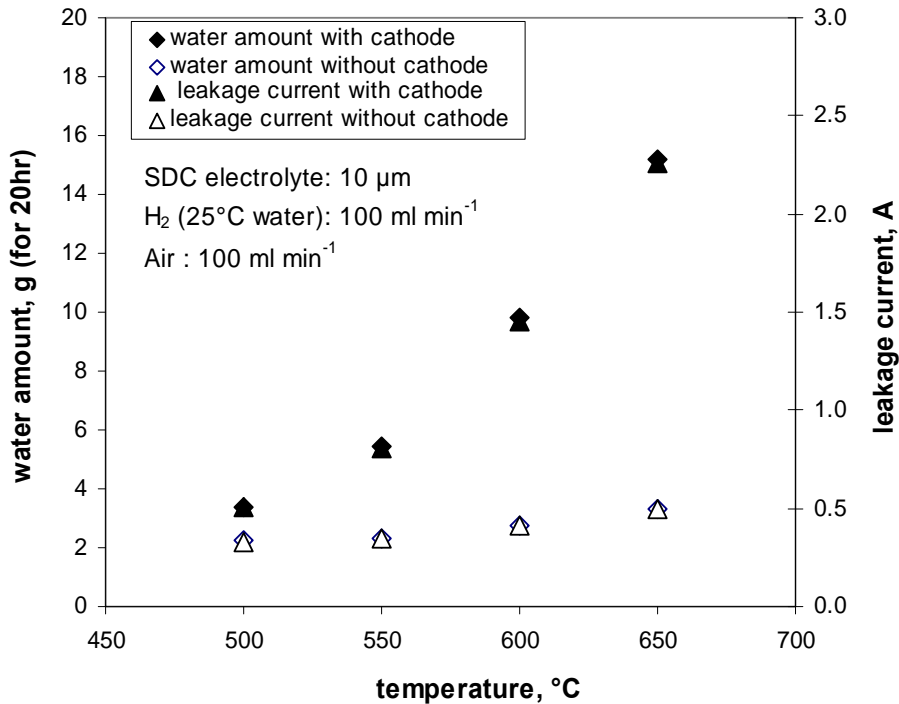


Figure 5-6 Water amount collected at anode gas outlet and leakage current at different cell temperatures, with and without the cathode.

It can be seen that both the water amount and the leakage current increased with the temperature. Astonishingly, the leakage current of the cell under the open circuit condition reached over 2.26 A at 650°C and 1.46 A at 600°C.

To clarify the cathode effect on the internal shorting, a cell from the same batch without a cathode was used for a similar water collection test under open circuit condition. The results of this test are also shown in Figure 5-6. It is clear that the water amount and leakage current density are tremendously decreased, reaching only 1/3 of the water amount of the cell with a cathode at 600°C. This result indicates that the internal shorting is not only dependent on the electronic conductivity of the SDC, but also on the kinetics of the oxygen reduction process. The cathode facilitates the oxygen reduction process and therefore greatly enhances the leakage current under open circuit conditions.

The cell with a cathode was also tested under a constant current density of 0.50A cm<sup>-2</sup> (0.675A) for 20 hrs at 600°C. The cell voltage under this condition is quite stable, approximately 0.69V. 11.9746 g water was collected during this period, corresponding to a leakage current of 1.108A.

In this study, the SDC electrolyte area of the cell without cathode was approximately 5.23 cm<sup>2</sup>. The SSC#3 cathode area was 1.35 cm<sup>2</sup>. We assume that the shorting current has two even distributions, one over the portion of the SDC electrolyte without the cathode, and the other over the whole cathode area. Based on Equations 5-1 to 5-4, the leakage current (I<sub>L</sub>) and leakage current density (i<sub>L</sub>), both with and without the cathode, can be calculated. The results are listed in Table 5-3.

Table 5-3 Water amount (for 20hr) and leakage current under open circuit condition at different temperatures and at 0.5 A cm<sup>-2</sup> at 600°C

Temperature [°C]	W <sub>w</sub> [g]	W <sub>w</sub> * [g]	I <sub>L</sub> [A]	I <sub>L</sub> * [A]	i <sub>L</sub> * [A cm <sup>-2</sup> ]	i <sub>c</sub> [A cm <sup>-2</sup> ]	i <sub>L</sub> [A cm <sup>-2</sup> ]
650	15.174	3.329	2.259	0.496	0.095	1.306	1.401
600	9.788	2.759	1.457	0.411	0.079	0.775	0.854
550	5.407	2.341	0.805	0.349	0.067	0.338	0.405
500	3.369	2.236	0.502	0.332	0.064	0.125	0.189
600#	11.975	2.759	1.783	0.411	0.079	1.016	0.595

\* without cathode, i<sub>L</sub> = i<sub>L</sub>\* + i<sub>c</sub>

# at 0.50 A cm<sup>-2</sup>, i<sub>L</sub> = i<sub>L</sub>\* + i<sub>c</sub> - 0.5

$$i_L^* = I_L^* / 5.23 \quad [A \text{ cm}^{-2}] \quad \text{Equation 5-2}$$

$$i_c = (I_L - I_L^*) / 1.35 \quad [\text{A cm}^{-2}] \quad \text{Equation 5-3}$$

$$i_L = i_L^* + i_c \quad [\text{A cm}^{-2}] \quad \text{Equation 5-4}$$

where  $I_L^*$  and  $i_L^*$  are leakage current and current density without the cathode,  $I_L$  and  $i_L$  are the leakage current and current density with the cathode, and  $i_c$  is the enhanced leakage current density at the cathode area due to the coverage of the SSC#3 composite cathode layer. From Table 5-3, it is clear that with the cathode, the leakage current density was increased almost 10 times in comparison to without the cathode at 600°C. The leakage current density dropped by up to 30% when the cell was operating at 0.5A cm<sup>-2</sup> at 600°C.

### 5.3.3 Internal shorting current density based on OCV deviation

A simple model is derived for the internal shorting current density calculation of the SDC cell, making use of the fact that the electrode overpotential  $\eta_s$  is typically small and linear with the current in SOFCs at operating temperatures. In general,

$$E = E_N - i (R_a + R_c + R_{int}) = V_0 - i R_t \quad \text{Equation 5-5}$$

where  $E$  is cell voltage,  $E_N$  is the Nernst potential of the cell reaction,  $i$  is the cell operating current density, and  $R_a$  and  $R_c$  stand for anodic and cathodic polarization resistance, respectively.  $R_{int}$  represents the internal ohmic resistance of the cell, which is typically approximated by the electrolyte resistance.  $R_t$  is the total resistance of the cell. All resistances are expressed as area-specific resistances [ $\Omega \text{ cm}^2$ ]. Under open circuit condition, Equation 5-5 changes to

$$\text{OCV} = E_N - i_L (R_a + R_c + R_{int}) = V_0 - i_L R_{t,cell} \quad \text{Equation 5-6}$$

where OCV is the cell open circuit voltage,  $i_L$  is the cell leakage current density.

The leakage current density  $i_{L, calc.}$  was calculated from Equation 5-6 by inserting the OCV value and cell resistance value,  $R_{t,cell}$  (an average of the cell resistances  $R_t$  and  $R_{cell}$  in Table 5-1 and Table 5-2). The results are listed in Table 5-4. The leakage current density based on the measured water amount,  $i_{L, meas.}$ , is also listed in this Table. It can be seen that  $i_{L, calc.}$  values are higher than  $i_{L, meas.}$  values, suggesting that the calculated leakage current density will be an overestimate using this simple model. This is due to the simple model neglecting the initial electrochemical overpotential loss of the electrodes. For a higher accuracy of data fitting, one can introduce non-linear Butler-Volmer equations for

the electrode over-potential calculations [16]. Here, we simply replace  $E_N$  with a parameter  $V_0$  in Equation 6-6 and do the fitting based on the  $i_{L, meas}$  value. It was found that the  $V_0$  values are in the range of 1.0 - 1.1 V. As we know, the  $V_0$  value for a YSZ electrolyte based SOFC is commonly in this range, and no leakage current is observed due to the pure ionic conductivity of YSZ. Sahibzada *et al* [18] developed a model to analyze the possible leakage current density of a 10 $\mu$ m- thick  $Gd_{0.1}Ce_{0.9}O_{1.95}$  electrolyte anode supported cell. Their calculation showed that  $i_L$  at OCV conditions could be as high as 0.610 A cm<sup>-2</sup> at 600°C, although they did not experimentally verify their model results. Results in this study clearly indicate that the leakage current densities at the tested conditions are truly measurable and intolerably high. Based on Equation 5-6, one may reach a conclusion that for an SDC electrolyte cell, both the thinner the electrolyte and the higher-performing the electrodes are, the higher the leakage current density will be. A thinner electrolyte will not only reduce the cell resistance ( $R_{t, cell}$ ), but also enhance the possibility of electrolyte defects, such as pinholes or cracks, spanning the entire electrolyte thickness, leading to an even lower OCV caused by gas leakage, and thus further decreasing the efficiency and increasing the fuel loss in the cell.

Table 5-4 Leakage current densities based on either OCV value or measured water amount

Temperature [°C]	$E_N$ [V]	OCV [V]	$R_{t, cell}$ [ $\Omega$ cm <sup>2</sup> ]	$i_{L, calc.}$ [A cm <sup>-2</sup> ]	$i_{L, meas.}$ [A cm <sup>-2</sup> ]	$V_0$ [V]
650	1.115	0.796	0.147	2.169	1.401	1.002
600	1.123	0.835	0.250	1.148	0.854	1.049
550	1.130	0.857	0.534	0.512	0.405	1.073
500	1.138	0.873	1.268	0.209	0.189	1.113

$E_N$ : Theoretical Nernst cell voltage at the tested condition,

OCV: measured cell open circuit voltage

$R_{t, cell}$  : average cell resistance value of  $R_i$  and  $R_{cell}$  (see Tables 5-2 and 5-3)

$i_{L, calc.}$ : calculated leakage current density based on Equation 5-6

$i_{L, meas.}$ : measured leakage current density based on collected water amount

$V_0$ : fitting parameter based on Equation 5-6

### 5.3.4 Low electrical efficiency due to internal shorting of the SDC electrolyte

T. Matsui *et al* have calculated that the anode-supported 10  $\mu\text{m}$  SDC electrolyte cell with ideal electrodes (i.e., zero electrode polarization) can reach an electrical efficiency of approximately 61% at a cell voltage of 0.72V in the same temperature range of this study [17]. In this study, we found that in the case of the cell operating at  $0.50 \text{ A cm}^{-2}$ ,  $600^\circ\text{C}$ , 5% fuel utilization, and 12.5% air utilization, the internal shorting current density was  $0.60 \text{ A cm}^{-2}$ . This means that the fuel loss due to internal shorting is 1.2 times higher than the fuel used for electrical power generation under this operating condition. Since the electronic conductivity of the SDC electrolyte depends on the temperature and anode side oxygen partial pressure, an increase in the fuel utilization will lead to a decrease in electronic conductivity of SDC, and therefore decrease the leakage current density across the electrolyte [16,17]. However, in real operation, the cell voltage will decrease due to increasing fuel utilization. As a result, the cell will operate at a lower efficiency.

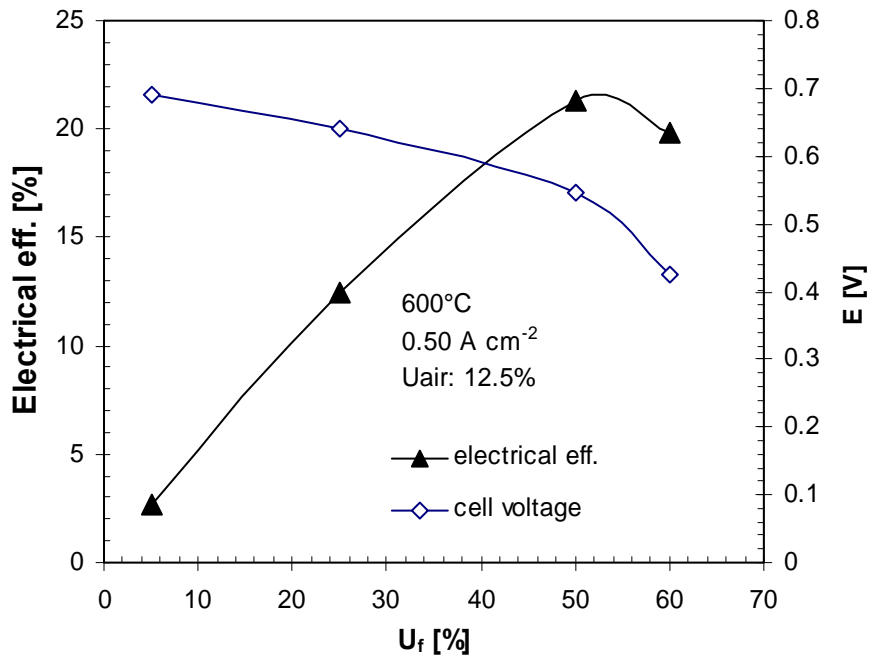


Figure 5-7 Fuel utilization ( $U_f$ ) and electrical efficiency (LHV) of the cell.

As indicated in Figure 5-7, in this study, for the SDC cell operating at  $0.5 \text{ A cm}^{-2}$  at  $600^\circ\text{C}$ , an increase in the fuel utilization from 5% to 50% leads to a decrease of the cell

voltage from 0.692V to 0.546V. Further increasing the fuel utilization to over 60% causes a sharp drop in the cell voltage. The highest electrical efficiency (based on Lower Heating Value) was only 21% at 50% fuel utilization. Accordingly, it seems difficult for the cermet supported, thin SDC electrolyte cell to reach high fuel utilization with high cell performance, due to severe internal shorting, although modeling results had suggested that it should be possible [16,17].

The calculation of the theoretical leakage current density  $i_L$  through the electrolyte is rather complex, as it depends on a number of factors [16]:

- The operating temperature, T
- The oxygen partial pressure distribution across the electrolyte,  $p_{O_2,el}$
- The electronic conductivity of the electrolyte,  $\sigma_e$ , which greatly depends on  $p_{O_2,el}$  and T, and can be significantly changed by the presence of impurities at the grain boundaries, or other phase inclusions generated during cell fabrication
- The ionic conductivity of the electrolyte,  $\sigma_i$ , which can be significantly reduced by the presence of impurities at the grain boundaries, or other phase inclusions generated during cell fabrication
- The electrode polarization resistance,  $R_{p, a+c}$
- The cell operating current density, i

It was observed in this study (see Table 5-3) that the  $i_L$  value under  $0.5A\text{ cm}^{-2}$  operating current density was smaller than that under open circuit conditions. These  $i_L$  values were 0.595 and  $0.854\text{ A cm}^{-2}$ , respectively. The effect of an increase in the cell operating current density is that it increases the average oxygen partial pressure in the electrolyte, resulting in a decrease in the  $\sigma_e$  value of the electrolyte, and thus also the  $i_L$ . However, the leakage current density under this condition is still over two orders of magnitude higher than that in the modeling result from [16].

### 5.3.5 The SDC conductivities in this study

As is widely known, a doped ceria electrolyte behaves as a mixed conductor. The ionic conductivity of SDC ( $\sigma_i$ ) is purely a function of temperature, but the electronic conductivity ( $\sigma_e$ ) is a function of both temperature and the local oxygen partial pressure ( $p_{O_2}$ ). The electronic conductivity of SDC is negligible at temperatures below 400°C and/or in an oxidizing environment [16]. However, the oxygen partial pressure at the anode ( $p_{O_2,anode}$ ) under the conditions of this study is typically in the range of  $10^{-25}$  to  $10^{-31}$  atm, which leads to the SDC electrolyte exhibiting a significant  $\sigma_e$ . The oxygen ionic conductivity ( $\sigma_i$ ) and electronic conductivity ( $\sigma_e$ ) of the doped-ceria electrolyte can be estimated as

$$\sigma_i = \frac{\sigma_{0,i}}{T} \exp\left(-\frac{E_{a,i}}{RT}\right) \quad \text{Equation 5-7}$$

$$\sigma_e = \sigma_{0,e} \frac{(p_{O_2,el})^{-1/4}}{T} \exp\left(-\frac{E_{a,e}}{RT}\right) \quad \text{Equation 5-8}$$

For  $Gd_{0.1}Ce_{0.9}O_{1.95}$  [18],  $\sigma_{0,i} = 2.706 \times 10^6$  [S K m<sup>-1</sup>],  $E_{a,i} = 61.748 \times 10^3$  [J mol<sup>-1</sup>];  $\sigma_{0,e} = 2.342 \times 10^{11}$  [S K atm<sup>1/4</sup> m<sup>-1</sup>], and  $E_{a,e} = 238.78 \times 10^3$  [J mol<sup>-1</sup>]. In this study, based on the measured  $R_{el}$  value and assuming that the resistance comes solely from the ionic conductivity of the 10µm-thick SDC electrolyte (thickness  $\delta_{el}$ ), we obtain  $\sigma_{0,i} = 4.3045 \times 10^6$  [S K m<sup>-1</sup>],  $E_{a,i} = 61.89 \times 10^3$  [J mol<sup>-1</sup>].

The electronic and ionic conductivities can be obtained through the ionic transference number ( $t_i$ ) and the total conductivity ( $\sigma_t$ ) of the electrolyte as measured.  $t_i$  and  $\sigma_t$  were calculated from Equations 5-7 to 5-12 [13, 20], under assumptions that no influence on the cell OCV value comes from electrode polarizations, and that no electrolyte defect (such as pinholes or cracking) and no sealing leakage occur in this study. The calculated  $\sigma_e$  and  $\sigma_i$  values at different temperatures are listed in Table 5-5.

$$t_i = \frac{OCV}{E_N} \quad \text{Equation 5-9}$$

$$\sigma_t = \frac{\delta_{el}}{R_{el}} \quad \text{Equation 5-10}$$

$$\sigma_i = t_i \sigma_t \quad \text{Equation 5-11}$$

$$\sigma_e = (1 - t_i) \sigma_t \quad \text{Equation 5-12}$$

It is worth mentioning that the calculated  $\sigma_e$  is related to the oxygen partial pressure within the electrolyte. For simplicity, the values of both  $\sigma_{0,e}$  and  $E_{a,e}$  in Table 5-5 were obtained by assuming that the  $p_{O_2,el} = 0.21 \text{ atm}$ , the highest value in the electrolyte (cathode side), for eqn (5-8).

Table 5-5 The conductivities of the SDC (GDC) electrolytes [14, 15, 18]

T [°C]	500	550	600	650	$\sigma_o$ [S K cm <sup>-1</sup> ]	$E_a$ [kJ mol <sup>-1</sup> ]	Reference
$\sigma_{i, \text{SDC}}$ [S m <sup>-1</sup> ]	0.59	1.16	1.92	3.01	302549	71.19	[14]
	0.66	1.25	2.08	3.20	255250	69.42	[15]
$\sigma_{i, \text{GDC}}$ [S m <sup>-1</sup> ]	0.24	0.40	0.63	0.94	27174	61.75	[18]
$\sigma_{t, \text{GDC}}$ [S m <sup>-1</sup> ]	0.355	0.649	1.019	1.415	43045	61.89	
$\sigma_{i, \text{SDC}}$ [S m <sup>-1</sup> ]	0.272	0.490	0.758	1.010	21807	61.75	In this study
$\sigma_{e, \text{SDC}}$ [S m <sup>-1</sup> ]	0.083	0.156	0.261	0.405	34132	69.87	

As listed in Table 5-5, the reported conductivities ( $\sigma_i$ ) of SDC ( $\text{Sm}_{0.2}\text{Ce}_{0.8}\text{O}_{1.9}$ ) can be as high as  $3.0 \text{ S m}^{-1}$  at  $650^\circ\text{C}$  and  $2.0 \text{ S m}^{-1}$  at  $600^\circ\text{C}$  [14, 15]. The measured  $\sigma_i$  value in this study was only about 1/3 to 1/2 of the reported  $\sigma_i$  value at the test temperature, implying that certain detrimental interactions might have taken place in the SDC electrolyte during the cell processing. The measured  $\sigma_i$  of the SDC in this study was slightly higher than that of GDC ( $\text{Gd}_{0.1}\text{Ce}_{0.9}\text{O}_{1.95}$ ), and the activation energy ( $E_a$ ),  $61.75 \text{ kJ mol}^{-1}$  was very close to that of GDC reported in [18].

### 5.3.6 Cathode contribution

The oxygen reduction process at the cathode includes diffusion, adsorption, dissociation, charge transfer, and oxygen ion dissolution into the SDC electrolyte. The

leakage current density on the bare SDC electrolyte is much smaller than that in the SDC covered with a cathode (see Table 5-3 and Figure 5-6). The apparent activation energies ( $E_{a,or}$ ) of oxygen reduction in both cases are quite different,  $15.96 \text{ kJ mol}^{-1}$  for the cell without a cathode and  $80.39 \text{ kJ mol}^{-1}$  for the cell with a cathode, indicating that the oxygen reduction mechanism was different. Although the bare SDC surface shows a certain catalytic function in oxygen reduction, the rate-determining step of the oxygen reduction process without a cathode is most likely the adsorption and dissociation of the oxygen, surface diffusion of oxygen species, or a combination of the two. This is because of the low activation energy. With the cathode present, the processes of adsorption and dissociation of oxygen are greatly enhanced by the higher effective surface area and catalytic role of the SSC cathode. With sufficient cathode activity and reaction area, the rate-determining step shifts to a combination of normal cathode process with the oxygen ion generation, dissolution, and transport in the electrolyte, i.e., ion conductive process of the electrolyte. The obtained  $E_a$  value ( $80.39 \text{ kJ mol}^{-1}$ ) with the cathode is between the activation energy average of the SSC cathode (approximately  $126 \text{ kJ mol}^{-1}$ , refer to Appendix B) and that of the ionic conductivity of the SDC electrolyte (approximately  $62 \text{ kJ mol}^{-1}$ ). In the case of an ideal cathode at OCV, the oxygen reduction process will be completely controlled by both the electronic and the ionic conductivities of the electrolyte.

### 5.3.7 Cell microstructure and EDS analysis

Figure 5-8 and Figure 5-9 show plane and cross-section views of the tested cell, including EDS analyses of the electrolytes. Although the SDC surface appears nearly fully dense with very few pin-holes, many irregular grains on the SDC electrolyte surface were observed after the  $1400^\circ\text{C}$  - 2hr co-firing and prior to cathode deposition (Figure 5-8 a). The cell cross-section reveals some defects existing in the electrolyte, which may be one of the contributing factors to the slightly lower OCV observed in this study compared to that of thicker SDC electrolytes reported previously in the literature. Figure 5-9 shows the EDS analysis results of a regular grain and an irregular grain in Figure 5-8a, marked with #1 and #2, respectively. EDS analysis results show that the irregular grains have a high Zr content, and have the appearance of micro-islands, so they are referred to as Zr-micro-islands in the

present work. The cross-section of the SDC electrolyte after sample polishing also reveals Zr-content inclusions.

It can be seen from the composition tables in Figure 5-9 that the irregular grain shows not only a high Zr content, but also an enriched Sm content, while the Ce content is substantially decreased. High Sm content in the irregular grain indicates that Sm has a higher solubility in those grains than in the bulk. Furthermore, since the grain size of the Zr-island is larger than that of the normal SDC grains, this second phase likely also has a higher vapour pressure or lower melting point, a faster grain growth rate, and higher sinterability than that of normal SDC during the cell co-firing. The high Sm content in the irregular grains also suggests that depletion of Sm-dopant from the bulk SDC composition has occurred, which could be one of the reasons for the low ionic conductivity ( $\sigma_i$ ) in this study.

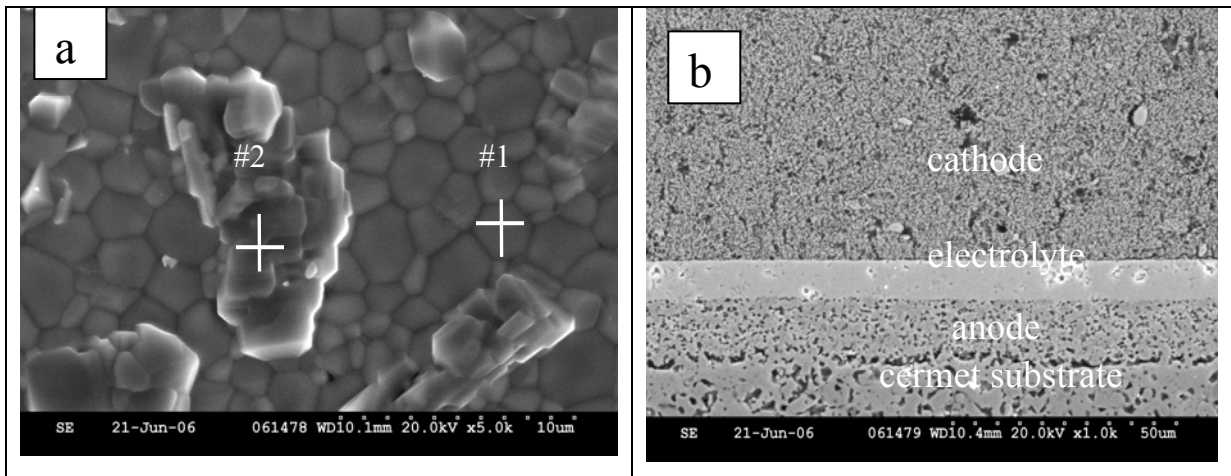


Figure 5-8 SEM images of the SDC electrolyte after cell test  
(a) SDC electrolyte surface (b) Cell cross-section

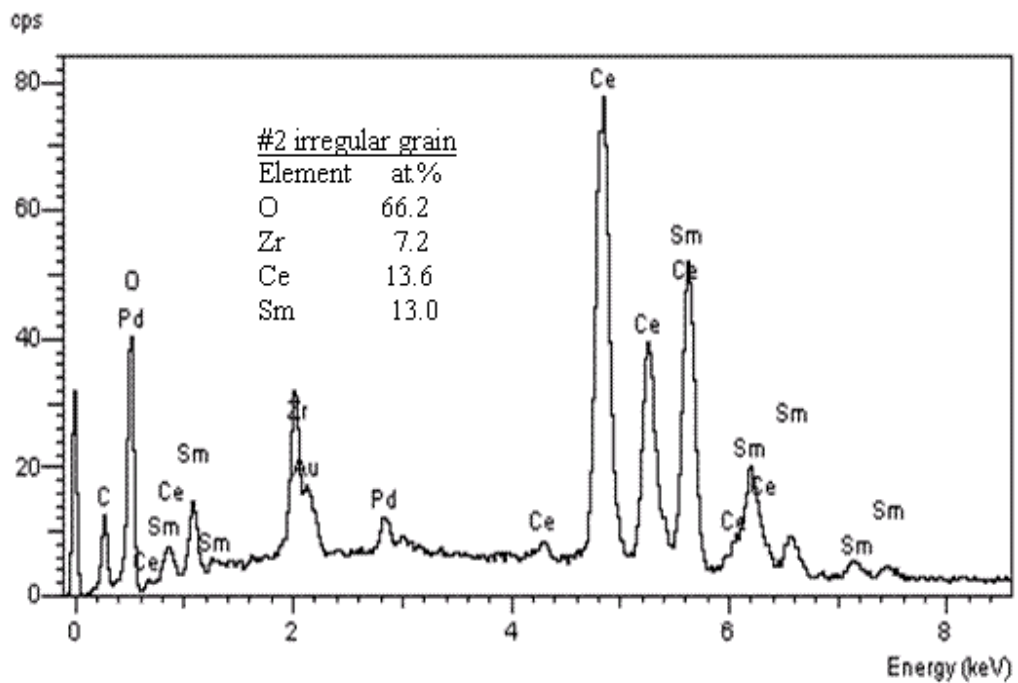
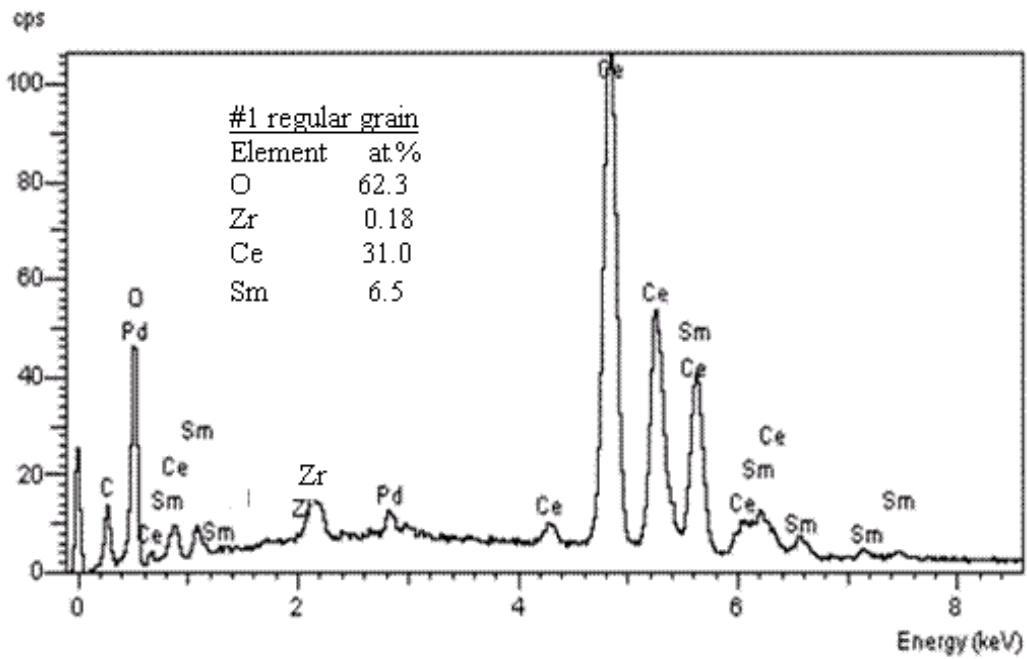


Figure 5-9 EDS analysis results at regular grain(#1) and irregular grain(#2) on the SDC electrolyte surface after co-firing (see Figure 5-8a).

The Zr-micro-islands are potentially detrimental to the cell performance. Tsoga *et al* [20] reported that the Zr-Ce-Gd-Y-O phase exhibits a conductivity two orders of magnitude lower than that of GDC. Since Sm-doped ceria and Gd-doped ceria have very similar conductivities, it is likely that the Zr micro-islands observed in this work may also consist of a very low conductivity phase, based on the analyzed compositions, and their similarity with the compositions studied by Tsoga *et al*. Simply based on the  $\sigma_e / \sigma_i$  ratios in Table 3-1 (see Chapter 3), it is noticed that the ratio of the electronic to ionic conductivity of the phase could be increased 7-35 times in comparison to that of the pure GDC, which means that the inclusions found in this study might contribute to a lower OCV. As discussed in Chapter 3, the formation of Zr-micro-islands is likely related to Zr migration from the NiO-YSZ substrate during the co-firing process.

## 5.4 Conclusions

Thin film (10 $\mu$ m) SDC electrolytes have been co-fired on porous NiO-SDC anodes with NiO-YSZ substrates. The SDC electrolyte cells, with and without cathodes, were tested in the temperature range of 500-650 $^{\circ}$ C. The cell with an SSC-SDC composite cathode showed a high electrochemical performance at temperatures ranging from 500 to 650 $^{\circ}$ C. A peak power density of 595 mW cm $^{-2}$  at 650 $^{\circ}$ C was obtained. However, the cell exhibited severe internal shorting due to the mixed conductivity of the SDC electrolyte. Both the amount of water collected from the anode outlet and the open circuit voltage (OCV) value indicated that the internal shorting current could reach 0.85 A cm $^{-2}$  or higher at 600 $^{\circ}$ C. The SSC-SDC composite cathode plays a key role in a fast oxygen reduction process, and in the intolerable internal shorting under OCV conditions observed in this study. A simple model was developed for the internal leakage current calculation. It appears that both higher electrode performance and thinner electrolytes lead to higher leakage currents in a thin SDC electrolyte cell. Zr-content inclusions were found at the surface and the cross-section of the SDC electrolyte, which could be one of the reasons for reduced OCV and lower oxygen ionic conductivity. Fuel loss due to internal shorting of the thin SDC electrolyte cell becomes a substantial concern for its use in applications requiring high fuel utilization and electrical efficiency. Future developments will require minimising

the electronic leakage current either by doped-ceria electrolyte composition modification or by deposition of electronic blocking layers to control the level of the electronic conductivity of the whole electrolyte layer.

## 5.5 References

1. S. de Souza, S. J. Visco, L. C. de Jonghe, *Solid State Ionics* 98 (1997) 57.
2. Z. Yang, K. S. Weil, D. M. Paxton, J. W. Stevenson, *J. Electrochem. Soc.* 150 (2003) A1188-A1201
3. W. Z. Zhu, S. C. Deevi, *Materials Research Bulletin* 38 (2003) 957.
4. C. Xia, W. Rauch, F. Chen, M. Liu, *Solid State Ionics* 149 (2002) 11.
5. S. Zha, W. Rauch, M. Liu, *Solid State Ionics* 166 (2004) 241.
6. G. Schiller, R. Henne, M. Lang, S. Schaper, 1999, *Proc. SOFC VI*, *Electrochem. Soc.*, p. 893–903.
7. N. P Brandon, A. Blake, D. Corcoran, D. Cumming, A. Duckett, K. El-Koury, D. Haigh, C. Kidd, R. Leah, G. Lewis, C. Matthews, N. Maynard, N. Oishi, T. McColm, R. Trezona, A. Selcuk, M. Schmidt, L. Verdugo, *J. Fuel Cell Science and Technology* 1 (2004) 61.
8. S. Zha, A. Moore, H. Abernathy, M. Liu, *J. of Electrochem. Soc.* 151 (2004) A 1128- A1133.
9. W. Wang, M. Mogensen, *Solid State Ionics* 176 (2005) 457.
10. Z. Shao, S. M. Haile, *Nature* 431 (2004) 170.
11. T. Matsui, T. Kosaka, M. Inaba, A. Mineshige and Z. Ogumi, *Solid State Ionics* 176 (2005) 663.
12. T. Miyashita, *J. Mater. Sci.* 41 (2006) 3183.
13. M. Liu and H. Hu, *J. Electrochem. Soc.* 143 (1996) L109.
14. V. V. Kharton, F. M. B. Marques and A. Atkinson, *Solid State Ionics* 174 (2004) 135.
15. S. P. S. Badwal, *Solid State Ionics* 52 (1992) 23.
16. R. T. Leah, N. P. Brandon, and P. Aguiar, *J. Power Sources* 145 (2005) 336.
17. T. Matsui, M. Inaba, A. Mineshige, and Z. Ogumi, *Solid State Ionics* 176 (2005) 647.
18. M. Sahibzada, R. A. Rudkin, B. C. H. Steele, I. S. Metcalfe, and J. A. Kilner, in: U. Stimming, et al.(Eds.), *SOFC V*, *Proceedings Vol. 97-40*, *Electrochemical Society*, NJ, 1997, p 244.

19. H. Iwahara, *J. Electrochem. Soc.* 52 (1992) 99.
20. A. Tsoga, A. Naoumidis and D. Stover, *Solid State Ionics* 135 (2000) 403.
21. X. Zhang, M. Robertson, S. Yick, C. Decès-Petit, E. Styles, W. Qu, Y. Xie, R. Hui, J. Roller, O. Kesler, R. Maric, D. Ghosh, *J. Power Sources* 160 (2006) 1211.

## 6. Chapter Six. A Study on Sintering Aids for SDC Electrolyte<sup>6</sup>

In this study, an addition of Co oxide or Cu oxide to  $\text{Sm}_{0.2}\text{Ce}_{0.8}\text{O}_{1.9}$  (SDC) was studied to improve the sinterability of SDC. It has been found that both Co and Cu oxide are very effective as sintering aids, and the SDC sintering temperature can be reduced from 1400°C without aids to below 1000°C with only 1at.% of either Cu oxide or Co oxide. As compared to the pure SDC, a slight decrease of ionic conductivity was observed in SDC with Cu sintering aid. There is no obvious effect on electrochemical property of SDC with Co sintering aid under 2.5at.%.

### 6.1 Introduction

Ceria-based ceramic materials doped with Sm and/or Gd have been acknowledged to be the most promising electrolytes for solid oxide fuel cells operating below 600 °C due to their high ionic conductivity and good compatibility with electrodes, especially with high performing Co-content cathodes. A maximum power density of anode supported thin ceria based electrolyte cells has been reported as over 880 mW cm<sup>-2</sup> at 600°C with H<sub>2</sub> fuel [1, 2]. However, the ceria electrolytes are difficult to densify below 1400 °C [3-6]. If a dense ceria-based electrolyte can be prepared at lower temperatures it can be co-sintered with the electrode components, which simplifies the fabrication process and reduces the cost, helping with porous electrode microstructure control and avoiding or alleviating phase diffusion and chemical interaction problems, which is believed to be an important technology barrier in the fabrication of bi-layered electrolyte cells by conventional TSC methods.

In order to sinter doped ceria materials at a lower temperature, several methods have proven effective, which can be classified into two categories: (1) Using ultra-fine powders at submicron and nanometer size by special synthesis methods, such as hydrothermal synthesis [7, 8], oxalate co-precipitation [9, 10], chemical combustion vapour

---

<sup>6</sup> A version of this chapter has been published as:

X. Zhang, C. Decès-Petit, S. Yick, M. Robertson, W.Qu, J. Roller, Y. Xie, R. Hui, O. Kesler, R. Maric, D. Ghosh, A study on sintering aids for  $\text{Sm}_{0.2}\text{Ce}_{0.8}\text{O}_{1.9}$  electrolyte, J. Power Sources 161 (2006) 480.

synthesis [11, 12] or intensive mechanical milling [13]; the decrease of the starting particle size enables the densification at a lower heating temperature because of the increased driving force (specific surface area) of sintering. However, a small pore size between ultra-fine particles produces a high capillary force in the powder compact which is the origin of low packing density and cracks formed during drying and firing [14, 15]. (2) Adding a sintering promoter or aid in a limited amount [3, 13]. It has been reported that  $\text{Mn}_2\text{O}_3$  and  $\text{Co}_3\text{O}_4$  promotes grain growth of doped Ceria even at initial stages of sintering, while  $\text{Ga}_2\text{O}_3$  promotes rearrangement of particles. The sintering temperature could be decreased from  $1600^\circ\text{C}$  to  $1400^\circ\text{C}$  by adding 1at.% of such aids [3].

In this work, we studied the influence of Co and Cu oxides as sintering aids on sintering behavior, conductivity, phase, and microstructure of SDC.

## **6.2 Experimental procedure**

### *Sample preparation*

Table 6-1 lists the starting chemicals and ceramic powder materials used in this study. Firstly, both Co and Cu nitrates were separately dissolved in ethanol through a ball milling process, using nalgene bottles with  $\varnothing 5$  mm YSZ balls, before adding SDC powder. Both nitrates were dissolved at 1.0 at.%, 2.5 at.% and 5.0 at.% of Co or Cu to the moles of the SDC powder. After adding SDC powder, ball milling was carried out for 40h, with subsequent drying at  $50^\circ\text{C}$  for 8h and separation of powders from the grinding media for thermal decomposition at  $500^\circ\text{C}$  for 5h in air. The obtained 7 types of powders, including one blank SDC powder (without Co or Cu additive), were pressed at 40-50 MPa into pillars of  $\varnothing 5$  mm and approximately 10 mm length and pellets of  $\varnothing 20$  mm and approximately 2.0 mm thick. The pillar samples were used for shrinkage-sintering studies using a Setsys 16/18 TMA (Setaram, France). The sintered pellet samples after surface polishing were used for XRD analysis and electrochemical characterization. Both NiO-SDC anode and  $\text{Sm}_{0.5}\text{Sr}_{0.5}\text{CoO}_3$  cathode were applied on the polished samples by stencil printing and co-sintered at  $1000^\circ\text{C}$  for 2hr in air. Measurements were performed in fuel cell operating conditions, i.e., at  $600^\circ\text{C}$  with 97%  $\text{H}_2$ +3%  $\text{H}_2\text{O}$  as anode gas and air as cathode gas, both at flow rates of  $100 \text{ ml}\cdot\text{min}^{-1}$ . Cyclic voltammetry curves were measured using a Solartron 1480 at a scan rate of  $0.5 \text{ mV s}^{-1}$ .

Table 6-1 Properties and supplier of starting materials

Material	Composition	Properties	Supplier
Co additive	Co(NO <sub>3</sub> ) <sub>2</sub> .6H <sub>2</sub> O	Formula Weight (FW) 291.04	Alpha Aesar, Lot#23282
Cu additive	Cu(NO <sub>3</sub> ) <sub>2</sub> .3H <sub>2</sub> O	FW 241.60	Alpha Aesar, Lot#K10N42
Electrolyte	Sm <sub>0.2</sub> Ce <sub>0.8</sub> O <sub>1.9</sub> (SDC)	FW 172.6, D50: 0.40 μm Surface area: 7.0 m <sup>2</sup> .g <sup>-1</sup>	Praxair Lot#03-P4687DM
Cathode	Sm <sub>0.5</sub> Sr <sub>0.5</sub> CoO <sub>3</sub> (SSCo)	D50: 0.80 μm Surface area: 5.16 m <sup>2</sup> .g <sup>-1</sup>	Praxair
Anode	NiO + SDC	NiO: D50: 1.0 μm Surface area: 4.0 m <sup>2</sup> .g <sup>-1</sup>	Novamet (SDC from Praxair)

*Sample characterization*

Powder characterization was performed using a Mastersizer 2000 (Malvern Instruments Ltd., UK) for particle size analysis and by using a SA3100 Surface Area Analyzer (Beckman Coulter<sup>TM</sup>, USA) for surface area analysis. The density of experimental pellets was measured by Archimedes' method at room temperature.

Table 6-2 Composition, particle size and surface area of powders used in this study

Powder composition	Appearance	Mean particle size* [μm]	BET Surface area [m <sup>2</sup> .g <sup>-1</sup> ]
blank-SDC	Yellow	0.18	7.15
5.0at.%Co-SDC	Green	0.17	8.25
5.0at.%Cu-SDC	Dark green	0.17	8.39

\*water as dispersant, 4 minute ultrasonic agitation.

Table 6-2 gives the composition, particle size and surface area of the powders in this study. It can be seen that there is a slight increase of the BET surface area of SDC with sintering aids after the powder processing. The increase of BET surface area of SDC after Cu nitrate or Co nitrate addition and pre-treatment at 500°C suggests the possible the formation of fine Co or Cu oxides on the SDC particle surface.

### 6.3 Results and discussion

#### *Powder pre-treatment condition*

Thermal decomposition of SDC powders with 5at.%  $\text{Co}(\text{NO}_3)_3 \cdot 6\text{H}_2\text{O}$  or  $\text{Cu}(\text{NO}_3)_2 \cdot 3\text{H}_2\text{O}$  was analysed from room temperature to  $800^\circ\text{C}$  in air flowing at  $60 \text{ ml min}^{-1}$  by TGA and DTA. As shown in Figure 6-1 and Figure 6-2, both Co and Cu nitrates are fully decomposed before  $300^\circ\text{C}$ , and the fastest decomposition rate happens at  $232^\circ\text{C}$  for  $\text{Co}(\text{NO}_3)_3$ , and  $252^\circ\text{C}$  for  $\text{Cu}(\text{NO}_3)_2$ . The DTA results also show the different temperatures for desorbing the adsorbed water in each nitrate.

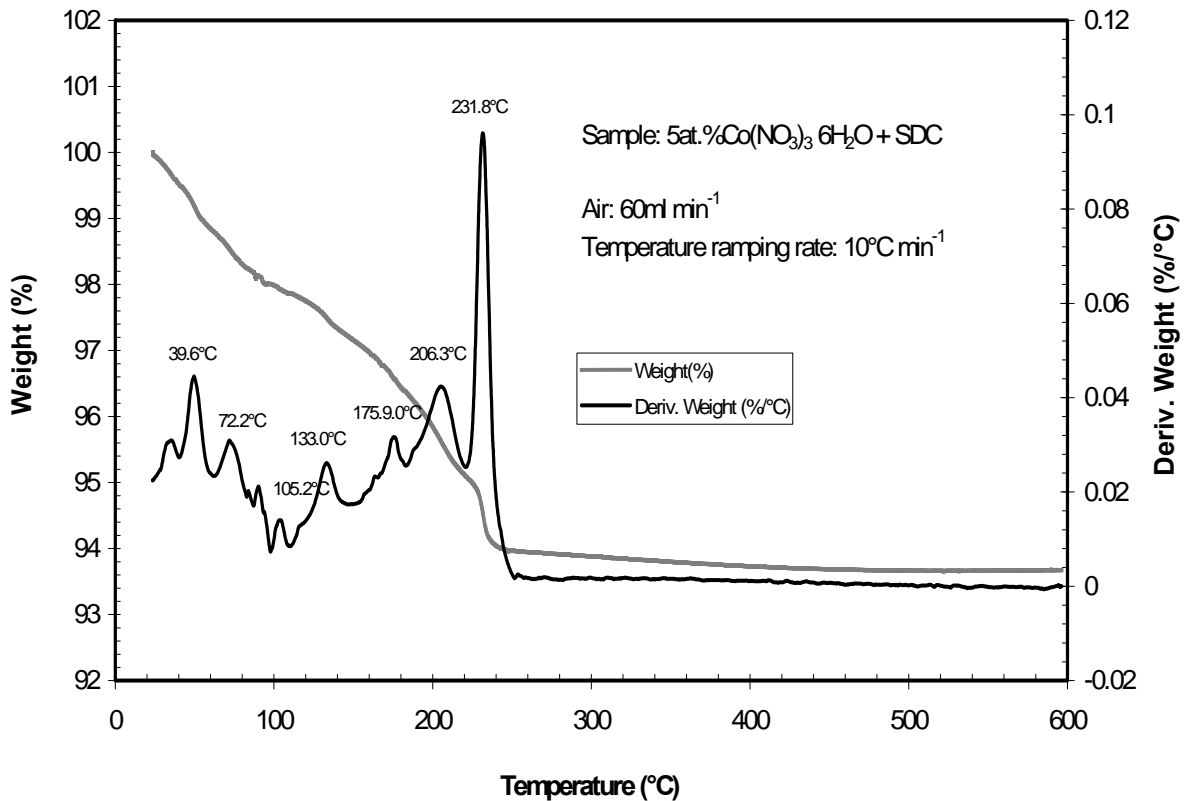


Figure 6-1 TGA of SDC powders with 5at%  $\text{Co}(\text{NO}_3)_3 \cdot 6\text{H}_2\text{O}$ .

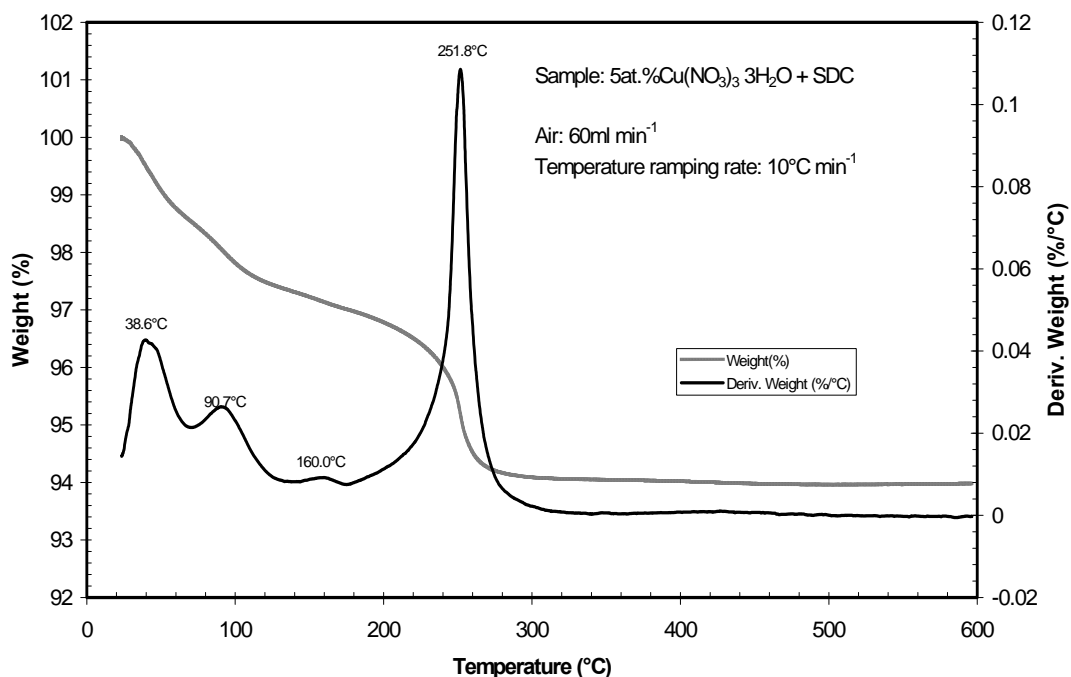


Figure 6-2 TGA of SDC powders with 5at% Cu(NO<sub>3</sub>)<sub>2</sub>·3H<sub>2</sub>O.

Based on the TGA results, all SDC powders with nitrates at designed content (0, 1, 2.5, and 5 at.% of Co or Cu) were treated for thermal decomposition at 500°C for 5h in air.

### *XRD results*

The lattice constant was determined using a D8-02 X-Ray Diffractometer (Bruker AXS GmbH, USA) with Cu-K<sub>α</sub> radiation at room temperature. The spectra were acquired from 2θ angles of 15° to 85° in steps of 0.02° per second. All samples were positioned on plasticine using a glass plate to align the sample in the holder. The results are shown in Figure 6-3. It can be seen that no clear impurity phase is present in the XRD patterns of the Co-containing specimens to 5at.% Co oxide addition. However, addition of only 1at.% Cu oxide in the as-fired sample results in CuO (Tenorite) phase at the surface. This CuO phase was removed after polishing the sample surface. As shown in Figure 6-4, the SDC lattice parameter shows limited variation with the Co or Cu (polished sample) contents. This may suggest that Co and Cu exist mainly on the SDC grain boundary, and do not enter the SDC lattice. Gauckler *et al* found evidence of a grain boundary phase with concentrated Co

content in  $Gd_{0.2}Ce_{0.8}O_{1.9}$  with Co oxide as sintering aid by electron energy loss spectroscopy mapping [16].

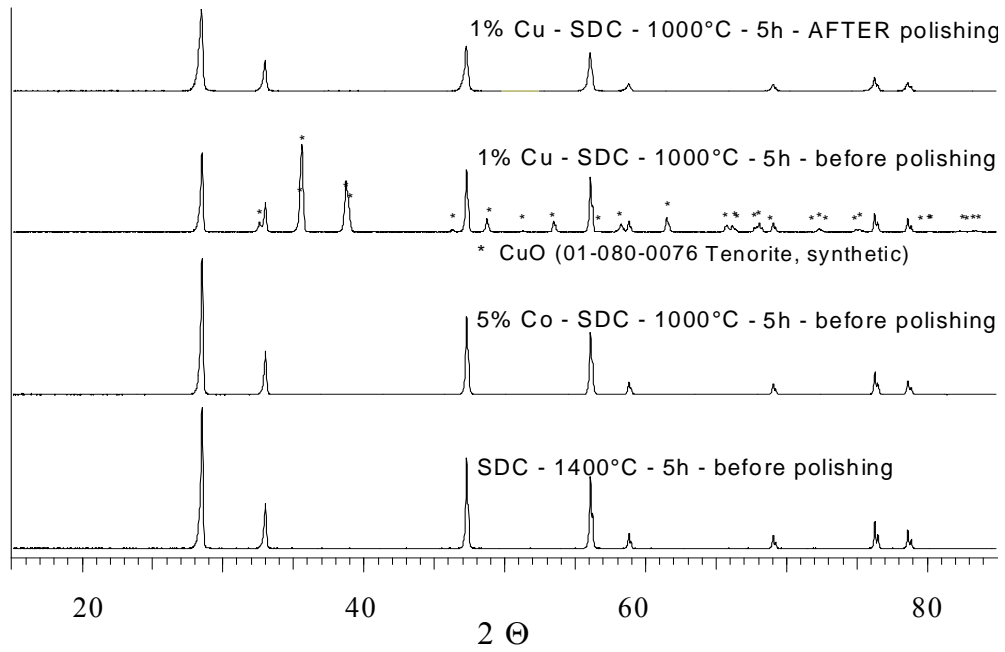


Figure 6-3 XRD patterns of sintered SDC with and without Cu or Co addition.

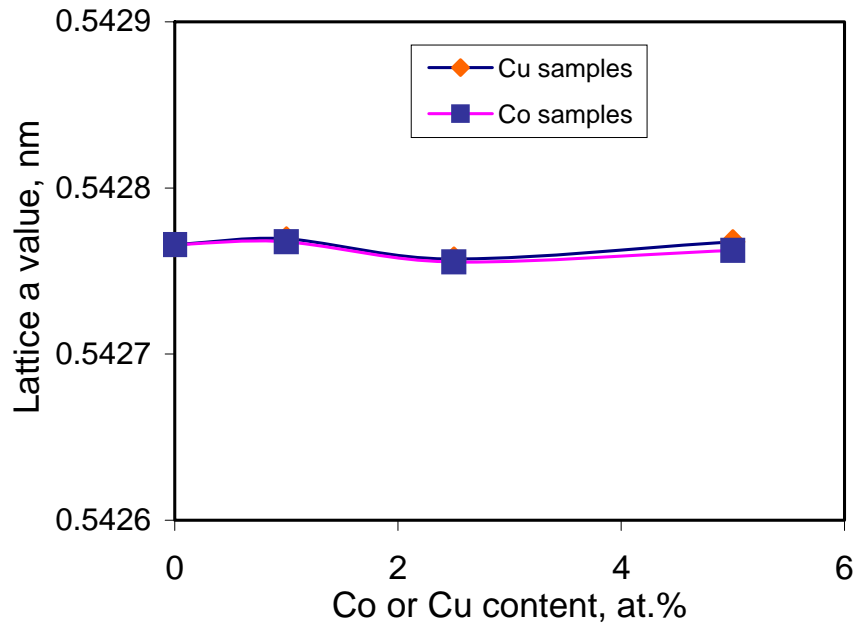


Figure 6-4 SDC lattice parameter variation with Co or Cu (polished sample) content.

### TMA sintering results

The effects of Co oxide or Cu oxide dopant on SDC sintering behaviour are shown in Figure 6-5 and Figure 6-6. It can be seen that the Co oxide or Cu oxide addition shifts the sintering curve towards lower temperature ranges from 1100°C and above for SDC to 800°C and above for Co oxide addition and 750°C for Cu oxide addition, significantly promoting the densification. It was found that increasing dopant amounts from 1 to 5at.% had a limited effect on the densification behaviour for both Co oxide and Cu oxide addition. Figure 6-6 shows the linear shrinkage rate as a function of temperature. This figure clearly shows that the maximum shrinkage rate ( $S_{max}$ ,  $\times 10^{-5} \text{ }^\circ\text{C}^{-1}$ ) changes with the type of dopant, and is in the following order:  $0.58 \times 10^{-5} \text{ }^\circ\text{C}^{-1}$  at 1290°C for SDC,  $0.70\text{-}0.72 \times 10^{-5} \text{ }^\circ\text{C}^{-1}$  at 913-975°C for Co-SDC and  $1.1 \times 10^{-5} \text{ }^\circ\text{C}^{-1}$  at 920°C for Cu-SDC. The difference between the temperatures of the maximum shrinkage rate of SDC alone and with Cu oxide or Co oxide addition is more than 200°C. Moreover, the Cu oxide and Co oxide addition enhances greatly the densification rate of SDC. A similar result for Co oxide addition was published by Zhang *et al* [13, 14]. Of the two oxides, Cu oxide is the most effective sintering aid. The measured sample density in Table 6-3 supports this result. Both liquid phase sintering and viscous flow sintering processes may contribute to the significant reduction of the sintering temperature with Co oxide or Cu oxide aids.

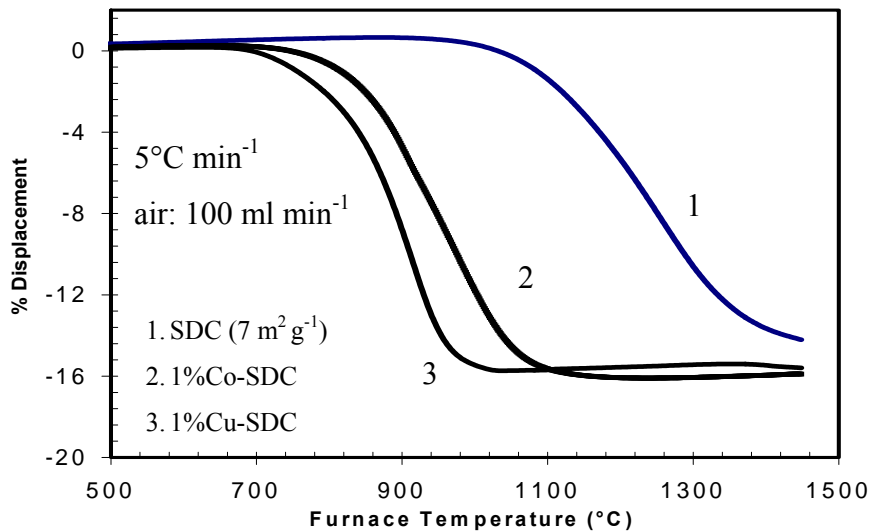


Figure 6-5 Linear shrinkage (displacement, %) versus sintering temperature at a heating rate of 5°C min<sup>-1</sup>.

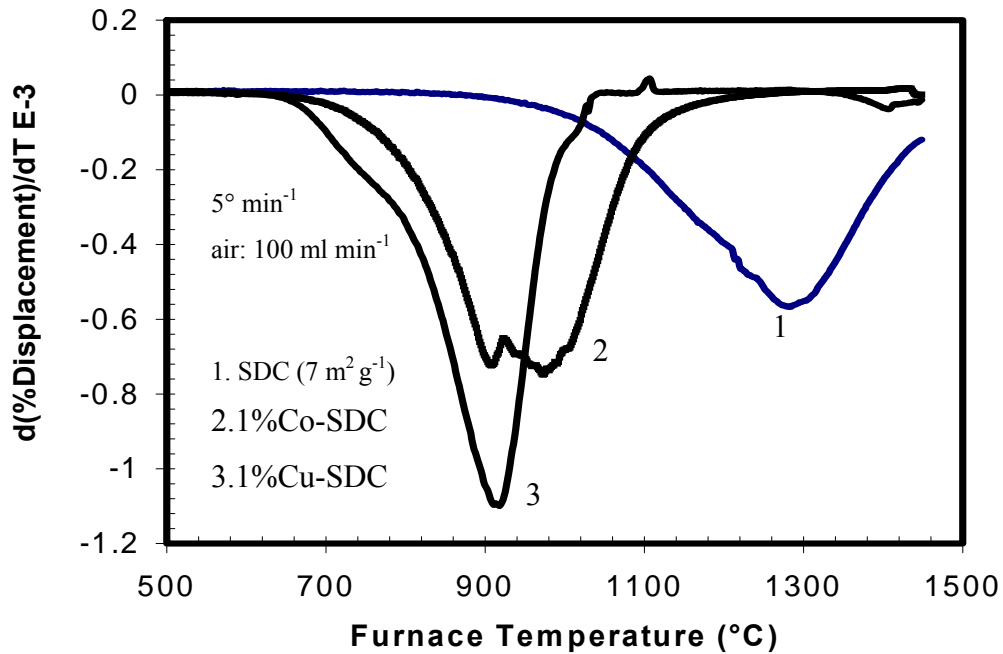


Figure 6-6 Linear shrinkage rate versus sintering temperature at a heating rate of  $5^{\circ}\text{C min}^{-1}$ .

Densities and grain sizes of the SDC pellets after sintering are listed in Table 6-3. The density of experimental pellets slightly decreased with the increase of sintering aids content; over 93% theoretical density of the SDC was reached.

Table 6-3 Sintering temperature, density and grain size of SDC samples after sintering

Sample	Ts[°C] (for 5hrs)	Density[g cm <sup>-3</sup> ]	Grain size[μm]
blank-SDC	1400	6.948	1-2
1.0at.%Co-SDC	1000	6.865	0.5-1
2.5at.%Co-SDC	1000	6.750	0.5-1
5.0at.%Co-SDC	1000	6.633	0.5-1
1.0at.%Cu-SDC	1000	7.004	SDC: 0.5-1,
2.5at.%Cu-SDC	1000	7.009	Cu-compound <sup>#</sup>
5.0at.%Cu-SDC	1000	6.981	>10μm

<sup>#</sup> a new phase appeared on the pellet surface with Cu sintering aids, named Cu-compound

*Electrochemical measurements*

Figure 6-7 shows the cyclic voltammetry curves at 600°C of three SDC electrolyte cells. The main results are listed in Table 6-4. It can be seen that the conductivity of SDC is approximately 0.021 S cm<sup>-1</sup>, which a slightly higher conductivity for 2.5%Co-SDC and a slightly lower conductivity for 1%Cu-SDC. The measured OCV at 600°C also shows that the addition of Co oxide or Cu oxide to SDC causes a slight decrease in the OCV value, indicating an increase of the ratio of electronic to ionic conductivities.

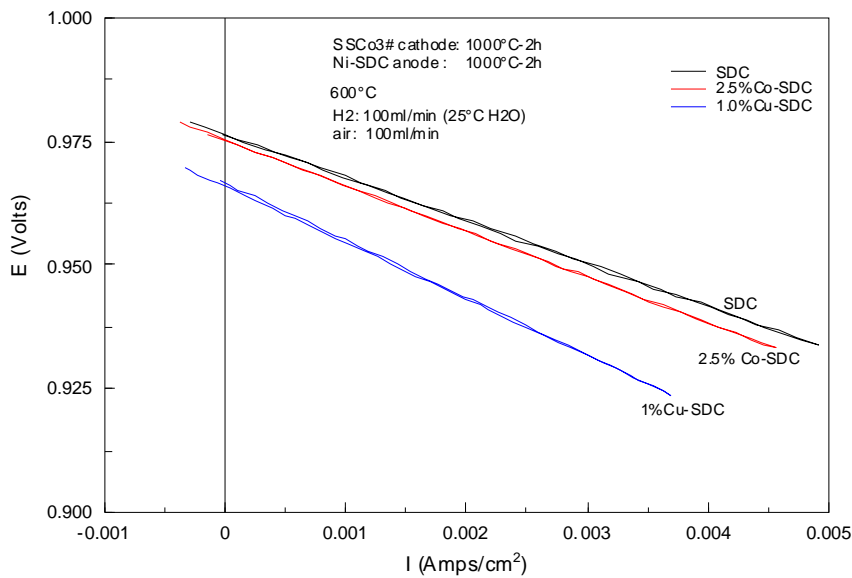


Figure 6-7 Cyclic voltammetry curves at 600°C of three SDC electrolyte cells.

Table 6-4 Electrolyte conductivity at 600°C

Electrolyte	SDC	2.5%Co-SDC	1.0%Cu-SDC
Electrode area [cm <sup>2</sup> ]	0.3529	0.3649	0.3598
Electrolyte thickness [cm]	0.1934	0.2068	0.1972
OCV [V]	0.976	0.975	0.966
Cell resistance [Ω cm <sup>2</sup> ]	9.199	9.21	11.41
Electrolyte conductivity [S cm <sup>-1</sup> ]	2.10 x10 <sup>-2</sup>	2.24 x10 <sup>-2</sup>	1.73 x10 <sup>-2</sup>

### SEM analysis

As shown in Figure 6-8a, the SDC without sintering aids sintered at 1400°C for 5hrs is dense with grain size approximately 1-3  $\mu\text{m}$ . In the case of 1%Co-SDC fired at 1000°C for 5hrs (Figure 6-8b), the surface is slightly rough and the morphology of the starting powder 1%Co-SDC appears on the surface. The measured density of a 1%Co-SDC pellet fired at 1000°C for 5hrs is slightly lower than that of SDC sintered at 1400°C for 5hrs (see Table 6-3).

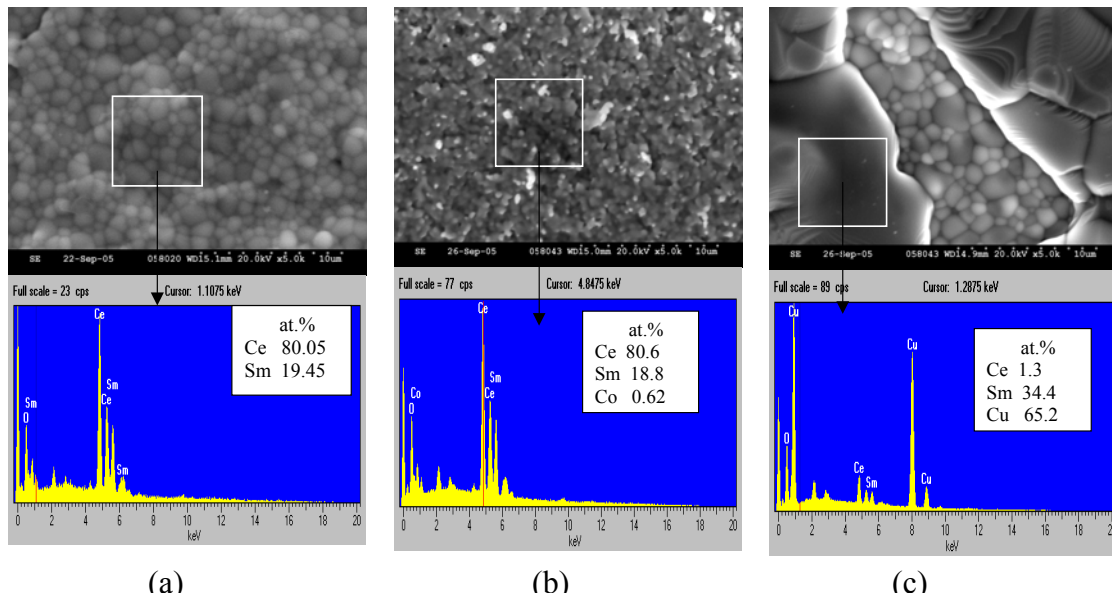


Figure 6-8 SEM and EDS analysis of (a) SDC, (b) 1%Co-SDC, (c) 1%Cu-SDC.

In the 1%Cu-SDC (Figure 6-8c), the SDC particles are well sintered at 1000°C. However, large CuO grains exist at the surface. The EDS result shows the accumulation of Cu at the large grain sites. The SEM image and EDS result validate the existence of  $\text{CuO}_x$  mixed with nearly 35% Sm oxide and 1% Ce oxide on the surface of the 1%Cu-SDC samples. Other Cu-SDC samples show a similar surface morphology. After surface polishing, EDS could not detect the tenorite CuO-rich phase, indicating that the new phase was generated and accumulated at the surface layer of the sample, possibly related to a vapour-condensation formation mechanism.

### *Sintering mechanism of SDC with sintering aids*

For pure SDC, grain boundary and bulk volume diffusion both govern the densification [16]. The linear shrinkage rate is expressed in [16] as follows

$$-\frac{dL}{Ldt} = \frac{\gamma V_a}{kT} \frac{AD_o}{G^n} \exp\left(\frac{-E_a}{kT}\right) \quad \text{Equation 6-1}$$

Here, L is the actual sample length,  $\gamma$  the surface energy,  $V_a$  the atomic volume. A,  $D_o$  and n are the parameters specific to the dominant diffusion mechanisms. For grain boundary diffusion,  $n=4$ , and for volume diffusion,  $n=3$ . G is the actual grain size, k the Boltzmann constant, and T the experienced temperature in Kelvin.  $E_a$  is the activation energy. Provided that A and G are independent of the density, the  $E_a$  of the densification can be determined by plotting  $\ln(-\frac{dL}{Ldt} T)$  versus  $1/T$  at a constant relative density for different heating rates. In most cases G is dependent on density, and the  $E_a$  of the densification can be obtained by plotting  $\ln(\frac{dL}{Ldt} TG^n)$  versus  $1/T$ . The grain size can be obtained from the sintered body and is a function of relative density. In this study, the SDC grain size was not drastically different with (1000°C for 5 hrs) and without (1400°C for 5hrs) sintering aids (see Figure 6-8).

The enhanced sintering behavior of SDC with cobalt oxide sintering aid was attributed to the existence of a Co oxide rich amorphous grain boundary film by Kleinlogel and Gauckler [17]. This grain boundary layer acts as a fast diffusion path during the densification. A model of activated solid-state sintering has been proposed by Johnson and German [18] based on the enhanced densification rate through the formation of a grain boundary layer for the addition of small amounts of aids to a base material. Zhang *et al* [19] elucidated the sintering mechanism of Fe-doped ceria with two different sintering models and found that doping with Fe introduces a viscous flow mechanism in the first stage of sintering. Eva *et al* [16] studied  $Gd_{0.2}Ce_{0.8}O_{1.9}$  (GDC) with 1mol% cobalt oxide by constant heating rate dilatometry. They concluded that cobalt oxide changes the grain boundary structure of GDC, resulting in enhanced mass transport and increased densification rates. While pure GDC exhibits a significant amount of surface diffusion, Co oxide doping enhances grain boundary diffusion. The sintering of Co oxide doped GDC occurs by rearrangement and grain boundary diffusion. The activation energies are  $467 \pm 31$

$\text{kJ mol}^{-1}$  and  $620 \pm 31 \text{ kJ mol}^{-1}$  for pure GDC and with for GDC 1 mol % cobalt oxide, respectively [36].

Meng *et al* [20] employed the Makipirtti-Meng equation for the sintering kinetics of SDC with addition of 5mol% cobalt oxide. They found that addition of cobalt oxide enhanced the densification rate greatly by changing the sintering mechanism. The shrinkage process can be divided into three stages with different apparent activation energies, based on SEM microstructural observation. For the first stage (800-850°C), the sintering relates to the sintering within aggregates ( $E_a = 66.4 \text{ kJ mol}^{-1}$ ). In the second stage (900-1000°C), it relates to acceleration of the surface diffusion and grain boundary diffusion through the amorphous layer ( $E_a = 468 \text{ kJ mol}^{-1}$ ). For the third stage (1050-1150°C), the sintering corresponds to bulk diffusion ( $E_a = 71.8 \text{ kJ mol}^{-1}$ ).

In this study, it seems that Co-SDC samples follow the above-mentioned activated solid-state sintering models [16-20]. The small grain size in the sintered Co-SDC samples suggests that most of the densification is accomplished by rearrangement of grains and grain boundary diffusion. However, in Cu-SDC samples, a new phase of low melting point with composition of Cu-Sm-Ce- $\text{O}_x$  was found, and the fast densification could be due to liquid phase diffusion under capillary action along with grain rearrangement.

## 6.4 Conclusions

Commercial 0.4 micrometer-sized SDC powder could be sintered to 93% of full density below 1000°C by adding 1at% Cu or Co oxide. Sintering of Cu- or Co-SDC powder at 1000°C gave sufficient density with limited grain growth of the original SDC powder. SDC with Cu addition shows the lowest sintering temperature and has its fastest sintering rate at 920°C, which is 300°C lower than that of the SDC powder. However, an impurity phase consisting of 65% Cu oxide and 35% Sm oxide was found at the surface after densification at 1000°C, which can be removed by surface polishing. SDC with 2.5at%Co shows limited impact on the SDC electrochemical properties, while reducing the sintering temperature to below 1000°C.

## 6.5 References

1. Z. Shao, S. M. Haile, *Nature* 431 (2005) 170.
2. X. Zhang, M. Robertson, C. Decès-Petit, Y. Xie, R. Hui, S. Yick, E. Styles, J. Roller, O. Kesler, R. Maric, and D. Ghosh, *J. Power Sources* 161 (2006) 301.
3. H. Yoshida, T. Inagaki, *J. Alloys and Compounds* 408-412 (2006) 632.
4. J. F. Braumard, C. Gault and A. Argoitia, *J. the less-Common Metals* 127 (1987) 125.
5. T. Kudo and H. Obayashi, *J. Electrochem. Soc.* 122 (1975) 142.
6. H. Yahiro, K. Eguchi and H. Arai, *J. Electrochem. Soc.* 135 (1998) 2077.
7. Y. Zhou and M. N. Rahaman, *Acta Materialia* 45 (1997) 3635.
8. K. Yamashita, K. V. Ramanujachary and M. Greenblatt, *Solid State Ionics* 81 (1995) 53.
9. J. Li, T. Ikegami, and T. Mori, *Acta Materialia* 52 (2004) 2221.
10. T. S. Zhang, J. Ma, Y. L. B. Kong, P. Hing, Y. J. Leng, S. H. Chan, and J. A. Kilner, *J. Power Sources* 124 (2003) 26.
11. D. J. Seo, K. O. Ryn, S. B. Park, K. Y. Kim and R. H. Song, *Materials Research Bulletin* 41 (2006) 359.
12. C. Kleinogel, L. J. Gauckler, *Solid State Ionics* 135 (2000) 567.
13. T. S. Zhang, J. Ma, Y. J. Leng, S. H. Chan, P. Hing, and J. A. Kilner, *Solid State Ionics* 168 (2004) 187.
14. T. S. Zhang, P. Hing, H. T. Huang and J. A. Kilner, *J. Eur. Ceram. Soc.* 21 (2001) 221.
15. J. S. Lee, K. H. Choi, B. K. Ryu, B. C. Shin and I. S. Kim, *Ceramics International* 30 (2004) 807.
16. E. Jud, C. B. Huwiler, and L. J. Gauckler, *J. Am. Ceram. Soc.* 88 (2005) 3013.
17. C. Keinogel and L. J. Gauckler, *Solid state Ionics* 135 (2000) 567.
18. R. M. German and B. H. Rabin, *Powder Metall.* 28 (1985) 7.
19. T. S. Zhang, P. Hing, H. T. Huang, and D. L. Johnson, *J. Mater. Sci.* 37 (2002) 997.
20. R. Yan, F. Chu, Q. Ma, X. Liu, and G. Meng, *Materials letter* 60 (2006) 3605.

## 7. Chapter Seven. A study on the Interaction between Electrolyte Materials<sup>7</sup>

Bi-layered electrolytes have been envisioned as a solution to improve fuel efficiency of solid oxide fuel cells operating at intermediate temperature compared to SOFCs using only doped ceria based electrolytes, but performance could be degraded if interfacial reactions occur during fabrication or operation. In the present work, interactions between Samaria Doped Ceria (SDC) and Yttria or Scandia Stabilized Zirconia (YSZ or SSZ) were studied. The effect of sintering aids on the formation of zirconia-ceria solid solutions was also investigated. A new phase was observed in the XRD pattern for each mixture. In the SDC-YSZ mixture, the new phase was completely formed at 1300°C, with further shrinkage observed when the temperature was increased to 1400°C. Adding sintering aids such as copper oxide or cobalt oxide significantly decreased the sintering temperature of the mixtures, and it also decreased the temperature above which the new phase appears. The new phase appeared at 1100°C with copper oxide and at 1200°C with cobalt oxide.

### 7.1 Introduction

In the development of intermediate to low temperature SOFCs, ceria-based electrolytes have been envisioned as a possible candidate for the electrolyte because of the higher ionic conductivity of ceria compared to zirconia. However, ceria-based materials such as samaria, gadolinia, or lanthana doped ceria exhibit some electronic conductivity [1-5] that is detrimental to the overall fuel efficiency of the cell.

The addition of an electronic blocking layer could represent an interesting solution to improve the fuel efficiency of ceria-based fuel cells. A thin layer of zirconia-based material has been deposited on one side of the ceria-based electrolyte to block the electronic conductivity [6, 7]. However, it has been reported in the open literature that a reaction occurs between ceria and zirconia based materials, which have been widely studied for car exhaust converters. Zhang *et al* [8] reported a possible interaction between yttria stabilized zirconia (8YSZ) and samaria doped ceria (SDC). While using micro-size powders of nickel

---

<sup>7</sup> A version of this chapter has been published as:

C.Decès-Petit, X.Zhang, R. Maric, Effect of sintering aids on the formation of zirconia-ceria solid solution, ECS Trans. 7 (2007) 2277.

oxide and 8YSZ for the substrate, NiO and SDC for the anode, and SDC for the electrolyte, islands of zirconia-rich phase were found on the electrolyte surface after co-sintering at 1400°C, as discussed in chapters 4 and 6. Recent work [9] on sintering of mixtures of nano-size powders of 8YSZ and SDC reported the formation of a solid solution at temperatures as low as 850°C.

In the present study, we examine in more detail the interaction between micro-size powders of ceria and zirconia during the sintering process and the influence of sintering aids on the densification process and the interactions.

## 7.2 Experimental procedure

Submicron powders of SDC, 8YSZ and scandia stabilized Zirconia (SSZ) were purchased from Praxair Specialty Ceramics, Tosoh Corp., and Daiichi Kigenso Kagaku Kogyo Corp., respectively. Cobalt and copper nitrites were purchased from Alpha Aesar. Table 7-1 summarizes the properties of each supplied material.

Table 7-1 Supplied materials properties

Material	Composition	Properties	Supplier
SDC	$\text{Sm}_{0.2}\text{Ce}_{0.8}\text{O}_{1.9}$	$D_{50} = 0.40 \mu\text{m} - S_{\text{area}} = 7.1 \text{ m}^2 \cdot \text{g}^{-1}$	Praxair Specialty Ceramics
8YSZ	$(\text{YO}_{1.5})_{0.16}(\text{ZrO}_2)_{0.84}$	$D_{50} = 0.46 \mu\text{m} - S_{\text{area}} = 7.0 \text{ m}^2 \cdot \text{g}^{-1}$	Tosoh Corp.
SSZ	$(\text{ScO}_{1.5})_{0.20}(\text{CeO}_2)_{0.01}(\text{ZrO}_2)_{0.79}$	$D_{50} = 0.46 \mu\text{m} - S_{\text{area}} = 7.0 \text{ m}^2 \cdot \text{g}^{-1}$	Daiichi Corp.
Co	$\text{Co}(\text{NO}_3)_2 \cdot \text{H}_2\text{O}$	Formula Weight (FW) 291.04	Alpha Aesar
Cu	$\text{Cu}(\text{NO}_3)_2 \cdot 3\text{H}_2\text{O}$	Formula Weight (FW) 241.60	Alpha Aesar

The preparation procedure of SDC with copper oxide or cobalt oxide as sintering aids was reported in a previous study [10] and batches prepared with 1 at% of sintering aid were used in this present work.

Four powder mixtures were ground dry for 5 minutes using an agate mortar and a pestle. The preparation ratios are given in Table 7-2. Four pellets were made from each powder mixture using 0.5 g for each pellet. Each pellet was pressed using a 13 mm pellet die and a hand press. The pressure was gradually increased to 50 MPa and maintained for 1 minute. One pellet from each mixture was sintered on a porous alumina plate following the

schedule described in Table 7-2. The ramp rate in heating and cooling was 3 °C min<sup>-1</sup>. The target temperature was maintained for 2 hours.

Table 7-2 Sample composition and sintering schedule

Mixture	Composition	Pellet identification	Sintering temperature, °C			
A	1 g 8YSZ + 1 g SDC 20	1	800	1000	1200	1400
		2	850	1050		
		3	900	1100	1300	
		4	950	1150		
B	1 g 8YSZ + 1 g SDC 20-1%Co	1	800	1000	1200	1400
		2	850	1050		
		3	900	1100	1300	
		4	950	1150		
C	1 g 8YSZ + 1 g SDC 20-1%Cu	1	800	1000	1200	1400
		2	850	1050		
		3	900	1100	1300	
		4	950	1150		
D	1 g SSZ + 1 g SDC 20-1%Co	1	800	1000	1200	1400
		2	850	1050		
		3	900	1100	1300	
		4	950	1150		

After sintering, the weight, thickness and diameter of each sample were measured to calculate the density. X-ray diffraction (XRD) was performed at room temperature using a Bruker D8-Advance diffractometer with Cu-K<sub>α</sub> radiation. Each diffractogram was acquired using a Sol-X sensor from 2θ angles of 20° to 80° with step size of 0.02° and 1 second per step. Lattice parameters were calculated based on the cubic structure of each electrolyte material as determined by XRD. The pellets were then re-sintered at a temperature of 200°C higher than the previous temperature, a temperature step high enough to avoid interference from the previous sintering.

## 7.3 Results

### 7.3.1 Sintering

Figure 7-1 shows the densities of each sample after sintering in the temperature range of 850 to 1400°C. Samples sintered at 800°C were too brittle to measure their diameters and thicknesses, and therefore no data were recorded for this sintering temperature.

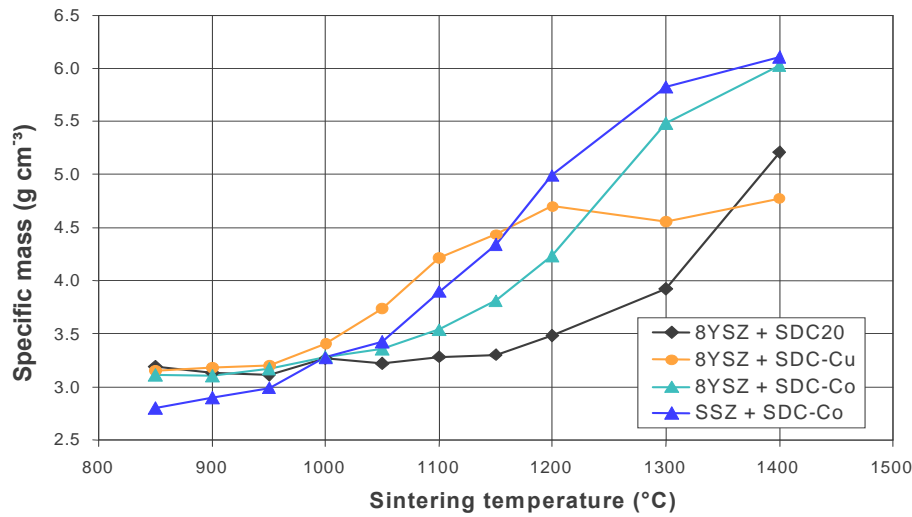


Figure 7-1 Density of sintered samples

It can be seen that no obvious change in the density was observed until 1150°C for the 8YSZ-SDC mixture. At 1400°C, the 8YSZ-SDC sample reached only 83% of the theoretical density. However, effects of sintering aids were clearly observed for the other samples. An increase in density was observed as early as 1000°C for samples containing sintering aids. Fully dense samples were obtained at 1400°C for samples containing cobalt as sintering aid. In the case of copper as a sintering aid, there was no further sintering enhancement between 1200 and 1400°C. At such high temperatures the vapour loss of copper aid could be the reason for this sintering behaviour. On the other hand, an influence of 8YSZ powder in the sintering process of the powder mixtures was obvious compared to a previous study (see Chapter 6, or reference [10]), where copper was found to enhance the most the sintering of SDC. In the case of the SSZ based mixture, there is a continuous change of the density that tends to reach the highest density after a sintering temperature of 1400°C. Higher sinter-ability of the SSZ powder than that of the YSZ powder has been already observed in previous studies (see chapter 2), and contributes to the high density of the SSZ+SDC-Co sample.

### 7.3.2 X-ray diffraction

Figure 7-2 presents the X-ray diffraction pattern obtained for each pellet after sintering and re-sintering. It can be noticed from Figure 7-2 that all the XRD patterns reveal that

SDC peaks are shrinking and disappearing with increasing sintering temperature above the temperature when interaction starts. For the mixture 8YSZ-SDC, that there is no obvious change in the pattern until 1100°C. From 1150°C, the peaks are broadening and weakening, indicating an increase of the crystal disorder. The initial two sets of separated peaks of ceria and zirconia were merged together into one set of peaks from 1300°C, indicating that the two starting electrolyte materials after solid state reaction have changed into a new solid solution or a new phase. When cobalt is used as sintering aid in a similar mixture, as illustrated in Figure 7-2.B, the peaks are broadening at 1050°C, and a single phase is clearly observed from 1200°C. When copper is used as sintering aid, the peaks are broadening from 1000°C and a single phase is clearly observed as low as 1100°C. In the case of the SSZ-SDC-1%Co mixture (Figure 7-2.D), peaks are broadening from a sintering temperature of 1050°C. However, a single phase is observed only after sintering at 1300°C.

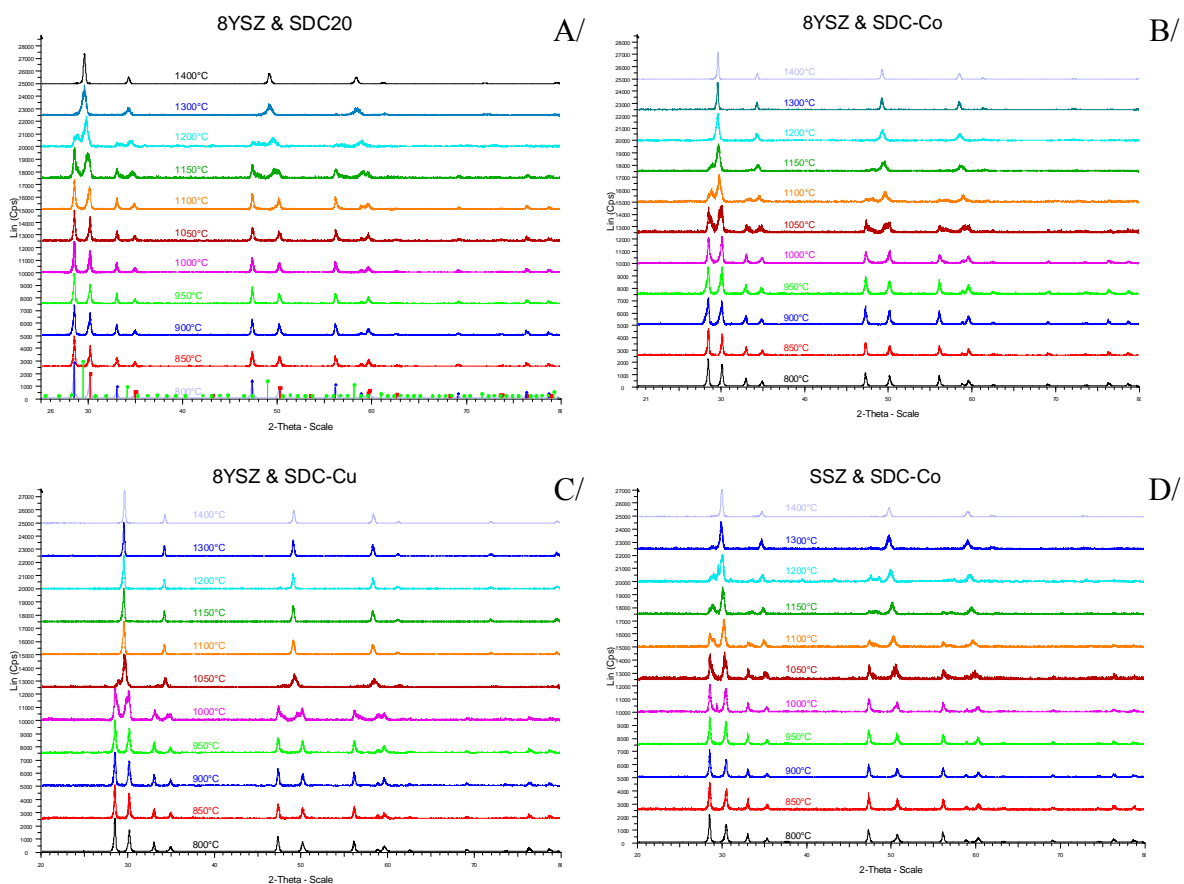


Figure 7-2 X-ray diffraction pattern for each temperature from 800 (lowest curve) to 1400°C (highest curve) for A/ pellets of 8YSZ-SDC, B/ pellets of 8YSZ-SDC-1%Co, C/ pellets of 8YSZ-SDC-1%Cu, and D/ pellets of SSZ-SDC-1%Co.

Changes in the lattice parameter for SDC in the different mixtures at different temperatures are reported in Figure 7-3(i). Each curve ends at a temperature corresponding to the last identified peak attributed to SDC diffraction. A slight decrease in the lattice parameter is observed in each mixture. This result is in agreement with a similar study [11] that reported a decrease in the lattice parameter for an increase in zirconia content in the ceria structure, assuming that interaction between the zirconia and ceria was increasing with the sintering temperature. In the case of the 8YSZ-SDC mixtures, a local maximum is observed at 950°C, which might be an artefact due to our experimental procedure, as the samples are cooled to room temperature for the X-ray diffraction. This might explain the discrepancy in the lattice parameter of SDC in the SSZ-SDC-1%Co mixture as well.

Figure 7-3(ii) displays the changes in the lattice parameters for 8YSZ and SSZ in the four different mixtures. The lattice parameter of SSZ has been referred to a different axis, as its lattice parameter is substantially different from that of 8YSZ. An abrupt change occurs at sintering temperature over 1000°C for 8YSZ-based mixtures. In the case of SSZ - SDC mixture, an abrupt change is observed from 950°C. This temperature difference seems related to the sinter-ability of two powders (see Figures 2-7 and 2-8 in Chapter 2). As shown in Figure 7-3(i) and (ii), the lattice parameters of YSZ and SSZ changed more than those of the SDC powder after the powder mixtures were sintered above 1000°C. The lattice parameter of the SSZ increased 0.0052nm, i.e., from 0.5096 at 1000°C to 0.5148nm at 1150°C. For the same temperature range, the SDC lattice only changed 0.006nm, i.e., from 0.5429 at 1000°C to 0.5423nm at 1150°C. A similar change rate was observed for the YSZ (0.0059nm, from 0.5139nm to 0.5198nm) and SDC lattice parameters (0.0010nm, from original 0.5431 to 0.5421nm) for the YSZ-SDC mixture between 1000°C and 1200°C. Both cases indicate a dominant diffusion rate of the larger cation,  $\text{Ce}^{4+}$  (0.097nm, cation radius) and/or  $\text{Sm}^{3+}$  (0.101nm) to the  $\text{ZrO}_2$ -phase ( $\text{Zr}^{4+}$  0.084nm), leading to expansion of its lattice. This gives an explanation of the observation that the SDC peaks are shrinking and disappearing with increasing temperature above 1000 °C in their XRD patterns. This result is also consistent to some extent with the EDS result (Figure 9-14 in chapter 9) of ‘Ce diffusion to Zr’ in the SSZ/SDC bi-layered electrolyte sintered at 1400°C.

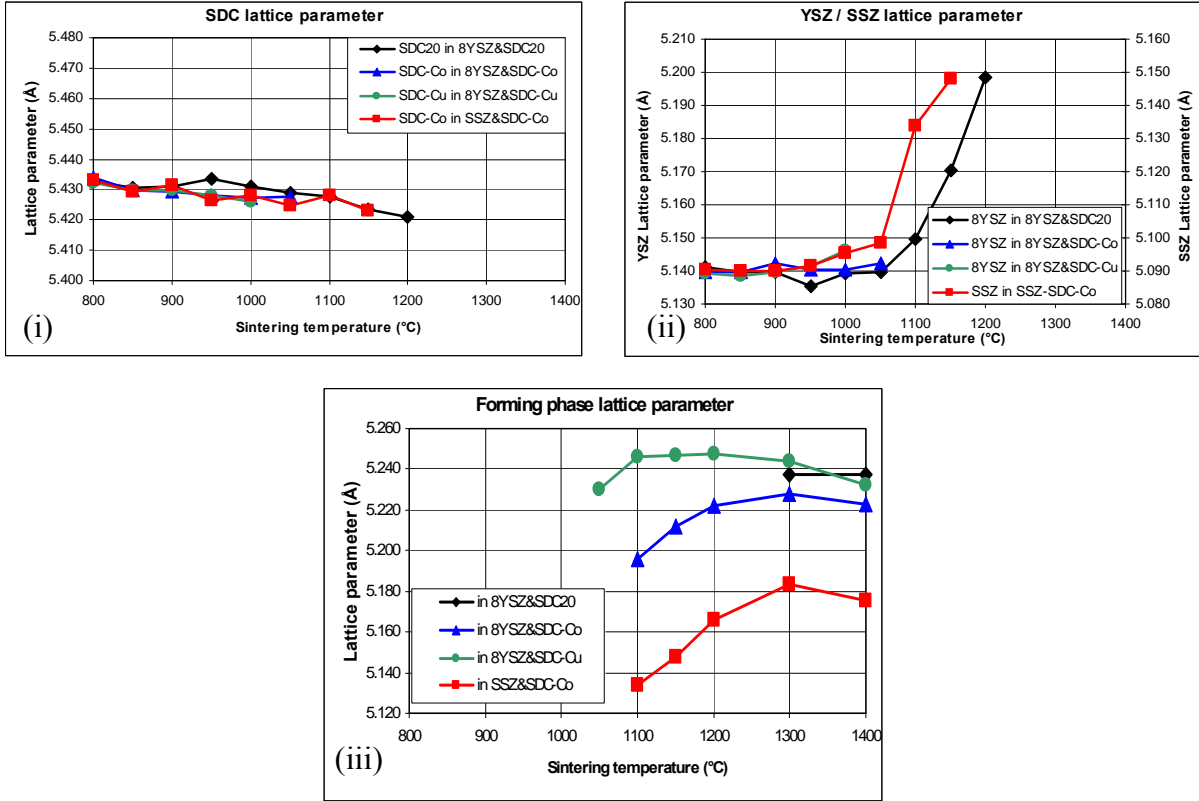


Figure 7-3 Lattice parameter of SDC (graph i), 8YSZ, SSZ (graph ii) and the forming phase (graph iii) for the different mixtures.

Changes of lattice parameter of the forming phase in the mixtures with sintering temperature are displayed in Figure 7-3(iii). For the mixtures based on 8YSZ, the lattice parameters tend to converge as the sintering temperature increases to 1400°C, from approximately 0.5220nm to 0.5240nm. For the SSZ-SDC mixture, the forming phase tends to increase its lattice parameter as the sintering temperature approaches 1400°C, and reaches 0.5175nm at 1400°C. The difference in the forming phase lattice parameters of these two mixtures is mainly attributable to fact that the SSZ lattice parameter is smaller than that of YSZ. It is worth mentioning that caution may be needed to interpret the lattice parameter changes due to the lack of an internal reference during the XRD analyses that would otherwise account for variations in the detector angle with respect to the analyzed sample from one experiment to the next.

## 7.4 Discussion

Table 7-3 summarizes the results of this study. A correlation can be observed between the sintering temperature from which a significant increase in the sample density is observed and the sintering temperature at which XRD peaks are broadening. This observation can be made for each mixture within 50°C.

Nonetheless, while the forming phase can be clearly identified at temperatures depending on the mixture, only samples with cobalt as sintering aids exhibited an asymptotic approach towards a theoretical density.

Table 7-3 Powder mixture results summary

<b>Powder mixture</b>	<b>Sample density starts to increase</b>	<b>Fully dense</b>	<b>XRD peak broadening</b>	<b>Forming phase clearly seen</b>
A	1200°C	>1400°C	1100°C	1300°C
B	1000°C	1400°C	1050°C	1200°C
C	1000°C	>1400°C	1000°C	1100°C
D	1000°C	1400°C	1050°C	1300°C

Mixtures with sintering aids show early changes in the density, almost 200°C lower than the same mixtures without sintering aids. This is in good agreement with previous studies [12, 13] where cobalt was found to enhance the grain boundary diffusion and with another study [14] that attributes the sintering enhancement to a reduction of copper, which would then react with the ceria and zirconia particles.

The forming phase is also seen at lower sintering temperature, approximately 100 to 200°C, for mixtures with sintering aids. It can be concluded that despite the decrease of the sintering temperature caused by the sintering aids, the formation of the solid solution phase between zirconia and ceria seems inevitable. This could be detrimental to the performance of fuel cells with bi-layer electrolytes when using high temperature processing.

Lybye *et al.* [15] reported that doping 2 at.% Co oxide has little effect on the conductivity of Sc and Y co-doped ZrO<sub>2</sub> (Sc<sub>0.16</sub>Y<sub>0.04</sub>Zr<sub>0.80</sub>O<sub>1.9</sub>); however, doping with the same amount of Ce oxide, the conductivity of the electrolyte dropped 40% from 0.275 to 0.172 S cm<sup>-1</sup> at 1000°C. Meanwhile, the electrolyte sinterability was decreased from their dilatometry analysis, by an approximately 50°C shift to higher temperature. They also

found that reduction of the Ce-doped electrolyte increases the conductivity due to the smaller amount of ceria dissolved in zirconia lattice.  $\text{Ce}^{4+}$  (0.097nm) reduction to  $\text{Ce}^{3+}$  (0.115nm) leads to a mismatch of the ionic size with  $\text{Zr}^{4+}$  (0.084nm), and generates electronic conductivity.

## **7.5 Conclusion**

In SDC-YSZ mixtures, the formation of zirconia-ceria solid solution, as a product phase was almost completed at 1300°C. Adding sintering aids such as copper oxide or cobalt oxide significantly decreased the sintering temperature of the mixtures, and it also decreased the temperature at which the solid state reaction appears. The product phase appeared at 1100°C with copper oxide and at 1200°C with cobalt oxide for the SDC powder with 1% of these sintering aids. The large  $\text{ZrO}_2$  lattice expansion reveals the dominant diffusion of the larger cation,  $\text{Ce}^{4+}$ , and/or  $\text{Sm}^{3+}$  from SDC to the  $\text{ZrO}_2$  lattice during the solid state reaction.

## 7.6 References

1. M. Sahibzadab, B. C. H. Steelea, K. Zheng, R. A. Rudkin and I. S. Metcalfeb, *Catalysis Today* 38 (1997) 459.
2. C. M. Kleinlogel and L. J. Gauckler, *J. Electroceram.* 5 (2000) 231.
3. M. Boaro, A. Trovarelli, J.-H. Hwang and T. O. Mason, *Solid State Ionics* 147 (2002) 85.
4. T. Shimonosuno, Y. Hirata, Y. Ehira, S. Sameshima, T. Horita and H. Yokokawa, *Solid State Ionics* 174 (2004) 27.
5. V. Thangadurai and W. Weppner, *Electrochem. Acta* 49 (2004) 1577.
6. Y. Jiang and A. V. Virkar, *J. Electrochem. Soc.* 150 (2003) A942.
7. J.-Y. Park, H. Yoon and E. D. Wachsman, *J. Am. Ceram. Soc.* 88 (2005) 2402.
8. X. Zhang, M. Robertson, C. ces-Petit, Y. Xie, R. Hui, S. Yick, E. Styles, J. Roller, O. Kesler, R. Maric, D. Ghosh, *Journal of Power Sources* 161 (2006) 301.
9. M. Price, J. H. Dong, X. H. Gu; S. A. Speakman, E. A. Payzant, T. M. Nenoff, *J. Am. Ceram. Soc.* 88 (2005) 1812.
10. X. Zhang, C. Decès-Petit, S. Yick, M. Robertson, W. Qu, Y. Xie, S. R. Hui, E. Styles, J. Roller, O. Kesler, R. Maric, D. Ghosh, *J. Power Sources* 162 (2006) 480.
11. V. S. Escribano, E. F. López, M. Panizza, C. Resini, J. M. Gallardo Amores, G. Busca, *Solid State Sciences* 5 (2003) 1369.
12. C. Kleinlogel and L. J. Gauckler, *Solid State Ionics* 135 (2000) 567.
13. E. Jud, C. B. Huwiler and L. J. Gauckler, *J. Am. Ceram. Soc.* 88 (2005) 3013.
14. S. Maschio, O. Sbaizero, S. Meriani and E. Bischoff, *J. Mat. Sci.* 27 (1992) 2734
15. D. Lybye, Y. Liu, M. Mogensen and S. Linderoth, SOFC IX, The Electrochemical Society Inc., Pennigton, NJ, 2005-07 (2005) 954.

## 8. Chapter Eight. Performance of LT-SOFCs with Bi-layered Electrolyte Structure<sup>8</sup>

Solid oxide fuel cells with a bi-layered electrolyte of 2 $\mu\text{m}$  SSZ and 4 $\mu\text{m}$  SDC were developed by using tape casting, screen printing, and co-firing processes. The cells reached power densities of 0.54W cm<sup>-2</sup> at 650°C and 0.85W cm<sup>-2</sup> at 700°C, with open circuit voltage (OCV) values larger than 1.02 V. The electrical leaking between anode and cathode through an SDC electrolyte has been blocked in the bi-layered electrolyte structure. However, both the electrolyte resistance ( $R_{el}$ ) and electrode polarization resistance ( $R_{p,a+c}$ ) increased in comparison to cells with single-layered SDC electrolytes. The formation of a solid solution of (Ce, Zr)O<sub>2-x</sub> during the sintering process and the flaws in the bi-layered electrolyte structure seem to be the main causes for the increase in the  $R_{el}$  value (0.32  $\Omega$  cm<sup>2</sup>) at 650°C, which is almost one order of magnitude higher than the calculated value.

### 8.1 Introduction

A high operating temperature is one of the main barriers to a wide-scale adoption of solid oxide fuel cell (SOFC) technology [1]. Therefore, much work is focused on the development of reduced temperature SOFCs [2]. The practical operating temperature of an SOFC is mainly determined by the conductivity and thickness of the electrolyte. Samaria-doped ceria (SDC) is a promising material for the electrolyte in reduced temperature SOFCs [3, 4]. SDC exhibits a relatively high conductivity of 0.1 S/cm at 800°C [5], 2-3 times higher than that of yttria-stabilized zirconia (YSZ). Its thermal expansion coefficient (12.5 x 10<sup>-6</sup> K<sup>-1</sup>) is also more compatible with that of the Ni-cermet anode and commercial ferritic stainless steel interconnects, than that of YSZ. Although the material exhibits better chemical and structural compatibility with electrodes as well as higher ionic conductivity than YSZ, the reduction of Ce<sup>4+</sup> to Ce<sup>3+</sup> induces n-type electronic conduction, which tends

---

<sup>8</sup> A version of this chapter has been published as:

X. Zhang, M. Robertson, C. Decès-Petit, W. Qu, O. Kesler, R. Maric, D. Ghosh, Solid oxide fuel cells with bi-layered electrolyte structure, *J. Power Sources*, 175 (2008) 800.

to decrease the power output of solid oxide fuel cells due to an internal electrical shorting. The problem can be partially solved by decreasing the operating temperature to below 600°C, as the SDC electrolytic domain is expanded at lower temperatures [6]. However, even at 600°C, the cell appears intolerant to internal shorting due to the low electronic resistance of the thin electrolyte [7]. It has been reported that this problem can be eliminated by using a barrier of a thin ZrO<sub>2</sub>-based electrolyte layer deposited on the anode side of the SDC electrolyte layer to improve the stability of the SDC layer under the reducing anode atmosphere. This configuration is generally called a bi-layered electrolyte structure [8-11]. The ionic conductivity of scandia-stabilized zirconia (SSZ) is the highest among all the ZrO<sub>2</sub>-based electrolytes [12]; however, it is not considered as a candidate electrolyte for reduced temperature SOFCs since its conductivity decreases rapidly with temperatures below 800°C [13]. When a bi-layer SDC/SSZ electrolyte is used, the SSZ layer acts mainly as the electronic barrier. If the SSZ layer thickness is in the range of a few micrometers to a few hundred nanometers, its relatively low conductivity will not contribute significantly to the overall ohmic loss of the bi-layer SDC/SSZ electrolyte for SOFCs.

For the fabrication of anode-supported SOFCs, wet ceramic processes such as screen printing and tape casting have been widely adopted, and have proven to be scalable and cost-effective [14]. A peak power density of 0.6 W cm<sup>-2</sup> at 700°C has previously been obtained in an anode-supported cell with a YSZ/SDC bi-layered electrolyte by electrophoretic deposition [15] and by screen printing and co-firing [9]. Recently, Wang et al. [16] used a multi-layer tape casting procedure to fabricate an anode-supported 5 μm SSZ/10 μm GDC bi-layered electrolyte cell. With an LSCF-GDC composite cathode sintered at 1100°C, they obtained a maximum power density of 0.63 W cm<sup>-2</sup> and an area-specific resistance (ASR) of 0.99 Ω cm<sup>2</sup> at 850°C in a single cell with H<sub>2</sub>/O<sub>2</sub> as the operating gases.

In this work, anode-supported cells with SSZ/SDC bi-layered electrolytes were fabricated by screen printing and co-firing under optimized processing conditions to control the layer thickness. The obtained cell results are promising for reduced temperature applications.

## 8.2 Experimental procedure

### 8.2.1 Starting materials and cell architectures

Table 8-1 lists the cell materials, thicknesses, and processing conditions used to fabricate the cells. The starting ceramic powder materials used in this study were commercially obtained (cf. Chapter 2). The cell structure consists of a NiO-YSZ cermet substrate, NiO-SSZ anode layer, SSZ/SDC bi-layered electrolyte, and SSC cathode. 1 at.%Co was added to the SDC powder for controlling the sintering behaviour—the treatment and sinterability improvements have been reported in our previous work [17]. A 57wt% NiO and 43wt% YSZ powder mixture was used for the NiO-YSZ cermet substrate. The composition of the NiO-SSZ anode was 56wt% NiO and 44wt% SSZ. The cell was fabricated by tape casting the substrate, screen printing the anode and the electrolyte on the substrate tape, and then co-firing at 1400°C for 2 hrs, followed by cathode printing and sintering *in-situ* during the test. Further details about the cell fabrication process and characterization can be found in Chapter 3 and references [4, 7, 9]. The cell used in this study was 16 mm in diameter. The printed  $\text{Sm}_{0.5}\text{Sr}_{0.5}\text{CoO}_3$  (SSC) cathode area was 0.50 cm<sup>2</sup>, which was the cell’s projected active area used in this work.

Table 8-1 Cell materials, thicknesses, and processing conditions

Cell component	Material	Thickness $\mu\text{m}$	Process	Firing condition		Porosity
Cathode	SSC	50	Stencil printing	<i>In-situ</i> heat up to 650°C at first, up to 800°C during test		~ 40%
Electrolyte	SDC-1%Co SSZ	4 2	Screen printing	1400°C	2hr	Dense and passes helium cross leak test [7, 9] 19% before reduction, 37% after reduction
Anode	NiO-SSZ	10	Screen printing			
Substrate	NiO-YSZ	800	Tape casting			

The average density of the cell substrate after the anode layer deposition was  $5.1 \text{ g cm}^{-3}$  measured by Archimedes' method. It indicated a 19.4% porosity in the NiO-YSZ cermet substrate based on the cermet substrate composition of 57wt% NiO. The substrate porosity increases to approximately 37% after full reduction of NiO to Ni with hydrogen gas, based on the theoretical densities of the materials.

## 8.2.2 Cell electrochemical and morphological characterizations

The cell electrochemical measurement was conducted in a lab-built horizontal button cell test station, which has been described in Chapter 3 and [4, 7, 9]. The cell was heated up to  $650^\circ\text{C}$  at a ramp rate of  $300^\circ\text{C h}^{-1}$ , and held at  $650^\circ\text{C}$  for 1hr for reduction and in-situ sintering of the cathode layer. The reduction was carried out by anode gas with  $\text{H}_2$  concentrations varying step-wise from 10%, 20%, 40%, 60%, to a final 100%, with  $\text{N}_2$  balance. Each concentration was held for 15 mins. The anode gas was first passed at a flow rate of  $100 \text{ ml min}^{-1}$  through a bubbler-type humidifier at room temperature. The humidified hydrogen gas (corresponding to 3%  $\text{H}_2\text{O}$  content) was then introduced to the anode side during the cell test. Ambient air was introduced at a flow rate of  $100 \text{ ml min}^{-1}$  to the cathode side. Electrochemical measurements were performed at temperatures ranging from  $550^\circ\text{C}$  to  $800^\circ\text{C}$ , and then during cool-down to  $550^\circ\text{C}$ . The I-V curve and impedance tests were performed at intervals of  $50^\circ\text{C}$  between  $550^\circ\text{C}$  and  $800^\circ\text{C}$ . Cell performance was measured with a Multi-channel Potentiostat/Galvanostat (Solartron 1480 8-channel multi-stat) coupled with a 1260 FRA using the software Corrview and Z-plot. The current-voltage-power (I-V-P) curves were obtained using linear sweep voltametry at a sweep rate of  $4 \text{ mV s}^{-1}$  from OCV to 0.3 V. The impedances were measured in the frequency range of  $10 \text{ kHz}$ - $0.1 \text{ Hz}$  with a perturbation potential amplitude of 50mV.

The morphologies of the tested cells were observed using a scanning electron microscope (SEM, Hitachi S-3500N), coupled with energy dispersive spectroscopy (EDS) and X-ray diffraction techniques for elemental and phase analysis, respectively. Each sample was coated with Au-Pd alloy before observation.

## 8.3 Results and discussion

### 8.3.1 Electrolyte thickness control

In order to effectively utilize the SSZ/SDC bi-layer electrolyte concept for reduced temperature SOFCs, the SSZ bottom layer should be as thin as possible and also be gas impermeable. We examined the paste solid loading and screen mesh effects on the SSZ layer thickness (see Table 8-2). It was found that by reducing the solid loading to 7.3 vol.% and increasing the screen mesh number from 200# to 325# (note: mesh number means the number of openings per square inch area), the final printed layer thickness per print-pass after sintering could be controlled to under 2 $\mu$ m. It was also noticed that the thickness of the anode layer played an important role in the final electrolyte quality during the co-firing at 1400°C for 2hrs. All the cells with bi-layered electrolytes and anode layer passed the 1 psi Helium cross-leakage test, indicating the intactness and density of the electrolyte layer, as illustrated in Figures 1 and 2.

Table 8-2 SSZ printed thickness with different SSZ loadings (Binder:SSZ =8:92 weight ratio)

Paste #	SSZ wt ratio*	SSZ vol ratio*	Density g cm <sup>-3</sup>	65mm x 65 mm dry print weight, g	Thickness, $\mu$ m	
					dry print	sintered
1	0.488	0.152	1.870	0.112	6.41	4.09
2	0.428	0.124	1.732	0.089	5.20	3.24
3	0.382	0.104	1.637	0.069	4.70	2.51
4	0.344	0.090	1.568	0.067	4.11	2.45
5	0.314	0.079	1.516	0.063	3.76	2.31
6	0.288	0.071	1.475	0.052	2.87	1.90
7	0.267	0.064	1.443	0.048	2.73	1.77
8	0.249	0.059	1.416	0.027	2.36	0.97

\* SSZ to (SSZ+ Organics)

The interdiffusion (or interaction) between electrolyte layers at co-firing conditions is the main concern, which has been reported in Chapter 7 [15, 19]. Figure 8-3 shows the EDS elemental mapping at the cross-section of the electrolyte portion of a cell. The results clearly indicate that the different layers of the anode, SSZ, and SDC can be easily identified. The interdiffusion (or interaction) zone, if it is generated during the co-firing,

seems to be within 1 $\mu$ m; otherwise, we would not have been able to clearly see the SSZ layer, which is designed and observed to have a thickness of 2 $\mu$ m.



Figure 8-1 SEM image of the bi-layered SDC/SSZ electrolyte surface

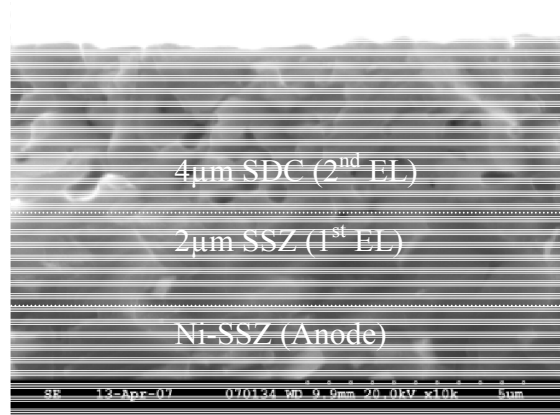


Figure 8-2 SEM image of cross-section of the bi-layered SDC/SSZ electrolyte.

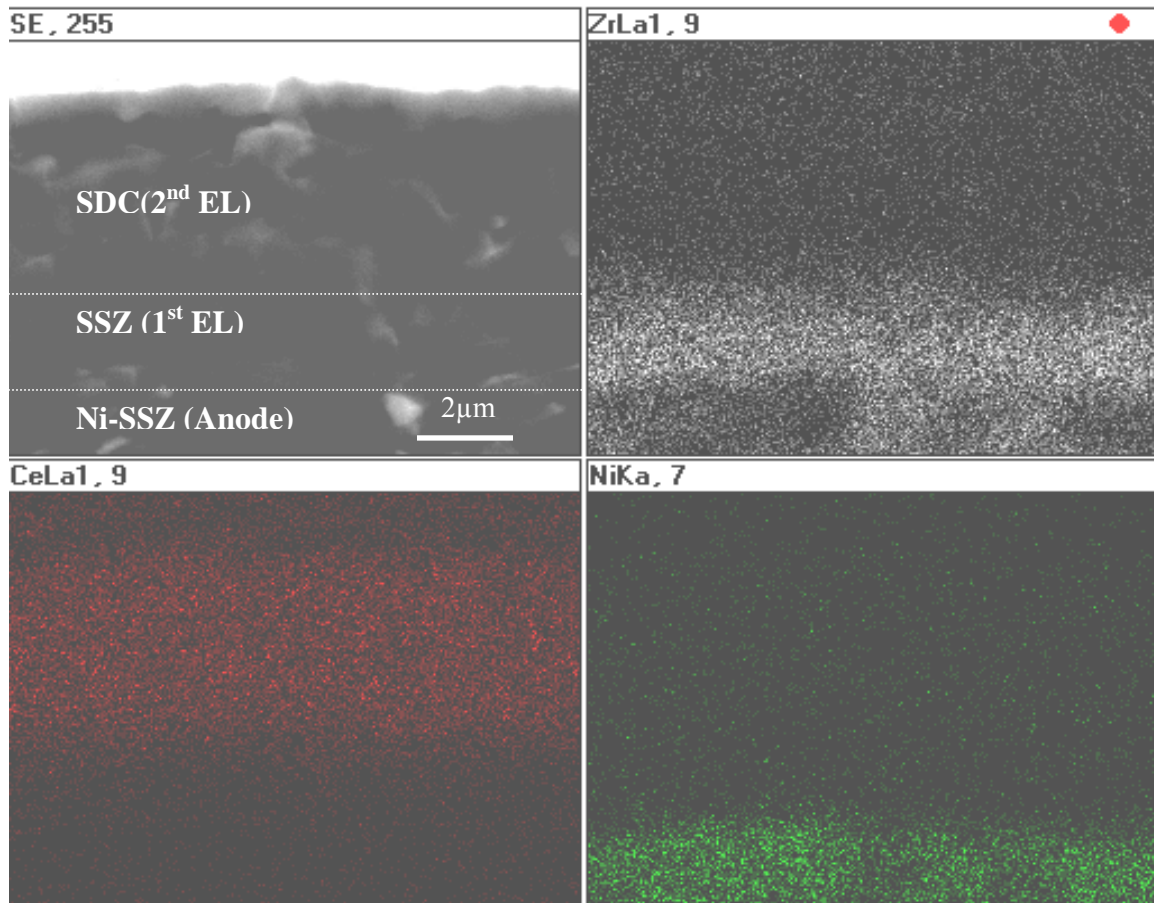


Figure 8-3 EDS element mapping (see Figure 8-2).

It is worthwhile to mention that SDC-1%Co oxide does not show any sinterability improvement in comparison to pure SDC [9]. In our previous work with bulk pellets, it showed about a 200–300°C difference in the temperature required for full densification [17], and many authors reported similar results. Hansch *et al.* [21] in their study of the influence of the addition of a pre-reacted mixture of manganese oxide and boron oxide on the densification behaviour of 8YSZ obtained similar discrepancy results between bulk pellets and thin layers of electrolytes with sintering aids. They explained that in the case of the pellets the amount of liquid phase is high enough to wet the grain boundaries, while in coating thin layers, the amount of the active phase is too low to fill the larger space between the single grains. As we know, a complete wetting of the grain boundaries is essential for the densification.

### 8.3.2 Cell test result

An SSC cathode was applied onto the surface of the bi-layered electrolyte by stencil printing, followed by drying and *in-situ* sintering at 650°C. The unit cell thus prepared was characterized for its electrochemical performance.

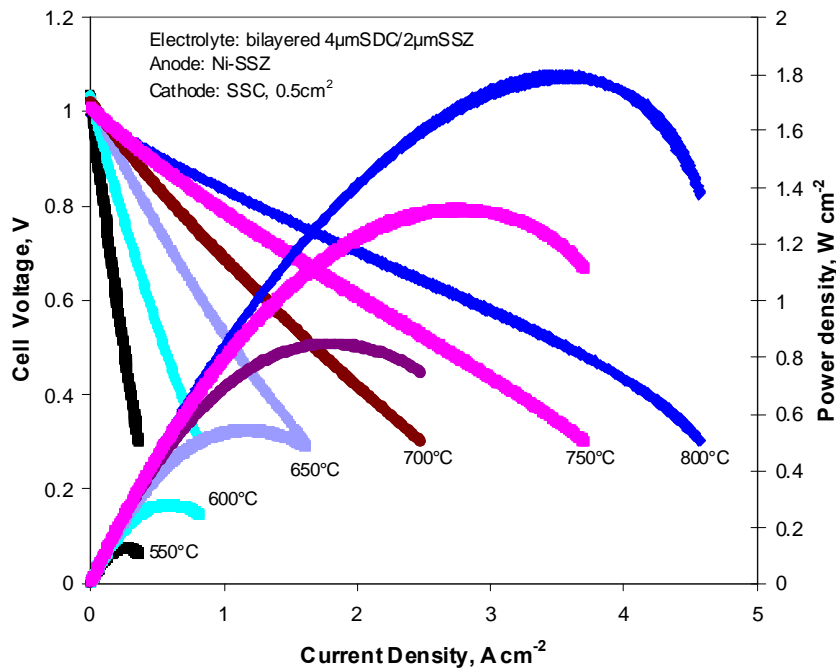


Figure 8-4 I–V–Power curves of the bi-layer electrolyte cell at different operating temperatures.

Figure 8-4 shows the cell performance with the SSC cathode *in-situ* sintered. It can be seen that the cell shows very high performance in the tested temperature range of 550–800°C. The peak power density reached 1.8 W cm<sup>-2</sup> at 800°C, and approximately 0.54W cm<sup>-2</sup> even at 650°C. What is most significant is that the cell showed a very high OCV value, 1.03 V, in comparison to the single-layer 20 μm-SDC electrolyte cells, which only showed an OCV of 0.84 V at 650°C in Chapter 4 and [18]. A high OCV value indicates that there is very low electronic conductivity and few physical defects (cracks, pin-holes, etc.) in the SSZ/SDC bi-layered electrolyte. Compared to the results in previously reported literature [9, 15, 16], our bi-layered cells fabricated by conventional ceramic processing showed an improved performance, and still exhibit significant power density even at 650°C.

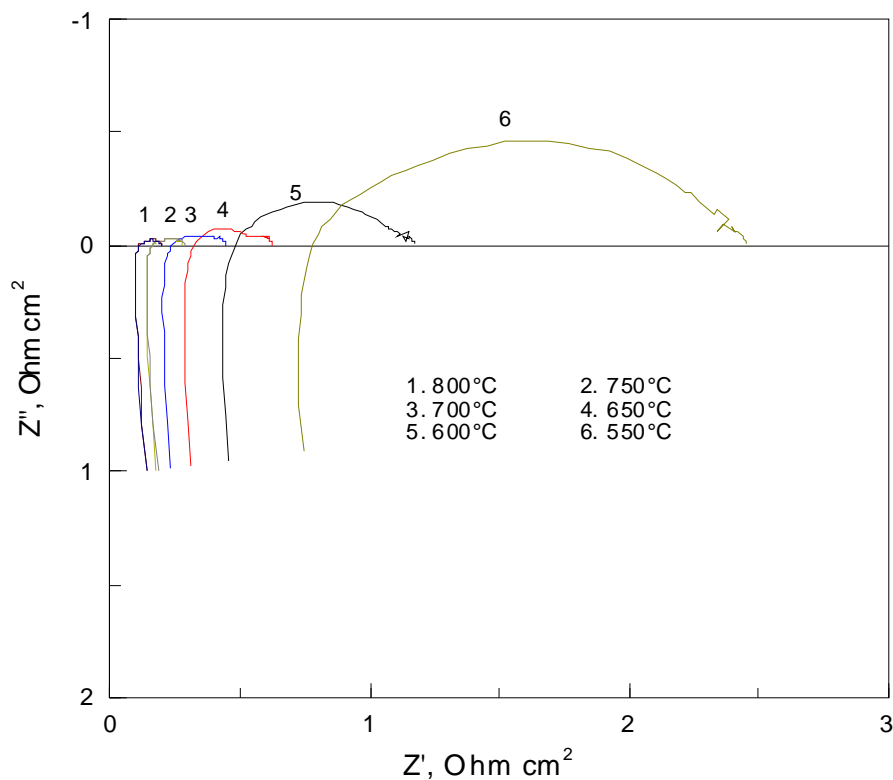


Figure 8-5 EIS spectra of the cell at different temperatures.

Figure 8-5 shows the electrochemical impedance spectra of the cell at different temperatures. The measured results are also listed in Table 8-3.

Table 8-3 Cell performance and cell resistances

Temperature [°C]	OCV [V]	PPD [W cm <sup>-2</sup> ]	R <sub>el</sub> [Ω cm <sup>2</sup> ]	R <sub>p,a+c</sub> [Ω cm <sup>2</sup> ]	R <sub>t</sub> [Ω cm <sup>2</sup> ]
550	1.037	0.127	0.760	1.717	2.477
600	1.038	0.281	0.461	0.704	1.165
650	1.025	0.545	0.311	0.390	0.701
700	1.023	0.850	0.222	0.211	0.433
750	1.009	1.326	0.152	0.127	0.278
800	0.994	1.800	0.105	0.091	0.196

OCV: open circuit voltage,

PPD: peak power density,

R<sub>el</sub>: SSZ/SDC bi-layered electrolyte ohmic resistance from EIS,

R<sub>p,a+c</sub>: electrode polarization resistance from EIS,

R<sub>t</sub>: cell resistance from EIS ( $R_t = R_{el} + R_{p,a+c}$ )

In comparison with our previous work on cells with thin SDC electrolytes (10μm) [7], it is very clear that the values of electrolyte resistance, R<sub>el</sub>, and electrode polarization resistances, R<sub>p,a+c</sub>, have increased significantly along with the increase in the OCV values. The reported R<sub>el</sub> and R<sub>p, a+c</sub> values of the cell with 10μm SDC electrolyte are only 0.10 Ω cm<sup>2</sup> and 0.12 Ω cm<sup>2</sup> at 600°C, respectively, while for the bi-layered electrolyte in this study they increased to 0.46 Ω cm<sup>2</sup> and 0.70 Ω cm<sup>2</sup>, respectively. The increase in R<sub>p, a+c</sub> may have had contributions from the electrodes, since the compositions in these two studies are different. In the case of the cell with SDC electrolyte, a Ni-SDC anode was used, while in this study of bi-layered electrolytes, however, the anode is Ni-SSZ. Since SDC has higher ionic and electronic conductivities than those of SSZ, the SDC mixed conductor in the anode will help to improve the anode performance. The previous study also used a composite SSC-SDC cathode, while this study uses a single phase SSC cathode. In addition, mixed conductivity in the electrolyte can make the apparent polarization resistance of the electrodes smaller than their actual values due to the electronic current that

passes through the electrolyte. Furthermore, an increment in  $R_{el}$  is obviously noticeable. In this study,  $R_{el}$  consisted of three parts:  $R_{el,SSZ}$ ,  $R_{el,SDC}$ , and  $R_{interface}$ . Based on the SSZ ionic conductivity of  $0.08 \text{ S cm}^{-1}$  [19] and  $0.076$  in this work (see Table 12-8 in Appendix B) at  $800^\circ\text{C}$ , the  $R_{el,SSZ}$  of the  $2\mu\text{m}$  thick SSZ electrolyte was approximately  $0.0025\text{-}0.0026 \Omega \text{ cm}^2$ . Meanwhile, the  $R_{el,SDC}$  of the  $4\mu\text{m}$  thick SDC electrolyte was estimated to be  $0.004\text{-}0.0043 \Omega \text{ cm}^2$ , according to our measured results and published conductivity data of SDC of  $0.10 \text{ S cm}^{-1}$  at  $800^\circ\text{C}$  [5], and  $0.091$  in this study (see Table 12-8 in Appendix B). In comparison with the  $R_{el}$  value ( $0.105\Omega \text{ cm}^2$ ) at  $800^\circ\text{C}$  shown in Table 8-3, both contributions can be considered negligible. Thus, the  $R_{interface}$  can be as high as  $0.099 \Omega \text{ cm}^2$ , over 90% of the total electrolyte ohmic resistance. It is well reported that the interdiffusion produced by the  $(\text{Zr,Ce})\text{O}_2$ -based solid solution leads to a conductivity that is two to four times lower than that of the SSZ, and is one order of magnitude lower than that of the SDC [19].

Table 8-4 Ionic conductivity ( $\sigma_i$ ) and electronic conductivity ( $\sigma_e$ ) of YSZ, GDC and the mixed composites at  $800^\circ\text{C}$  [20]

Material	Nominal composition	$\sigma_i$ [ $\text{S m}^{-1}$ ]	$\sigma_e$ [ $\text{S m}^{-1}$ ]
YSZ	$\text{Zr}_{0.85}\text{Y}_{0.15}\text{O}_{1.93}$	5.4	$7.29 \times 10^{-11}$
GDC	$\text{Ce}_{0.80}\text{Gd}_{0.20}\text{O}_{1.90}$	8.7	$8.18 \times 10^{-4}$
Reaction product	$\text{Ce}_{0.37}\text{Zr}_{0.38}\text{Gd}_{0.18}\text{Y}_{0.07}\text{O}_{1.87}$	0.125	$3.99 \times 10^{-4}$
Interlayer	$\text{Ce}_{0.43}\text{Zr}_{0.43}\text{Gd}_{0.10}\text{Y}_{0.04}\text{O}_{1.93}$	0.603	$3.88 \times 10^{-4}$

Table 8-4 lists the ionic conductivity and electronic conductivity of YSZ, GDC, and the mixed composites at  $800^\circ\text{C}$  [20]. It is well known that the interaction produces a poor ionic conducting phase. This gives an explanation as to why such a thin layer (even less than  $1\mu\text{m}$ ) dominates the  $R_{el}$  value in the bi-layered electrolyte. The thickness of the  $(\text{Zr,Ce})\text{O}_2$ -based solid solution formed at the SSZ/CGO interface during high temperature sintering plays a key role in the  $R_{el}$  value. The  $R_{interface}$  in this study is almost 3 times lower than a previously reported value of  $0.283 \Omega \text{ cm}^2$  for the SSZ/GDC system, which showed an interdiffusion layer zone of approximately  $3\mu\text{m}$  in thickness by EDS mapping [18]. The thickness of the interdiffusion layer zone is obviously related to the starting material and

processing conditions. We used an SSZ/SDC electrolyte combination and fired at 1400°C for 2 hours, while Wang et al. [16] used SSZ/GDC fired at the same sintering temperature, but for 4hrs. Since interdiffusion is a thermally activated process, reducing sintering temperature and sintering time should be an effective approach to reducing the  $R_{\text{interface}}$ . However, we found that when decreasing the sintering temperature to 1300°C, the bi-layered electrolyte is not well bonded together, and also the electrolyte, especially the SDC layer, is not well sintered. As a result, there is no improvement in the cell quality or cell performance.

We calculated the apparent activation energy for the total electrical conduction of the bi-layered electrolyte based on the values listed in Table 8-3 and found that the apparent activation energy is 64.77 kJ mol<sup>-1</sup>, which is very close to what we obtained before for a single-layered SDC electrolyte (61.75 kJ mol<sup>-1</sup>, see Chapter 5 and [7]) and other published values of 61.75 kJ mol<sup>-1</sup> [16] and 64.0 kJ mol<sup>-1</sup> [6]. This reveals that the conduction mechanism of the bi-layered electrolyte had not changed significantly from the main electrolyte of SDC in this study.

The results obtained in this study illustrate that the fabrication of anode-supported electrolyte films for planar SOFCs with an SSZ electrolyte electron-blocking layer is possible by multi-layer screen printing on tape-cast substrates. The technique is both cost-effective and feasible. The results achieved have met the performance targets set at the beginning of this dissertation work. The interfacial reaction between SSZ and SDC can be tailored to some extent to reach a higher cell performance. Future work will focus on cell stability and further cell performance improvement.

## **8.4 Conclusion**

Cermet-supported solid oxide fuel cells with bi-layered electrolytes of SSZ and SDC were successfully prepared by multi-layer screen printing on tape cast NiO-YSZ cermet substrates. No cracking or delaminating was observed after co-firing at 1400°C for 2hrs. The open circuit voltage of the cell reached over 1.02 V below 750°C, and the maximum power density reached 1.8 W cm<sup>-2</sup> at 800°C. The internal shorting of a single-layer SDC electrolyte cell has been mostly eliminated. The OCV value at 650°C reached 1.025V.

Electrochemical impedance measurement results revealed that the ohmic resistance at the SSZ/SDC interface ( $R_{\text{interface}}$ ) dominates the whole electrolyte resistance. Meanwhile, the electrode polarization resistance ( $R_{\text{p, a+c}}$ ) is approximately half of the total cell resistance over the temperature range from 650 to 800°C. This work demonstrates that cost-effective wet ceramic processing can be useful for bi-layered electrolyte cell fabrication. The demonstrated cell performance is very attractive for SOFC applications, and has met the performance targets set at the beginning of this dissertation work.

## 8.5 References

1. S. P. S. Badwal, K. Foger, *Ceramics International* 22 (1996) 257.
2. W. S. Jang, S. H. Hyun, S. G. Kim, *Journal of Material Science* 37 (2002) 2535.
3. Z. Shao, S. M. Haile, *Nature* 431 (2004) 170.
4. X. Zhang, M. Robertson, S. Yick, C. Deces-Petit, E. Styles, W. Qu, Y. Xie, R. Hui, J. Roller, O. Kesler, R. Maric, D. Ghosh, *Journal of Power Sources* 160 (2006) 1211.
5. T. Shimonosono, Y. Hirata, Y. Ehira, S. Sameshima, T. Horita, H. Yokokawa, *Solid State Ionics* 174 (2004) 27.
6. V. V. Kharton, F. M. Figueiredo, L. Navarro, E. N. Naumovich, A. V. Kovalevsky, A. A. Yaremchenko, A. P. Viskup, A. Carneiro, M. B. Marques, J. R. Frade, *Journal of Materials Science* 36 (2001) 1105.
7. X. Zhang, M. Robertson, C. Deces-Petit, W. Qu, O. Kesler, R. Maric, D. Ghosh, *Journal of Power Sources* 164 (2007) 668.
8. T. Tsai, E. Perry, S. Barnett, *J. Electrochem. Soc.* 144 (1997) L130-L132.
9. X. Zhang, M. Robertson, C. Deces-Petit, Y. Xie, R. Hui, S. Yick, E. Styles, J. Roller, O. Kesler, R. Maric, D. Ghosh, *Journal of Power Sources* 161 (2006) 301.
10. D. Yang, X. Zhang, S. Nikumb, C. Deces-Petit, R. Hui, R. Maric, D. Ghosh, *Journal of Power Sources* 164 (2007) 182.
11. C. Brahim, A. Ringuede, E. Gourba, M. Cassir, A. Billard, P. Briois, *Journal of Power Sources* 156 (2006) 45.
12. Y. Arachi, H. Sakai, O. Yamamoto, Y. Takeda, N. Imanishai, *Solid State Ionics* 121 (1999) 133.
13. T. Ishii, T. Iwata, Y. Tajima, A. Yamaji, *Solid State Ionics* 57 (1992) 153.
14. Y. Lin, S. A. Barnett, *Electrochemical and Solid-State Letters* 9 (2006) A285-A288.
15. M. Matsuda, T. Hosomi, K. Murata, T. Fukui, M. Miyake, *Journal of Power Sources* 165 (2007) 102.
16. Z. Wang, J. Qian, J. Cao, S. Wang, T. Wen, *Journal of Alloys and Compounds* 437 (2007) 264.
17. X. Zhang, C. Deces-Petit, S. Yick, M. Robertson, O. Kesler, R. Maric, D. Ghosh, *Journal of Power Sources* 162 (2006) 480.

18. M. Price, J. Dong, X. Gu, S. A. Speakman, E. A. Payzant, T. M. Nenoff, *Journal of the American Ceramic Society* 88 (2005) 1812.
19. D. S. Lee, W. S. Kim, S. H. Choi, J. Kim, H. W. Lee, J. H. Lee, *Solid State Ionics* 176 (2005) 33.
20. A. Tsoga, A. Naoumidis, D. Stover, *Solid State Ionics* 135 (2000) 403.

## 9. Chapter Nine. Stability Study of Cermet Supported SOFCs with Bi-layered SDC-SSZ Electrolyte<sup>9</sup>

Performance and stability of five cermet supported button-type solid oxide fuel cells featuring a bi-layered electrolyte (SSZ/SDC), an SSC cathode, and a Ni-SSZ anode, were analyzed using polarization curves, impedance spectroscopy, and post-mortem SEM observation. Two cells were tested up to 300 hours at 650°C in H<sub>2</sub>/air conditions, with and without DC bias. The results showed performance decay that manifested primarily as an increase in polarization resistance of approximately 2.5 mΩ cm<sup>2</sup> h<sup>-1</sup> at OCV. Polarization curves and impedance spectra measured over time revealed that the increase in polarization resistance was more significant close to open circuit voltage (OCV), suggesting a decrease in electrochemical kinetics as the main mechanism responsible for the decay. In addition, the initial series resistance was more than five times higher than the expected resistance corresponding to the ohmic drop in the electrolyte, reflecting a possible inter-reaction between the electrolyte layers that occurred during the sintering stage. In-situ and ex-situ sintered cathodes showed no obvious difference in cell performance or decay rate. The stability of the cells with and without electrical load was also investigated and no significant influence of DC bias was recorded. Based on the experimental results presented, we preliminarily attribute the performance degradation to electrochemical and microstructural degradation of the cathode.

### 9.1 Introduction

The benefits of ceria as an electrolyte material in solid oxide fuel cells include higher ionic conductivity and better compatibility with high performance mixed ionic and electronic conductive (MIEC) cathode materials than the conventional zirconia-based electrolyte. However, these benefits of ceria-based electrolytes are partially offset by its considerable electronic conductivity under certain operating temperature and atmospheric

---

<sup>9</sup>A version of this chapter has been published as:

X. Zhang, J. Gazzarri, M. Robertson, C. Decès-Petit, O. Kesler, Stability study of low temperature SOFCs with bilayered electrolyte, *Journal of Power Sources*, 185 (2008) 1049.

conditions. This phenomenon results in an electronic current flowing across the electrolyte, leading to a reduction in open circuit voltage, fuel utilization, and electrical efficiency [1]. A possible way to alleviate this problem is to coat the ceria-based electrolyte with a thin layer of stabilized zirconia, blocking the flow of electrons [2]. For example, Yahiro et al [3] added a thin (1.5  $\mu\text{m}$ ) protective layer of YSZ on the fuel side of an yttria-doped ceria electrolyte (1.5 mm) supported SOFC, increasing the OCV and enhancing power density. This type of cell is commonly called a bi-layered electrolyte SOFC. Matsuda *et al* [4] reported a peak power density of  $0.6\text{W cm}^{-2}$  at  $700^\circ\text{C}$  using an anode supported cell structure with thin YSZ/SDC bi-layered electrolyte deposited by electrophoresis deposition. In Chapter 3 and [5], we obtained the same peak power density in a similar bilayered electrolyte configuration using TSC technique. In Chapter 8 and [6], we developed cells with SSZ/SDC bi-layered electrolytes, showing a peak power density of  $0.85\text{ W cm}^{-2}$  at  $700^\circ\text{C}$ , much higher than that reported by Wang *et al* [7].

Although the bi-layered electrolyte cell strategy has successfully prevented internal shorting in ceria-based electrolyte cells and has enabled compatibility with high-performance MIEC cathodes [8], cell performance stability has scarcely been reported in the literature. In the present contribution, we study performance and stability of cermet-supported button cells with bi-layered SSZ / SDC electrolytes.

## **9.2 Experimental procedure**

### *Button cell preparation and testing*

Table 9-1 shows the cell materials and the geometrical characteristics of our cells. Details of the cell preparation were given elsewhere [5, 6]. Five cells of the same composition and the same anode and electrolyte fabrication process, and cathode deposition process, were labelled A, B, C, D and E in this report. After deposition of the cathode layer, the cells were mounted on a test jig and were heated at  $5^\circ\text{C}/\text{min}$  to  $650^\circ\text{C}$  and held for the reduction of the anode layer along with the in-situ sintering of the cathode (cells A, B, and C). The hydrogen partial pressure on the anode side was gradually increased (10, 20, 40, 60, 100%  $\text{H}_2$ , balance  $\text{N}_2$ , at 15 minute intervals) to reduce the NiO to Ni. The anode reduction and cathode in-situ sintering time was approximately 1.5 hrs. The anode fuel stream, with a flow rate of  $100\text{ ml min}^{-1}$ , passed first through a bubbler

humidifier at room temperature before entering the anode chamber, while ambient air (100 ml min<sup>-1</sup>) flowed on the cathode side. In cells A, B, and C, the SSC cathode was fired in-situ at 650°C. In cell D and cell E, the cathode was pre-fired ex-situ at 1000°C for 2hr, and then coated with a wet layer of SSC to ensure good electrical contact against the current collecting mesh. In all cells, the cathode geometric area was 0.5cm<sup>2</sup>, with variation within 5% in practice. Impedance measurements were performed at 650°C at OCV with an amplitude of 50 mV. The frequency ranged from 0.1 Hz to 100 kHz, with 10 data points per decade. Polarization and impedance were measured over time at 650°C, with an intermediate excursion to 800°C in cell A and to 1000°C in cell B, and a pre-test excursion to 700°C in cells D and E. Table 9-2 indicates the details of the testing procedure.

Table 9-1 Cell materials, thicknesses, and processing conditions

Cell component	Material	Thickness [μm]	Process	Firing condition
cathode	Sm <sub>0.5</sub> Sr <sub>0.5</sub> CoO <sub>3</sub> (SSC)	40-50	stencil printing	a) in-situ at 650°C-1.5h (A, B, C)
				b) ex-situ at 1000°C for 2hr (D, E)
electrolyte	Sm <sub>0.2</sub> Ce <sub>0.8</sub> O <sub>1.9</sub> (SDC)	5 ± 1		
	Sc <sub>0.2</sub> Ce <sub>0.01</sub> Zr <sub>0.79</sub> O <sub>1.9</sub> (SSZ)	3 ± 1	screen printing	1400°C, 2hr
anode	NiO-SSZ	10-15		
substrate	NiO-YSZ	800-1000	tape casting	

Table 9-2 Testing strategy of the five bi-layered electrolyte button cells

Cell #	Time elapsed until each EIS measurement [hr]	Remarks
A	0, 0.33, 6, 6.84	Excursion to 800°C between 0.33 and 6hr.
B	0, 0.33, 90, 115, 138, 144	Held at 0.75 V while not measuring EIS. Excursion to 1000°C between 138 and 144hr.
C	1, 53, 150, 216, 218, 306	Held at 0.5 A/cm <sup>2</sup> for 150hr, then OCV for 156hr.
D	0, 0.16, 2, 89	Held at OCV throughout the test.
E	0, 100	Held at 0.70V throughout the test

## 9.3 Results

Figures 9-1 to 9-13 show the DC and impedance behaviour of the five cells, taken at different times after anode reduction. The cell performance showed deterioration at times longer than 7 hours, primarily manifested as an increase in polarization resistance near OCV. Cell C also showed some (20%) increase in series resistance.

### 9.3.1 Cell A

This cell was not subjected to long-term testing. It was tested with the purpose of measuring the cell performance at different temperatures and the performance evolution during the initial several hours after the anode reduction process at 650°C. During the 0.33hr to 6hr period, the cell was heated up to 800°C and cooled down to 550°C at 50°C intervals, measuring the polarization curve at each temperature. The cell performance results and microstructure analysis have been published [6] and were discussed in Chapter 9. Table 9-3 gives a brief summary of the cell performance as a function of temperature. The cell reached a peak power density of 1.8 W cm<sup>-2</sup> at 800°C, and of 0.5W cm<sup>-2</sup> at 650°C with OCV ranging from 0.99 to 1.04 V over this temperature range.

Table 9-3 Initial performance of cell A as a function of temperature

T [°C]	OCV [V]	PPD [W cm <sup>-2</sup> ]
550	1.04	0.13
600	1.04	0.28
650	1.03	0.55
700	1.02	0.85
750	1.01	1.33
800	0.99	1.80

Figure 9-1 shows the impedance results of this cell at 650°C recorded at different times. Between 0.33hr and 6hr the cell temperature was increased up to 800°C and decreased back to 650°C. The labels indicate the times at which the measurements were started. The evolution of the impedance spectrum in Figure 9-1(Top) shows some performance improvement with time. Generally, this behaviour is attributed to the

completion of the anode reduction (a process with sluggish kinetics at 650°C), and initial electrochemical improvement of the cathode [9].

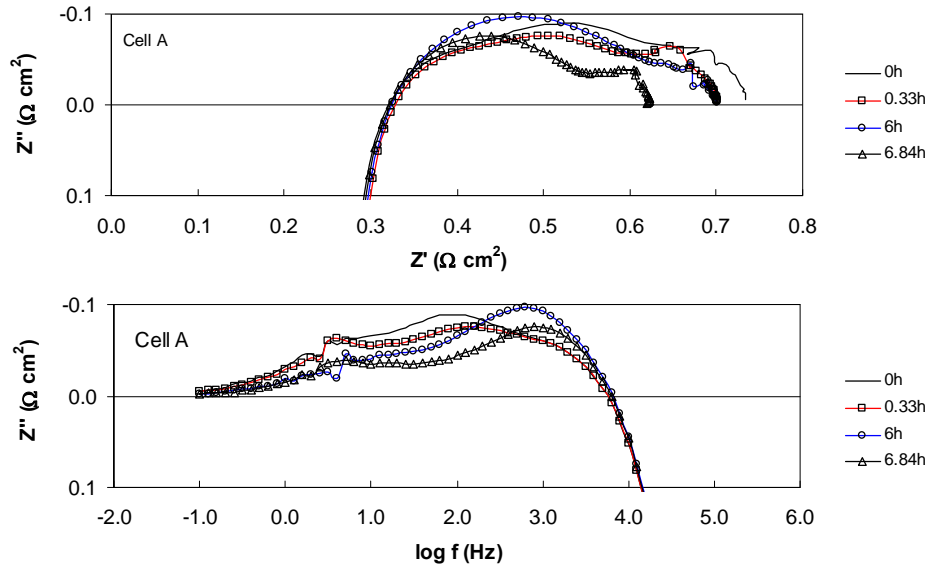


Figure 9-1 Nyquist plot of the impedance evolution of cell A, tested at OCV at 650°C. Top: Nyquist plot. Bottom: imaginary impedance vs. frequency. The legend on the right indicates the time in hours elapsed since the beginning of the test.

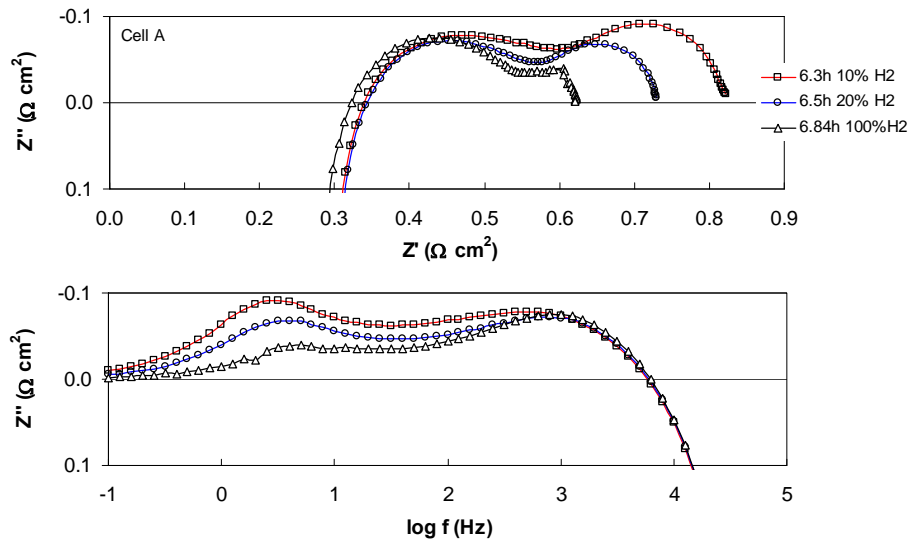


Figure 9-2 Influence of H<sub>2</sub> dilution on the cell impedance. Top: Nyquist plot. Bottom: imaginary impedance vs. frequency. Testing conditions: 650°C, OCV, 10, 20 and 100 % H<sub>2</sub>, balance N<sub>2</sub> / air (flow rates for both anode and cathode are 100 ml min<sup>-1</sup>).

In order to improve our understanding of the possible contributors to the performance improvement, we measured the impedance spectra using different hydrogen concentrations at the anode.

Figure 9-2 shows the result of changing the hydrogen concentration at the anode of cell A. The labels in the figure indicate the time at which the impedance measurement was performed. It is apparent that the low frequency process (with relaxation peak frequency within the range 1Hz-10Hz) is the most affected by hydrogen concentration, while the high frequency process (with relaxation peak frequency within the range 100Hz-1000Hz) is less affected. Thus, we attribute the low frequency arc to the anode process of the hydrogen oxidation reaction. In addition, we have compared the cathode relaxation frequency in this dataset with symmetric cells consisting of SSC cathodes on SDC electrolytes, and found both to appear within the 100Hz – 1000Hz range. Therefore, we link the high frequency arc mainly to the cathode process.

The imaginary impedance vs. frequency plot given in Figure 9-1(Bottom) reveals that the relaxation frequency changes with time mostly in the high frequency range. In electrodes with RC behaviour, the peak frequency depends inversely on the electrode polarization resistance,  $R_p$ . A decrease in the value of  $R_p$  will cause an increase in the peak frequency if the capacitance  $C_{dl}$  of the electrochemical double layer is constant. The peak frequency of the cathode process does increase with time during this test, suggesting an improvement in the cathode process. Therefore, the performance improvement of cell A is likely mostly related to a decrease in the cathode polarization resistance. Similarly, with decreasing  $H_2$  concentration, a small shift of relaxation peak frequency to lower frequency is observed as depicted in Figure 9-2 (Bottom), indicating an increase in the anode polarization resistance with the decrease in the anode hydrogen concentration. Finally, Figure 9-2 (Top) also reveals that there is an increase in series resistance,  $R_s$ , with the decrease in hydrogen concentration. Since the conductivity of ceria is decreased under higher  $p_{O_2}$  at the anode side, it would be reasonable to expect the ceria layer of the electrolyte to become less conductive with decreasing  $H_2$  concentration at the anode. Although we add the dense SSZ layer at the anode side, a change in conductivity could still occur due to pinholes or micro-cracks in the SSZ layer that allow the anode reactant to be in contact with SDC. In fact the OCV value (1.03V) of the cells is slightly lower than the

theoretical Nernst potential (1.15V), suggesting the presence of such micro-defects in our cells.

### 9.3.2 Cell B

Figures 9-3 to 9-5 show the results for cell B. This cell has been tested under potentiostatic operation at 0.75V for approximately 113 hours after the cell reduction at 650°C. Consistently with what had been observed in cell A, Figure 9-3 and Figure 9-5 show a small improvement in cell performance during the first seven hours after cell reduction. Held over 113hr at a constant voltage of 0.75V at 650°C, this cell showed a decay of approximately  $0.92 \text{ mA cm}^{-2} \text{ h}^{-1}$  after the initial cell performance improvement (Figure 9-3). After 113hr of potentiostatic operation at 0.75V, the cell was held at OCV for 20 hours and during this period the cell temperature was varied up to 850 and back down to 550°C for performance-temperature measurements. The calculated degradation rate at OCV was  $1.25 \text{ mA cm}^{-2} \text{ h}^{-1}$ . Subsequently, the cell was heated up to 1000°C and held for 2hr to improve cathode sintering over 138 – 144hr, then returned to 0.75V potentiostatic operation at 650°C for another 14hr, with a calculated degradation rate of  $0.44 \text{ mA cm}^{-2} \text{ h}^{-1}$ . Table 9-4 summarizes the main results and degradation rates for the different periods.

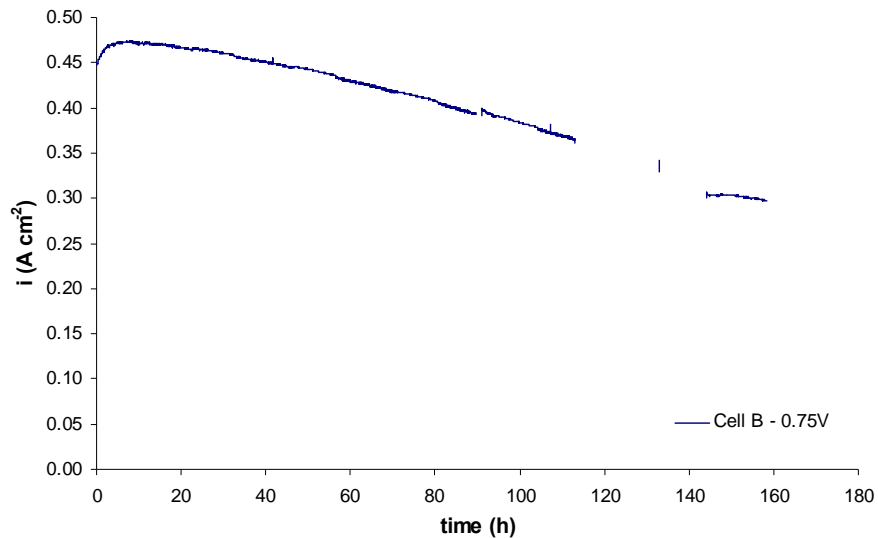


Figure 9-3 Current density delivered by cell B as a function of time, in potentiostatic mode at 0.75V. After a short activation period, the performance decays steadily throughout the testing time.

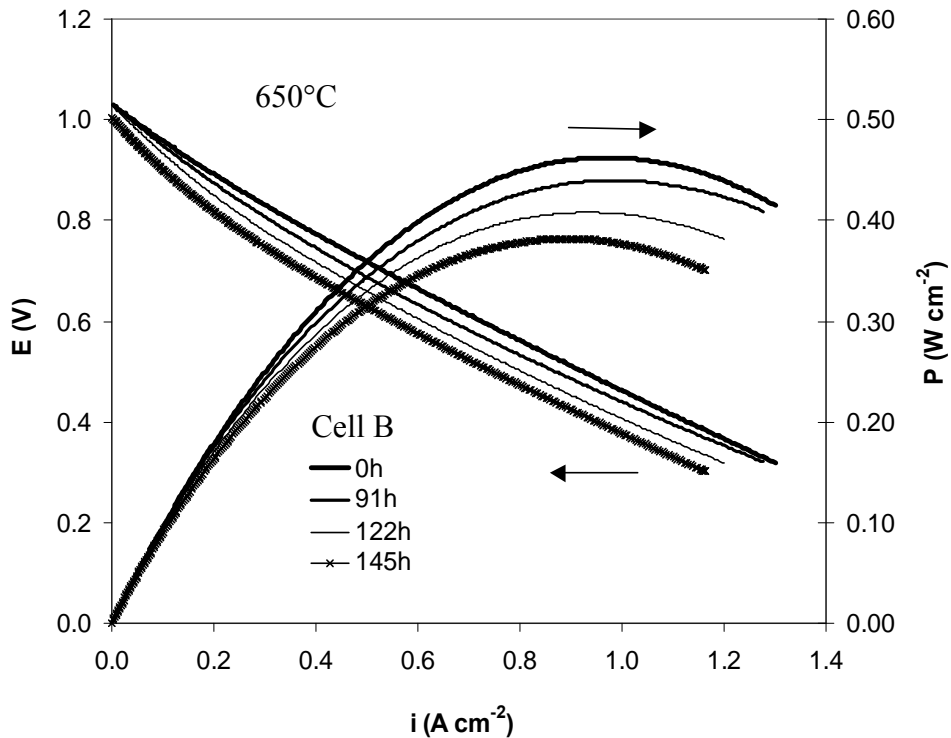


Figure 9-4 I-V and power density curves showing the time evolution of the electrochemical performance of cell B. The decay is more significant below  $0.3 \text{ A cm}^{-2}$  than it is at high polarizations. Legend indicates time elapsed in hours.

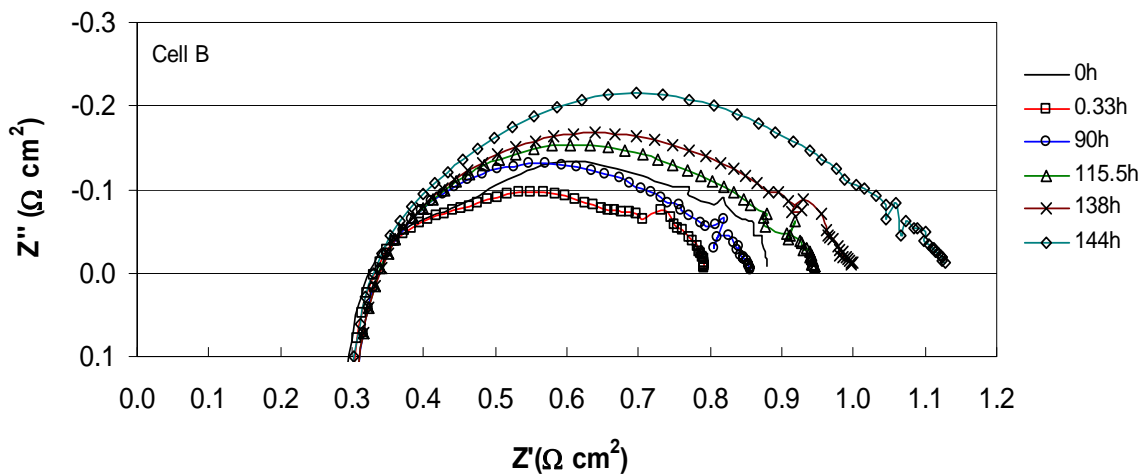


Figure 9-5 Nyquist plot of the impedance evolution of cell B, taken at OCV at 650°C. An excursion to 1000°C took place between 138 and 144hr. Legend indicates time elapsed in hours.

The DC polarization curves (Figure 9-4) revealed larger performance deterioration below  $0.3 \text{ A cm}^{-2}$  than above that current density. Since activation polarization governs the region close to OCV, the decay is likely related to an electrochemical kinetic loss of the electrode processes. The complex impedance evolution (Figure 9-5) shows an initial convolution of at least three arcs that coalesced over approximately 90 hours into a single arc shape, followed by a constant-shape size increase. The peak frequency decreased slightly over the 150 - 250 Hz range, which is attributable to the cathode process, as stated in the cell A section. Thus, the performance decay can be attributed to an increase in cathode electrochemical resistance. In-situ sintering the cathode at a higher temperature improved the performance stability at this test stage; however OCV loss ( $994-1022 = -18 \text{ mV}$ ) and performance loss ( $0.303-0.341 = -0.038 \text{ A cm}^{-2}$  at  $0.75 \text{ V}$ ) were observed after the heat treatment at  $1000^\circ\text{C}$  for 2hr.

Table 9-4 A summary of the performance and degradation rates of cell B

Time [hr]	0	7	50	113	133	145	158.5
$i \text{ [A cm}^{-2}\text{]}$	0.450	0.473	0.443	0.366	0.341	0.303	0.297
Degradation rate [mA cm <sup>-2</sup> h <sup>-1</sup> ]	/	-3.28	0.70	1.20	1.25	/	0.44
Comment							

### 9.3.3 Cell C

Cell C was tested at a constant current density of  $0.5 \text{ A cm}^{-2}$  for over 150hr, then left at OCV for another 157 hours at  $650^\circ\text{C}$  without any additional temperature excursion. The results are shown in Figure 9-6, showing a voltage decay of  $0.07 \text{ V}$  (from  $0.69 \text{ V}$  down to  $0.62 \text{ V}$ ) with a non-linear time dependence under constant current density, with an average rate of  $0.47 \text{ mV h}^{-1}$ . The average decay rate at OCV was approximately  $0.32 \text{ mV h}^{-1}$ , calculated based on the cell voltage drop (from  $0.62 \text{ V}$  to  $0.57 \text{ V}$ ) at  $0.5 \text{ A cm}^{-2}$ . This cell was the only one to show an obvious increase in series resistance during impedance testing, as shown in Figure 9-7. However, its increase in polarization resistance was far larger.

Like cell B, the complex impedance showed an early-stage coalescence of multiple arcs (two in the case of cell C) into one arc, followed by further shape-invariant growth. Performance degradation was more evident at low rather than high DC polarizations, as seen in Figure 9-8. The trend in peak frequency was similar to that observed in cell B, indicating that the cathode performance loss was the main contributor to decay.

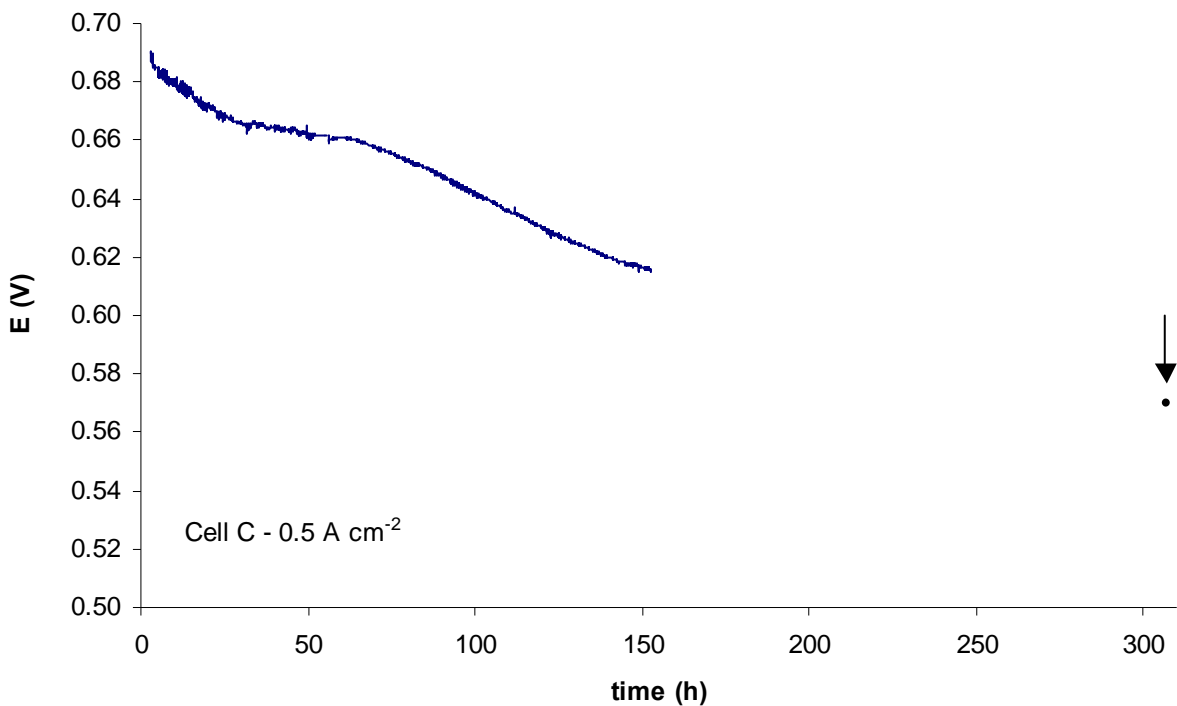


Figure 9-6 Potential delivered by cell C as a function of time, in galvanostatic mode at 0.5 A cm<sup>-2</sup>. The data point indicated with the arrow was calculated based on the polarization curve performed at 307hr.

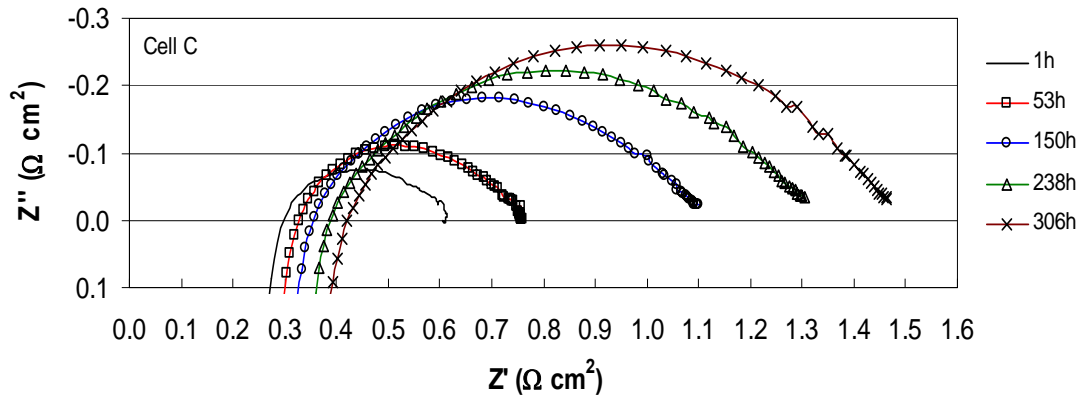


Figure 9-7 Nyquist plot of the impedance evolution of cell C, at OCV at 650°C. An excursion to 0.75 V (OCV= 0.983 V) took place after 53hr.

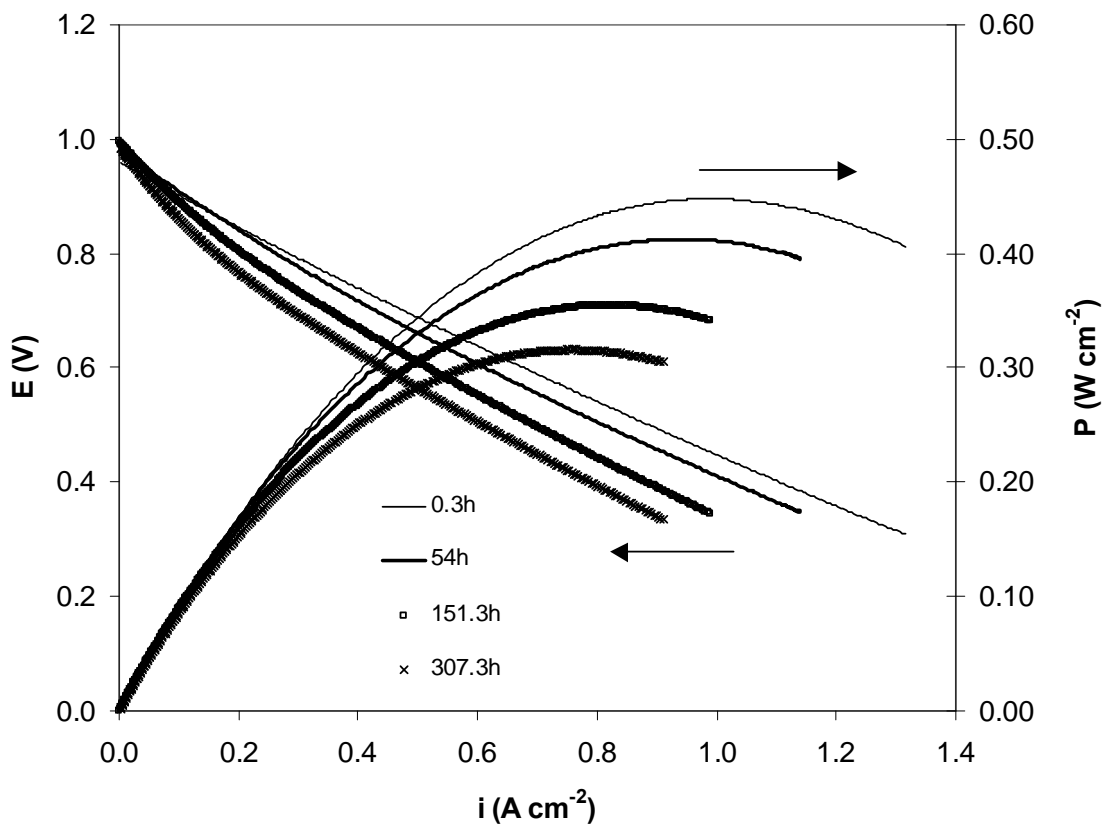


Figure 9-8 I-V and power density curves showing the time evolution of the electrochemical performance of cell C. Legend indicates time elapsed in hours.

### 9.3.4 Cell D

Cell D was held at OCV for approximately 89 hours after cell reduction, and showed a similar decay in performance as cells B and C, i.e. a shape-preserving impedance arc growth (Figure 9-9). This result is surprising, since cell D had an *ex-situ* sintered cathode (1000°C for 2hr in air). Based on our results for cell B, it was thought that with an *ex-situ* sintered cathode, the cell stability could be improved. However, neither the rate of decay nor the initial performance and initial ohmic loss were significantly different from those of the other cells for the sintering temperature used. Figure 9-10 shows the I-V and power density curves of cell D at the starting time (0hr) and the ending time (90hr) of the test at 650°C. The average decay rate was calculated based on the I-V results shown in Figure 9-10, resulting in  $0.84 \text{ mV h}^{-1}$  under  $0.5 \text{ A cm}^{-2}$  from 0.68 to 0.605V, or  $0.78 \text{ mA cm}^{-2} \text{ h}^{-1}$  under 0.75V from 0.35 to 0.28  $\text{mA cm}^{-2}$ .

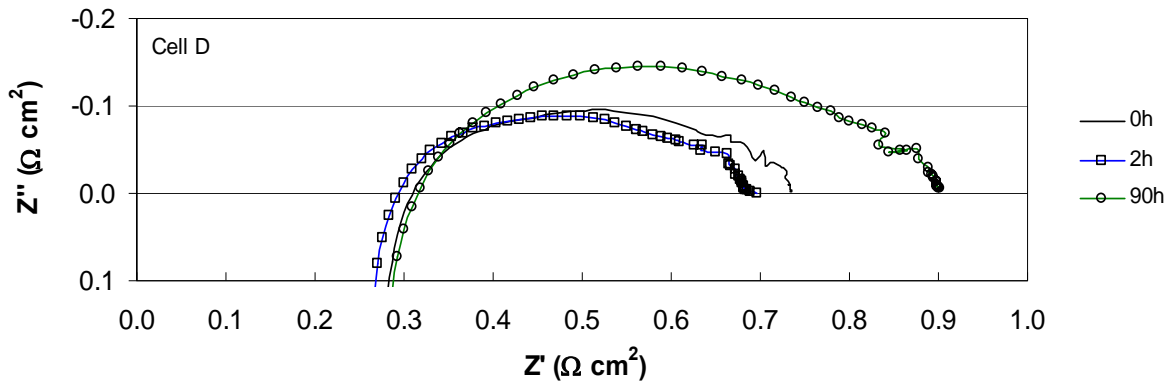


Figure 9-9 Nyquist plot of the impedance evolution of cell D at OCV at 650°C. The cell temperature was increased to 700°C before the first test indicated as 0hr.

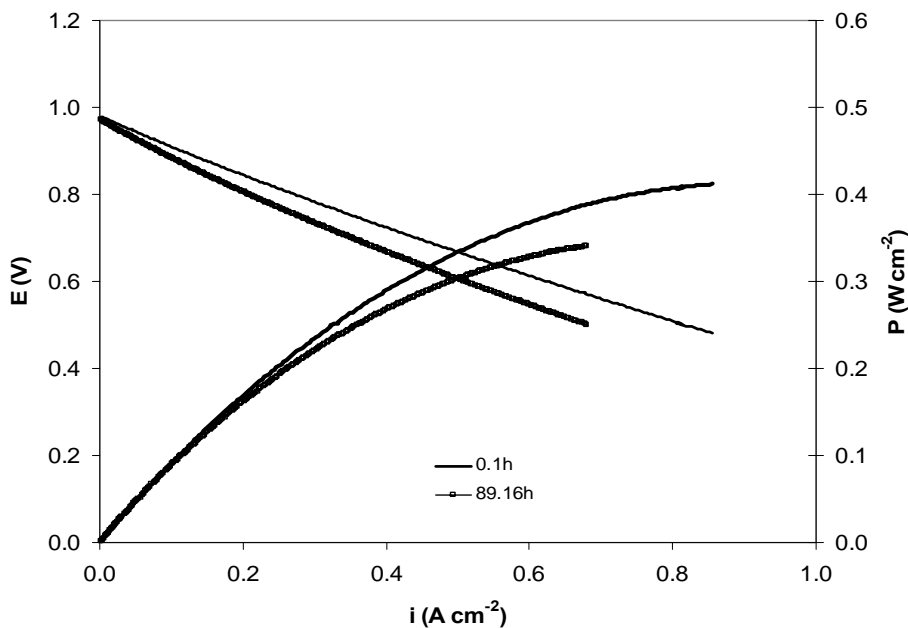


Figure 9-10 I-V and power density curves showing the time evolution of the electrochemical performance of cell D. Legend indicates time elapsed in hours.

### 9.3.5 Cell E

We tested another cell (cell E) with an *ex-situ* sintered cathode to further clarify the influence of DC bias on cathode stability. This cell was tested under potentiostatic operation at 0.70V for 100hrs at 650°C.

Figure 9-11 shows the current density change with time. This cell showed an OCV of 0.982 V (see Figure 9-12), and the degradation rate was  $0.73\ mA\ cm^{-2}\ h^{-1}$  over a 100h period, from  $0.436$  to  $0.363\ A\ cm^{-2}$ . Interestingly, the OCV values of cells D and E with *ex-situ* sintered cathodes were slightly lower than those of the other cells. The lower OCV (0.98V) seems to be related to the cathode sintered at 1000°C for 2hr. As described before for cell B, a similar OCV loss was also observed after heating up to 1000°C during the final period of testing (see Figure 9-4 and Table 9-2). Two mechanisms may be responsible for this change: the sintering of the cathode layer that generates thermal stresses in the electrolyte, eventually causing its damage, and/or cobalt diffusion into the electrolyte layer that promotes mixed conductivity of the bi-layered electrolyte. Both will lead to either Nernst potential loss, and/or partial reduction of the ceria in the SDC layer, with its consequent increase in electronic conductivity and internal shorting. Further investigation

of the possible mechanism is needed. Cell E did not show a sign of higher stability compared to *in-situ* sintered cathodes.

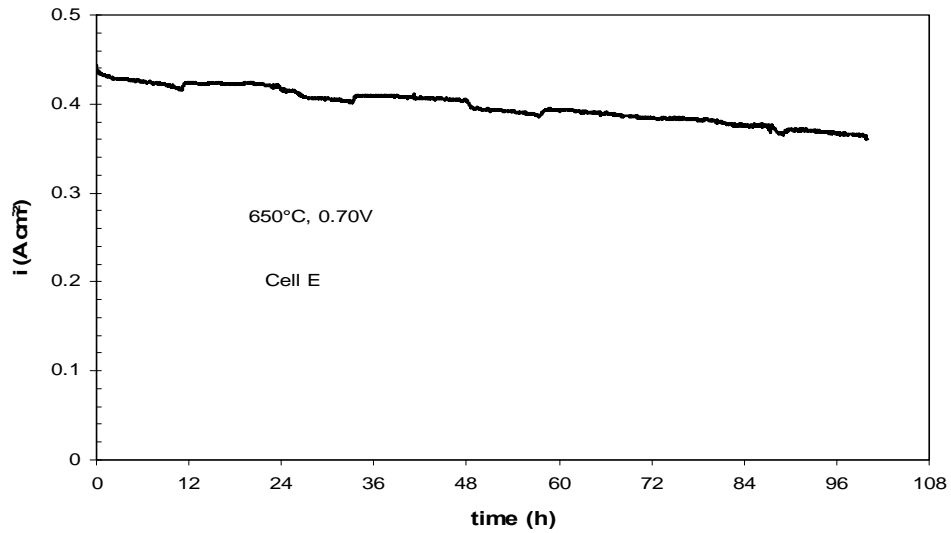


Figure 9-11 Current density delivered by cell E as a function of time, in potentiostatic mode at 0.70V.

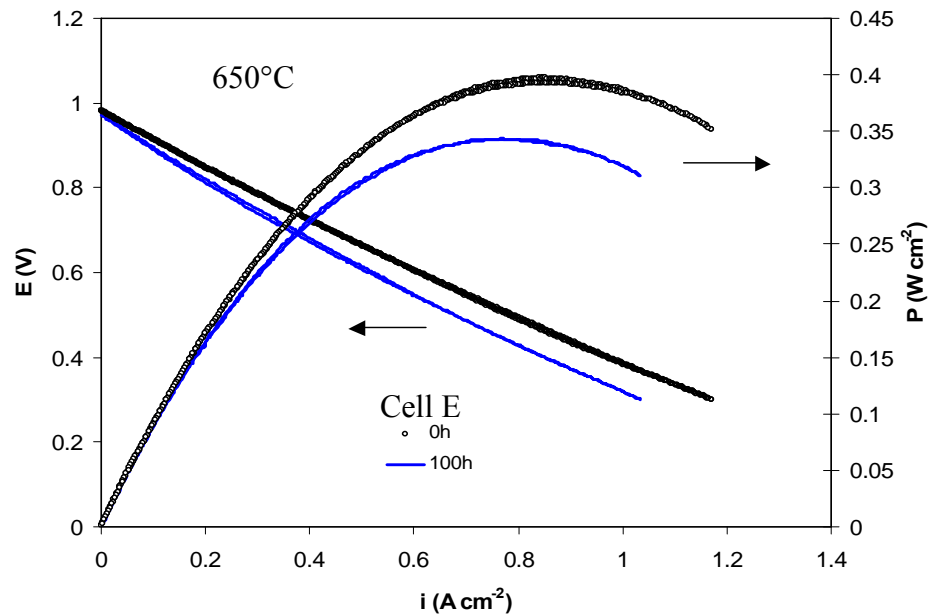


Figure 9-12 I-V and power density curves showing the time evolution of the electrochemical performance of cell E. Legend indicates time elapsed in hours.

## 9.4 Discussion

### 9.4.1 Incubation period

All cells in this test showed some initial performance improvement. We will refer to this initial stage as an incubation period. Typical signs are an initial decrease of the  $R_p$  at OCV (Figure 9-1, Figure 9-5, and Figure 9-9) during which the cell performance increases, or the cell resistance decreases. In cell A, the electrode polarization resistance  $R_p$  drops from 0.44 (0hr) to 0.32  $\Omega \text{ cm}^2$  during the first 6.84hr, while the series resistance  $R_s$  shows almost no change. As described in the experimental procedure section, the test procedure for cell reduction lasted approximately 1.5hr, followed by the electrochemical measurements. In agreement with the observation that after the nominal reduction period, the OCV was 1.03V at 650°C, the impedance results in Figure 9-1 reveal that the reduction of the cermet anode was likely not completed. The shrinking of the low frequency arc (anode) with time further supports this statement. Comparing the low frequency impedance of the anode process, the reduction process seems to finish after the first 6 hours. It is worth mentioning that after the measurement at 0.33hr, cell A was heated up to 800°C for a temperature dependent performance test. Therefore, the cell must have experienced an accelerated reduction process during the 0.33hr to 6hr period. It is noteworthy that the low frequency arc preserves its shape between 6 and 6.84hr. Further improvement in cell performance is attributed to cathode microstructural stabilization.

Based on the analysis presented in section 9.3.2 for cell B, we concluded that the incubation time for cell B was 7hr long, at which time the performance reached a maximum (see Figure 9-3). Cell C exhibited a much shorter incubation time of less than 3hr, while the incubation time for cells D and E were within 2hr. We conclude that the extent of this incubation period depends on the temperature and electrode microstructures. This behaviour is attributable to the processes of anode reduction and cathode sintering, with both processes nearing completion after the first few hours at operating temperature.

### 9.4.2 Performance degradation

After performance stabilization, cells B, D and E showed an increase in polarization resistance with no or very small change in series resistance. Cell C (Figure 9-7) shows an increase in both series and polarization resistance, with the increase in series resistance  $R_s$  being much smaller than the increase in polarization resistance,  $R_p$ . Table 9-5 summarizes the  $R_s$  and  $R_p$  change during the first 90 to 150hr of testing time for the four long-term tested cells. It is clear that most of the cells showed relatively stable  $R_s$  values, approximately  $0.30\text{-}0.33 \Omega \text{ cm}^2$  over the tested periods. Only cell C showed a 20% increase in  $R_s$  during the stability test. Figure 9-13 shows the increase in polarization resistance for the four long-term tested cells. All four cells show comparable degradation trends. For example, the average decay rate of cell C illustrated in Figure 9-6 for the first 150hr at  $0.5 \text{ A cm}^{-2}$  was  $0.5 \text{ mV h}^{-1}$ , while during 150hr to 300hr at OCV, the decay rate was  $0.3 \text{ mV h}^{-1}$ . Assuming that cathode microstructural instability was the main cause of degradation, we had expected that with an ( $1000^\circ\text{C}\text{-}2\text{hr}$ ) *ex-situ* sintered cathode, the performance stability might be improved. However, cell D and cell E, featuring *ex-situ* sintered cathodes, degraded  $0.78 \text{ mA cm}^{-2} \text{ h}^{-1}$  at OCV, and  $0.73 \text{ mA cm}^{-2} \text{ h}^{-1}$  at  $0.75\text{V}$ , respectively. Figure 9-3 and Figure 9-6 also indicate that the performance decay of the cells with *in-situ* sintered cathodes is only mildly dependent on whether the cell was under polarization or at OCV. Figure 9-13 shows general consistency in the observed increase in  $R_p$ , largely independently of DC bias and cathode sintering strategy, averaging  $2.5 \text{ m}\Omega \text{ cm}^2 \text{ h}^{-1}$  at OCV. Similar conclusions were reported by Becker *et al.* in their study of LSCF cathodes at  $700^\circ\text{C}$  [10]. However, this observation contrasts with results reported in [11, 12], where the authors point out that the decay rate changes with high current densities.

Table 9-5 Summary of the cell resistances obtained in this work (initial and 116hr (B), 150hr (C), 90hr(D) and 100hr(E) ) quantified using series and polarization resistance ( $650^\circ\text{C}$ , OCV)

cell	$R_s^0$ [ $\Omega \text{ cm}^2$ ]	$R_s^{\text{final}}$ [ $\Omega \text{ cm}^2$ ]	$R_p^0$ [ $\Omega \text{ cm}^2$ ]	$R_p^{\text{final}}$ [ $\Omega \text{ cm}^2$ ]
A	0.32	-	0.42	-
B	0.33	0.34	0.55	0.61
C	0.30	0.36	0.31	0.74
D	0.31	0.31	0.43	0.59
E	0.33	0.34	0.38	0.51

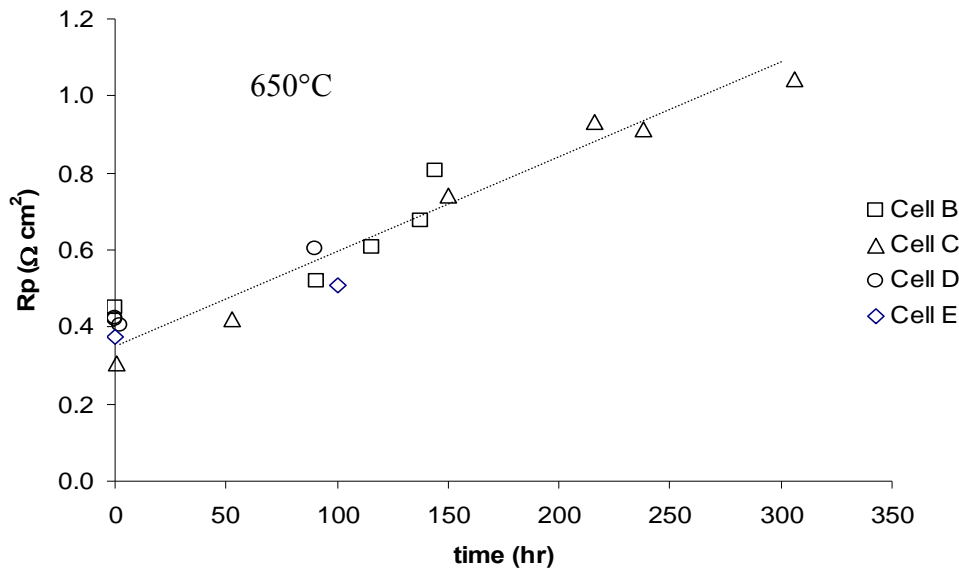


Figure 9-13 Polarization resistance evolution with time for cells B, C, D and E. Average Rp increase is  $2.5 \text{ m}\Omega \text{ cm}^2 \text{ h}^{-1}$ .

Commonly to all long-term tests, the increase in polarization resistance is larger at OCV than it is under polarization. Figure 9-4, Figure 9-8, and Figure 9-10 illustrate this statement, where the slope of the polarization curve shows a more important change close to OCV than it does above approximately  $0.4 \text{ A cm}^{-2}$ . This observation suggests the decay of certain electrochemical processes. Comparing the recorded impedance spectra of all the cells, it is clear that the impedance increase within the 100 Hz – 1000 Hz range is predominant over those at other frequencies. Based on the results and analysis and the fact that the anodes used in this work had already been tested under similar conditions, showing good stability, it is reasonable to attribute most of the observed cell performance degradation to the cathode. A typical degradation mechanism affecting the cathode microstructure is chromium poisoning [13, 14], a result of evaporation of chromium from stainless steel interconnectors. This phenomenon is ruled out in the present work, since no chromium-containing material is present at high temperature in our experimental setup. Two possible degradation mechanisms are proposed in this work. These mechanisms include: 1) coarsening of the microstructure due to sintering for the in-situ sintered

cathodes; 2) diffusion of strontium away from the SSC cathode, leading to strontium depletion that significantly decreases the performance of cobaltite cathodes [15].

### 9.4.3 Bi-layered electrolyte resistance

From Table 9-4, the initial series resistance,  $R_s$  is consistent throughout all the cells, approximately  $0.30\text{-}0.33 \Omega \text{ cm}^2$ , indicating good experimental repeatability. However, this value is well above the series resistance calculated using the SDC thickness ( $4\text{-}6\mu\text{m}$ ) and SSZ thickness ( $2\text{-}4 \mu\text{m}$ ) and conductivities ( $0.03\text{-}0.04 \text{ S cm}^{-1}$  for SDC [16] and  $0.02\text{-}0.03 \text{ S cm}^{-1}$  for SSZ [17] at  $650^\circ\text{C}$ ). The theoretical  $R_s$  for those cells based on the electrolyte thickness is only approximately  $0.03\text{-}0.06 \Omega \text{ cm}^2$ . The likely cause of the higher observed  $R_s$  is the formation of an inter-reaction layer between the SDC and SSZ layers, formed probably during the sintering stage [6, 18], and resulting in a low-conductivity zone in the bi-layered electrolyte. Zr and Ce concentrations across the bi-layered electrolyte were analysed by EDS, as shown in the right-hand side image of Figure 9-14. The EDS elemental analysis results showed a clear diffusion of Ce into the SSZ layer. In our previous work on powder interaction between SSZ and SDC (refer to Chapter 8), we found that the lattice parameter change mainly occurred in the SSZ powder rather than in SDC powder when the powder mixture was heated over  $1100^\circ\text{C}$ , indicating the dominant diffusion of the larger cation,  $\text{Ce}^{4+}$  into the SSZ lattice, leading to expansion of the SSZ lattice. Those interaction results in low ionic conductivity of the electrolyte have been well documented (cf. chapter 5, 7, 8) and [6]. The existence of voids observed in the SEM images (Figure 9-14) between the electrolyte layers could be another contributor due to a decrease in area of the conductive path through the electrolyte layers. Although most of the cell structure showed good adhesion between layers and normal electrode microstructure in post mortem microstructural observation, we did observe some detached areas (Figure 9-15). It is difficult to be certain about the stage at which this detachment occurred. However, it is logical to assume that this interface had been weakly bonded *a priori*. In the third place, a small contribution to the large initial series resistance is the incomplete sintering of the SDC layer, also evident in Figure 9-15. While all three of these phenomena could have contributed to the higher observed values of  $R_s$ , the first two of these phenomena would also have had implications on the electrode electrochemical

performance due to the shadowing effect that such blocking layers have on cells with large aspect ratios [19, 20]. The growing  $R_s$  in the cell C test seems attributable to the possible detachment between the electrolyte layers.

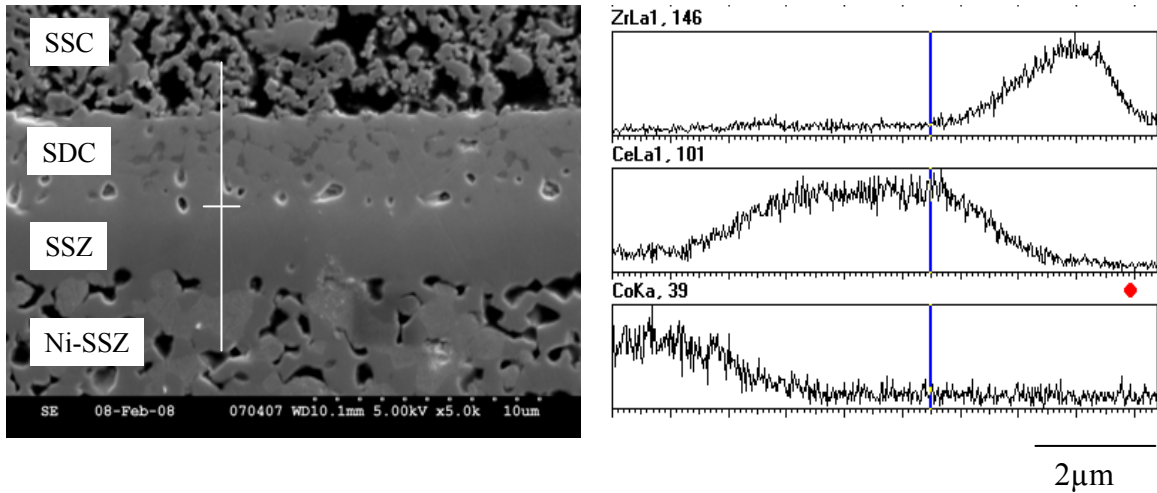


Figure 9-14 SEM micrograph of the bi-layered electrolyte in contact with the electrodes of cell D. While SSZ shows excellent sintering, SDC exhibits some porosity that could partially contribute to the abnormally high initial series resistance observed in all cells. The line scan mark in the SEM imageshows the location of the element analysis. The element analysis results are shown in the right figure.

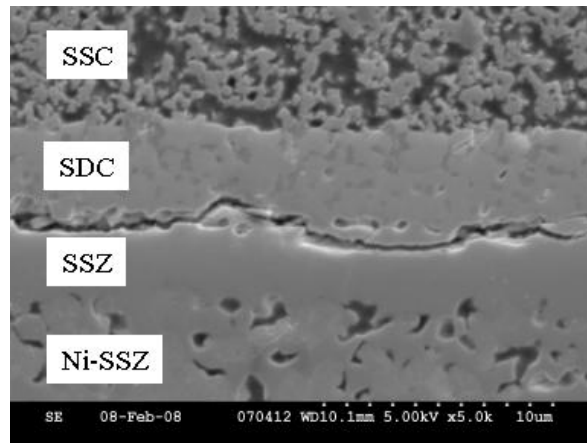


Figure 9-15 Post-test SEM micrograph showing a delamination between the SSZ and SDC electrolyte layers in cell D. This separation was observed in several spots across the cell, and may have been partially responsible for the large initial series resistance observed in all specimens.

In the next chapter, the use of pulsed laser deposition (PLD) is reported for deposition of bi-layered electrolytes on the cermet supports to eliminate the interaction between the two electrolyte materials during the high temperature co-firing.

## **9.5 Conclusions**

The long term (up to 300hr) testing of four cermet – supported button cells with bi-layered SSZ/SDC electrolytes resulted in continuous performance decay, mostly manifested as an increase in polarization resistance, mostly at low polarizations, close to OCV. This observation, along with the frequency range at which most of the impedance growth is evident, led us to attribute the decay to a decrease in the cathode performance. Common observations were the initial change in the impedance arc shape from a multiple to a single arc, followed by an increase in size with no further shape change.

The series resistance observed initially in all cells was invariably higher than the theoretical series resistance. The most likely cause for this observation is the presence of an interaction layer or partial delamination between the electrolyte layers. Microscopic examination showed a weakened adhesion between the SDC and SSZ electrolyte layers, a phenomenon likely contributing to the anomalous  $R_s$ . Sintering of the SSC cathode ex-situ did not result in any obvious performance difference, regardless of whether the cell was held at OCV or under polarization during the testing time.

## 9.5 References

1. X. Zhang, M. Robertson, C. Deces-Petit, W. Qu, O. Kesler, R. Maric, D. Ghosh, J. Power Sources 164 (2007) 668.
2. K. Eguchi, T. Setoguchi, T. Inoue and H. Arai, Solid State Ionics 52 (1992) 165.
3. H. Yahiro, Y. Baba, K. Eguchi, and H. Arai, J. Electrochem. Soc. 135 (1988) 2077.
4. M. Matsuda, T. Hosomi, K. Murata, T. Fukui, M. Miyake, J. Power Sources 165 (2007) 102.
5. X. Zhang, M. Robertson, C. Deces-Petit, Y. Xie, R. Hui, S. Yick, E. Styles, J. Roller, O. Kesler, R. Maric, D. Ghosh, J. Power Sources 161 (2006) 301.
6. X. Zhang, M. Robertson, C. Decès-Petit, W. Qu, O. Kesler, R. Maric, D. Ghosh, J. Power Sources 175 (2008) 800.
7. Z. Wang, J. Qian, J. Cao, S. Wang, T. Wen, J. Alloys and Compounds 437 (2007) 264.
8. T. L. Nguyen, K. Kobayashi, T. Honda, Y. Iimura, K. Kato, A. Neghisi, K. Nozaki, F. Tappero, K. Sasaki, H. Shirahama, K. Ota, M. Dokiya, T. Kato, Solid State Ionics 174 (2004) 163.
9. S. Koch, Fuel Cells 6 (2006) 117.
10. M. Becker, PhD Dissertation, University Karlsruhe, Germany (2007).
11. R. Barfod, M. Mogensen, T. Klemensoe, A. Hagen, Y. Liu, Proc. SOFC IX, 1 (2005) 524.
12. A. Hagen, R. Barfod, P. Hendriksen, Y.-L. Liu, and S. Ramousse, J. Electrochem. Soc. 153 (2006) A1165.
13. S. Paulson and V. Birss, J. Electrochem. Soc. 151 (2004) A1961.
14. E. Konysheva, J. Electrochem. Soc. 153 (2006) A765.
15. S. P. Simner, M. D. Anderson, M. H. Engelhard and J. W. Stevenson, Electrochem. Solid-State Lett. 9 (2006) A478.
16. V. V. Kharton, F. M. B. Marques, A. Atkinson, Solid State Ionics 174 (2004) 135.
17. J. W. Fergus, J. Power Sources 162 (2006) 30.
18. N. Sakai, T. Hashimoto, T. Katsube, K. Yamaji, H. Negishi, T. Horita, H. Yokokawa, Y. Ping Xiong, M. Nakagawa, Y. Takahashi, Solid State Ionics 143 (2001) 151.

19. J. Gazzarri and O. Kesler, *J. Power Sources* 167 (2007) 430.
20. J. Gazzarri and O. Kesler, *J. Power Sources* 176 (2008) 155.

## 10. Chapter Ten. LT-SOFCs with Pulsed Laser Deposited Bi-Layered Electrolyte<sup>10</sup>

Solid oxide fuel cells with bilayered electrolyte have been successfully fabricated by using a pulsed laser deposition, showing enhanced performance at low operating temperatures. The cells reach power densities of  $0.5 \text{ W cm}^{-2}$  at  $550^\circ\text{C}$  and  $0.9 \text{ W cm}^{-2}$  at  $600^\circ\text{C}$ , with open circuit voltage (OCV) values larger than  $1.04\text{V}$ . The bilayered electrolyte contains a  $6 \sim 7 \mu\text{m}$  thick samaria-doped ceria (SDC) layer deposited over a  $\sim 1\mu\text{m}$  thick scandia-stabilized zirconia (SSZ) layer. Electrical leaking between the anode and cathode through the SDC electrolyte, due to the reduction of  $\text{Ce}^{4+}$  to  $\text{Ce}^{3+}$  in reducing environments when using a single layer SDC electrolyte, has been eliminated by adopting the bi-layer electrolyte concept. Both SSZ and SDC layers in the bilayered electrolyte prepared by the pulsed laser deposition (PLD) technique are the highly conductive cubic phases. Poorly conductive  $(\text{Zr}, \text{Ce})\text{O}_2$ -based solid solutions or  $\beta$ -phase SSZ were not found in the bilayered electrolyte prepared by PLD due to the low processing temperatures of the technique. Excellent reliability and flexibility of the PLD technique makes it a very promising technique for the fabrication of thin electrolyte layers for SOFCs operating at reduced temperatures.

### 10.1 Introduction

High operating temperature is one of the main barriers for wide scale adoption of solid oxide fuel cell (SOFC) technology [1]. Therefore, much research work is focused on the development of low temperature SOFCs operating at approximately  $500\text{-}600^\circ\text{C}$  [2-4]. To achieve the objective of low operating temperatures, a number of approaches from the viewpoint of new materials, novel processes, and unique architectures must be examined.

The practical operating temperature of SOFCs is mainly determined by the conductivity and thickness of the electrolyte. Samaria-doped ceria (SDC) is a promising

---

<sup>10</sup> A version of this chapter has been published as:

D. Yang, X. Zhang, C. Decès-Petit, R. Hui, R. Maric, D. Ghosh, Low temperature SOFCs with pulsed laser deposited bi-layer electrolyte, *J. Power Sources*, 164 (2007) 182.

material for use as the electrolyte in reduced temperature SOFCs and has been investigated widely over the past two decades [3, 4]. SDC exhibits a relatively high conductivity of 0.1 S/cm at 700 °C [5], 2-3 times higher than that of yttria-stabilized zirconia (YSZ). Its thermal expansion coefficient ( $12.5 \times 10^{-6} \text{ K}^{-1}$ ) is also more compatible with that of the Ni-cermet anode and commercial ferritic stainless steel interconnects, than that of YSZ. Although the material exhibits better chemical and structural compatibility with electrodes as well as higher ionic conductivity than YSZ, the reduction of  $\text{Ce}^{4+}$  to  $\text{Ce}^{3+}$  induces n-type electronic conduction which tends to decrease the power output of solid oxide fuel cells due to internal electrical shorting.

The problem can be eliminated by using a barrier of thin scandia-stabilized zirconia (SSZ) deposited between the SDC layer and the anode to improve the stability of the SDC layer under the reducing atmosphere. The ionic conductivity of SSZ is the highest among all the  $\text{ZrO}_2$ -based electrolytes [6]. However, it is not considered as a candidate electrolyte for reduced temperature SOFCs because its conductivity decreases rapidly with temperature below 800°C [7]. When a bi-layered SDC/SSZ electrolyte is used, the SSZ layer acts mainly as a barrier against electronic conductivity, and its layer thickness can be in the range of a few tens to a few hundreds of nanometers. Therefore, its relatively low conductivity will not contribute significantly to the overall ohmic loss of the bi-layered SDC/SSZ electrolyte for SOFCs. For the fabrication of a bi-layer SDC/SSZ electrolyte on anode-supported SOFCs, wet ceramic processes such as screen printing and tape casting have been used. These processes normally require processing temperatures over 1300°C. At such high co-firing temperatures, doped ceria (i.e., SDC) reacts easily with stabilized zirconia (e.g., SSZ, YSZ) to form  $(\text{Zr}, \text{Ce})\text{O}_2$ -based solid solutions that have a very low ionic conductivity [8, 9]. Ohmic loss due to the low-conductive interfacial layer will result in poor performance of SOFCs [10]. In addition, highly conductive cubic phase SSZ, stabilized at high temperatures, will transform to a less conductive  $\beta$ -phase when SSZ is cooled below 800°C. To avoid those issues, low temperature fabrication techniques (under 800°C) such as pulsed laser deposition (PLD) are attractive. PLD is an emerging physical vapor deposition technique that offers better control over the film properties, such as microstructures, chemical composition, density, and interfacial properties than that by conventional wet ceramic processes. Grain sizes from a few nanometers to a few hundred

nanometers can be easily prepared by selecting appropriate processing parameters. Recently, an enhancement of ionic conduction was found in nanocrystalline SSZ, whose specific grain boundary conductivity is 1-2 orders of magnitude higher than that of the microcrystalline specimen at 700-850°C [11]. The PLD technique usually can operate at low processing temperatures, which can suppress grain growth to achieve nanocrystalline materials.

Lower temperature processes such as PLD are particularly suitable for the fabrication of miniaturized SOFCs based on multilayer thin films. This method not only can deposit a dense electrolyte thin layer, but also porous anode and cathode layers. Therefore, it possesses the potential for automation. In addition, this technique holds promise for improved quality control and integrated multiple layers to enhance the reliability, performance and durability of the resulting product, while reducing the fabrication costs.

The focus of this research is on the development of the PLD process to fabricate SDC/SSZ bi-layered electrolytes with controlled microstructures, density, and interfacial properties. Si (100) wafers and NiO-SDC modified NiO-YSZ cermet discs were used as the substrates in this study. The Si substrates were used to develop the optimal PLD processing parameters for the deposition of a dense and highly conductive bi-layered SDC/SSZ electrolyte. The bi-layer electrolyte was then deposited on porous anode substrates under optimized processing conditions, and their structures and morphologies were characterized by XRD and SEM. A unit cell that utilized the PLD prepared bi-layer electrolyte and wet-processing prepared NiO-SDC anode and  $\text{Sm}_{0.5}\text{Sr}_{0.5}\text{CoO}_3$ -25wt% SDC composite cathode (designated as SSC#3 in this dissertation work) was tested for its electrochemical performance.

## **10.2 Experimental procedure**

### *Starting Materials and cell substrates*

Table 10-1 lists the starting materials used in this study. All the materials for wet ceramic processing and PLD processing were commercially obtained. Figure 10-1 shows a schematic drawing of the cell structure and its fabrication methods.

Table 10-1 Chemical composition, properties, suppliers of starting materials

Name	Composition	Properties	Supplier
SSC	$\text{Sm}_{0.5}\text{Sr}_{0.5}\text{CoO}_3$	D50: 0.80 $\mu\text{m}$ Surface area: 5.16 $\text{m}^2 \text{g}^{-1}$	Praxair
SDC	$(\text{SmO}_{1.5})_{0.2}(\text{CeO}_2)_{0.8}$	D50: 0.40 $\mu\text{m}$ Surface area: 7.08 $\text{m}^2 \text{g}^{-1}$	Praxair
SSZ	$(\text{ScO}_{1.5})_{0.20}$ $(\text{CeO}_2)_{0.01}(\text{ZrO}_2)_{0.79}$	D50: 0.46 $\mu\text{m}$ Surface area: 7.0 $\text{m}^2 \text{g}^{-1}$	Daiichi chemicals
YSZ	$(\text{YO}_{1.5})_{0.16}(\text{ZrO}_2)_{0.84}$	D50: 0.46 $\mu\text{m}$ Surface area: 7.0 $\text{m}^2 \text{g}^{-1}$	Tosoh
NiO-f	NiO type F	D50: 1.0 $\mu\text{m}$ Surface area: 4.0 $\text{m}^2 \text{g}^{-1}$	Novamet
NiO-s	NiO-standard	D50: 16.0 $\mu\text{m}$ Surface area: < 1 $\text{m}^2 \text{g}^{-1}$	Novamet
Silicon wafer	Si (100)	(100) orientation, p-type, 10 ~ 30 $\Omega$	Polishing Corporation of America

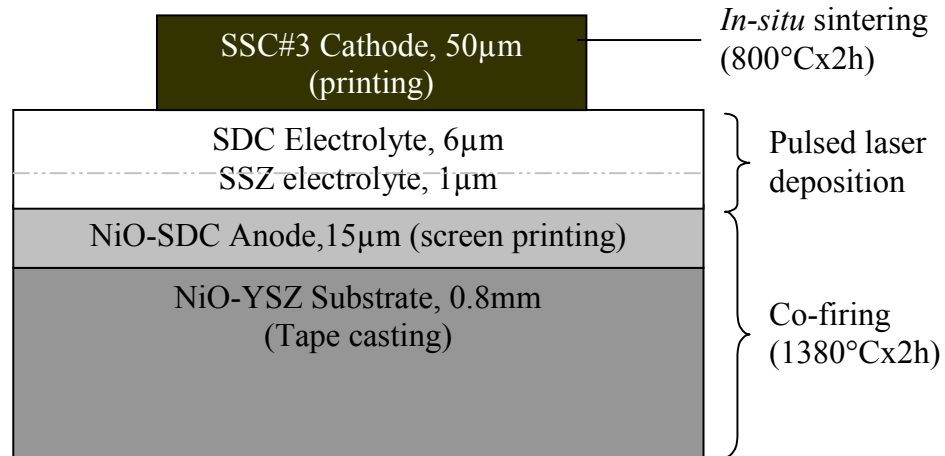


Figure 10-1 A schematic drawing of the cell structure and its fabrication methods.

The cell substrate was a NiO-YSZ cermet consisting of 57 wt% NiO and 43 wt%YSZ, prepared by the tape casting method. A NiO-SDC anode layer was applied by screen-printing on the cell substrate. The composition of the NiO-SDC anode was 47 wt.% SDC and 53 wt.% NiO. The cell substrate with the anode, of 20mm diameter (cut by a punch), was fired at 1380°C for 2hr. The heat-treated cell substrate was 17.5 mm in diameter and 0.8 mm in thickness. The NiO-SDC anode layer is approximately 15  $\mu\text{m}$  thick, with an average surface roughness of approximately 0.66  $\mu\text{m}$  measured by profilometry (Wyko NT9100 profilometer, USA). The average density of the cell substrate after the anode layer deposition was 5.10  $\text{g cm}^{-3}$ , measured by Archimedes' method. It indicates a 19.7 % porosity in the NiO-YSZ cermet substrate based on the cermet substrate composition of 53 wt.% NiO. The substrate porosity was calculated to increase to approximately 37% after reducing NiO to Ni with the hydrogen gas.

#### *Pulsed Laser Deposition (PLD) of electrolytes*

The bilayered SDC/SSZ electrolyte films were deposited by ablating a 90 mm diameter rotating SDC target (SDC, 99.9%, from Praxair) and an SSZ target (prepared by slip casting and sintering at 1500°C for 5hr), consecutively, in an advanced deposition chamber (PVD. Inc., PLD-3000, USA) by means of a pulsed KrF excimer laser ( $\lambda = 248$  nm, Lambda Physik, LPX-210i, USA), at a repetition rate of 50 Hz. The laser beam was focused down to a spot size of  $\sim 4 \text{ mm}^2$  on the target surface. The on-target laser beam fluence was adjusted to approximately 3 to 5  $\text{J/cm}^2$ . Silicon wafers [(100) orientation, p-type,  $\rho = 10\text{-}30 \ \Omega \text{ cm}$ , from Polishing Corporation of America, USA] and NiO-YSZ substrates with NiO-SDC anode were used.

Before introducing a Si wafer into the deposition chamber, it was cleaned by acetone, isopropyl alcohol, and then etched in 2.5 % HF acid for five minutes to remove the native oxide. No further cleaning was necessary for the NiO-SDC modified NiO-YSZ substrates. After loading the substrate, the system was pumped down to a base pressure below  $2 \times 10^{-7}$  Torr using a turbo-molecular pump. The substrate was then heated, under vacuum, using a programmable non-contact radiation heater. The substrate to be coated was facing the target, with a stand-off distance of 12 cm. To achieve uniform deposition over the entire substrate surface, the laser beam was rastered over the radius of the rotating

target. Oxygen gas pressure was adjusted to be 0 to 5.32 Pa (40 mTorr) during deposition. Detailed information about the deposition processes has been given elsewhere [12].

The film structure was examined by X-ray diffraction (XRD, X-Pert MRD Philips, The Netherlands) with monochromatized Cu  $K_{\alpha}$  in the  $\theta_0$ - $2\theta$  thin film configuration, where  $\theta_0$  was fixed at  $0.5^\circ$  for single layer films and  $0.5$  to  $3^\circ$  for bi-layer films. The cross-sections of the laser deposited SDC/SSZ bi-layer films were investigated by SEM (Hitachi FE-SEM S-4500, Japan) using the new super ExB filter technology. FE-SEM images were taken at a magnification of 100,000x with a 5 kV beam voltage. Based on the deposition rates obtained from the similar deposition condition on the silicon wafer, the thickness of the bi-layer electrolyte on cell substrates was approximately  $1\mu\text{m}$  SSZ plus  $6 \sim 7\mu\text{m}$  SDC.

#### *Cell characterization*

The surface of the PLD deposited bi-layer electrolyte appears shiny and transparent. The electrolyte shows a very low helium gas cross leakage rate,  $0.05 \text{ ml min}^{-1} \text{ cm}^{-2}$  at 13.8kPa (approximately 2psi), indicating that the electrolyte layer was almost fully dense. A SSC#3 cathode layer consisting of 75 wt.% SSC and 25 wt.% SDC with surface area of  $0.551 \text{ cm}^2$  was applied to the centre of the bi-layer electrolyte by stencil printing, and dried at  $100^\circ\text{C}$  for 1h. The thickness of the cathode layer was approximately  $40\text{-}50\mu\text{m}$  after *in-situ* sintering at  $800^\circ\text{C}$  for 2hr.

The cell electrochemical testing setup and the test procedure are similar to those previously stated. The cell was heated up to  $800^\circ\text{C}$  at a ramp rate of  $300^\circ\text{C h}^{-1}$ , and held at  $800^\circ\text{C}$  for 2hr for *in-situ* sintering of the cathode layer. The temperature was then decreased down to  $700^\circ\text{C}$  for the reduction of the anode and for the measurements of cell electrochemical performance. Ambient air was introduced at a flow rate of  $100 \text{ ml min}^{-1}$  to the cathode side. Hydrogen gas with the same flow rate was first passed through a bubbler-type humidifier at room temperature. The humidified hydrogen gas (corresponding to 3%  $\text{H}_2\text{O}$  content) was then introduced to the anode side during the cell test. Electrochemical measurements were performed at temperatures ranging from  $700$  to  $450^\circ\text{C}$ . Cell performance was measured with a Multi-channel Potentiostat/Galvanostat (Solartron 1480

8 channel multi-stat) with Corrview software. Current-voltage-power (I-V-P) curves were obtained using linear sweep voltametry at a sweep rate of  $4 \text{ mV s}^{-1}$  from OCV to 0.3V.

## **10.3 Results and discussion**

### **10.3.1 On Si(100) substrate**

The PLD technique was used to deposit thin films of SDC and SSZ on Si(100) substrates at the substrate temperature range of  $200 \sim 600^\circ\text{C}$  and reactive oxygen gas atmosphere of  $1 \text{ mTorr} \sim 40 \text{ mTorr}$ . By varying the deposition temperatures and oxygen gas pressures, SDC and SSZ films with various crystallite sizes, density and interfacial properties were grown successfully. XRD results indicate that both SDC and SSZ films were crystallized to cubic phases (PDF card # 75-0158 for SDC and card # 75-0158 for SSZ [13]) at relatively low deposition temperatures ( $\sim 200^\circ\text{C}$  for SDC and  $\sim 400^\circ\text{C}$  for SSZ, respectively). The density of the SDC films increases with an increase in the deposition temperature, while for SSZ it decreases with an increase in the deposition temperature. The densities of  $200^\circ\text{C}$  and  $400^\circ\text{C}$  SDC films are only 63% and 70%, respectively, of the density of the  $600^\circ\text{C}$  SDC films. In contrast, the  $200^\circ\text{C}$  SSZ film is denser than that of the  $400^\circ\text{C}$  and  $600^\circ\text{C}$  SSZ films. The densities of the  $400^\circ\text{C}$  and  $600^\circ\text{C}$  films are 82% and 77%, respectively, of the density of  $200^\circ\text{C}$  film of SSZ. The reasons for such a different behaviour of the two materials are not clear, since the physical phenomena of laser-target interaction and film growth are quite complex. Film growth and quality are dependent on a few fundamental parameters, namely, the substrate temperature, the kinetic energy of the deposition flux, and the deposition rate. Substrate temperature affects the mobility of the deposited atoms on the surface, and surface rearrangements are possible at higher temperatures, while at low temperature they are inhibited. The rate at which material impinges on the surface (i.e., the deposition rate) is highly dependent on the material that is to be deposited. The bandgap energy of ceria, which is  $\sim 3.2 \text{ eV}$  [14], is smaller than the photon energy of the KrF laser, which is  $\sim 5.0 \text{ eV}$ . Strong absorption of laser energy by ceria creates electron-hole pairs with considerable kinetic energy that couple with lattice vibrations leading to fast ablation of ceria with a high deposition rate. A high deposition

rate and low substrate temperature will result in a more porous film because of the reduced opportunity for film relaxation and surface rearrangement; therefore, SDC films deposited at low temperature are very porous. High substrate temperatures increase the mobility of the deposited atoms. Surface and bulk diffusion and re-crystallization occur, yielding larger crystallites; therefore, more dense SDC films were obtained at high substrate temperatures. In contrast to SDC, zirconium oxide (i.e. SSZ) has a bandgap energy of  $\sim 5.8$  eV [15], which is higher than the photon energy of a KrF laser. Relatively weak absorption of the laser energy, primarily through the multiphoton absorption mechanism by zirconium oxide, causes a weak ablation and low deposition rate. The low deposition rate allows SSZ film relaxation to occur; therefore, a more dense SSZ film with small grains can be formed at low substrate temperatures. As the substrate temperatures increase, the mobility of the deposited SSZ atoms increase, which allows the formation of larger grains, thereby slightly decreasing the film density of SSZ at high substrate temperatures.

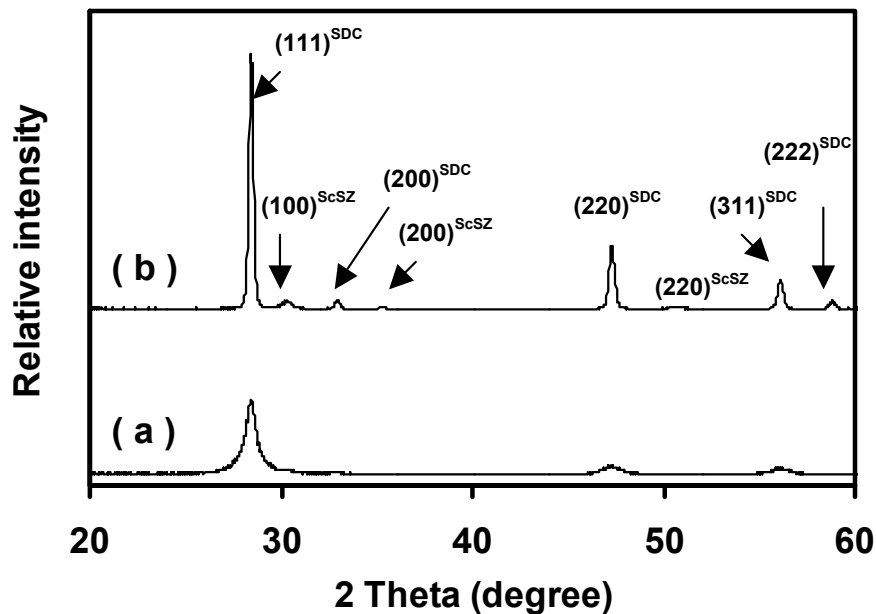


Figure 10-2 XRD spectra of SDC/SSZ bi-layer films deposited on silicon wafers at (a) 200 °C and (b) 600 °C in 40 mTorr  $O_2$ .

Figure 10-2 shows the XRD spectra of SDC/SSZ bi-layer films deposited on silicon wafers at 200 °C and 600 °C in 40 mTorr  $O_2$  process gas. The XRD spectra consist of

diffraction peaks originating from both cubic SDC and SSZ phases. Peak assignment is shown in Figure 10-3 for the SDC top layer and the SSZ layer underneath. No peak shift due to  $(\text{Zr}, \text{Ce})\text{O}_2$ -based solid solutions or additional peaks due to  $\beta$ -phase SSZ were found in the diffraction pattern, which indicates that during the deposition process, no chemical reaction occurred at the interface between SDC and SSZ. This means that the PLD technique is an excellent technique for growing both highly conductive cubic SSZ and SDC phases at very low processing temperatures. The laser deposition process can indeed stabilize the SSZ cubic phase at low temperatures that prohibits the phase transition from the more conductive cubic phase to the less conductive  $\beta$ -phase that occurs during the cooling step for most of the high temperature wet-ceramic processes. The SDC layer shows a strong (111) preferential orientation on the top of the cubic phase SSZ at both temperatures. The XRD peaks for the bi-layer film deposited at  $200^\circ\text{C}$  are quite broad and not well-defined, indicating that the grain size of the low temperature deposited bi-layer film is small and its crystallinity is poor. As the deposition temperature increases, the full-width at half maximum of the XRD peaks decreases, indicating that the grain size and crystallinity of films increases with the increase in deposition temperatures.

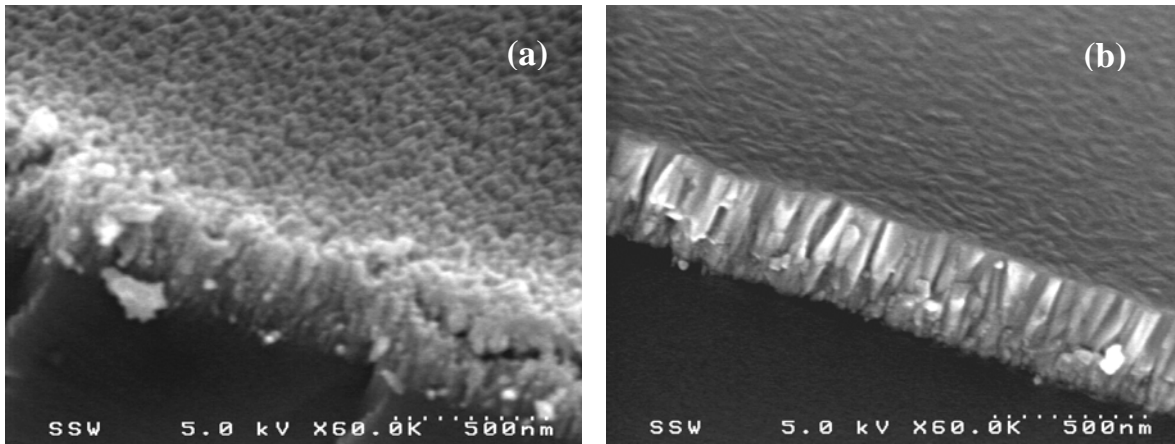


Figure 10-3 FE-SEM micrographs of SSZ/SDC bi-layer films deposited on silicon wafers at a substrate temperature of (a)  $200^\circ\text{C}$ , and (b)  $600^\circ\text{C}$  in 40 mTorr of  $\text{O}_2$ .

Figure 10-3 shows cross-sectional FE-SEM micrographs of SSZ/SDC bi-layer films deposited at a temperature of  $200^\circ\text{C}$  and  $600^\circ\text{C}$  in 5.32 Pa of oxygen. At  $200^\circ\text{C}$ , both SSZ and SDC layers contain small grains. The SDC layer is very porous, while the SSZ layer is

relatively dense. At 600°C, both SSZ and SDC layers contains columnar grains oriented perpendicularly to the substrate and are very dense. The grain diameter for the SDC layer is approximately 60-70 nm, while for the SSZ film it is approximately 30-40 nm. The surface of the 600 °C film is very smooth and does not show any cracks or pin-holes. The FE-SEM results are consistent with the XRD results.

All the above results clearly indicate that by simply selecting the process parameters of the PLD technique, bi-layer SDC/SSZ films with various microstructures, density, and interfacial properties can be deposited. It is obvious that a dense and gas impermeable layer is required for the electrolyte layer in SOFCs; therefore, appropriate process parameters should be selected for producing a dense SDC/SSZ bi-layer electrolyte for SOFCs. When considering the application of the PLD technique for the deposition of anode and/or cathode layers in SOFCs, where very porous structures are desired, different process parameters should be used to produce a microstructure similar to that shown in Figure 10-4 (a). The flexibility of the PLD process makes it a very promising technique for the fabrication of all solid-state devices based on multilayer thin films, such as miniaturized SOFCs.

### **10.3.2 On NiO-SDC modified NiO-YSZ substrates**

PLD processing was also used to deposit the SSZ/SDC bi-layered electrolyte on NiO-YSZ substrates with NiO-SDC anodes. The anode substrates were prepared and characterized for their surface roughness and helium gas permeability before the PLD processing. The surface roughness of the cermet substrates was approximately 0.66 $\mu\text{m}$  after the NiO-SDC modification. The SEM micrograph in Figure 10-4 (a) shows that the unmodified face is quite rough and uneven, with a roughness of approximately 1.5 $\mu\text{m}$ . The anode modified surface consists of a crack-free, smooth layer with small size and uniform crystallites, as shown in Figure 10-4 (b). The cross-sectional view in Figure 10-4 (c) shows that the NiO-SDC anode layer consists of much smaller grains (1 ~ 2  $\mu\text{m}$ ) compared to the NiO-YSZ substrate (10 ~ 20 $\mu\text{m}$ ).

SDC films of approximately 2  $\mu\text{m}$  thick were initially deposited on the anode substrates at the substrate temperatures ~500-600 °C and oxygen pressure of ~ 5-40 mTorr. The Low Angle XRD results confirmed that SDC films on the anode substrates were

indeed single-phase SDC with fluorite-type structure. The 2  $\mu\text{m}$  SDC film coated anode substrates had decreased He permeability, up to five times compared to the anode substrates alone. However, the cross-leakage of the samples was too high to conduct cell performance tests. FE-SEM examination of the SDC coated anode revealed the failure of the 2  $\mu\text{m}$  SDC layer to cover the  $\sim 1\text{-}2$   $\mu\text{m}$  diameter pinholes, existing on the anode surface. A much thicker SDC layer was needed in order to achieve the required gas tightness, which increases the electrical resistance of the electrolyte layer significantly.

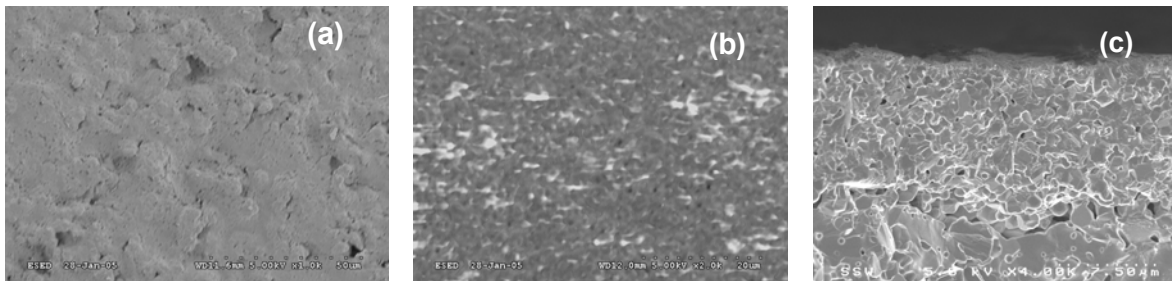


Figure 10-4 SEM Micrograph of surface view of (a) unmodified NiO-YSZ anode, (b) NiO-SDC modified NiO-YSZ and (c) cross-sectional view of NiO-SDC modified NiO-YSZ.

In order to effectively utilize the SSZ/SDC bi-layer electrolyte concept for reduced temperature SOFCs, the SSZ bottom layer should be as thin as possible and also be gas impermeable. The SSZ cannot directly be deposited on anode substrates prepared in this manner, since it requires a relatively thick SSZ layer to achieve the required gas tightness. Therefore, an additional NiO-SDC layer of about  $1\text{-}2\mu\text{m}$  thickness was initially deposited by PLD on the anode surface. This layer reduces the gas leakage of the anode substrate significantly and provides a smoother surface for the deposition of the SSZ layer due to the nanostructural nature of the PLD films. After the deposition of the additional NiO-SDC layer, SSZ of above  $0.5\text{-}1\mu\text{m}$  thick was deposited by PLD at substrate temperatures of  $\sim 200\text{-}400$   $^{\circ}\text{C}$  in  $\sim 5\text{-}20$  mTorr of oxygen pressure. Following the SSZ layer, a relatively thick SDC layer of approximately  $7\text{-}8\mu\text{m}$  was deposited at substrate temperatures of  $\sim 400\text{-}600$   $^{\circ}\text{C}$  in  $\sim 5\text{-}20$  mTorr. The surface and cross section of the bi-layer electrolyte was examined by FE-SEM (cross section shown in Figure 10-5). No cracks or pin-holes were found in the SEM micrographs. The measured He leakage of those bi-layer electrolyte coated anode substrates were less than  $0.05$   $\text{ml min}^{-1} \text{cm}^{-2}$  at  $13.8\text{kPa}$  He. The above results clearly indicate that the PLD technique is a suitable method to deposit dense and gas

impermeable layers not only on smooth surfaces such as silicon wafers but also on porous ceramic substrates such as NiO-SDC modified NiO-YSZ cermet.

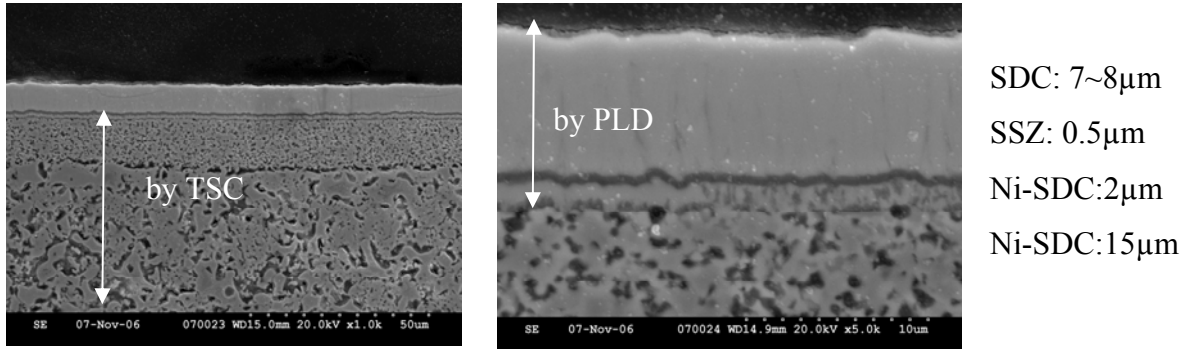


Figure 10-5 Cross section images of cell with bi-layered electrolyte deposited by PLD.

### ***Cell performance***

A composite cathode was then applied onto the surface of the bi-layer electrolyte by stencil printing, followed by drying and *in-situ* sintering. The unit cell thus prepared was characterized for its electrochemical performance. Figure 10-6 shows the cell performance with the SSC cathode *in-situ* sintered at 800°C for 2hr. It can be seen that the cell shows very high performance in the tested temperature range of 450-700°C. What is most significant is that the cell shows a very high OCV value, 1.04V, in comparison to the single 20  $\mu\text{m}$ -SDC electrolyte cell, which has an OCV of only 0.87 V at 600°C [9]. A high OCV value indicates that there is very low electronic conductivity and few physical defects (cracks, pin-holes, etc.) in the SSZ/SDC bi-layer electrolyte. A summary of the cell performance is listed in Table 10-2. In this table the series resistance  $R_s$ , polarization resistance  $R_p$ , and cell total resistance  $R_t$  are obtained from the cell impedance measurement (cf. Figure 10-7). The peak power density reaches 1.6  $\text{W cm}^{-2}$  at 700°C, and approximately 0.5  $\text{W cm}^{-2}$  even at 550°C, the highest performance ever reported with this type of bi-layered electrolyte structure. The high cell performance also indicates that the interfacial reaction between SSZ and SDC is successfully alleviated or eliminated due to the low deposition temperatures.

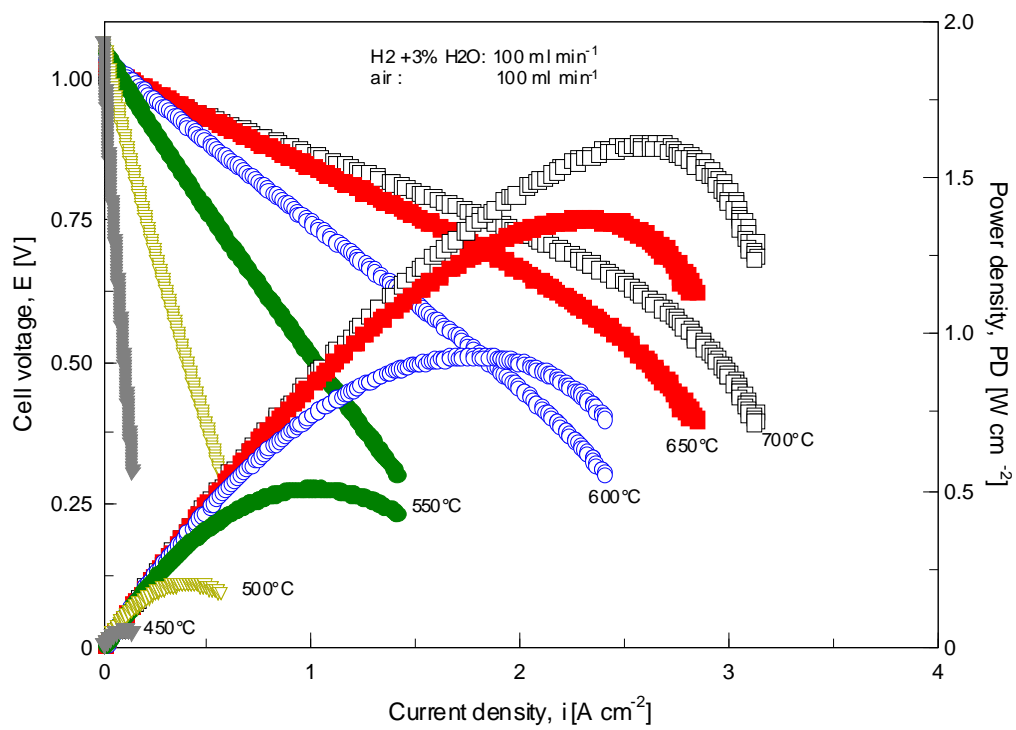


Figure 10-6 I-V and power curves at different temperatures

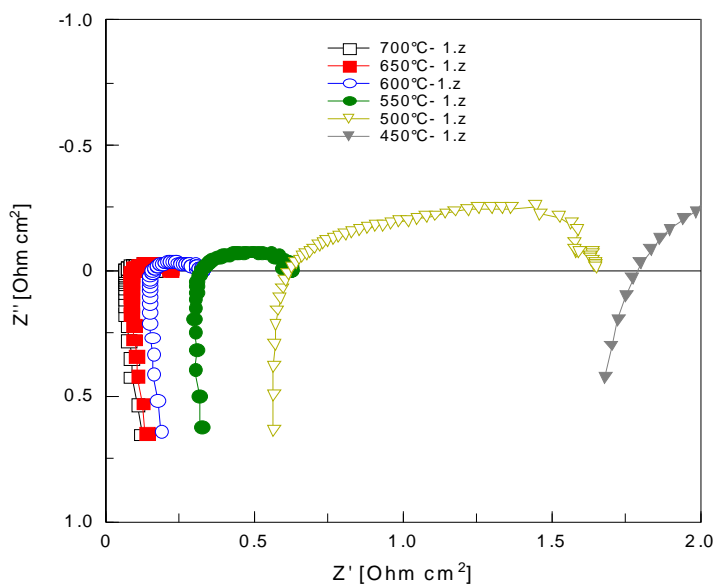


Figure 10-7 EIS results at different temperatures.

Table 10-2 A summary of the cell electrochemical performance

<b>Temperature (°C)</b>	<b>OCV (V)</b>	<b>Power (W cm<sup>-2</sup>)</b>	<b>R<sub>s</sub> (Ω cm<sup>2</sup>)</b>	<b>R<sub>p</sub> (Ω cm<sup>2</sup>)</b>	<b>R<sub>t</sub> (Ω cm<sup>2</sup>)</b>
450	1.066	0.051	1.780	4.992	6.772
500	1.062	0.200	0.618	1.058	1.676
550	1.051	0.509	0.299	0.311	0.609
600	1.038	0.955	0.157	0.165	0.321
650	1.022	1.376	0.092	0.125	0.217
700	1.006	1.619	0.069	0.099	0.168

#### **10.4 Conclusion**

The PLD technique has been used in this study to deposit SDC/SSZ bi-layer electrolytes on Si(100) substrates and on NiO-SDC modified NiO-YSZ cell substrates. By varying the deposition process parameter conditions, SDC/SSZ bi-layer electrolyte films with various crystallite sizes, density, and interfacial properties were successfully grown. The PLD technique was able to deposit the highly conductive cubic phases for both SSZ and SDC layers. Interfacial reaction between the SSZ and SDC layers that forms low conductivity (Zr, Ce)O<sub>2</sub>-based solid solutions was eliminated due to the low processing temperatures of the PLD technique. A unit cell that uses a PLD SSZ/SDC bi-layer electrolyte shows very high performance (1.38 W cm<sup>-2</sup>) and high open circuit voltage (1.022V) at 650°C. Comparing to wet ceramic processes that require high processing temperatures, the PLD method is a very promising low temperature process for the deposition of high quality thin electrolyte layers for low temperature SOFCs.

## 10.5 References

1. S. P. S. Badwal, K. Foger, *Ceramic International* 22 (1996) 257.
2. K. Eguchi, T. Setogushi, T. Inoue, H. Arai, *Solid State Ionics* 52 (1992) 165.
3. B. Zhu, *J. Power Sources* 93 (2001) 82.
4. Z. Shao, S. M. Haile, *Nature* 431 (2004) 170.
5. T. Shimonosono, Y. Hirata, Y. Ehira, S. Sameshima, T. Horita, H. Yokokawa, *Solid State Ionics* 174 (2004) 27.
6. Y. Arachi, H. Sakai, O. Yamamoto, Y. Takeda, N. Imanishi, *Solid State Ionics* 121 (1999) 133.
7. T. Ishii, T. Iwata, Y. Tajima, *Solid State Ionics* 57 (1992) 153.
- a. A. Tsoga, A. Gupta, A. Nanoumidis, P. Nikolopoulos, *Acta Mater.* 48 (2000) 4709.
8. M. Price, J. Dong, X. Gu, *J. Am. Ceram. Soc.* 88 (2005) 1812.
9. Xinge Zhang, Mark Robertson, Cyrille Decès-Petit, Wei Qu, Olivera Kesler, Radenka Maric, Dave Ghosh, *J. Power Sources* 175 (2008) 800.
10. S. Boughaba, G. I. Sproule, J. P. McCaffrey, M. Islam and M. J. Graham, *Thin Solid Films* 358 (2000) 104.
11. D. Yang, Conference proceeding of the International Conference on Processing & Manufacturing of Advanced Materials (Thermec' 2006), Vancouver, July 4-8, 2006
12. Powder Diffraction File-2 database, Joint Committee on Powder Diffraction Standards, International Centre for Diffraction Data, USA, 1996.
13. Z. Orel, B. Orel, *Phys. Status Solidi B*, 186 (1994) K33–K36.
14. N. Nicolso, A. Lobert, B. Leibold, *Sens. Actuators B* 8 (1992) 253.

## 11. Chapter Eleven. Summary of Dissertation Work and Outlook

As stated early in this dissertation, the general goal of this dissertation work is through understanding cell materials and cell processing technologies to develop SOFCs with both sufficient electrical efficiency and electrochemical performance at operating temperature below 650°C, called “low temperature SOFC development”. The results achieved in this work have met the performance targets set at the beginning of this dissertation work. The main results are summarised as follows.

- Samaria-doped ceria (SDC) electrolyte cells with Ni-SDC anode and SSC-SDC composite cathode have been successfully fabricated by using a conventional ceramic processing technology and the cell size has been enlarged from ½”- 1” button cells (for laboratory cell material and cell structure studies) up to 8cm x 8cm square cells with or without holes (for short stack development by industrial partners). Along with the cell fabrication technology development, many engineering challenges, such as cell functional layer cracks during screen-printing, electrolyte cracking and spallation, cell deformation during co-firing, and hole-zone induced cell cracks, have been solved in a timely manner. Hundreds of SDC electrolyte cells with a uniform and dense electrolyte with thickness down to 10µm have been fabricated and tested.
- The SDC cell performance reaches as high as 0.9W cm<sup>-2</sup> at 600°C. This encouraging cell performance has been verified by two European partners using the cells (of size 5cm x 5cm) developed by the author.
- A further study of the SDC electrolyte cell showed that internal shorting will be an obstacle to reaching high fuel utilization and high electrical efficiency. A specific experiment has been designed for the leakage current measurement. The measured leakage current density under open circuit condition reaches 0.85A cm<sup>-2</sup> at 600°C, which limits fuel utilization and electrical efficiency. The internal shorting is due to the mixed conductivity behaviour of the SDC electrolyte, a common challenge (problem) that many developers are facing and to which many researchers are trying to find a solution.

- Modification of the electrolyte layer through an SSZ/SDC bi-layered electrolyte structure has been pursued thereafter in this dissertation work. The bi-layered electrolyte button cells and 5cm x 5cm cells based on conventional ceramic processing technology have been fabricated and evaluated. The performance of the bi-layered cells reaches 0.74V at 0.5A/cm<sup>2</sup> at 650°C with H<sub>2</sub> fuel, meeting the performance target as described in Chapter 1 of this dissertation. However, the cells with bi-layered electrolyte structure showed long-term stability issues, which have been identified to be related to the cathode stability, as described in Chapter 9. Meanwhile, the impedance results indicate that the interaction between electrolyte layers requires special fabrication methods to avoid.
- Pulsed laser deposition (PLD) of the bi-layered electrolyte has been used in this work to understand the influence of the interaction between layered electrolytes. A cell with bi-layered electrolyte of 1μm SSZ and 6μm SDC prepared by PLD exhibits much higher performance, 1.4 W cm<sup>-2</sup> at 650°C, compared to wet-ceramic produced electrolytes, with limited internal shorting (OCV 1.022V). Such high performance of this cell structure is reported for the first time in the open literature.
- Adding sintering aids such as copper oxide or cobalt oxide significantly decreased the sintering temperature of ceria powder. The results of interaction between zirconia- and ceria- powder materials showed the formation of zirconia-ceria solid solution, that was completely formed at 1300°C. The new phase appeared at lower temperatures if ceria modified by sintering aid at 1100°C with copper oxide and at 1200°C with cobalt oxide. Interestingly, the observed inter-diffusion of the electrolyte materials of the bi-layered electrolyte cells fabricated by co-firing occurred within 1.5 to 2μm. Both XRD analysis of the powder mixture and EDS analysis at the cross-section of the bi-layered cells indicated the diffusion of Ce into the Zr-phase.

Based on the results achieved so far, and cell material knowledge and cell fabrication experience gained from this work, an outlook for future development of low temperature SOFCs is presented as follows.

### ***11.1 Cell material development***

The electrolyte is an important component for SOFC development. To date, there are limited electrolyte material systems suitable for low temperature SOFC development [1]. Among the preferred zirconia-based electrolyte materials, 10%Sc<sub>2</sub>O<sub>3</sub>-1% CeO<sub>2</sub> stabilized ZrO<sub>2</sub> seems a rational candidate with respect to its conductivity and stability [2]. Because of the conductivity limitation of the ZrO<sub>2</sub>-based electrolytes, it is still difficult to meet the electrolyte resistance requirement of 0.15Ω cm<sup>2</sup> below 600°C with this electrolyte unless the thickness of a dense ZrO<sub>2</sub>-based electrolyte can be practically fabricated down to the micrometer or even sub-micrometer size range. For ceria-based electrolyte materials, poor stability at low oxygen partial pressure requires the finding of new ideal co-dopants and doping levels to improve stability (i.e., to reduce the electronic conductivity) and still retain adequate ionic conductivity [3]. Although decreasing the operating temperature minimises the reduction of the ceria-based electrolyte, it requires electrolyte thickness reduction to compensate the decrease in the ionic conductivity. As observed in the dissertation work, a decrease in thickness of the SDC electrolyte resulted in a lower open circuit voltage. Therefore, uncertainty remains in this approach. For LSGM-based materials, regardless of their high cost, Ga evaporation under reducing atmospheres [4], low chemical compatibility with Ni-based anodes [5], and cost-effective thin LSGM electrolyte processing are big challenges. Therefore, new electrolyte materials of highly pure O<sup>2-</sup> ionic conductivity, good chemical stability, and chemical compatibility with electrodes essentially remain as a key area for the future development of low temperature SOFCs.

### ***11.2 Cell structure***

A highly performing cathode is necessary for low temperature SOFC development. Promising mixed conductive cathode materials react with the zirconia electrolyte materials, resulting in cell performance loss and durability concerns. Therefore, anode supported cell with a dense ceria-based electrolyte is preferred for the state-of-the art anode supported zirconia-based electrolyte cell structure. In order to reduce the electrolyte resistance, both zirconia electrolyte and ceria barrier layer should be as thin as possible. For operating temperatures of 600°C ± 50°C, a bi-layered electrolyte cell structure shows certain

advantages in regards to good cell performance. This dissertation work has demonstrated that electrolyte resistances of bi-layered electrolyte cells by co-firing and by PLD are approximately  $0.3 \Omega \text{ cm}^2$  [6] and  $0.09 \Omega \text{ cm}^2$  [7] at  $650^\circ\text{C}$ , respectively. The SSC cathodes used in this work show cathode resistances ( $R_c$ ) of approximately  $0.1 \Omega \text{ cm}^2$  at  $600^\circ\text{C}$ , and  $0.06 \Omega \text{ cm}^2$  at  $650^\circ\text{C}$ . Therefore, a bi-layered cell structure is capable of meeting the cell performance requirements ( $R_t$  less than  $0.5 \Omega \text{ cm}^2$ ) at operating temperature below  $650^\circ\text{C}$ . The main issue is the development of a cost-effective fabrication technology to mitigate the interaction between the two electrolyte layers.

### ***11.3 Ultra-thin electrolyte SOFCs operating at lower temperature***

Ultra-thin electrolyte cells will be an interesting research area for SOFCs operating below  $500^\circ\text{C}$ , such as portable micro-SOFCs. Based on the  $R_{el}$  requirement of  $0.15 \Omega \text{ cm}^2$ , the thickness of ceria-based electrolytes or bi-layered electrolytes has to be 5 micrometers or less. Such electrolyte thickness is possible to be fabricated by wet ceramic processing as demonstrated in Chapter 8, but ensuring the processing quality control will be difficult and important. Meanwhile, electrodes, especially the cathode will be another challenge for retaining cell performance. Although the ceria-based electrolyte is promising for low temperature SOFCs, its electronic conductivity problem at elevated temperatures has to be solved. Since the electronic conductivity of ceria-based electrolytes becomes negligible at temperatures below  $500^\circ\text{C}$ , the future development of lower temperature SOFCs may use ultra-thin ceria-based electrolytes as a good approach to retain adequate cell performance at such a low temperature range.

### ***11.4 Electrolyte utilization in ultra-thin electrolyte cell***

When the electrolyte thickness is reduced to micrometer and sub micrometer for compensating the electrolyte resistance at a lower temperature, electrolyte utilization will be an emerging issue. This is because of the electrolyte contacts with porous electrodes possessing pores sized at almost the same dimension of the electrolyte thickness in the state-of-the art SOFC electrodes. The electrolyte may not effectively function at those micro-pore areas, and the shadowing effect will limit the electrolyte utilization as a whole

[8]. In this regard, nano-particle sized electrode configurations and their processing methods have to be explored in order to improve the electrolyte utilization.

### ***11.5 Low temperature cost-effective deposition approaches for bi-layered electrolyte cells***

Low temperature SOFC cathodes commonly react with preferred electrolyte material stabilized zirconia during operation and form an insulating zirconate phase. A dense barrier layer of doped ceria is required to avoid the reaction. Because inter-diffusion between ceria and zirconia occurs at temperatures as low as 1000°C, conventional fabrication techniques, which incorporate a high temperature sintering step to densify the electrolyte, suffer an electrolyte resistance beyond that of the individual electrolyte layers. An alternative direct deposition process with processing temperature less than 1000°C is recommended in this regard. Vacuum based physical vapor deposition methods, including pulsed laser deposition, magnetron sputtering, and electron beam evaporation, have been demonstrated as having this capability. However, vacuum based physical vapor deposition methods inevitably have a high implementation cost, which not only arises from the requirement of a controlled vacuum environment during deposition and the limited scalability to large area substrates, but also from the relatively low deposition rates. In order to meet the target cost for the commercialization of SOFCs (< \$400/kW), only cost-effective processes should be considered for the fabrication of the bi-layered electrolyte. Besides the approaches used in this dissertation work, suspension thermal spraying technique and spray pyrolysis technique are recommended for the future development due to their potential of low cost and low substrate temperature deposition of a dense ceria thin film on the top surface of a zirconia electrolyte substrate at processing temperature less than 700°C [9].

### ***11.6 Metal-supported LT-SOFC development***

Although conventional ceramic-supported solid oxide fuel cells (SOFCs) demonstrate a good cell performance at reduced operating temperature of 650°C or below, the intrinsic brittleness of the cermet substrate generates two main drawbacks. One is the difficulty in scaling up the cell size to the m<sup>2</sup> level in order to meet a large demand on power output. The second drawback is that the cermet substrate alone takes over 90% of the total cell

material cost, which limits the SOFC cost reduction to meet the market requirement (\$400/kW). Metal-supported SOFCs offer many advantages over conventional ceramic-supported SOFCs [10]. Due to their good thermal conductivity and ductility, metal-supported SOFCs may both improve thermal shock resistance and alleviate internal temperature gradients. Switching from ceramic supports to metal supports also allows use of conventional metal joining and forming techniques, and mitigates the challenges on sealing and electrical connection (contact). The most significant advantages of using metal supports are the opportunity to significantly reduce the material and manufacturing costs of SOFC stacks and to provide sufficient mechanical strength for cell size scale-up to meet large power outputs in practice. Despite these potential merits, a metal-supported cell has to operate below 600°C owing to metal oxidation. Two big challenges lie ahead. One is the missing of a practical deposition technology of thin ceramic coatings on porous metal supports. The other is the lack of a stable metal support with well-defined material and microstructure. The processing challenges have seriously impeded the development of metal-supported SOFCs. Therefore, low temperature cost-effective deposition approaches for bi-layered electrolyte cells (as stated in the section 11.5) are important for low temperature metal-supported SOFC development.

### ***11.7 Cathode stability issue***

Improving cathode stability is a key to improving the bi-layered electrolyte cell stability. Several approaches are recommended for future research: 1) modify the cathode composition and microstructure, to improve CTE matching with the electrolyte, 2) improve the cathode bonding strength with the electrolyte by optimizing cathode sintering process, 3) study degradation mechanisms of mixed conductive cathodes on ceria-based electrolytes.

## **11.8 References**

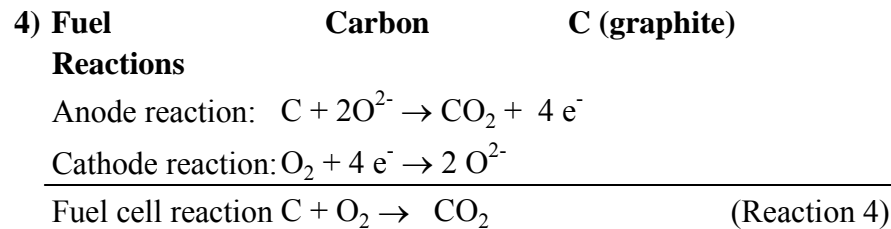
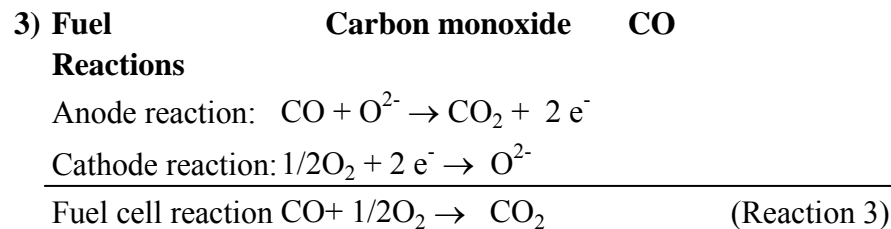
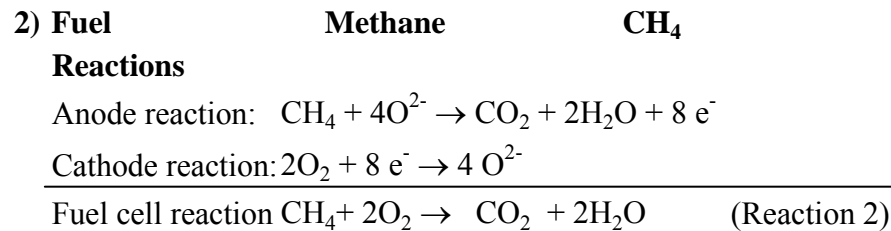
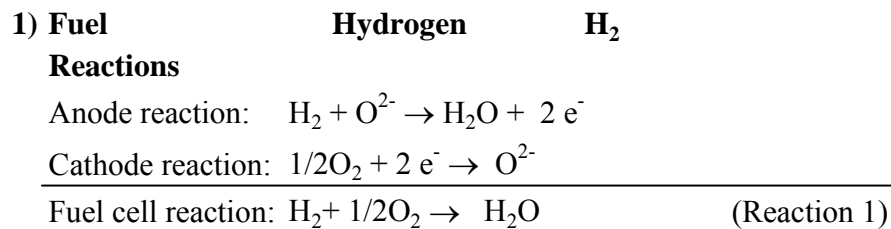
1. J. W. Fergus, *J. Power Sources* 162 (2006) 30.
2. A. Lee, I. Lee, Y. Jeon and R. Song, *Solid State Ionics* 176 (2005) 1021.
3. R. Hui, J. Roller, S. Yick, X. Zhang, C. Decès-Petit, Y. Xie, R. Maric and D. Ghosh, *J. Power Sources* 172 (2007) 493.
4. K. Yamaji, T. Horita, M. Ishikawa, N. Sakai and H. Yokokawa, *Solid State Ionics* 121 (1999) 217.
5. X. Zhang, S. Ohara, R. Maric, K. Mukai, T. Fukui, H. Yoshida, M. Nishimura, T. Inagaki, and K. Miura, *J. Power Sources* 83 (1999) 170.
6. X. Zhang, M. Robertson, C. Decès-Petit, W. Qu, O. Kesler, R. Maric, D. Ghosh, *J. Power Sources* 175 (2008) 800.
7. D. Yang, X. Zhang, C. Decès-Petit, R. Hui, R. Maric, D. Ghosh, *J. Power Sources* 164 (2007) 182.
8. J. I. Gazzarri and O. Kesler, *J. Power Sources* 167 (2007) 430.
9. Y. Xie, R. Neagu, C. Hsu, X. Zhang, and C. Deces-Petit, *J. Electrochem. Soc.* 155 (2008) B 407.
10. S. Hui, D. Yang, Z. Wang, S. Yick, C. Decès-Petit, W. Qu, A. Tuck, R. Maric, D. Ghosh, *Journal of Power Sources* 167 (2007) 336.

## 12. Appendices

### Appendix A. Thermodynamic calculations

Four types of fuels are used for the thermodynamic calculations. They are hydrogen (H<sub>2</sub>), methane (CH<sub>4</sub>), carbon monoxide (CO), and carbon (C). Air is used as the oxygen source for the cell reactions.

The cell reactions are listed below:



From Lange's Handbook 15<sup>th</sup> ed., the enthalpies ( $\Delta H_f^\circ$ ) and Gibbs energies ( $\Delta G_f^\circ$ ) of formation, entropies ( $S^\circ$ ), and heat capacities ( $C_p^\circ$ ) of the reaction species of the above reactions (1)-(4) are listed in Table 12-1.

Table 12-1 Enthalpies and Gibbs energies of formation, entropies, and heat capacities of the reaction species (Data from Lange's Handbook 15<sup>th</sup> edition)

Species	$\Delta H_f^\circ$ [kJ/mol]	$\Delta G_f^\circ$ [kJ/mol]	$S^\circ$ [J/(molK)]	$C_p^\circ$ [J/(molK)]
C (s)	0	0	5.74	8.517
CH <sub>4</sub> (g)	-74.6	-50.5	186.3	35.7
CO (g)	-110.53	-137.16	197.66	29.14
CO <sub>2</sub> (g)	-393.5	-394.4	213.8	37.1
H <sub>2</sub> (g)	0	0	130.68	28.84
H <sub>2</sub> O(g)	-285.8	-237.1	70.0	75.4
O <sub>2</sub> (g)	0	0	205.2	29.4

At a temperature of T, the standard Gibbs free energies  $\Delta G_T^\circ$  and Nernst potentials  $E_{N,T}$  of Reactions (1)-(4) are calculated based on Equations 12-1 to 12-13. The calculation results are listed in Tables 12-2 to 12-5.

$$\Delta H^\circ = \Sigma(\Delta H_{f,j}^\circ)_{\text{products}} - \Sigma(\Delta H_{f,i}^\circ)_{\text{reactants}} \quad (\text{Equation 12-1})$$

$$\Delta G^\circ = \Sigma(\Delta G_{f,j}^\circ)_{\text{products}} - \Sigma(\Delta G_{f,i}^\circ)_{\text{reactants}} \quad (\text{Equation 12-2})$$

$$\Delta S^\circ = \Sigma(\Delta S_j^\circ)_{\text{products}} - \Sigma(\Delta S_i^\circ)_{\text{reactants}} \quad (\text{Equation 12-3})$$

$$\Delta C_p^\circ = \Sigma(\Delta C_{p,j}^\circ)_{\text{products}} - \Sigma(\Delta C_{p,i}^\circ)_{\text{reactants}} \quad (\text{Equation 12-4})$$

$$\Delta H_T^\circ = \Delta H^\circ + \Delta C_p^\circ (T-298) \quad (\text{Equation 12-5})$$

$$\Delta G_T^\circ = \Delta G^\circ + \Delta S^\circ (T-298) \quad (\text{Equation 12-6})$$

$$E^{\circ} = \Delta G^{\circ} / (nF) \quad (\text{Equation 12-7})$$

$$E^{\circ}_T = E^{\circ} + \Delta S^{\circ} (T-298) / (nF) \quad (\text{Equation 12-8})$$

$$E_N = E_T^{\circ} + \frac{RT}{4F} \ln p_{O_2(C)} + \frac{RT}{2F} \ln \frac{P_{H_2(A)}}{P_{H_2O(A)}} \quad (\text{Equation 12-9, for Reaction 1})$$

$$E_N = E_T^{\circ} + \frac{RT}{4F} \ln p_{O_2(C)} + \frac{RT}{8F} \ln \frac{P_{CH_4(A)}}{P_{CO_2(A)} P_{H_2O}^2} \quad (\text{Equation 12-10, for Reaction 2})$$

$$E_N = E_T^{\circ} + \frac{RT}{4F} \ln p_{O_2(C)} + \frac{RT}{2F} \ln \frac{P_{CO(A)}}{P_{CO_2(A)}} \quad (\text{Equation 12-11, for Reaction 3})$$

$$E_N = E_T^{\circ} + \frac{RT}{4F} \ln p_{O_2(C)} + \frac{RT}{4F} \ln \frac{1}{P_{CO_2(A)}} \quad (\text{Equation 12-12, for Reaction 4})$$

$$\text{Theor. eff.} = \Delta G^{\circ}_T / \Delta H^{\circ}_T \quad (\text{Equation 12-13})$$

The typical SOFC exhibits an ohmic resistance behaviour during the operation with a typical Voc of approximately 1 V. Assuming that the cell operates at  $i = 0.5 \text{ A cm}^{-2}$  under fuel utilization  $U_f = 80\%$  at 873K, based on Equations (1-4) and (1-14) (cf. Chapter 1), the required values for cell efficiency ( $\varepsilon$ ), cell voltage ( $V_{\text{cell}}$ ), and cell resistance ( $R_t$ ) can be calculated and are listed in Table 12-6.

$$R_t = (V_{\text{oc}} - V_{\text{cell}}) / i \quad (\text{Equation 1-4})$$

$$\varepsilon = \frac{\Delta G^{\circ}_T}{\Delta H^{\circ}_T} \times \frac{V_i}{E^{\circ}_T} \times U_f \quad (\text{Equation 1-14})$$

Table 12-2 Thermodynamic calculation results of Reaction 1 using hydrogen as fuel

H <sub>2</sub> fuel								
T [K]	298	673	773	873	973	1073	1173	1273
$\Delta H^{\circ}_T$ [kJ/mol]	-241.83	-245.55	-246.55	-247.54	-248.54	-249.53	-250.52	-251.52
$\Delta G^{\circ}_T$ [kJ/mol]	-228.61	-211.95	-207.51	-203.07	-198.63	-194.18	-189.74	-185.30
Theor. efficiency[%]	0.945	0.863	0.842	0.820	0.799	0.778	0.757	0.737
$E^{\circ}_T$ [V]	1.1847	1.0984	1.0753	1.0523	1.0293	1.0063	0.9833	0.9602
$E_{N,T}$ [V]*	1.2193	1.1765	1.1651	1.1537	1.1423	1.1309	1.1195	1.1081

\*under ambient atmosphere      anode      97%H<sub>2</sub>+3%H<sub>2</sub>O      cathode      air

Table 12-3 Thermodynamic calculation results of Reaction 2 using methane as fuel

CH <sub>4</sub> fuel								
T [K]	298	673	773	873	973	1073	1173	1273
$\Delta H^{\circ}_T$ [kJ/mol]	-802.56	-798.88	-797.89	-796.91	-795.93	-794.94	-793.96	-792.98
$\Delta G^{\circ}_T$ [kJ/mol]	-801.11	-799.18	-798.66	-798.15	-797.63	-797.12	-796.60	-796.09
Theor. efficiency[%]	0.998	1.000	1.001	1.002	1.002	1.003	1.003	1.004
$E^{\circ}_T$ [V]	1.0379	1.0354	1.0347	1.0340	1.0334	1.0327	1.0320	1.0314
$E_{N,T}$ [V]*	1.0627	1.0916	1.0992	1.1069	1.1146	1.1223	1.1300	1.1377

\*under ambient atmosphere      anode      95%CH<sub>4</sub>+2%CO<sub>2</sub>+3%H<sub>2</sub>O      cathode      air

Table 12-4 Thermodynamic calculation results of Reaction 3 using carbon monoxide as fuel

CO fuel								
T [K]	298	673	773	873	973	1073	1173	1273
$\Delta H^{\circ}_T$ [kJ/mol]	-282.98	-285.50	-286.17	-286.84	-287.51	-288.18	-288.85	-289.52
$\Delta G^{\circ}_T$ [kJ/mol]	-257.23	-224.81	-216.17	-207.52	-198.88	-190.23	-181.59	-172.94
Theor. efficiency[%]	0.909	0.787	0.755	0.723	0.692	0.660	0.629	0.597
$E^{\circ}_T$ [V]	1.3330	1.1650	1.1202	1.0754	1.0306	0.9858	0.9410	0.8962
$E_{N,T}$ [V]*	1.3676	1.2432	1.2100	1.1768	1.1436	1.1104	1.0772	1.0441

\*under ambient atmosphere      anode      97%CO+3%CO<sub>2</sub>      cathode      air

Table 12-5 Thermodynamic calculation results of Reaction 4 using carbon as fuel

Carbon fuel								
T [K]	298	673	773	873	973	1073	1173	1273
$\Delta H^{\circ}_T$ [kJ/mol]	-393.51	-393.81	-393.88	-393.96	-394.04	-394.12	-394.20	-394.28
$\Delta G^{\circ}_T$ [kJ/mol]	-394.39	-395.47	-395.76	-396.05	-396.34	-396.63	-396.92	-397.21
Theor. efficiency[%]	1.002	1.004	1.005	1.005	1.006	1.006	1.007	1.007
$E^{\circ}_T$ [V]	1.0219	1.0247	1.0255	1.0262	1.0270	1.0277	1.0285	1.0292
$E_{N,T}$ [V]*	1.0121	1.0025	1.0000	0.9974	0.9949	0.9923	0.9898	0.9872

\*under ambient atmosphere      anode      97%CO<sub>2</sub>      cathode      air

Table 12-6 Relation of cell efficiency with cell voltage and cell resistance for different fuels

<b>Fuel type</b>	<b>eff. (e) [%]</b>	<b>30</b>	<b>40</b>	<b>50</b>	<b>60</b>
H <sub>2</sub>	V <sub>cell</sub> [V]	0.481	0.641	0.802	0.962
	R <sub>t</sub> [ $\Omega$ cm <sup>2</sup> ]	1.038	0.717	0.397	0.076
CH <sub>4</sub>	V <sub>cell</sub> [V]	0.387	0.516	0.645	0.774
	R <sub>t</sub> [ $\Omega$ cm <sup>2</sup> ]	1.226	0.968	0.709	0.451
CO	V <sub>cell</sub> [V]	0.557	0.743	0.929	
	R <sub>t</sub> [ $\Omega$ cm <sup>2</sup> ]	0.885	0.514	0.142	
C	V <sub>cell</sub> [V]	0.383	0.510	0.638	0.766
	R <sub>t</sub> [ $\Omega$ cm <sup>2</sup> ]	1.234	0.979	0.724	0.469

#### **A short summary**




It is clear that for an SOFC to reach 50% electrical efficiency, the total cell resistance may vary with different types of fuels. For H<sub>2</sub>, it should be approximately 0.4 $\Omega$  cm<sup>2</sup>, while for carbon it can be 0.72  $\Omega$  cm<sup>2</sup>, due to their thermodynamic efficiency difference.

## **Appendix B. Electrolyte conductivity and cathode characterization**

### **Materials: YSZ (8Y), SSZ, SDC, and SSC**

Electrolyte preparation was carried out by powder cold pressing at 50MPa for 2 minutes with a die of 20mm in diameter, then firing for 5hr at 1400°C for YSZ and SSZ, and at 1450°C for SDC. The electrolyte pellets are then polished to remove potential contamination during the firing. SSC cathodes are applied to both surfaces of the electrolyte pellets, after the thickness of the electrolytes was recorded. Table 12-7 details the information obtained about the electrolytes and symmetric cells.

Table 12-7 Information of the electrolytes and symmetric cells

<b>Cell configuration</b>	<b>SSC/SDC/SSC</b>	<b>SSC/SSZ/SSC</b>	<b>SSC/YSZ/SSC</b>
Electrolyte material	SDC	SSZ	YSZ
Sample appearance			
Thickness of electrolyte (cm)	0.0490	0.0715	0.0691
Diameter of electrolyte (cm)	1.545	1.53	1.564
Sintering condition	1450°C x5hr	1400°C x5hr	1400°C x5hr
Electrolyte density (g/cm <sup>3</sup> )	7.01	5.87	5.88
Cathode material	SSC	SSC	SSC
Diameter of electrode A (mm)	8.00	9.00	8.00
Area of electrode (cm <sup>2</sup> )	0.50	0.64	0.50
Sintering condition before measurement	in situ heating up to 950°C	in situ heating up to 850°C	in situ heating up to 850°C

### **Characterization: density, electrolyte conductivity and cathode performance**

Density was determined by Archimedes method, and by weight and volume calculations. Conductivity testing was performed using symmetric cells with in-situ

sintered SSC cathodes. Measurements were conducted in air in the temperature range of 500-850°C at 50°C intervals, by EIS and by potentiodynamic tests at scan rates of 4mV/sec in the range of  $\pm 200$ mV. Cathode polarization resistances were obtained from the EIS measurement.

## **Results**

### **1. Electrolyte conductivity**

Figure 12-1 is the Arrhenius plot of the conductivity of the three electrolytes SDC, SSZ, and YSZ used in this study. Table 12-8 summarizes the measured conductivity results of these electrolyte materials.

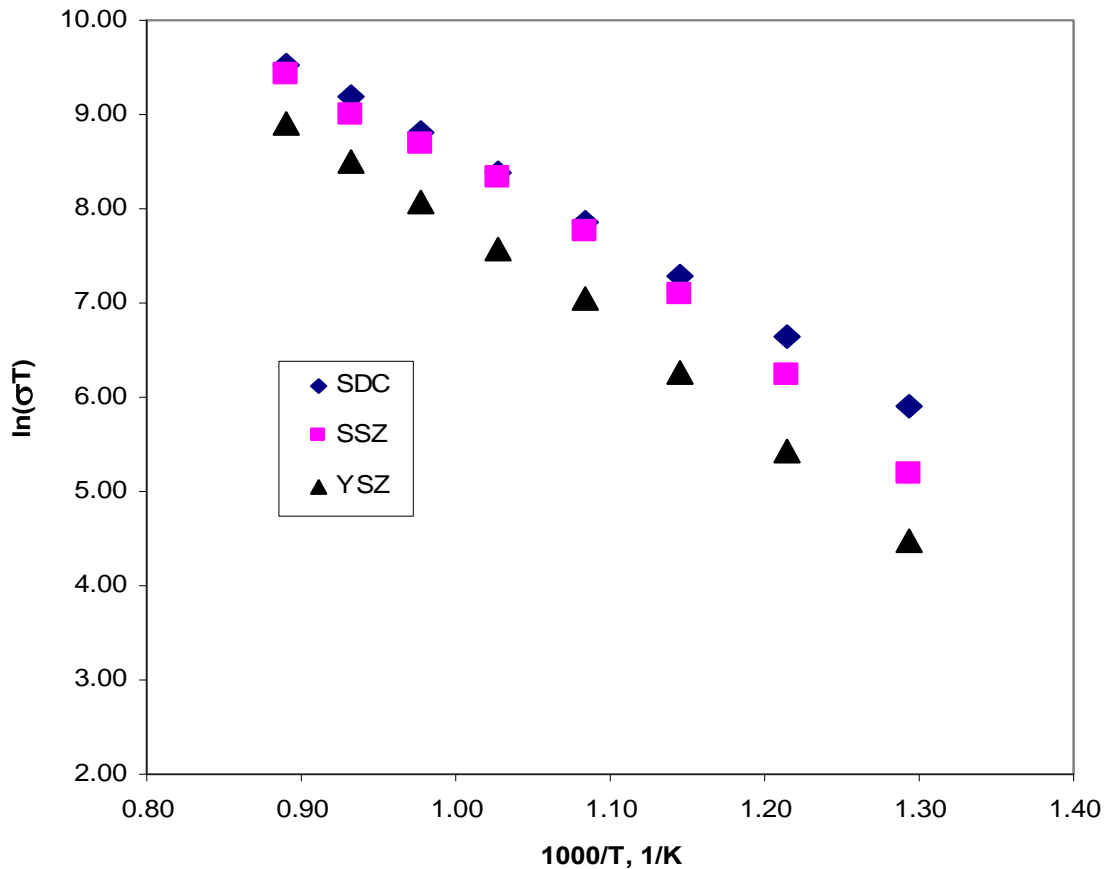


Figure 12-1 Measured conductivities of SDC, SSZ, and YSZ electrolytes used in this study.

Table 12-8 Conductivity results of the three electrolytes SDC, SSZ, and YSZ, in this study

Temperature (°C)	1000/T (1/K)	Conductivity (S m <sup>-1</sup> )		
		SDC	SSZ	YSZ
500	1.294	0.4717	0.2298	0.1136
550	1.215	0.9277	0.6207	0.2757
600	1.145	1.6713	1.3880	0.6016
650	1.083	2.8319	2.5516	1.2409
700	1.028	4.5062	4.2369	1.9859
750	0.977	6.5990	5.8027	3.0935
800	0.932	9.1349	7.5931	4.5530
850	0.890	12.1243	11.2000	6.4937

According to the Arrhenius equation (1-12), we have  $\ln(\sigma T) = a - b/T$  (here  $\sigma$  is the conductivity,  $T$  is absolute temperature,  $a$  and  $b$  are coefficients) and  $E_a = bR$  (here  $R$  is the gas constant). Fitting the experimental data with this formula, we have the activation energy  $E_a$  values of the electrolytes, listed in Table 12-9.

Table 12-9 Fitting results for electrolyte conductivity

Temperature	Parameter	SDC	SSZ	YSZ
500-650°C	a	18.01	21.18	20.25
	b	9.37	12.34	12.20
	$E_a(\text{kJ mol}^{-1})$	77.87	102.61	101.43
650-850°C	a	16.88	16.60	17.50
	b	8.26	7.98	9.67
	$E_a(\text{kJ mol}^{-1})$	68.64	66.36	80.36
500-850°C	a	17.63	18.78	18.75
	b	9.04	10.33	10.95
	$E_a(\text{kJ mol}^{-1})$	75.14	85.88	91.03

Our results are in good agreement with results published by others for the same or similar compositions [1, 2]. For example, Bunčan *et al.* reported [3] the conductivity of SDC as 1.67–2.08 S m<sup>-1</sup> at 600°C, and 8.3–9.8 S m<sup>-1</sup> at 800°C based on similar EIS measurements with different electrode materials: Au, Pt, Ag, or LSCF.

It has been claimed that GDC and SDC are the best candidates for LT-SOFCs due to high ionic conductivity and good compatibility with mixed conductivity cathode materials, in spite of the obvious problem of electronic internal leakage. The results shown in Figure 12-1 seem to question the claim of doped ceria being a much better ionic conductor than any zirconia, unless the temperature is well below 600°C. The SSZ electrolyte used in this study also exhibits high ionic conductivity.

## **2. Cathode performance**

Using similar symmetric cells for electrolyte conductivity measurement, two samples with the composite cathodes SSC#3, pre-sintered at 1000°C for 2hr on the SDC electrolytes, were also tested in this study.

The results are listed in Table 12-10 along with pure SSC cathode resistances. The obtained SSC cathode activation energy is approximately 125–132 kJ mol<sup>-1</sup>, comparable to the literature 131 kJ mol<sup>-1</sup> [4]. It is clear that the resistance of SSC is slightly better than the SSC#3 (with 25wt% SDC), which is a typical composite cathode in this dissertation work. It seems that the ionic conductivity of pure SSC cathode material is sufficiently high. Common SSC+SDC composite cathode approach may only benefit to thermo-mechanical and microstructural stability of the cathode. The measured cathode resistances using symmetric cells seem slightly higher than in the thin SDC electrolyte cells which demonstrate an  $R_p$  at 600°C of approximately 0.1Ω cm<sup>2</sup>. There are two possible explanations for this deviation: one is that in the cermet-supported SDC cell, the cell temperature may be slightly higher than the monitored temperature due to the internal shorting mechanism. The second is that using the symmetric cell to get the  $R_c$  may not be very reliable because one of the electrodes is working as a cathode (oxygen reduction), while the other electrode is working as an anode (oxygen evolution). The  $R_c$  obtained in this way is half of the  $R_p$  in the EIS measurement, under an assumption that both oxygen

reduction and evolution have the same resistance, which may be not valid. However, this approach is accepted by some renowned research groups [5, 6].

Table 12-10 SSC and SSC#3 cathode resistances on SDC electrolyte obtained from symmetric cells

Temperature (°C)	1000/T (1/K)	Cathode resistance $R_c$ ( $\Omega \text{ m}^2$ )		
		SSC	SSC#3-1	SSC#3-2
450	1.386	3.871	6.124	3.756
500	1.293	1.268	1.514	1.206
550	1.215	0.404	0.533	0.444
600	1.145	0.118	0.152	0.173
650	1.083	0.041	0.062	0.071
700	1.028	0.015	0.027	0.016
$E_a$ ( $\text{kJ mol}^{-1}$ )		131.4	127.7	125.6

## References

1. M. Mogensen, D. Lybye, K. Kammer, N. Bonanos, SOFCIX, 2005-07 (2005) 1068.
2. S. Wang, T. Kobayashi, M. Dokiya, T. Hashimoto, J. Electrochem. Soc. 147 (2000) 3606.
3. H. Duncan, A. Lasia, SOFCIX, 2005-07 (2005) 1081.
4. Y. Liu, W. Rauch, S. Zha, M. Liu, Solid State Ionic 166 (2004) 261.
5. W. G. Wang, M. Mogensen, Solid State Ionics 176 (2005) 457.
6. Z. Shao, S. M. Haile, Nature 431 (2004) 170.

## **Appendix C. Publication list**

As the first author or co-author, the following journal papers and conference presentations have been published during my dissertation work period.

### Refereed Journals

1. Xinge Zhang, Javier Gazzarri, Mark Robertson, Cyrille Decès-Petit, Olivera Kesler, Stability study of low temperature SOFCs with bilayered electrolyte, *J. Power Sources* 185 (2008) 1049-1055.
2. Xinge Zhang, Mark Robertson, Cyrille Decès-Petit, Wei Qu, Olivera Kesler, Radenka Maric, Dave Ghosh, Solid oxide fuel cells with bi-layered electrolyte structure, *J. Power Sources* 175 (2008) 800-805.
3. Yongsong Xie, Roberto Neagu, Ching-Shiung Hsu, Xinge Zhang, and Cyrille Decès-Petit, Spray pyrolysis deposition of electrolyte and anode for metal-supported solid oxide fuel cell, *J. Electrochem. Soc.* 155 (2008) B 407.
4. Rob Hui, Justin Roller, Sing Yick, Xinge Zhang, Cyrille Decès-Petit, Yongsong Xie, Radenka Maric and Dave Ghosh, A brief review of the ionic conductivity enhancement for selected oxide electrolytes, *J. Power Sources* 172 (2007) 493-502.
5. Xinge Zhang, Mark Robertson, Cyrille Decès-Petit, Wei Qu, Olivera Kesler, Radenka Maric, Dave Ghosh, Internal shorting and fuel loss of a low temperature solid oxide fuel cell with SDC electrolyte, *J. Power Sources* 164 (2007) 668-677.
6. Dongfang Yang, Xinge Zhang, Suwas Nikumb, Cyrille Decès-Petit, Rob Hui, Radenka Maric, Dave Ghosh, High performance low temperature SOFC prepared by pulsed laser deposition, *J. Power Sources* 164 (2007) 182-188.
7. Yongsong Xie, Xinge Zhang, Mark Robertson, Radenka Maric and Dave Ghosh, Measurement of the interface adhesion of solid oxide fuel cells by indentation, *J. Power Sources* 162 (2006) 436-443.
8. Xinge Zhang, Cyrille Decès-Petit, Sing Yick, Mark Robertson, Olivera Kesler, Radenka Maric, Dave Ghosh, A study on sintering aids for  $\text{Sm}_{0.2}\text{Ce}_{0.8}\text{O}_{1.9}$  electrolyte, *J. Power Sources* 162 (2006) 480-485.

9. Xinge Zhang, Mark Robertson, Sing Yick, Cyrille Decès-Petit, Edward Styles, Wei Qu, Yongsong Xie, Rob Hui, Justin Roller, Olivera Kesler, Radenka Maric, Dave Ghosh,  $\text{Sm}_{0.5}\text{Sr}_{0.5}\text{CoO}_3 + \text{Sm}_{0.2}\text{Ce}_{0.8}\text{O}_{1.9}$  composite cathode for cermet supported thin  $\text{Sm}_{0.2}\text{Ce}_{0.8}\text{O}_{1.9}$  electrolyte SOFC operating below  $600^\circ\text{C}$ , *J. Power Sources* 160 (2006) 1211-1218.
10. Radenka Maric, Cyrille Decès-Petit, Rob Hui, Xinge Zhang, Dave Ghosh and Murata Kenji, Preparation and characterization of nanocrystalline  $\text{Ba}_2\text{In}_{2-x}\text{M}_x\text{O}_5$ ,  $\text{M} = \text{Ce}, \text{Zr}$ , *J. Electrochem. Soc.* 153 (2006) A1505-1510.
11. Xinge Zhang, Mark Robertson, Cyrille Decès-Petit, Yongsong Xie, Rob Hui, Sing Yick, Edward Styles, Justin Roller, Olivera Kesler, Radenka Maric, Dave Ghosh, NiO-YSZ cermet supported low temperature solid oxide fuel cells, *J. Power Sources* 161 (2006) 301-307.
12. Rob Hui, Radenka Maric, Cyrille Decès-Petit, Edward Styles, Wei Qu, Xinge Zhang, Justin Roller, Sing Yick, Dave Ghosh, Ko Sakata, and Murata Kenji, Proton Conduction in Ceria-doped  $\text{Ba}_2\text{In}_2\text{O}_5$  Nanocrystalline Ceramic at Low Temperature, *J. Power Sources* 161 (2006) 40-46.

#### Conference Presentations and Proceedings

1. Xinge Zhang, Mark Robertson, Cyrille Deces-Petit, Yongsong Xie, Stability of bi-layered electrolyte SOFCs, FC seminar-2008, Pheonix.
2. Radenka Maric, Roberto Neagu, Xinge Zhang, Justin Roller, High performance cathode fabricated by RSDT, FC seminar-2008, Pheonix.
3. J. Gazzarri, X. Zhang, O. Kesler and Q. Wang, Numerical simulation of the performance decay of a bi-layered electrolyte SOFC, 214th ECS Meeting – Honolulu, 2008.
4. Xinge Zhang, Mark Robertson, Cyrille Decès-Petit, Wei Qu, Olivera Kesler, Radenka Maric, Dave Ghosh, Fabrication and characterization of cermet supported cell with SDC electrolyte, SOFC X, 2007, 899-903
5. Adam Tuck, Xinge Zhang, Rob Hui, Wei Qu, Cyrille Deces-Petit, Yongsong Xie, Justin Roller, Kyong-Bok Min, Mark Robertson, Sing Yick, Radenka Maric, Dave

- Ghosh, Development status of SOFC cell and stack technology at NRC-IFCI, SOFC X, 2007, 285-294.
6. Yong Song Xie, Roberto Neagu, Ching-Shing Hsu, Xinge Zhang and Cyrille Deces-Petit, Spray pyrolysis deposition of electrolyte and anode for metal supported SOFC, SOFC X, 2007, 787-794
  7. Cyrille Deces-petit, Xinge Zhang, Radenka Maric, Effect of sintering aids on the formation of zirconia-ceria solid solution, SOFC X, 2007, 2277-2282
  8. Xinge Zhang, Mark Robertson, Sing Yick, Cyrille Deces-Petit, Edward Styles, Wei Qu, Yongsong Xie, Rob Hui, Justin Roller, Olivera Kesler, Radenka Maric, Dave Ghosh, Ethanol fueled cermet-supported thin SDC electrolyte SOFC at 600°C, 1<sup>st</sup> Hydrogen and Fuel Cell 2007 International Conference, Vancouver, May, 2007
  9. Yongsong Xie, Xinge Zhang, Mark Robertson, Radenka Maric, Dave Ghosh, Mechanical strength and interface adhesion of a solid oxide fuel cell with doped ceria electrolyte, Thermec-2006, Vancouver, July, 2006
  10. Wei Qu, Dave Ghosh, Xinge Zhang, Radenka Maric, "Characterization of commercial borosilicate based glasses for solid oxide fuel cell sealing", presented to the 30<sup>th</sup> International Conference & Exposition on Advanced Ceramic & Composites, Symposium 3 - the 3rd International Symposium on Solid Oxide Fuel Cells, Cocoa Beach, Florida, January 22-27, 2006.

Papers accepted or submitted

1. Yongsong Xie, Roberto Neagu, Ching-Shiung Hsu, Xinge Zhang, Cyrille Decès-Petit, Wei Qu, Rob Hui, Sing Yick, Mark Robertson, Radenka Maric, and Dave Ghosh, Thin film solid oxide fuel cells deposited by spray pyrolysis, J. Fuel Cell Science and Technology, in press.
2. Ching-Shiung Hsu, Bing-Hwai Hang, Yongsong Xie, Xinge Zhang, Enhancement of solid oxide fuel cell performance by double-layer LSCF cathode, J. Electrochem. Soc., in press.

The PhD candidate would like to thank the Department of Mechanical Engineering and the Faculty of Graduate Studies at University of British Columbia for providing this study opportunity and financial support.